Seismological tools for geothermal exploration and monitoring

vorgelegt von
M. Sc.
Tania Andrea Toledo Zambrano
ORCID: 0000-0002-6870-2194

an der Fakultät VI - Planen Bauen Umwelt
der Technischen Universität Berlin
zur Erlangung des akademischen Grades

Doktor der Naturwissenschaften
-Dr. rer. nat.-

genehmigte Dissertation

Promotionsausschuss:
Vorsitzender: Prof. Dr. Thomas Neumann
Gutachterin: Prof. Dr. Charlotte Krawczyk
Gutachter: Prof. Dr. Hansruedi Maurer (ETH Zürich)
Gutachterin: Prof. Dr. Maren Brehme (TU Delft)
Gutachter: Dr. Philippe Jousset (GFZ Potsdam)
Tag der wissenschaftlichen Aussprache: 13. April 2021

Berlin 2021

A las mujeres de mi vida: María, Tania, Ana

Acknowledgements

Building this thesis has been a great challenge I could have hardly accomplished without the support system of colleagues, friends, and family. I have been incredibly blessed to be accompanied by all of you throughout the highs and lows of this adventure called PhD. In that sense, I like to think of this thesis not as *mine* but as *ours*.

To Charlotte Krawczyk: Lotte, I am grateful for your constant support and dedication not only to me but to the entire group. In the last years I have scarcely met someone as dedicated and hardworking as you. You are somewhat of an inspiration to me of what it means to be a woman in science. Although fully committed to various tasks, you took the time to discuss with me how to move forward with my work. I am grateful to you for pushing me to order my ideas and to exercise seeing the *bigger picture* in the things I do. I think this is something I will carry with me from this day on, so thank you.

To Philippe Jousset: Thank you for your support, creativity, and unceasing good humor throughout the past 4 years. Despite the many commitments, you made sure to be available to discuss any doubts or crazy ideas I had. I am very grateful for your trust in my capacity and judgement. At times I thought you trusted me too much but I am now happy you did because it pushed me to think independently and accomplish things I previously did not think I would be capable of. As part of your *scientific children* group, I am happy to consider you not only a supervisor but also a friend.

To Hansruedi Maurer: Thank you for your sustained guidance and support over the last 4+ years. From my seeking of your advice upon the end of my master program, to the quick responses to any doubts I had along the way. You have been very present and available one-call away. On our video conferences, I was continuously amazed at your efficiency and your ability to spot details from my slides without seeing the processing. This encouraged me to meticulously reason things through and constantly ask myself the question *why*. Thank you for trusting me and for taking so much time to help me become a researcher. It has been such a pleasure to work and learn so much from you.

To my GFZ colleagues working for the GEMex Project: Katrin Kieling, Anna Jentsch, David Bruhn. You have been my project *dream team*: from the direction and organizational aspects including the equipment handling for the fieldwork campaign, to the open data and knowledge sharing. Frankly, this work could have never reached the quality it has today without your valuable contributions. I left every project meeting feeling proud to belong to such well-rounded and hardworking group, and I look forward to a future project together again.

To Emmanuel Gaucher, Anne Obermann, Joana Martins, Arie Verdel: Thank you for your trust in my capacity and for the time you took to share with me your expertises. I have been incredibly lucky to collaborate and learn so much from you. Working with you has been like *tickling the brain*. I left every meeting with you feeling both excited and motivated to continue learning. Thus, I look forward to working closely with you in the future.

To my Mexican colleagues: Thank you for the nice collaborations and for the fun and efficient field campaign. I was happy to work with such flexible and optimistic group that looks beyond the obstacles to find suitable solutions on the go.

To Kemal Erbas: Thank you for your enthusiasm, openness, and trust in my ideas. Despite my being a young researcher, you took my proposals seriously and allowed me to explore them without hesitation. Your energy was always contagious and I enjoyed our work dynamic together with Malte and David. Thank you also for your motivation when I was low and for encouraging me to believe more in myself.

To Malte Metz and David Naranjo: Thank you for the enthusiastic, eager to learn, and hands-on dynamic you brought into our work group. Working with you was very encouraging and did not feel like work at all. I learned so much from/and with you, and I look forwards to see what you work on in the future.

To Michael Weber: Thank you for sharing your wisdom with me over the last years. From casually dropping on my desk the latest paper I needed to read for my research to the many deep conversations about life and where to go in the future. In every situation when I thought I have reached a dead end, you somehow managed to find solutions. And you even made it seem so easy! Thanks to you, I shall always keep in mind to make a task *list* wherever I go. Thank you for believing and nurturing not only the researcher in me but the human being as well.

To Anke Lerch (the Career Center and the Welcome Center teams): Thank you for our many conversations, your guidance, and the thought-provoking questions about the future. I am very grateful for your work guiding young researchers like me, and for the constant reminders to look after the person beyond the scientist.

To my dear GFZ colleagues: Thank you for making my experience at the GFZ a very enjoyable one, and for the delightful conversations over coffee breaks and over our famous *Mahlzeit*.

To all my friends: In particular to Sr. Gabriela, Femia, Rahel, Mauro, Lydia for your constant calls and messages of support reminding me of the *heart* behind the *brain*. It was a joy to have you so close to me despite the distance. You never failed to let me know you were there for me through this challenging journey and beyond, so thank you.

To my amazing roommates: Not only were you feeding me during the last strides of my PhD, you managed to make me laugh when I thought I was done for good. Thank you for your friendships and for encouraging me to look forward to the future.

A mi familia: En especial a mi mamá y a mi abuelita. Doy gracias a Dios por el regalo de ustedes, su optimismo, humor y fortaleza. You are at my core, and I am who I am because of you. Thank you for reminding me to focus on the good, to smile, and to always enjoy and be grateful for the ride.

Zusammenfassung

Wichtige Aspekte der geothermischen Exploration und Nutzung sind die Bewertung und Reduzierung der natürlichen und/oder induzierten Seismizität, die Abbildung und Ressourcenbewertung eines geothermischen Reservoirs, sowie die Überwachung der Auswirkungen der Explorationsaktivitäten. In dieser Arbeit werden die Analysen und Anwendungen verschiedener seismologischer Methoden zur Planung, Erkundung und Überwachung geothermischer Felder vorgestellt. Die untersuchten und hier weiterentwickelten Methoden umfassen das Design für den Aufbau und die Bewertung mikroseismischer Netzwerke, die lokale Erdbebentomographie, die *Ambient-Noise*-Tomographie und die Coda-Wellen-Interferometrie. Diese Techniken werden angewendet, um die geothermischen Felder Los Humeros (Mexiko), Theistareykir (Island) und Reykjanes (Island) zu untersuchen.

Die Geometrie seismologischer Arrays ist essentiell für eine gute Bestimmung seismischer Ereignisse mit kleinen Lokationsungenauigkeiten. Ein sequenzieller Algorithmus zum Design des Arrays, der eine Qualitätskennzahl auf der Grundlage des D-Kriteriums verwendet, wurde benutzt, um das seismische Netzwerk in Theistareykir zu erweitern und die Geometrie des Reykjanes-Netzwerks zu testen. Unter der Annahme von mittleren Ablesefehlern von $t_p = 0.2$ s und $t_s = 0.4$ s für P- und S- Wellen verbessert das erweiterte Theistareykir-Netzwerk die berechneten Hypo-Zentren um 0.2 km innerhalb des neuen Netzes. Das Reykjanes-Netz könnte andererseits um bis zu 18 Stationsstandorte reduziert werden und dennoch vergleichbare Lokationsgenauigkeiten erzielen. Diese Studie zeigte die Wichtigkeit vor den eigentlichen Feld-Experimenten Tests möglicher Array-Designs durchzuführen um die Kosten für ein geothermisches Projekt (erforderliche Anzahl von Sensoren) zu optimieren und gleichzeitig gute Lokationen für erwartete seismische Ereignisse zu erhalten (Nutzen/Kostenverhältniss).

Um die seismischen Strukturen der geothermischen Felder Los Humeros und Theistareykir zu charakterisieren, wurden an beiden Standorten eine lokale Erdbebentomographie und eine *Ambient-Noise*-Tomographie berechnet. Eine lokale Erdbebentomographie ist in Gebieten mit hoher Seismizität und guter Strahlenabdeckung (Erdbeben/Stationsgeometrie) möglich. Eine *Ambient-Noise*-Tomographie hängt nur von einer guten und ausreichend dichten Stationsverteilung ab. Mit den Ergebnissen dieser Studien wurden dann erstmals die seismischen Strukturen und die Dynamik dieser beiden produzierenden Felder ermittelt.

Die Seismizitätsverteilung in Los Humeros wurde verwendet, um Strukturen und potenzielle Verbesserungen in der Durchlässigkeit einiger Störungszonen zu charakterisieren. Das abgeleitete Vp-Modell wurde mit Bohrloch-Daten und Ultraschall-Messungen an Gesteinsproben kombiniert, um die Grenzen verschiedener geologischer Einheiten abzuschätzen. Das Vp/Vs-Modell wurde dann in Kombination mit Widerstandsdaten und Oberflächen-CO_2-Messungen verwendet, um die Geometrie der leitfähigen Tonkappe abzuleiten (Vp/Vs $\leq$ 1.65 und

Widerstand $\leq$ 10 Ωm), um Fluide zu identifizieren (reduzierte Vp Werte, Vp/Vs $\geq$ 1.71 und Widerstände zwischen 10-60 Ωm) und um gasführende Bereiche zu lokalisieren (Vp/Vs $\leq$ 1.55 und hohe CO_2-Konzentrationen). Eine ähnliche Studie wurde in Theistareykir durchgeführt, wo das Vs-Modell mit Widerstandsdaten kombiniert wurde, um magmatische und/oder hydrothermale Körper zu identifizieren (Vs $\leq$ -7 %, Widerstände $\leq$ 30 Ωm). Eine wichtige Schlussfolgerung aus diesen Studien ist, dass die Kombination von seismischen Eigenschaften mit zusätzlichen geologischen und/oder geophysikalischen Daten Mehrdeutigkeiten vermeidet und robuste Interpretationen der Dynamik und Struktur eines geothermischen Reservoirs liefert.

Weiterhin wurde eine Coda-Wellen-Interferometrie-Technik (Dehnungsmethode) auf zwei Jahre Ambient-Noise-Daten im Geothermiefeld Theistareykir angewendet, um mögliche Geschwindigkeitsänderungen aufgrund der Nutzung des Feldes zu überwachen. Hier waren die Auswirkungen der Injektions- und Produktionsveränderungen auf das $\Delta v/v$-Verhältnis sehr gering und nur eine kleine, möglicherweise produktionsbedingte, langfristige Geschwindigkeitsreduktion wurde festgestellt (-0.05 %/Jahr innerhalb des Produktionsbereichs im Vergleich zum regionalen Wert von -0.04 %/Jahr). Solche Beobachtungen sind für die sichere langfristige Ausbeutung von geothermischen Feldern von großer Bedeutung. Obwohl es noch keine Standardpraxis ist, ist die Berechnung dieser Änderungen weiterhin sehr nützlich, um aseismische Prozesse vor potenziell ausgelösten/induzierten großen seismischen Ereignissen zu steuern, sie ergänzen weiterhin die mikroseismische Überwachung.

Mit diesen Ergebnissen trägt die vorgelegte Arbeit zu den Bemühungen der Internationalen Energieagentur bei, die Nutzung von Geothermie zu entwickeln und zu erhöhen.

Abstract

Important aspects of geothermal exploration and exploitation are the assessment and mitigation of natural and/or induced seismicity, the imaging and resource assessment of a geothermal reservoir and the monitoring of the effects of the exploitation activities. With this thesis the analysis and application of various seismological tools for the planning, exploration, and monitoring of geothermal fields are given. The methods explored and further developed include survey design for microseismic network construction and assessment, local earthquake tomography, ambient noise tomography, and coda wave interferometry. These techniques were applied to study Los Humeros (Mexico), Theistareykir (Iceland) and Reykjanes (Iceland) geothermal fields.

The geometry of seismological arrays is essential for high quality seismic event retrieval and minimal location errors. A sequential survey design algorithm that uses a quality measure based on the *D-criterion* was applied to extend the seismic network at Theistareykir and to qualify the geometry of the Reykjanes network. Assuming mean picking errors of t_p = 0.2 s and t_s = 0.4 s, the extended Theistareykir network presented an improvement of $\sim$ 0.2 km for the computed hypocentral components of seismic events located within the new network. Conversely, we estimated that the Reykjanes network could spare up to 18 of its station locations and obtain comparable location errors nonetheless. This study showed the importance of prior survey design experiments to optimize the expenses for a geothermal project (required number of sensors) while obtaining good location estimates of expected seismic events (benefit/cost relations).

To characterize the seismic structures at Los Humeros and Theistareykir geothermal fields, a local earthquake tomography and an ambient noise tomography were computed at both locations, respectively. A local earthquake tomography is feasible in areas with high seismicity and good ray coverage (earthquake/station geometries). On the other hand, an ambient noise tomography depends on a good and sufficiently dense station distribution. With the results of these studies, the seismic structures and the dynamics of these two producing fields were obtained for the first time.

The seismicity distribution at Los Humeros was used to characterize structures and potential permeability enhancements in some of the existing faults. The retrieved Vp model was combined with available well log data and ultrasonic pulse measurements of collected rock samples to estimate the boundaries of different geologic units. The Vp/Vs model was then used in combination with resistivity data and surface CO_2 measurements to deduce the geometry of the conductive clay cap (Vp/Vs $\leq$ 1.65 and resistivities $\leq$ 10 Ωm), to identify fluid (Vp reduction, Vp/Vs $\geq$ 1.71, and resistivities between $\sim$ 10-60 Ωm), and to locate gas bearing regions (Vp/Vs $\leq$ 1.55 and high surface CO_2 concentrations). A similar study was

carried out at Theistareykir, where the Vs model was combined with resistivity data to identify magmatic and/or hydrothermal bodies (Vs $\leq$ -7 %, resistivities $\leq$ 30 Ωm). An important conclusion from these studies is that the combination of seismic properties with additional geological and/or geophysical data avoids ambiguities and provides robust interpretations of the dynamics and structure of a geothermal reservoir.

Finally, a coda wave interferometry technique (stretching method) was applied to two years of ambient noise records at the Theistareykir geothermal field with the aim to monitor possible velocity changes due to the exploitation activities. Here, the effects of the injection and production changes were very small on the computed $\Delta v/v$ ratio and only a small long-term velocity reduction (possibly due to production) was detected (-0.05 %/year at the producing field compared to a regional -0.04 %/year). Such observations are also very relevant for the safe long-term continuation of exploitation activities. Although not yet a standard practice, the computation of these changes is very useful to control aseismic processes prior to potentially triggered/induced large seismic events and is complementary to microseismic monitoring.

With these results, this thesis contributes to the efforts of the International Energy Agency to develop and increase the use of geothermal energy.

Table of Contents

List of Figures

List of Tables

1

Introduction

1.1 General context

The Industrial Revolution started in the late eighteenth and early nineteenth century with the replacement of manual labor by machinery operated mainly with fossil fuels. Since then, scientists have pointed out to the rapid increase of greenhouse gases emissions (40% more CO_2 compared to pre-industrial times) leading to a critical rise of global temperatures (*IPCC*, 2013, 2014).

In a world with increasing energy demands, clean alternatives have become essential for climate change mitigation and policy making (e.g. the Paris Agreement of 2015). Promising sources to meet these demands include geothermal energy and heat production. According to the *International Energy Agency* (2011), if implemented, developed, and encouraged, geothermal energy could contribute ca 3.5% (1400 TWh per year) of the global electricity production by 2050, thus preventing the emission of almost 800 megatons (Mt) of CO_2 per year. In addition, the generated geothermal heat could contribute ca 3.9% (1600 TWh thermal energy) of the projected global heat energy by 2050. To meet these targets, the International Energy Agency recommends, among others, the development of databases, protocols, and tools for geothermal resource assessment, management, and monitoring.

1.2 Geothermal resources and their assessment

A geothermal resource requires a circulating fluid, heat, and adequate rock permeability to extract energy. Temperatures of at least 120°C and permeability rates of ≥50 L/s at depths of at least 3 km are necessary in Europe for deep geothermal, for example, to achieve economic power production (*Hirschberg et al.*, 2015; *Huenges and Ledru*, 2010). Similarly, temperatures above 70°C at depths of 2-3 km are needed for direct heating purposes (*Hirschberg et al.*, 2015). *Hirschberg et al.* (2015) advice, however, to distribute this service to nearby end users to limit the energy loss due to transportation.

There are two types of geothermal resources (*International Energy Agency*, 2011):

- Hydrothermal resources: These systems make use of the natural high rock permeability and existing aquifers for their economic exploitation. They are common near plate boundaries and are often associated to active volcanism and seismicity (*Hamza et al.*, 2008; *International Energy Agency*, 2011).

- Hot rock resources: These are hot and dry systems with limited permeability. For their exploitation to be profitable, their permeability must be first significantly enhanced so that fluid circulation between injection and production wells can be achieved. The rock volume is stimulated to create and open fractures by hydraulic fracturing, hence the common name *enhanced geothermal systems* (EGS).

The successful exploitation of a geothermal reservoir requires a thorough priory resource assessment. This involves estimating the underground temperature, the presence and extent of fluids (mainly for hydrothermal systems), the degree of permeability (e.g. fracturing, faulting, and anisotropy), and the 3D geometry of the resource (*Hirschberg et al.*, 2015). To this purpose, several geophysical prospecting surveys are usually a prerequisite in the exploration phase of a geothermal target. These techniques include, among others, magneto telluric (MT) (e.g. *Benediktsdóttir et al.*, 2019; *Karlsdóttir et al.*, 2012), gravity (e.g. *Portier et al.*, 2020), and active and passive seismic (e.g. *Martins et al.*, 2020b; *Muksin et al.*, 2013; *Toledo et al.*, 2020a) surveys.

1.3 Passive seismic as a tool for exploration and monitoring of geothermal resources

Passive seismic imaging uses natural and/or induced seismicity or, conversely, the continuously recorded ambient seismic noise to characterize the 3D geometry of the reservoir and its seismic properties. Seismic properties such as the compressional P-wave (Vp) velocity, the shear S-wave (Vs) velocity, and the Vp/Vs ratio can be used as tools to derive lithologies, changes of fluid content, rock porosity, and temperature of geothermal systems (e.g. *Calò and Dorbath*, 2013; *De Matteis et al.*, 2008; *Jousset et al.*, 2011; *Martins et al.*, 2020b; *Muksin et al.*, 2013; *Toledo et al.*, 2020a). These seismic properties are to be assessed, however, in complementarity with other geophysical and geological methods for robust interpretations. Additionally, in seismically active geothermal settings, the study of local seismicity helps defining the geometry of existing faults and possible fluid pathways in the subsurface.

In addition to their imaging potential, passive seismic techniques have proven to be robust tools for monitoring time-lapse changes of geothermal systems. Monitoring procedures include the observation of Vp and Vs variations (e.g. *Calò and Dorbath*, 2013), and changes in micro-seismicity ($M_L \leq 2.0$) levels detected with sensitive seismic networks. The latter is relevant during the stimulation phase of an EGS (hydraulic fracturing), as well as in any sort of fluid injection or re-injection activity which can cause the rise of underground fluid pressure. Although microseismicity is considered beneficial for reservoir characterization, when the earthquake magnitudes are large enough, they risk being felt by surrounding communities, or worse, cause structural damage. Such effects could contribute to a field's closure due to a lack of social acceptance. Risk mitigation approaches include, for instance, the implementation of traffic light systems where geothermal operations are controlled in attention to the detected seismicity (e.g. *Bommer et al.*, 2006; *Häring et al.*, 2008).

A more recent approach for monitoring geothermal systems is the study of the variations in the coda of surface waves retrieved from the cross-correlation of seismic ambient noise (e.g. *Hillers et al.*, 2015; *Sánchez-Pastor et al.*, 2019). This technique has previously been successful in monitoring changes in the medium properties of volcanoes and active fault zones (e.g. *Obermann et al.*, 2013; *Sens-Schönfelder and Wegler*, 2006), and is particularly useful in less seismically active areas. In addition, the changes in the coda wave could potentially reveal aseismic processes which can help understand the underground stress evolution (*Bourouis and Bernard*, 2007).

1.4 Objectives and outline of the thesis

This thesis contributes to the efforts of the *International Energy Agency* (2011) by applying and extending several existing and novel passive seismic methods in support of the exploration and monitoring of various geothermal fields. The experiences gained throughout these studies then bring about a set of recommendations for the geothermal resource assessment and monitoring of future sites.

The seismology methods explored in this thesis are presented in several chapters and take part in various peer-reviewed publications. They are summarized in Table 1.1.

Table 1.1: Seismological tools explored in this thesis

Methodology	Purpose
Survey design theory for seismic network construction and assessment	*Exploration and monitoring planning*
Local earthquake tomography	*Exploration*
Ambient noise tomography	*Exploration*
Coda wave interferometry	*Monitoring*

The underlying theory and principles of the methods are presented in Part I. Chapter 2 provides an introduction to seismic wave propagation, ray, and inversion theory, Chapter 3 describes the main concepts of the earthquake location problem and survey design theory, Chapter 4 introduces the main principles for local earthquake tomography, and Chapter 5 presents the concepts for ambient seismic noise tomography and coda wave interferometry.

Then, Part II consists in the application of these techniques to three case studies. They are outlined as follows:

- Chapter 6: The study and application of a survey design algorithm for constructing (Theistareykir - NE Iceland) and evaluating (Reykjanes - SW Iceland) seismic networks dedicated for microseismicity retrieval (*Toledo et al.*, 2020b).
- Chapter 7: The use of local seismicity for imaging the Vp and Vp/Vs ratio structures of a producing geothermal field in Mexico (Los Humeros). Final interpretations were made taking into account available geological, geophysical, and petrophysical data (*Toledo et al.*, 2019, 2020a).

- Chapter 8: The use of seismic ambient noise for imaging the Vs structure and monitoring temporal velocity changes of a producing geothermal field in Iceland (Theistareykir) (*Toledo et al.*, 2021).

Finally, Part III discusses the obtained results (Chapter 9) and concludes with recommendations for future studies (Chapter 10).

1.5 List of publications

The list of publications associated to this thesis are:

- Chapter 6: Optimized experimental network design for earthquake location problems: Applications to geothermal and volcanic field seismic networks, *Journal of Volcanology and Geothermal Research*, 2020, (391) by Tania Toledo, Philippe Jousset, Hansruedi Maurer, Charlotte Krawczyk (*Postprint*)

- Chapter 7: Local Earthquake Tomography at Los Humeros Geothermal Field (Mexico), *Journal of Geophysical Research: Solid Earth*, 2020, 125, by Tania Toledo, Emmanuel Gaucher, Philippe Jousset, Anna Jentsch, Christian Haberland, Hansruedi Maurer, Charlotte Krawczyk, Marco Calò, Ángel Figueroa (*Postprint*)

  with its associated data publication:

  Dataset of the 6G seismic network at Los Humeros, 2017-2018. *GFZ Data Services. Other/Seismic Network*, 2019, by Tania Toledo, Emmanuel Gaucher, Malte Metz, Marco Calò, Angel Figueroa, Joel Angulo, Philippe Jousset, Katrin Kieling, Erik Saenger.

- Chapter 8: Ambient seismic noise monitoring and imaging at the Theistareykir geothermal field (Iceland), *in preparation*, 2021, by Tania Toledo, Anne Obermann, Philippe Jousset, Arie Verdel, Joana Martins, Kemal Erbas, Anette Mortensen, Charlotte Krawczyk

Part I

Methods and concepts

2

Seismic wave propagation, ray, and inversion theory

This chapter provides a brief introduction to the elastic wave equation and the seismic wave types as described in *Shearer* (2009) and *Bormann et al.* (2012). Later, I describe the main concepts of ray theory following *Lee and Stewart* (1981) and *Rawlinson and Sambridge* (2003), and inverse theory according to *Menke* (2012). These concepts are used throughout this thesis to design and qualify seismic networks, locate seismicity in an investigation area, and compute tomographies.

2.1 The elastic wave equation

Seismic waves can be approximated as elastic waves that travel through the Earth, with a propagation velocity that depends on the medium's elasticity and the wave type. For a continuous medium the equation of motion is written as:

$$\rho \frac{\partial^2 u_i}{\partial t^2} = \frac{\partial \tau_{ij}}{\partial j} + \mathbf{f}_i \tag{2.1}$$

where ρ, u_i, τ_{ij}, and $\mathbf{f}_i$ correspond to the material density, the displacement, the stress tensor, and the body force term, respectively. i and j are numbers between 1 and 3 corresponding to the cartesian directions x, y, and z. Assuming a homogeneous isotropic media, the equation of motion outside the source region becomes:

$$\rho \ddot{\mathbf{u}} = (\lambda + 2\mu)\nabla\nabla \cdot \mathbf{u} - \mu\nabla \times \nabla \times \mathbf{u} \tag{2.2}$$

where λ and μ are the Lamé parameters, and $\mathbf{u}$ and $\ddot{\mathbf{u}}$ are the displacement vector and its second time derivative, respectively. The first term of Eq. 2.2 contains a divergence or scalar product ($\nabla \cdot \mathbf{u}$) which describes a shear and a volume change. The second term contains a curl or rotation term ($\nabla \times \mathbf{u}$) which represents a pure shear motion (change of shape without modifying the volume). The displacement vector $\mathbf{u}$ can be decomposed as the sum of a rotation free $\mathbf{u}^r$ and a divergence free $\mathbf{u}^d$ terms:

$$\mathbf{u} = \mathbf{u}^r + \mathbf{u}^d \tag{2.3}$$

If we apply the divergence and curl to Eq. 2.2, we obtain:

$$\frac{\partial^2(\nabla \cdot \mathbf{u})}{\partial^2 t} = \frac{\lambda + 2\mu}{\rho}\nabla^2(\nabla \cdot \mathbf{u}^r) \tag{2.4}$$

and

$$\frac{\partial^2(\nabla \times \mathbf{u})}{\partial^2 t} = \frac{\mu}{\rho}\nabla^2(\nabla \times \mathbf{u}^d) \tag{2.5}$$

Eqs. 2.4 and 2.5 refer to the solutions of the wave equation for the two *body* waves types: the compressional (P-) and the shear (S-) waves. Their velocities are defined as:

$$V_p = \sqrt{\frac{\lambda + 2\mu}{\rho}} \tag{2.6}$$

and

$$V_s = \sqrt{\frac{\mu}{\rho}} \tag{2.7}$$

The P-wave is faster than the S-wave, and is also referred to as the *primary* wave. The S-wave is also known as the *secondary* wave. It can be differentiated as polarized in the horizontal (SH waves) and vertical planes (SV waves), and travels only through solids. This property is particularly useful in geothermal contexts, where the identification of fluids and fluid pathways is necessary for characterizing a prospect reservoir.

The presence of the Earth's free surface gives way to two *surface* wave types: the Rayleigh and the Love waves. Rayleigh waves propagate in the horizontal direction with an elliptical and retrograde particle motion (P-SV). Love waves are faster than Rayleigh waves and consist of pure SH waves and a particle motion perpendicular to the direction of propagation. The amplitudes of both surface wave types decrease with depth and their velocities are slower than those of *body* waves.

2.2 The Green's function

The Green's functions (G) are the solutions to the wave equation for δ-function sources activated at ($\mathbf{x}_0$, t_0) and evaluated at a point ($\mathbf{x}$, t). It is expressed by:

$$\frac{\partial^2 G}{\partial t^2}(\mathbf{x}, t; \mathbf{x}_0, t_0) - c^2 \Delta G(\mathbf{x}, t; \mathbf{x}_0, t_0) = \delta(\mathbf{x} - \mathbf{x}_0)\delta(\mathbf{t} - \mathbf{t}_0) \tag{2.8}$$

where a δ-function is defined as

$$\delta(x) = \begin{cases} \infty & x = 0 \\ 0 & x \neq 0 \end{cases} \tag{2.9}$$

The Green's function between two points represents the wave propagation between them and contains the information of the medium response.

2.3 Introduction to ray theory

The seismic ray method is a high frequency approximation of the wave equation for body waves propagating in smoothly varying media. Assuming the seismic energy is originated by a point source (e.g. earthquake), a seismic wave propagates away from such point along wavefronts (planes perpendicular to the direction of propagation). Seismic rays are then defined as the normals to such wavefronts and pointing in the direction of the wave propagation. In ray theory, only one point on the wavefront is tracked rather than the complete wavefield.

For a heterogeneous earth model, travel times between a source and a receiver are obtained by solving the Eikonal equation describing the wave propagation:

$$(\nabla \mathbf{t})^2 = [s(\mathbf{r})]^2 \tag{2.10}$$

where $\nabla \mathbf{t}$ is the travel time gradient, $s(\mathbf{r})$ represents the medium slowness, and $\mathbf{r}$ is the position vector (x, y, z). For an isotropic medium of slowness $s(\mathbf{r})$, the travel time t needed for a ray to travel from source point A ($\mathbf{r}_A = (x_A, y_A, z_A)$) to receiver point B ($\mathbf{r}_B = (x_B, y_B, z_B)$) along raypath L is given by:

$$t_{AB} = \int_L s(\mathbf{r}) dl \tag{2.11}$$

where dl represents the differential path length. The ray equation can be derived from the Eikonal equation as:

$$\frac{\partial}{\partial l}\left(s(\mathbf{r})\frac{\partial \mathbf{r}}{\partial l}\right) = \nabla\left(s(\mathbf{r})\right) \tag{2.12}$$

Eq. 2.12 is typically used to derive the ray propagation path of a seismic wave.

There are several methods to derive ray path geometries to provide accurate travel time estimates. These include, among others, ray tracing (e.g. *Červený*, 1987, 2001), finite difference solutions to the Eikonal equation (e.g. *Moser*, 1989; *Podvin and Lecomte*, 1991; *Vidale*, 1988), and the application of network/graph theory using Fermat's principle (e.g. *Moser*, 1991). In this work, I summarize the main principles of three ray tracing methods (shooting, bending, and pseudo-bending) and the finite difference method. These techniques are later used in Chapter 3 and Chapter 4 to estimate ray path geometries and travel times for earthquake locations and seismic tomography.

2.3.1 The shooting method

Provided that the medium velocity and source and receiver locations are known, the shooting method consists in iteratively adjusting the initial projection ray angle (from the source) until the ray end reaches the receiver as close as possible (Figure 2.1).

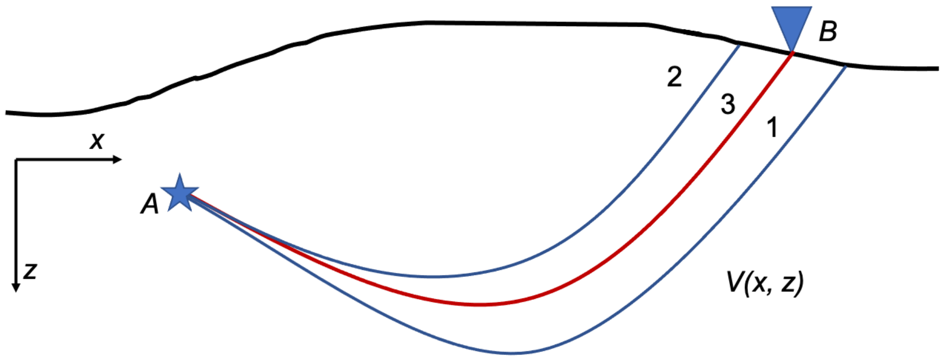

Figure 2.1: Schematic representation of the shooting method. A and B represent the source and receiver positions, respectively, located in a medium with velocity $V(x, z)$. The angle projection at the source of ray 1 is iteratively adjusted until the ray passes as close as possible to the receiver position (ray 3). Modified from *Rawlinson and Sambridge* (2003)

For a constant velocity model, the ray path is a straight line that connects the source and receiver, and the travel time varies linearly with the ray distance. In the case of a layered model, the ray trajectories follow Snell's Law at the interfaces between the layers:

$$\frac{\sin\theta_i}{v_i} = \frac{\sin\theta_r}{v_r} \tag{2.13}$$

where θ_i and θ_r are the incident and refracted angles, and v_i and v_r are the layer velocities where the incident and refracted rays are contained.

For the 3D case, the ray paths are obtained by solving the following set of equations (*Sambridge and Kennett*, 1990):

$$\begin{cases} \frac{\partial x}{\partial t} = v\sin\theta_i\cos\theta_a \\ \frac{\partial y}{\partial t} = v\sin\theta_i\sin\theta_a \\ \frac{\partial z}{\partial t} = v\cos\theta_i \\ \frac{\partial\theta_i}{\partial t} = -\cos\theta_i\left(\frac{\partial v}{\partial x}\cos\theta_a + \frac{\partial v}{\partial y}\sin\theta_a\right) + \frac{\partial v}{\partial z}\sin\theta_i \\ \frac{\partial\theta_a}{\partial t} = \frac{1}{\sin\theta_i}\left(\frac{\partial v}{\partial x}\sin\theta_a - \frac{\partial v}{\partial y}\cos\theta_a\right) \end{cases} \tag{2.14}$$

where θ_i and θ_a are the incident and azimuthal angles, respectively. The travel time is then obtained by numerical integration of Eq. 2.11.

2.3.2 The bending method

The bending method (Figure 2.2) consists in iteratively adjusting the ray path geometry until finding the true ray path which satisfies Fermat's principle (the ray must follow a *minimum* time path).

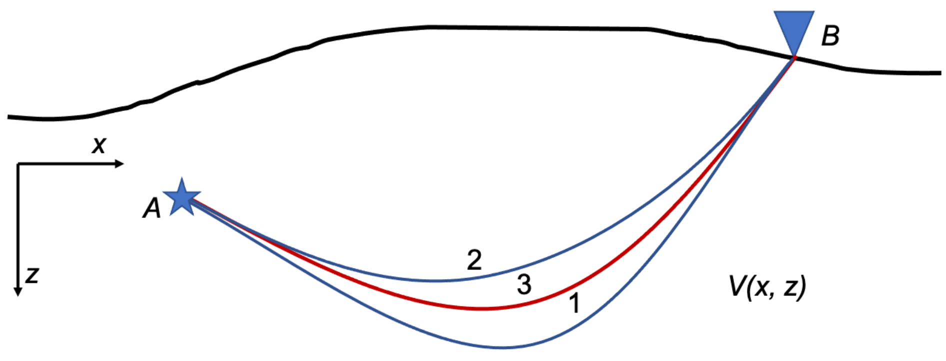

Figure 2.2: Schematic representation of the bending method. A and B represent the source and receiver positions, respectively, located in a medium with velocity $V(x, z)$. The geometry of ray 1 is iteratively adjusted until it satisfies Fermat's principle (ray 3). Modified from *Rawlinson and Sambridge* (2003)

For a continuous 3D velocity model, the ray path is obtained by solving a modified version of Eq. 2.11 (*Julian and Gubbins*, 1977):

$$t = \int_{q_A}^{q_B} s\mathbf{F}dq \tag{2.15}$$

where the position vector $\mathbf{r}$ in Eq. 2.11 is now expressed as a function of q as $\mathbf{r}$ = x(q) + y(q) + z(q). Then:

$$\mathbf{F} = \frac{dl}{dq} = \sqrt{\dot{x}^2 + \dot{y}^2 + \dot{z}^2} \tag{2.16}$$

where $\dot{x}$, $\dot{y}$, and $\dot{z}$ are the differentials with respect to q. The ray path is then obtained by solving the Euler-Lagrange system of equations (*Julian and Gubbins*, 1977):

$$\begin{cases} \frac{d}{dq}\frac{\partial}{\partial \dot{x}}(s\mathbf{F}) = \frac{\partial}{\partial x}(s\mathbf{F}) \\ \\ \frac{d}{dq}\frac{\partial}{\partial \dot{y}}(s\mathbf{F}) = \frac{\partial}{\partial y}(s\mathbf{F}) \\ \\ \frac{\partial \mathbf{F}}{\partial q} = 0 \end{cases} \tag{2.17}$$

where in this case $q = l/L$. The system of equations 2.17 is nonlinear but can be linearized by assuming:

$$x^1(q) = x^0(q) + \xi^0(q) \tag{2.18}$$

For an initial ray path $x^0(q)$ that crosses the source and receiver, the equations are now solved iteratively for perturbation $\xi^0(q)$, such that the estimated ray path $x^1(q)$ is improved (*Julian and Gubbins*, 1977).

2.3.3 The pseudo-bending method

Um and Thurber (1987) developed a faster modified version of the bending method. Starting with a ray with three points linearly interpolated, the middle point is updated such that the travel time is minimized (Figure 2.3). Then, each line segment is halved and the middle points are updated once more. This procedure continues until the change in travel time between iterations satisfies a convergence criterion.

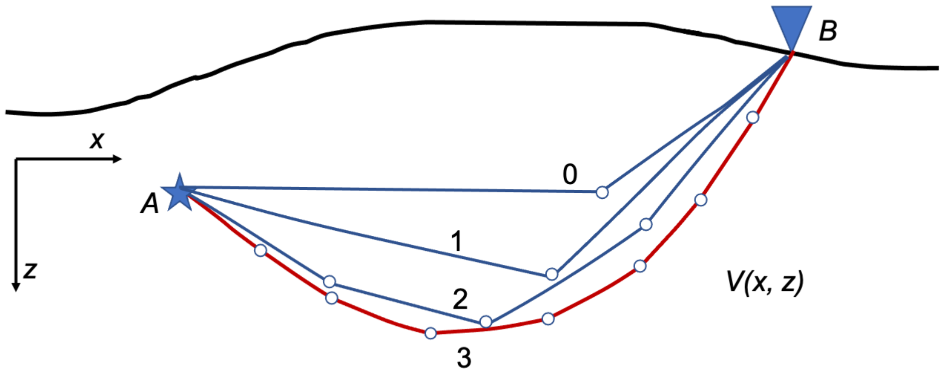

Figure 2.3: Schematic representation of the pseudo bending method. A and B represent the source and receiver positions, respectively, located in a medium with velocity $V(x, z)$. First, an initial guess with three points is provided (ray 0). Then, the center of ray 0 is updated to better satisfy the ray equation (ray 1). Each line segment is halved and their mid points updated once more (ray 2). This process is carried out iteratively until a convergence criterion is satisfied (ray 3). Modified from *Rawlinson and Sambridge* (2003)

2.3.4 The finite difference method

The finite difference consists in progressively integrating travel times along the velocity nodes of a parameterized medium. Consider, for example, the Eikonal equation for the 2D case:

$$\left(\frac{\partial t}{\partial x}\right)^2 + \left(\frac{\partial t}{\partial z}\right)^2 = [s(x, z)]^2 \tag{2.19}$$

If the travel time to source point A (Figure 2.4) is t_0, then the travel time to points B_i can be calculated as (*Vidale*, 1988):

$$t_{B_i} = t_0 + \frac{h}{2}(s_{B_i} + s_{A_i}) \tag{2.20}$$

where h is the even distance between the nodes, and s_{B_i} and s_{A_i} are the slowness at points B_i and A_i, respectively. If the travel times to A (t_0), B_1 (t_1), and B_2 (t_2) are known, then the travel time to C_1 (t_3) can be approximated by substituting the following differential terms into Eq. 2.19:

$$\begin{cases} \frac{\partial t}{\partial x} = \frac{1}{2h}(t_1 + t_3 - t_0 - t_2) \\ \\ \frac{\partial t}{\partial z} = \frac{1}{2h}(t_2 + t_3 - t_0 - t_1) \end{cases} \tag{2.21}$$

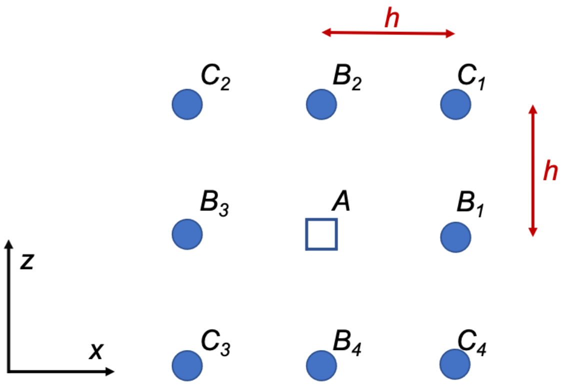

Figure 2.4: The finite difference method proposed by *Vidale* (1988) to find the first arrival travel time field assuming a continuous velocity medium. See text for details. Modified from *Rawlinson and Sambridge* (2003)

Finally, the travel time in C_1 (t_3) is given by:

$$t_3 = t_0 + \sqrt{2(h\bar{s})^2 - (t_2 - t_1)^2} \tag{2.22}$$

where $\bar{s}$ is the mean velocity of the four nodes. The travel times to the next set of grid points is determined by progressively solving equations along squares of increasing size around the source point. This method is called the expanded square formalism. For the extended 3D derivation see *Vidale* (1990).

Unlike ray tracing methods, this approach does not explicitly determine the ray path. One common way to obtain it is to first compute the travel time gradient ∇t across the medium (*Podvin and Lecomte*, 1991), and then follow it back from receiver to source (*backtracing*).

2.4 Introduction to inverse theory

Inverse theory is a set of mathematical methods used to derive useful information of the physical world from observed data (*Menke*, 2012). In relation to geothermal exploration, this information includes accurate earthquake locations and the seismic structure of a geothermal field.

In contrast to the forward problem, where data is predicted using a known model and model parameters:

$$\text{model parameters} \rightarrow \text{model} \rightarrow \text{data prediction}$$

the inverse problem aims to estimate some model parameters from observed data:

$$\text{data} \rightarrow \text{model} \rightarrow \text{model parameters}$$

In matrix form, the linear discrete notation can be written as:

$$\textit{Forward problem:}\ \mathbf{d} = \mathbf{G}\mathbf{m} \tag{2.23}$$

$$\textit{Inverse problem: } \mathbf{m} = \mathbf{G}^{-g}\mathbf{d} \tag{2.24}$$

where $\mathbf{d}$, $\mathbf{m}$, and $\mathbf{G}$ denote the data vector, the model parameters, and the model, respectively. $\mathbf{G}$ corresponds to the true physical processes in the subsurface when it relates the true model parameters $\mathbf{m}^{true}$ with $\mathbf{d}^{obs}$. Similarly, a set of estimated data $\mathbf{d}^{est}$ can be calculated using model parameters $\mathbf{m}^{est}$.

There are several approaches for solving the inverse problem. Back-projection techniques (e.g. *Gilbert*, 1972; *Gordon et al.*, 1970), gradient methods (e.g. *Eberhart-Phillips*, 1993; *Menke*, 2012; *Thurber*, 1983), and global optimization (*Mosegaard and Sambridge*, 2002; *Sambridge and Mosegaard*, 2002) are among common inversion techniques. In this thesis, I only introduce the damped least squares approach (gradient method), given it is the inversion technique used in Chapter 6 and Chapter 7.

2.4.1 The linear inverse problem

The usual procedure to solve the inverse problem is to iteratively compute $\mathbf{d}^{est}$, compare it to $\mathbf{d}^{obs}$, and update $\mathbf{m}^{est}$ such that the misfit between $\mathbf{d}^{est}$ and $\mathbf{d}^{obs}$ is minimized (*Tarantola*, 2005).

Then $\mathbf{m}^{est}$ is given by:

$$\mathbf{m}^{est} = \mathbf{G}^{-g}\mathbf{d}^{obs} \tag{2.25}$$

where $\mathbf{G}^{-g}$ is the generalized inverse (*Menke*, 2012). In a purely *over-determined* problem (more data points than model parameters), it is defined as:

$$\mathbf{G}^{-g} = (\mathbf{G}^T\mathbf{G})^{-1}\mathbf{G}^T \tag{2.26}$$

where $\mathbf{G}^T$ is the transpose of $\mathbf{G}$.

In the case of an *under-determined* problem (more model parameters than data points):

$$\mathbf{G}^{-g} = \mathbf{G}^T(\mathbf{G}\mathbf{G}^T)^{-1} \tag{2.27}$$

Underdetermined problems have infinite number of solutions with no inconsistencies.

If a problem is simultaneously *over-* and *under-determined* due to more data points than model parameters and trade-offs between the model parameters, it is called a *mixed-determined* problem. The solution to these problems is:

$$\mathbf{m}^{est} = (\mathbf{G}^T\mathbf{G} + \gamma\mathbf{I})^{-1}\mathbf{G}^T\mathbf{d} \tag{2.28}$$

where γ corresponds to a damping factor (*Levenberg*, 1944; *Marquardt*, 1963), and I is an identity matrix. The reader is referred to *Menke* (2012) and *Lee and Stewart* (1981) for extended derivations. Eq. 2.28 is also known as the *damped least squares solution.*

2.4.2 Nonlinear inversion

In the case of nonlinear functions $g = g(m)$, the inverse problem can be solved by first linearizing g. This is achieved by expanding it into Taylor series and omitting the higher order terms. Then the linearized set of functions is:

$$g(m)_i = g(m^{init})_i + G_{ik} + \Delta m_k \tag{2.29}$$

where i and k are the indexes for the data points and model parameters, respectively, and $\Delta m_k = m_k - m_k^{init}$. In this case, G is also known as the Jacobi matrix and it contains the sensitivities or partial derivatives with respect to the model parameters.

The inverse problem is then solved by iteratively adjusting vector Δm such that the estimated and observed data are as close as possible. In other words, starting the first iteration with m^{init}:

$$m_{i=0}^{est} = m^{init} \tag{2.30}$$

the next iterations are given as:

$$\mathbf{m}_{i+1}^{est} = m_i^{est} + \mathbf{G}^{-g}\Delta d \tag{2.31}$$

where $\Delta d = d^{obs} - g(m^{est})$.

2.4.3 Analysis of the solution robustness

There are several methods to assess the quality of the solution post-inversions. Within inversion theory, these include the analysis of the data resolution matrix, the model resolution matrix, the model covariance matrix, the spread function, among others (*Menke*, 2012).

2.4.3.1 Data resolution matrix

Starting with the forward calculation of $\mathbf{d}^{est}$, one can retrospectively analyze how well it fits the data $\mathbf{d}^{obs}$:

$$\mathbf{d}^{est} = \mathbf{G}\mathbf{m}^{est} = \mathbf{G}[\mathbf{G}^{-g}\mathbf{d}^{obs}] = [\mathbf{G}\mathbf{G}^{-g}]\mathbf{d}^{obs} = \mathbf{N}\mathbf{d}^{obs} \tag{2.32}$$

where the square matrix $\mathbf{N}$ is also known as the data resolution matrix. If for example $\mathbf{N}$=$\mathbf{I}$, then $\mathbf{d}^{est}$=$\mathbf{d}^{obs}$, and the prediction error is zero. The diagonal elements of the data resolution matrix are also called the *data importance*. They indicate how much weight a datum has for its own prediction.

It is worth noting that $\mathbf{N}$ depends only on $\mathbf{G}$, which describes the model and the experiment design. Therefore, this matrix can be explored beforehand in the experiment design phase to maximize the benefit of the recovered data.

2.4.3.2 Model resolution matrix

The model resolution matrix characterizes whether the model parameters can be resolved independently. Starting with the inverse formulation, $\mathbf{m}^{est}$ and $\mathbf{m}^{true}$ are related by:

$$\mathbf{m}^{est} = \mathbf{G}^{-g}\mathbf{d}^{obs} = \mathbf{G}^{-g}[\mathbf{G}\mathbf{m}^{true}] = [\mathbf{G}^{-g}\mathbf{G}]\mathbf{m}^{true} = \mathbf{R}\mathbf{m}^{true} \tag{2.33}$$

where the square matrix $\mathbf{R}$ is also known as the model resolution matrix. The diagonal values of $\mathbf{R}$ indicate the resolution of each model parameter and range from 0 to 1. If $\mathbf{R}$=$\mathbf{I}$, each model parameter is uniquely determined. Non-zero off-diagonal elements in the matrix indicate trade-offs between the model parameters.

2.4.3.3 Spread function

To better understand the trade-offs between the different model parameters, one can have a closer look at the off-diagonal elements of $\mathbf{R}$. The spread function measures the size of these diagonal elements and it is given by:

$$\text{spread}(\mathbf{R}) = \sum_{i=1}^{M}\sum_{j=1}^{M} w(i,j)\mathbf{R}_{ij}^2 \tag{2.34}$$

where for the $(i,\ j)$ element of matrix $\mathbf{R}$, $w(i,j)$ corresponds to a weighting factor that measures its physical distance with respect to the diagonal element. When $\mathbf{R}$=$\mathbf{I}$, then spread($\mathbf{R}$) = 0.

2.4.3.4 Model covariance matrix

The covariance matrix relates how the data errors are "mapped" into the calculated model parameters $\mathbf{m}^{est}$. Assuming uncorrelated data with equal variance σ_d^2, the model covariance for the least squares solution is given by:

$$\text{cov }\mathbf{m} = \sigma_d^2[\mathbf{G}^T\mathbf{G}]^{-1} \tag{2.35}$$

If the data errors have a Gaussian distribution, then the square root of the diagonal elements of cov $\mathbf{m}$ correspond to the errors in the model parameters.

3

Earthquake location and survey design

The deployment of local seismic networks is a common practice to retrieve, monitor, and mitigate natural and/or induced seismicity among several applied fields including underground storage, oil and gas, and geothermal energy exploitation. Although considerable efforts are dedicated to the development of standardized data-acquisition and inversion techniques, adequate survey design analysis are rarely performed prior to the deployment of a network. Nevertheless, the success of a microseismicity study relies on well constrained event locations, which can be improved beforehand with the network configuration choice.

This chapter introduces the main concepts of earthquake location and survey design to construct and qualify optimal seismic networks for microseismicity retrieval.

3.1 Basic principles of earthquake location

Hypocenter determination is an ongoing field of research given its potential to provide information on the active processes in the subsurface (e.g. *Maxwell*, 2009; *Wilkinson et al.*, 2004). A wide range of techniques have been proposed for the earthquake location problem including: ray based (*Aki and Richards*, 1980; *Kissling et al.*, 1994), grid search methods (*Lomax*, 2005; *Sambridge and Kennett*, 1986, 2001), wave-field back-propagation (*McMechan*, 1982; *Witten and Artman*, 2011), waveform stacking (*Cesca and Grigoli*, 2015; *Kao and Shan*, 2007), among others.

Ray based methods are, however, more commonly used due to their simplicity, fast computation, and available inversion packages. Many of these methods are based on Geiger's algorithm (*Geiger*, 1912), where the source location is derived by carrying out an inversion that iteratively minimizes observed and synthetic arrival times of body waves (*Aki and Richards*, 1980). The locations accuracies rely, among others, on the network geometry, the number of available phases, and the accurate picking of these wave phases (*Pavlis*, 1986).

3.1.1 Earthquake location by iterative methods

The location of an earthquake is a classical nonlinear problem which typically involves the adjustment of model parameters $\mathbf{m}^{est}$ (event position coordinates $\mathbf{x}_o$, $\mathbf{y}_o$, $\mathbf{z}_o$, and origin time $\mathbf{t}_o$) such that they satisfy the observed data $\mathbf{d}^{obs}$ (P- and S- wave arrival times $\mathbf{t}_p$ and $\mathbf{t}_s$) in relation to a mapping operator $\mathbf{G}$. The damped least squares solution is given by:

$$\mathbf{m}^{est} = \mathbf{m}_0 + (\mathbf{G}^T\mathbf{G} + \gamma\mathbf{I})^{-1}\mathbf{G}^T\Delta\mathbf{d} \tag{3.1}$$

Oftentimes, the square matrix $\mathbf{G}^T\mathbf{G}$ is near singular and the inversion stability depends on its ability to be inverted. In the event location problem, kernel $\mathbf{G}$ is built with the sensitivities of travel times with respect to the hypocentral coordinates -source point A (x_A, y_A, z_A)- and the origin time (*Lee and Stewart*, 1981):

$$\mathbf{G} = \begin{cases} \left.\frac{\partial t}{\partial x}\right|_A = -s\left.\frac{dx}{dl}\right|_A \\ \left.\frac{\partial t}{\partial y}\right|_A = -s\left.\frac{dy}{dl}\right|_A \\ \left.\frac{\partial t}{\partial z}\right|_A = -s\left.\frac{dz}{dl}\right|_A \\ \left.\frac{\partial t}{\partial t_0}\right|_A = 1 \end{cases} \tag{3.2}$$

where:

$$\cos\alpha_A = \left.\frac{dx}{dl}\right|_A ; \cos\beta_A = \left.\frac{dy}{dl}\right|_A ; \cos\gamma_A = \left.\frac{dy}{dl}\right|_A \tag{3.3}$$

α_A, β_A, and γ_A are also known as the instantaneous direction angles of the ray at point A. s corresponds to the medium slowness at point A and dl represents the differential ray path length. The sensitivities of matrix $\mathbf{G}$ are directly related to the survey design and are calculated in this work using *Podvin and Lecomte* (1991) finite-difference time-field calculations and a back-raytracing routine (See Section 2.3).

3.2 Experimental survey design

The main goal of experimental survey design is the selection of a network geometry (or data subset) that would maximize the information (benefit) gathered from the inversions at a minimum acquisition and/or computational cost (e.g. *Maurer et al.*, 2010).

The benefit of an inversion can be directly quantified with the information or eigenvalue content ($\lambda_i : i = 1, ..., N$) of matrix $\mathbf{G}^T\mathbf{G}$ (*Curtis et al.*, 2004). Errors in the data propagate into $\mathbf{m}^{est}$ with λ_i factors. In other words, the propagation error can become very large if a λ_i is very small, making the inversion unstable altogether. Mathematically, the goodness of matrix $\mathbf{G}^T\mathbf{G}$ can, therefore, be expressed in terms of non-zero eigenvalues.

From Section 2.4.3.4, we know that the inversion accuracy is given by the model covariance matrix:

$$\text{cov } \mathbf{m} = \sigma_d^2[\mathbf{G}^T\mathbf{G}]^{-1} \tag{3.4}$$

In the earthquake location problem, σ_d^2 corresponds to the variance of onset-time determination. The eigenvalues of matrix $(\mathbf{G}^T\mathbf{G})^{-1}$ provide the shape of the location confidence ellipsoid, and the confidence volume is proportional to $1/\det(\mathbf{G}^T\mathbf{G})$ (*Buland*, 1976; *Flinn*, 1965). Previous works for determining optimum network geometries (*Kijko*, 1977; *Rabinowitz and Steinberg*, 1990) rely on the confidence ellipsoid as an indicator for goodness of network performance (*Hardt and Scherbaum*, 1994).

3.2.1 The *D-criterion*

A wide range of options have been proposed to quantify the goodness of a dataset (*Curtis*, 1999a; *Maurer et al.*, 2010). In this work I base this quantity in terms of $\mathbf{G}^T\mathbf{G}$, also known as the approximate Hessian matrix. Not only is this matrix contributing to the solution's model covariance (and hence on the event location precision), but its ability to be inverted determines the success of model parameter reconstruction.

One popular quality measure for the earthquake location problem is the determinant of $\mathbf{G}^T\mathbf{G}$, also known as the *D-criterion*. The main benefit of this measure is its sensibility to the entire eigenvalue spectrum (*Hardt and Scherbaum*, 1994; *Kijko*, 1977; *Rabinowitz and Steinberg*, 1990). Several quality measures based on the *D-criterion* have been proposed and tested by e.g. *Curtis* (1999a) and *Maurer et al.* (2010). In this work I chose a modified version of the multi-source function defined by *Rabinowitz and Steinberg* (1990) as:

$$\Theta = \sum_{i=1}^{N} \gamma_i \log\left(\frac{1}{\det(G_i^T G_i) + \delta}\right) \tag{3.5}$$

where N stands for the total number of earthquakes, and γ_i corresponds to a weighting factor assigned to each event i. In a Bayesian framework, weights γ_i can also be considered as prior probabilities for the hypocenters (*Chaloner and Verdinelli*, 1995). In this study the weights reflect a combination of a prior probability and an event importance (*Steinberg and Rabinowitz*, 2003). A small value δ is introduced in Eq. 3.5 to stabilize the optimization procedure for cases where the determinant would be zero (under-determined case). By minimizing the objective function Θ one would in some sense also minimize the confidence volumes of the studied seismic events.

3.2.2 Optimization approaches for survey design

Having chosen a quality measure, the remaining components to construct the sensitivities of matrix $\mathbf{G}$ (Eq. 3.2) are:

1. Target earthquake locations
   These can be defined by analyzing the previous seismological history in a target region.

2. A representative velocity model

3. Potential sensor locations
   The *potential deploying areas* are defined by detectability (e.g. minimum detecting magnitudes) and accessibility.

Then, the aim of survey design is to find the optimal source-receiver configuration, such that the quality measure Θ is minimized. There are several approaches for the optimization including the use of global optimizers like simulated annealing (e.g. *Kraft et al.*, 2013), Bayesian statistical experimental design (e.g. *Coles and Curtis*, 2011a), and sequential survey design (e.g. *Curtis et al.*, 2004; *Guest and Curtis*, 2009). The latter, although does not guarantee global optimality, is flexible and faster to compute and allows addressing benefit (Θ)/cost (number of stations) concepts.

Sequential design consists in stepwise removing (destructive) or adding (constructive) seismic stations at a location that effectively minimizes Θ. In a destructive sequential design framework, **G** is first constructed with of all possible sensitivity entries, namely all detecting station positions. Then, Θ values are calculated after removing each recording sensor. These values are then compared and the position associated to the minimum Θ value (possibly redundant information) is removed. This process is carried out in a step-wise fashion depleting the *potential deploying area.* In the end, each station position has an assigned "order" of importance number.

To demonstrate the use of this scheme, Figure 3.1a shows the construction of a 5 station network for locating a single event at 3 km depth (pink point). After defining a detection radius (dashed red circle), the *deploying area* is fully populated with potential station locations (Figure 3.1b). The station positions are then removed in each step when effectively minimizing the objective function Θ. Notice how in the station placement, locations close and far away from the seismic source have higher importance (must be located first). In fact, the geometry in Figure 3.1a resembles a quadripartite, which is also seen in *Rabinowitz and Steinberg* (1990) and *Hardt and Scherbaum* (1994). Figure 3.1c shows the benefit/cost curve of the experiment. Note how Θ is vastly reduced after installing only four stations. Adding more stations after that also reduces the objective function, however in a much smaller proportion.

This destructive sequential survey design approach is applied in Chapter 6 to extend a seismic network dedicated for the microseismicity monitoring of a producing geothermal field (Theistareykir in NE Iceland), and to qualify the geometry of an already deployed temporary network (Reykjanes in SW Iceland).

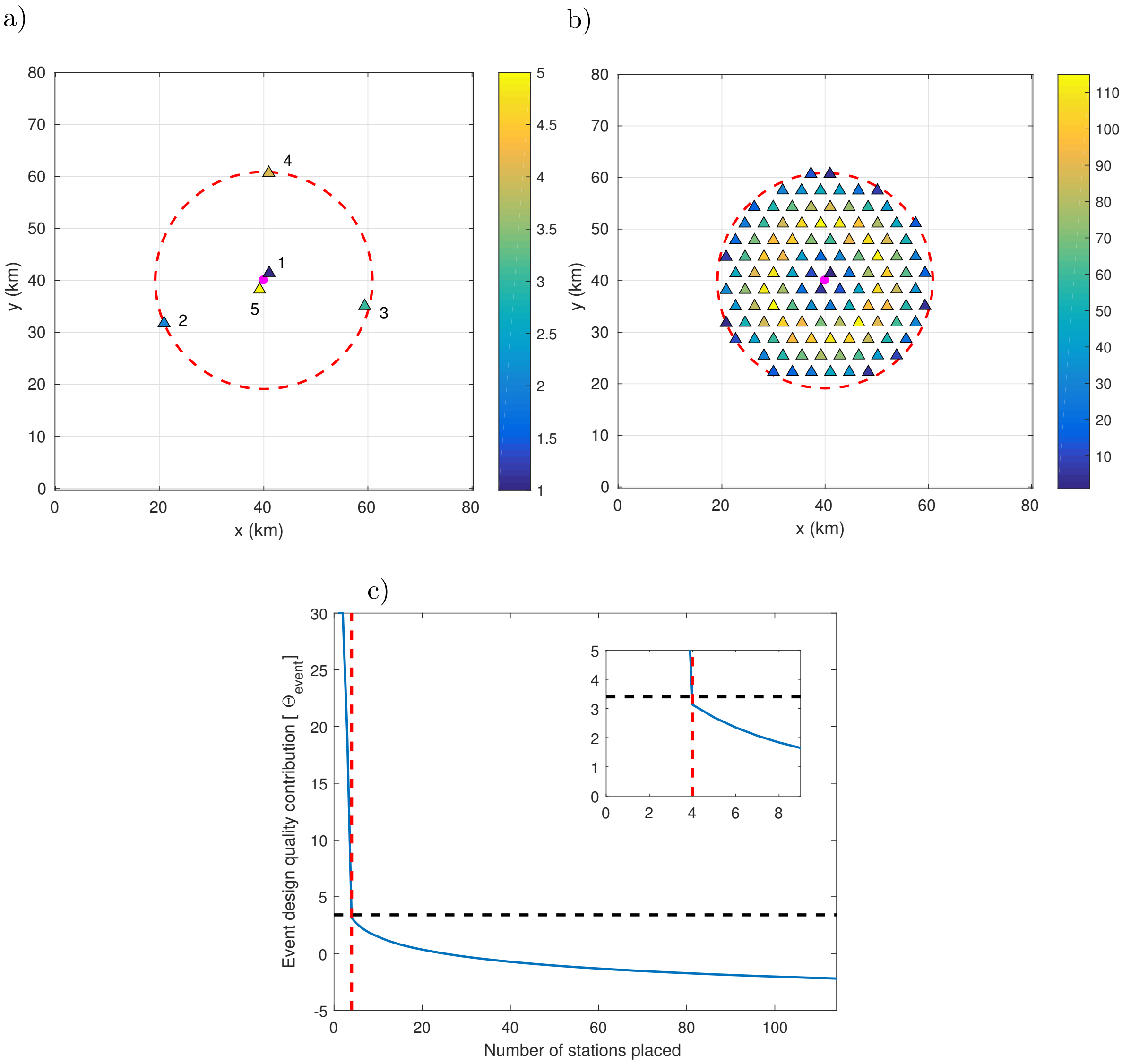

Figure 3.1: Survey design example for an event at 3 km depth with M_L 0.8. a) 5 stations setup. b) 115 stations setup. The colorbar shows the order of placed stations. c) Design quality Θ of the survey setup for each number of placed stations. The dashed red line represents station point 4, and the horizontal dashed black line the limit of $\Theta = 3.4$ (see figure inset). Taken from *Toledo et al.* (2020b)

4

Principles for local earthquake tomography

Local earthquake tomographies are classical coupled inverse problems, where the earthquake location and 3D velocity models are derived using the arrival times of body waves (P- and S-waves). They are typically obtained by first computing the joint inversion of a 1D velocity model and earthquake locations. Then, this so called *minimum* 1D velocity model is used as an initial estimate for a 3D joint inversion (e.g. *Muksin et al.*, 2013; *Thurber*, 1983).

In this chapter, I first describe the formulation for the coupled 1D velocity model and earthquake location problem according to *Kissling et al.* (1994). Then I introduce the 3D local earthquake tomography formulation following *Rawlinson and Sambridge* (2003) and *Thurber* (1983).

4.1 The coupled 1D velocity model and earthquake location problem

The travel times of body waves $\mathbf{t}$ can be expressed as a nonlinear function of station coordinates $\mathbf{st}$, the hypocentral parameters $\mathbf{h}$, and the velocity model $\mathbf{v}$:

$$\mathbf{t}(\mathbf{st}, \mathbf{h}, \mathbf{v}) \tag{4.1}$$

As described in Chapter 2, an *a priori* velocity model can be used to calculate synthetic travel times $\mathbf{t}^{est}$. The difference between $\mathbf{t}^{obs}$ (observed travel times) and $\mathbf{t}^{est}$ ($\Delta\mathbf{t}$) can then be expanded as a function of the difference between estimated and true model parameters. Applying a first-order Taylor expansion to Eq. 4.1 (*Kissling et al.*, 1994):

$$\Delta\mathbf{t} = \mathbf{t}^{obs} - \mathbf{t}^{est} = \sum_{k=1}^{4} \frac{\partial t}{\partial h_k} \Delta h_k + \sum_{n=1}^{N} \frac{\partial t}{\partial v_n} \Delta v_n + e \tag{4.2}$$

where Δh_k and Δv_n are the hypocentral and velocity model parameter perturbations, respectively. In matrix notation, the coupled relation between hypocenter and velocity model parameters can be written as (*Kissling et al.*, 1994):

$$\Delta \mathbf{t} = \mathbf{t}^{obs} - \mathbf{t}^{est} = H\mathbf{h} + M\mathbf{m} + \mathbf{e} \tag{4.3}$$

where:

H: matrix containing the partial derivatives of travel times with respect to the hypocentral parameters

M: matrix containing the partial derivatives of travel times with respect to the velocity model parameters

h: vector of hypocentral parameter perturbations

m: vector of velocity parameter perturbations

e: vector of travel time error

Then, Eq. 4.3 can be solved using the damped least squares inversion method detailed in Section 2.4.1 and the travel times computed with the shooting method described in Section 2.3.1. This is the approach adopted in the Velest software (*Kissling et al.*, 1994; *Maurer*, 1993). Velest calculates the damped least squares solution for a set of earthquakes and a multilayered velocity model of fixed thicknesses. A scalar term associated to each station is also provided in the inversion to account for deviations due to near surface velocities below the stations (station corrections).

To avoid being trapped in a local minimum, *Kissling et al.* (1994) advise the computation of several inversions using different initial velocity models. Finally, the minimum 1D velocity model corresponds to the final model with lowest associated RMS (root-mean-square) error.

4.2 3D travel time tomography

After obtaining the minimum 1D velocity model, the classical steps for retrieving 3D tomographic images are (*Rawlinson and Sambridge*, 2003):

- Model parametrization
- Forward calculation
- Inversion
- Solution quality

The software I used to compute a local earthquake tomography for Los Humeros geothermal field (Mexico) in Chapter 7 is called SIMUL2000 (*Eberhart-Phillips*, 1990; *Eberhart-Phillips and Michael*, 1998; *Evans et al.*, 1994; *Thurber*, 1983).

4.2.1 Model parametrization

Prior to an inversion, a region must be discretized into smaller cells or grid points (model parameters) from which the final velocity values can be computed. Various model parametrization types include constant velocity blocks, velocity node grids, and triangulated velocity grids (Figure 4.1). To calculate the velocity values at any point (x, y, z), SIMUL2000 uses a grid of velocity nodes (Figure 4.1b) interpolated with the function (*Thurber*, 1983):

$$V(x,y,z) = \sum_{i=1}^{2}\sum_{j=1}^{2}\sum_{k=1}^{2} V(x_i,y_j,z_k)\left(1-\left|\frac{x-x_i}{x_2-x_1}\right|\right)\left(1-\left|\frac{y-y_j}{y_2-y_1}\right|\right)\left(1-\left|\frac{z-z_k}{z_2-z_1}\right|\right) \quad (4.4)$$

where x_i, y_j, and z_k correspond to the eight grid points that surround point (x, y, z).

Then, to maximize the recovered information, an adequate model parametrization is suggested by *Evans et al.* (1994) and *Husen et al.* (2000, 2003) as a grid with as small as possible node spacing, that maintains a fairly homogeneous ray density.

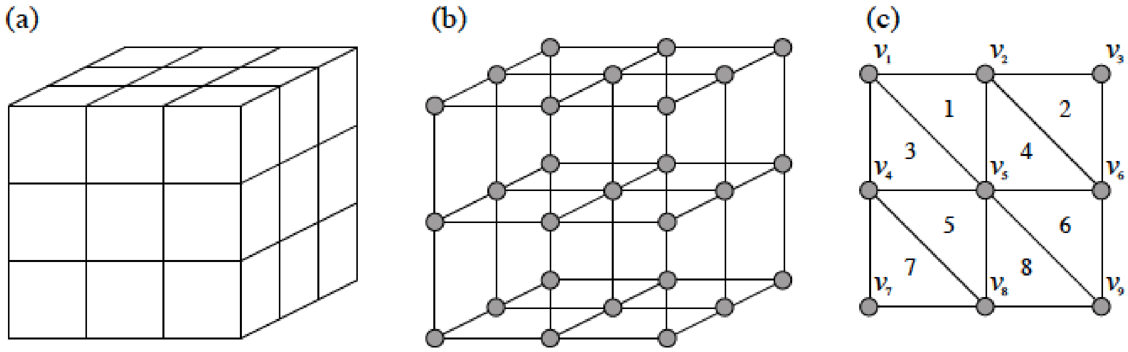

Figure 4.1: Various types of model parametrization: a) constant velocity blocks, b) grid of velocity nodes, c) triangulated velocity grid for constant velocity gradient cells (*White*, 1989). Taken from *Rawlinson and Sambridge* (2003)

4.2.2 Forward and inverse calculations

Similar to the 1D model case, the travel time residuals of the linearized system can be written as (*Thurber*, 1983):

$$\Delta \mathbf{t} = \mathbf{t}^{obs} - \mathbf{t}^{est} = \sum_{k=1}^{4}\frac{\partial t}{\partial h_k}\Delta h_k + \sum_{n=1}^{N}\frac{\partial t}{\partial v_n}\Delta v_n + e \quad (4.5)$$

where in this case the model parameters v_n are the nodes of a 3D velocity grid. The sensitivities of travel times with respect to the hypocentral parameters ($\partial t/\partial h_k$) are given by Eq. 3.2. The partial derivatives of travel times with respect to the velocity parameters involve the integrals along the ray path:

$$\frac{\partial t}{\partial v_n} = \int_{\text{source}}^{\text{station}} -\left\{\frac{1}{V(x,y,z)}\right\}^2 \frac{\partial V(x,y,z)}{\partial v_n} dl \quad (4.6)$$

where v_n is the *nth* velocity parameter and dl is a ray segment. In terms of slowness $s_n = 1/v_n$; $S(x,y,z) = 1/V(x,y,z)$ and dividing the ray path into M segments:

$$\frac{\partial t}{\partial s_n} = \sum_{m=1}^{M}\frac{\partial S(x_m,y_m,z_m)}{\partial s_n} L \quad (4.7)$$

where L is the ray length, (x_m, y_m, z_m) is the midpoint of the mth path segment, and $\partial S/\partial s_n$ can be calculated using Eq. 4.4.

Ray geometries in Chapter 7 are obtained using the pseudo-bending method (*Um and Thurber*, 1987) described in Section 2.3.3. SIMUL2000 uses the damped least squares approach to solve the inverse problem (Section 2.4.1). Finally, the tomography quality in Chapter 7 is assessed using a synthetic checkerboard test and a resolution matrix analysis (Section 2.4.3).

5 Ambient seismic noise tomography and coda wave interferometry

In previous chapters I have mainly discussed concepts of classical earthquake seismology. These techniques are, however, restricted to seismically active regions. Good resolution of a local earthquake tomography is, for example, limited to areas with even ray coverage (homogeneous distribution of local earthquakes and seismic stations). In practice, an adequate ray coverage is difficult to control, especially in aseismic regions. Ambient seismic noise (AN) techniques offer suitable alternatives to study these regions and increase the resolution by turning the seismic stations into (virtual) sources.

In this chapter I provide an introduction to the origins of ambient noise and the reconstruction of Green's functions between receiver pairs. Then I describe the main principles for ambient noise tomography (ANT) and ambient noise methods used for monitoring purposes (CWI, coda wave interferometry).

5.1 Origins of ambient noise

The ambient noise field is generated by a wide range of forces of both anthropological and natural origin. The sources producing the ambient noise field vary depending on the frequency range under study (*Bormann et al.*, 2012; *Nakata et al.*, 2019).

At higher frequencies (1-10 Hz), the ambient noise is generally human-generated ("cultural" noise) (e.g. *Campillo et al.*, 2011; *McNamara and Buland*, 2004). Urban sources include cars, trains, electrical grids, and machinery that operate in the neighborhood of a recording seismic station. Other natural short-period noise sources include glacier calving (*O'Neel et al.*, 2007) and the effects of wind on the Earth's surface (*Withers et al.*, 1996).

Intermediate frequencies (0.03-1 Hz) are primarily dominated by ocean microseism (e.g. *Bromirski and Gerstopft*, 2009; *Díaz*, 2016; *Gutemberg*, 1936). However, the noise in this period range can also be affected by extra-tropical storms and tropical cyclones (*Ebeling and Stein*, 2011; *Sufri et al.*, 2014), and the presence of sea ice (*Anthony et al.*, 2014; *Grob et al.*, 2011; *Stutzmann et al.*, 2009). Two prominent peaks in this spectrum are also known as the primary (0.05-1 Hz) and the secondary (0.1-0.3 Hz) microseism peaks. These peaks are mainly dominated by fundamental mode surface waves of still debatable origin (*Landès et al.*, 2010).

Finally, long period signals (0.002-0.03 Hz) are generally attributed to ocean infragravity waves also called the Earth's *Hum*. These waves are produced by storm-forced, shoreward-directed winds (*Ardhuin et al.*, 2015; *Bromirski and Gerstopft*, 2009; *Nakata et al.*, 2019; *Webb*, 2007).

Given that oceanic and atmospheric processes have a strong influence on the ambient seismic noise, it is not surprising that the ambient noise also experiences seasonal variations (*Landès et al.*, 2010).

5.2 Green's function reconstruction

This section outlines the main concepts of the Green's function retrieval using cross-correlation and time reversal principles (*Campillo and Paul*, 2003; *Derode et al.*, 2003a,b; *Wapenaar*, 2004; *Wapenaar and Fokkema*, 2006). The description and analogies in this section are based on the thesis of *Obermann* (2014).

Consider two receivers A and B, and a source C placed in an inhomogeneous medium (Figure 5.1). The signal emitted by source C ($e(t)$) is recovered in receivers A ($S_A(t)$) and B ($S_B(t)$) as the convolution (*) of the signal with the impulse response of the medium (Green's function) between A and C ($h_{AC}(t)$) and B and C ($h_{BC}(t)$):

$$\begin{aligned} S_A &= e(t) * h_{AC}(t) \\ S_B &= e(t) * h_{BC}(t) \end{aligned} \tag{5.1}$$

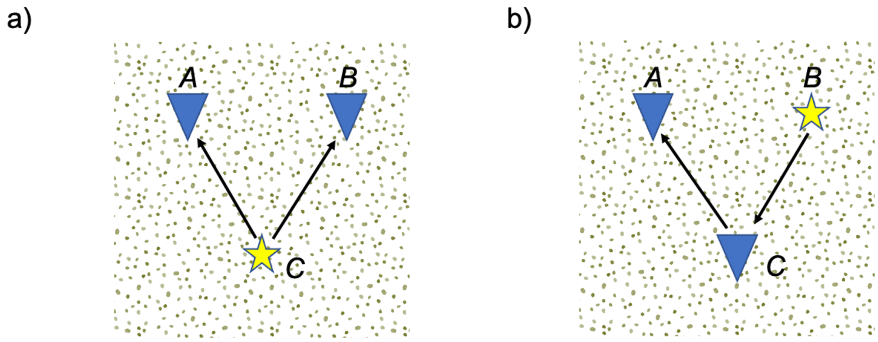

Figure 5.1: Illustration of the time reversal principle. a) Point C is a source that emits a signal recorded at A and B. b) Point B emits a signal that is mirrored by C and recorded by A. Triangles mark the receiver positions, and the stars correspond to the source locations. Modified from *Obermann* (2014).

The correlation C_{AB} between the signals recorded at A and B can be then written as:

$$\begin{aligned} C_{AB}(\tau) &= S_A(t) * S_B(-t) \\ C_{AB}(\tau) &= h_{AC}(t) * h_{BC}(-t) * f(t) \end{aligned} \tag{5.2}$$

where τ is the correlation time and $f(t)$ is given by:

$$f(t) = e(t) * e(-t) \tag{5.3}$$

By the principle of source-receiver reciprocity we know that the signal emitted from B to C is identical to the signal travelling from C to B. Therefore, $h_{BC}(t) = h_{CB}(t)$ and:

$$C_{AB}(\tau) = h_{AC}(t) * h_{CB}(-t) * f(t) \tag{5.4}$$

If we consider the case of Figure 5.1b where the point B is now the source position and C is a mirror point, the signal recorded at A will be given by:

$$S_A(t) = h_{BC}(-t) * h_{AC}(t) \tag{5.5}$$

where Eq. 5.2 and Eq. 5.4 are still dependent on point C.

The time reversal principle states that the back-propagation of a mirrored (in time) signal recorded at a receiver concentrates back at the original source. If we simulate a series of points C_i (scatterers/mirror points) surrounding A and B, and point A corresponding to a source emitting a signal in all directions, then the points C_i and B will record $h_{AC_i}(t)$ (and re-emit $h_{AC_i}(-t)$) and h_{AB}, respectively. If the number of mirror points C_i is very large, we can assume that there is a time reversed wave that back-propagates to A and is recorded at B as $h_{AB}(-t)$. That is to say, this time reversal experiment is given by the sum of Green's functions between A and B in positive and negative lag times and is analogous to the cross-correlation definition (*Derode et al.*, 2003a,b; *Obermann*, 2014):

$$\sum_{C_i} h_{AC_i}(t) * h_{C_iB}(-t) = h_{AB}(t) + h_{AB}(-t) \tag{5.6}$$

This translates in practice to the reconstruction of Green's functions between different receiver pairs from the cross correlation of ambient noise records (*Campillo and Paul*, 2003; *Wapenaar*, 2004; *Wapenaar and Fokkema*, 2006). The reconstruction of the Green's function holds if the noise sources are evenly distributed around the receivers, and if the medium is highly heterogeneous, such that the scatterers can act as mirrors or secondary sources.

In practice, the noise sources are not evenly distributed resulting many times in asymmetrical correlograms (e.g. different amplitudes for the causal and acausal parts). This behavior implies that the correlations have not converged to the Green's functions. *Hadziioannou et al.* (2009) points out, however, that a full convergence is not necessary for monitoring purposes.

In addition, the ambient noise wavefield is also "polluted" by the signal of earthquake sources which do not comply with the requirements of Green's function retrieval. To remove these signals, and enhance the Green's functions recovery, several authors propose different pre-processing and stacking schemes. Some schemes include (*Nakata et al.*, 2019): the averaging of causal and acausal parts of correlograms, spectral whitening, time domain running averages, frequency domain normalization (e.g. *Bensen et al.*, 2007; *Groos et al.*, 2012), one-bit normalization (e.g. *Cupillard et al.*, 2011; *Hanasoge and Branicki*, 2013; *Larose et al.*, 2004; *Shapiro and Campillo*, 2004), phase weighted stacking (e.g. *Baig et al.*, 2009; *Schimmel and Paulssen*, 1997; *Schimmel et al.*, 2011), directional balancing (*Curtis and Halliday*, 2010), Welch's method of overlapping time windows (*Seats et al.*, 2012; *Welch*, 1967), the application of curvelet denoising filters (*Stehly et al.*, 2011), and sequences of selection and noise suppression filters (e.g. *Boué et al.*, 2014; *Nakata et al.*, 2015).

There are three main lines of research based on the study ambient noise: noise-based seismic imaging, monitoring the continuous changes in the medium properties, and studies of the spatio-temporal distribution of seismic sources. In this thesis, I apply methods for the first two applications. Hence, their fundamentals are outlined in the next sections.

5.3 Ambient noise travel time surface wave tomography

This section gives an overview of seismic noise-based surface wave imaging based on the work of *Nakata et al.* (2019).

The first ideas for using ambient noise for the purpose of imaging were introduced by *Aki* (1957) and *Claerbout* (1968). However, the potential of this technique was not fully exploited until the improvement of computational and storage capabilities. *Sabra et al.* (2005a); *Shapiro and Campillo* (2004) were the first to extract surface waves from the cross-correlation of ambient noise, which led to the first applications of noise-based passive seismic imaging in California (*Sabra et al.*, 2005b; *Shapiro et al.*, 2005). Since then, this technique has been widely exploited for imaging at various scales (e.g. *Bensen et al.*, 2008; *Mordret et al.*, 2015; *Obermann et al.*, 2016) and more recently for geothermal exploration by *Granados et al.* (2020); *Lehujeur et al.* (2017); *Martins et al.* (2020b); *Planès et al.* (2020).

As described in the previous section, the Green's function reconstruction holds if the noise sources are evenly distributed around a medium, which is typically not the case in the real world. As a matter of fact, most of the noise sources (atmospheric and ocean driven) are located at the Earth's surface. This results in the dominant reconstruction of surface waves (mainly their fundamental modes) from the cross-correlations of ambient noise. The inhomogeneous distribution of noise sources contribute to asymmetric correlograms (even for the surface waves), which leads to difficulties in extracting their amplitude information (*Stehly et al.*, 2006). However, *Garnier and Papanicolaou* (2009) have shown that the travel time of these waves can be effectively estimated even if the Green's function have not fully converged.

Given that the main information recovered from cross-correlations are surface waves, it is not surprising that the primary application for imaging is the ambient noise surface wave tomography (ANSWT). Having obtained the travel time paths (*N(N-1)/2*) from N stations (virtual sources), tomographies can be obtained using traditional ray methods (Section 2.3 and Section 2.4.1).

5.3.1 Properties of Surface waves

Surface waves propagate along the surface with their amplitudes decaying with depth. Assuming, for example, a surface wave $u_{sw}(x, z, t, \omega)$ at a single frequency propagating in the x direction (*Nakata et al.*, 2019):

$$u_{sw}(x, z, t, \omega) \approx \xi(z, \omega) \exp[i(\omega t - k(\omega)x)] = \xi(z, \omega) \exp[i\omega(t - x/C(\omega))] \tag{5.7}$$

where t, ω, u, k, and ξ correspond to time, frequency, depth, displacement, wavenumber, and the eigenfunction representing the wave amplitude decay with depth, respectively. The phase velocity $C(\omega)$ is given by:

$$C(\omega) = \frac{\omega}{k(\omega)} \tag{5.8}$$

and the group velocity $U(\omega)$ by:

$$U(\omega) = \left(\frac{\partial k(\omega)}{\partial \omega}\right)^{-1} \tag{5.9}$$

with both velocities being related by

$$U(\omega) = \frac{C(\omega)}{1 - \frac{\omega}{C(\omega)}\frac{\partial C}{\partial \omega}} \tag{5.10}$$

Dispersion is an important property of surface waves, with wavenumbers (k) being dependent on the frequency (ω) (*Levshin et al.*, 1989). This translates in the energy of surface waves being concentrated at the top-most layers, where $\xi(z, \omega)$ is largest (typically reaching a thickness of half a wavelength). Higher frequencies sample the shallow subsurface, while larger frequencies reach deeper levels. This behavior leads to the possibility of using surface group and phase velocities at different frequencies (or periods) to constrain velocities at different depths.

For a single receiver pair, it is possible to measure 4 types of dispersion curves: phase and group velocity propagations of Love and Rayleigh waves. The choice of the different components account for different wave types. There are several ways to measure the dispersion curves, with the frequency time analysis (FTAN *Levshin et al.*, 1989) being a popular choice.

5.3.2 Ambient noise surface wave tomography

The most standard steps of ANSWT are (*Nakata et al.*, 2019):

1. Pre-processing of the collected continuous seismic data
2. Cross-correlation computation between different station pairs
3. Measuring group and/or phase travel times from the causal and acausal parts of correlograms ZZ, RR, RZ, ZR for Rayleigh waves and TT for Love waves
4. Quality control and travel time selection prior to the inversions
5. 2D surface wave tomography: frequency dependent group and/or phase velocity maps for Rayleigh and/or Love waves

6. 1D inversion of regionalized dispersion curves at every station location to construct a final 3D Vs model. This step is also called time to depth conversion.

These are the steps also adopted in Chapter 8 to image the Theistareykir geothermal field in Iceland, which has a limited earthquake-related ray coverage.

5.4 Noise-based monitoring

This section gives an overview of principles of seismic noise-based monitoring based on the work of *Nakata et al.* (2019).

An application of seismic interferometry is the monitoring of structural and velocity changes by measuring the distortions of so called "coda" waves (*Sens-Schönfelder and Wegler*, 2006; *Snieder*, 2002). This technique is commonly known as coda wave interferometry (CWI) and has been successfully applied in volcano monitoring (e.g. *Brenguier et al.*, 2008b; *Obermann et al.*, 2013), observations of environmental conditions (e.g. *Hillers et al.*, 2014; *Mordret et al.*, 2016), earthquake related observations (e.g. *Brenguier et al.*, 2008a; *Wegler and Sens-Schönfelder*, 2007), geotechnical applications (e.g. *Planès and Larose*, 2013), and more recently for geothermal field monitoring (e.g. *Hillers et al.*, 2015; *Obermann et al.*, 2015; *Sánchez-Pastor et al.*, 2019; *Taira et al.*, 2018).

The principle was first introduced by *Poupinet et al.* (1984) to measure velocity changes from the coda of repeatable earthquakes (*doublets* or *multiplets*). They compared different seismic events that occurred on the Calaveras Fault in California and noticed small phase shifts in time which can be explained by velocity changes in the medium. The time-domain version of this concept was later proposed by *Snieder et al.* (2002). This technique, though powerful, requires the acquisition of repeatable signals (sources), which is oftentimes non feasible (e.g. earthquakes and use of explosives). With the introduction of seismic interferometry the technical and logistic efforts required to obtain repeating signals could finally be circumvented thus allowing the use of ambient noise also for monitoring (*Sens-Schönfelder and Wegler*, 2006).

There are two common techniques used to quantify the velocity changes from coda waves: the moving-window cross-spectral analysis introduced by *Poupinet et al.* (1984) and the stretching method introduced by *Sens-Schönfelder and Wegler* (2006). Both of them are based on the principle that small changes in the medium Δv would result in small time shifts Δt of the arriving waves:

$$\frac{\Delta t}{t} = -\frac{\Delta v}{v} = \epsilon \tag{5.11}$$

where we refer the velocity change as an *apparent velocity change* due to the assumption that it is homogeneous in space. ϵ is known as the *relative* travel time change and is constant for all lapse times under the same assumption. To observe variations, both methods compare a "current" correlogram (u_l) to a reference signal (u_k), typically constructed as the stacked cross-correlation function over the entire recording period.

5.4.1 Stretching technique

The main idea behind the stretching technique is to stretch or compress the time axis of a current correlogram (u_l) by a factor $t \rightarrow t(1 \pm \epsilon)$ such that the correlation coefficient ($C_{k,l}$) with respect to u_k is maximized (Figure 5.2a,c):

$$C_{k,l}(\epsilon) = \sum_{t=t_{min}}^{t_{max}} \frac{u_k(t)u_l(t(1 \pm \epsilon))}{\sqrt{u_k^2(t)u_l^2(t(1 \pm \epsilon))}} \tag{5.12}$$

The stretching of a curve is simulated simply by modifying the sample interval by $dt(1+\epsilon)$. Then, the value $1 - C_{k,l}$ (*decorrelation*) indicates the remaining waveform change that cannot be explained with the simulated homogeneous velocity change (stretching).

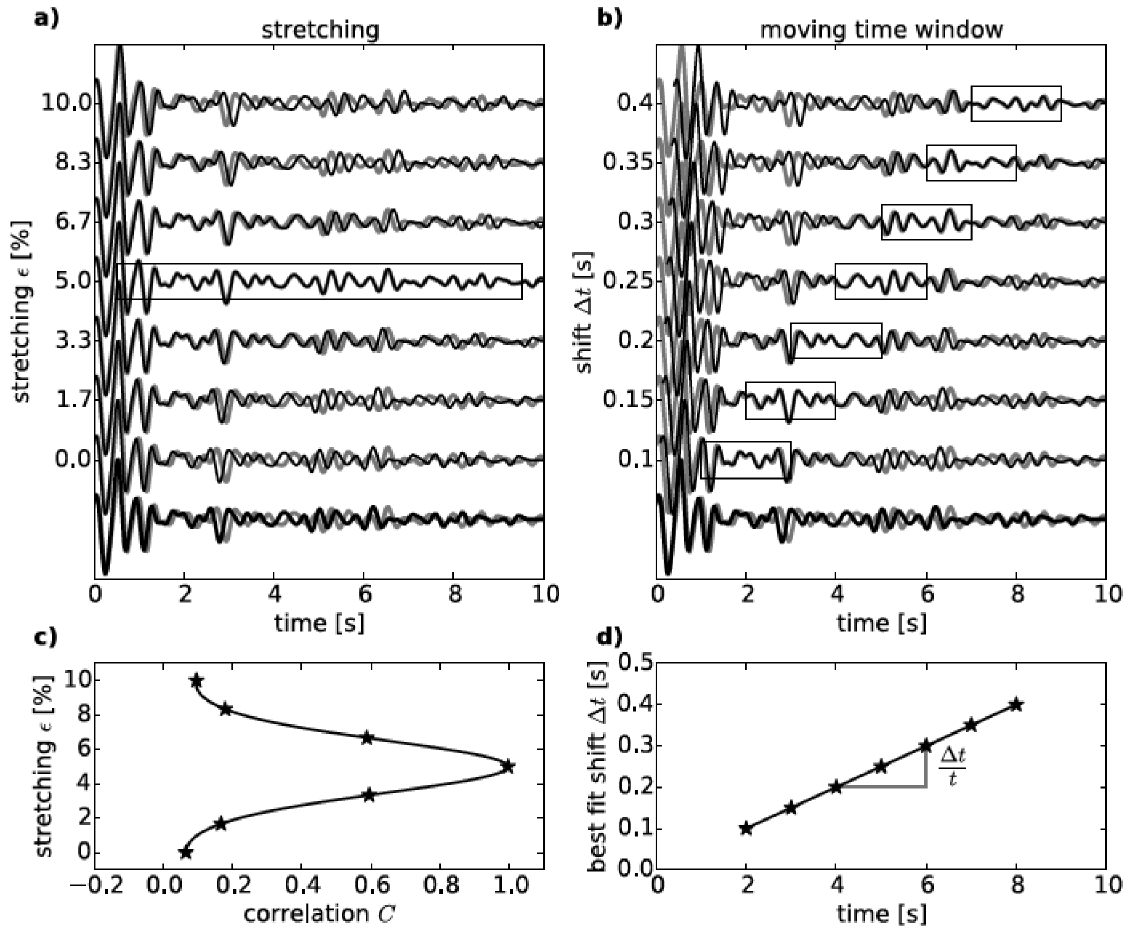

Figure 5.2: Synthetic illustration of the stretching (a, c) and MWCS methods (b, d). a) Comparison of a reference (gray lines) with respect to stretched (black lines) waveforms. c) Correlation coefficients for each stretched waveform in a). b) Comparison of a reference waveform (gray lines) with respect to fixed moving window segments (black lines). d) Linear regression for the obtained best time shifts with respect to time. The maximum associated ϵ is, in both cases, 5%. Taken from *Nakata et al.* (2019)

5.4.2 Moving window cross-spectral analysis

In contrast to using a long time window, the MWCS technique compares several short time windows (with length t_w and centered at t_i) of a current correlogram (u_l) with respect to a reference u_k. The waveform distortion if then given by the time shift Δt required to match the reference trace (Figure 5.2b). The similarity between u_l and u_k at a local time t_i is given by (*Nakata et al.*, 2019, Chapter 9):

$$C^i_{k,l}(\Delta t) = \sum_{t=t_i-t_w/2}^{t_i+t_w/2} \frac{u_k(t)u_l(1 \pm \Delta t)}{\sqrt{u_k^2(t)u_l^2(1 \pm \Delta t)}} \tag{5.13}$$

A linear function is then fitted with the collected time shifts $\Delta t_{max}(t_i)$ that maximize $C^i_{k,l}(\Delta t)$ (Figure 5.2d). The final $\Delta t/t$ is then obtained by measuring the slope of the linear function.

5.4.3 Comparison of both methods

Hadziioannou et al. (2009) made a detailed comparison of both methods showing better results for the stretching technique in noisy conditions. On the other hand, the stretching technique can be biased by changes of frequency content (*Zhan et al.*, 2013). In addition the MWCS does not suffer from the amplitude changes that result from the assumption of stretching a waveform.

In Chapter 8, I apply the stretching technique to 2 years of ambient noise seismic records collected at the Theistareykir geothermal field (NE Iceland) to investigate possible changes in the reservoir due to exploitation related activities.

Part II

Applications

6

Optimized experimental network design for microseismicity location and monitoring

This chapter focuses on the application of survey design tools described in Chapter 3 to extend a seismic network dedicated for microseismicity monitoring at the Theistareykir geothermal field (NE Iceland). The same principles were then used to qualify an existing network recording microseismicity at the Reykjanes Peninsula (SW Iceland).

Optimized experimental network design for earthquake location problems: Applications to geothermal and volcanic field seismic networks

Tania Toledo, Philippe Jousset, Hansruedi Maurer, Charlotte Krawczyk

Article published in *Journal of Volcanology and Geothermal Research*, 2020.
https://doi.org/10.1016/j.jvolgeores.2018.08.011

Abstract: We constructed a network optimization scheme based on well-established survey design tools to design and qualify local and regional microseismic monitoring arrays dedicated for geothermal exploration and volcano monitoring. The optimization routine is based on the traditional minimization of the volume error ellipsoid of the linearized earthquake location problem (D-criterion) with the twist of a sequential design procedure. Seismic stations are removed one by one to obtain networks for constraining the locations of multiple hypothetic earthquakes with varying local magnitudes. The sequential approach is simple and allows the analysis of benefit/cost relations. Cost curves are computed for all hypothetic events to reveal the minimum optimal number of stations given specific design experiment objectives.

The scheme is first demonstrated on three test design experiments. Later, we use the routine to augment an existing seismic network for monitoring

microseismicity in a geothermal field in NE Iceland (Theistareykir). The resulting 23 station network would become the backbone of a reservoir behavior and exploitation activity study. Hypothetic event locations and magnitude relations are taken from a previous regional seismicity study and coincide with geothermal injection and production areas. Sensitivities are calculated with a known 1D velocity model profile using a finite-difference back-ray tracer, and body wave amplitudes are computed from known local magnitude relations. Finally, expected earthquake location accuracies are calculated via multiple Monte Carlo experiments.

The design routine is later used to qualify an existing seismic network located in SW Iceland (Reykjanes). The seismic array is reduced to strategic positions, and benefit and expected accuracies are quantified to observe whether costs could have been optimized had a previous network design experiment been performed.

Overall, we explore quick and flexible tools for designing and qualifying networks for many applications at various scales.

6.1 Introduction

Since the mid 70s, the identification of economically attractive reservoirs and their exploitation for geothermal heat energy have been the aim of numerous projects worldwide (*Dyer et al.*, 2008; *Tester et al.*, 2006). Parameters such as heat source, reservoir, and preferential fluid pathways geometries, the availability and characteristics of underground fluids, and the knowledge of the recharge area are some of the main targets for the exploration of both conventional and enhanced geothermal systems (EGS). These parameters rarely show surface manifestations, and are therefore mostly assessed by geophysical techniques such as microseismic monitoring.

Several studies have shown that geothermal and volcanic systems are usually associated with high levels of natural and/or induced microseismic activity (e.g. Soultz-sous-Forêts (*Cuenot et al.*, 2008), Hengill (*Jousset et al.*, 2011), Basel (*Majer et al.*, 2007), Merapi volcano (*Surono et al.*, 2012), Reykjanes (*Blanck et al.*, 2018b, this issue), Krafla (*Foulger et al.*, 1983)).

These events are good indicators of the active processes in the subsurface. Accurate event location can potentially help identify the reservoir boundaries; the shape, size, position, and/or growth of active fractures or faults (*Philips et al.*, 2002); and, when correlating the seismicity evolution with time, the migration patterns of injection fluids. Well-constrained events also improve results of further seismic studies such as earthquake tomography, attenuation and anisotropy structural analysis, and source mechanism determination with first arrival wave polarity (e.g. *Blanck et al.*, 2018b, this issue) for an overall better understanding of a geothermal field and/or volcanic hazard assessment. In the best case scenario, high precision micro-earthquake locations serve as guides for further drilling and development of a geothermal field (e.g. *Jousset et al.*, 2016). In a similar way, volcanic hazard studies can be enhanced with better seismic event precision (e.g. *Surono et al.*, 2012).

High precision hypocentral parameters are the aim of most passive microseismic studies and considerable effort is currently dedicated to develop standardized data-processing and inversion techniques. These methods range from ray-based (e.g. *Aki and Richards*, 1980; *Kissling et al.*, 1994) and grid search methods (e.g. *Lomax*, 2005; *Sambridge and Kennett*, 1986, 2001), to wave-field back-propagation (e.g. *McMechan*, 1982; *Witten and Artman*, 2011) and waveform stacking (e.g. *Cesca and Grigoli*, 2015; *Kao and Shan*, 2007), among others. Ray-based or arrival time inversion techniques with travel time picking are to this day the most common choice in microseismic experiments given their formulation simplicity, their relatively fast computation despite the large amounts of data, the availability of inversion packages, and the proven results in numerous case studies. Several of these standard automated location routines rely on Geiger's algorithm (*Geiger*, 1912), where the location is derived by carrying out an inversion that iteratively minimizes observed and synthetic travel times of body waves (*Aki and Richards*, 1980). For simplicity and inversion stability, event location is usually first performed using a 1D reference velocity model. This assumption can limit the location accuracy, given the systematic biases that are introduced by 3D velocity changes. This effect is normally alleviated by including source and/or station correction terms and/or jointly inverting the travel time data for both hypocenters and velocity structure in local earthquake tomography studies (e.g. *Eberhart-Phillips* (1990); *Ellsworth* (1977); *Kissling et al.* (1994); *Michelini* (1995); *Roecker* (1981); *Thurber* (1992)).

It has been pointed out by several authors that the success, reliability, and accuracy of the results strongly depend on acquired data quality mainly given by the number of available phases, accurate picking (if needed) (*Pavlis*, 1986), and network geometry (*Kijko*, 1977; *Rabinowitz and Steinberg*, 1990; *Uhrhammer*, 1980). Although we have limited influence on the micro-earthquake occurrence, we can maximize the information content of an experiment by designing optimal network configurations or by selecting an optimal subset of an existing dense dataset (e.g. *Maurer et al.*, 2010). Ideally one can think of improving results precision by using a large number of seismometers, in practice however, geothermal exploration and seismic monitoring in general is strongly constrained by budget. On top of that, no additional information can ever compensate missing or inadequate data required for resolving a target parameter, hence the critical importance of the survey design choice.

The usual procedure in geothermal exploration or volcano monitoring is to deploy a number of seismometers (6 or more) covering a prospect area or volcano, and record continuously over a period of time at sampling rates higher than 50 Hz. Often the seismic network is designed following a heuristic approach with some basic guidelines: the expected microseismic events should be located within the array forming an azimuthal gap of less than $\sim 180°$ (*Valtonen et al.*, 2013), and the average inter-station spacing should be of the average hypocentral depths.

In some cases, standard designs involve specific configurations required for existing inversion and analysis tools. The later choice can be quite restrictive when encountering field and/or instrumentation constrains. Heuristic design can also lead to difficulties in evaluating potential error estimations. Several inversion tests would be needed to find an adequate design that effectively minimizes potential errors, leading to a considerably large computational cost.

Alternative network design strategies have been introduced in the framework of experimental design (ED) for a variety of applications (e.g. *Coles and Curtis*, 2011a; *Curtis*, 1999b; *Glenn and Ward*, 1976; *Jones and Foster*, 1986; *Kraft et al.*, 2013; *Maurer and Boerner*, 1998; *Nuber et al.*, 2017; *Uhrhammer*, 1980; *Wilkinson et al.*, 2006). The main concept is to minimize (or maximize) an objective function representing optimum network performance, which is in many cases related to the eigenvalue content of the linearized inverse earthquake location problem. One popular functional for the earthquake location problem is the *D-criterion* first implemented by *Kijko* (1977) and later exploited by *Rabinowitz and Steinberg* (1990) to monitor a single point source using the DETMAX algorithm (*Mitchell*, 1974). Later *Steinberg et al.* (1995) extended these principles to obtain networks dedicated to monitor fault lines and multiple seismic sources by introducing a multi-source objective function. The *D-optimal* concept for event location network design is also implemented in the software program OPTINET (*Shimsoni et al.*, 1992).

The *D-criterion* is however only applicable in linearized design problems. Geoscientific experiments on the other hand exhibit a complex non-linearity which only increases with the number of optimizing parameters and observables. This makes nonlinear optimization still very prohibitive at large scales due to its large computational demand, however some efforts in this direction have been made with promising results. *Coles and Curtis* (2011a), for example, presented a practical approach for fully non-linear Bayesian statistical experimental design by introducing a generalization of the *D-criterion* which they called D_N optimization. This function benefits from linearized methods to make the optimization computationally feasible in comparison to other non-linear approaches. They applied the algorithm to construct a seafloor microseismic network for monitoring an offshore petroleum field and compared its performance with a network acquired with linearized Bayesian sequential design, with better results using their method.

Hardt and Scherbaum (1994) studied the potential for multi-purpose designs addressing objectives such as tomography, focal mechanisms, and source-parameter estimation for an aftershock experiment. Their work uses a simulated annealing approach (*Kirkpatrick et al.*, 1983) that reduces a synthetic temperature to search for the global minimum of the objective function. Their results primarily point out that different research objectives require different network configurations. Later *Kraft et al.* (2013) extended this algorithm to include the possibility of using 3-D velocity models by adding a finite-difference ray tracer to compute travel-times. They also introduce the construction of event detection thresholds by using the Brune source model (*Brune*, 1970, 1971) to compute body-wave amplitudes and compare them to local noise level amplitudes for augmenting a microseismic network in northern Switzerland (*Kraft et al.*, 2013).

Although global optimizers provide optimal configurations, its use may require extensive computations as different initial configurations would be needed to check for the stability of the solutions. Moreover, global optimizers can be quite restrictive when addressing changes in the theoretical station positions due to field conditions, and many more calculations would be then necessary to produce an alternative station configuration that accounts for these new constrains. These facts motivated *Curtis et al.* (2004) to use a sequential design approach for a 2D microseismic monitoring example with sources placed inside a borehole. The idea consisted of removing receiver positions that represent redundant data in a stepwise fashion. In this paper we shall explore a similar approach in 3D for constructing and qualifying passive seismic networks for geothermal exploration purposes. This sequential optimization concept not only reduces the computation time for network design but it also facilitates addressing the benefit/cost question, which is oftentimes overlooked.

One main goal of this study is to apply fast and well-established linearized sequential survey design tools to a new problem: constructing and qualifying microseismic arrays dedicated to monitor geothermal operations. Therefore, after introducing a brief theoretical background for earthquake location problems and relevant concepts of experimental design theory, we present the used algorithm with the particular emphasis of treating large amounts of hypothetical sources of varying local magnitudes to obtain optimal positions for a given number of seismic stations. The chosen scheme is robust, simple, and addresses concepts like benefits and costs. It is also particularly useful for qualifying and augmenting networks with existing stations. We therefore first introduce three simple test cases to demonstrate the chosen approach. Later, we present the two case studies where the algorithm was used to augment (Theistareykir case study), and test the network quality of an existing array (Reykjanes case study).

Although global optimality cannot be guaranteed by sequential methods -whether the metric used is linearized or non-linear-, the technique hereby explored arrives to quick designs with good performance nonetheless. Linearized sequential design poses less computational costs which makes these techniques more efficient in cases where quick designs are needed such as post-earthquake aftershock studies. It could also provide a framework for potential design-during-deployment (DDD).

The word "linearized" here and throughout this manuscript refers to the fact that the quality metric used to assess each design relies on a linearized information measure. Hence, even if a Bayesian formulation -which includes an *a priori* distribution of models- is used, such a measure can only provide an approximation to the true measure of information expected to be provided by each design. Whether or not the globally optimal experiment under that information measure is found has nothing to do with the measure, and therefore has nothing to do with linearization.

Global optimality can be obtained when using linearized design quality metrics if a global optimization algorithm is used (such as a simple grid search over design space). By contrast, *Guest and Curtis* (2009) use sequential methods to design experiments using fully nonlinearized quality measures; so although for each design their quality metric will give a more robust assessment of the amount of information than linearized metrics (but of course more costly to evaluate), the sequential methods that they applied, while fast to converge, will not in general find the globally optimal design under that metric.

6.2 Background theory and synthetic examples

6.2.1 Basic principles of earthquake location and inverse theory

Micro-earthquake location is a classical nonlinear inverse problem that aims to obtain a set of model parameters $\mathbf{m}$ (event position coordinates $\mathbf{x}_o$, $\mathbf{y}_o$, $\mathbf{z}_o$, and origin time $\mathbf{t}_o$) from observed data $\mathbf{d}^{obs}$ (P and S wave arrival times $\mathbf{t}_p$ and $\mathbf{t}_s$) assuming a mapping operator $\mathbf{G}$ that relates them. The linearized system of equations representing the forward problem is expressed as:

$$\mathbf{d} = \mathbf{G}\mathbf{m} \tag{6.1}$$

where $\boldsymbol{G}$ corresponds to the true physical processes in the subsurface when it relates a true model of the subsurface $\mathbf{m}^{true}$ with $\mathbf{d}^{obs}$. In a similar fashion any set of predicted data $\mathbf{d}^{est}$ can be calculated using an estimated set of model parameters $\mathbf{m}^{est}$ assuming a known forward operator or data kernel $\boldsymbol{G}$. In the event location problem, $\boldsymbol{G}$ is comprised by the sensitivities of travel times with respect to the hypocentral coordinates and the origin time. These sensitivities are calculated in this work by using *Podvin and Lecomte* (1991) finite-difference time-field calculations and a back-raytracing routine.

One usual procedure to tackle the inverse problem is to iteratively compute forward modeled data $\mathbf{d}^{est}$ and compare it to the observed dataset $\mathbf{d}^{obs}$ such that the misfit between the two is minimized (*Tarantola*, 2005). To achieve a better search of the global minima, the problem is commonly solved by adding regularization constrains that tackle instabilities due to data uncertainties (*Levenberg*, 1944; *Marquardt*, 1963). The damped least-squares solution to the inverse problem of Eq. 6.1 is given by:

$$\mathbf{m}^{est} = (\mathbf{G}^T\mathbf{G} + \gamma\mathbf{I})^{-1}\mathbf{G}^T\mathbf{d} \tag{6.2}$$

where γ corresponds to the damping factor, and I is an NxN identity matrix with N being the number of model parameters contained in $\boldsymbol{m}$ (4 for this case). Square matrix $\mathbf{G}^T\mathbf{G}$ is often near singular, and inversion stability strongly depends on its ability to be inverted. The reader is referred to *Menke* (2012) and *Lee and Stewart* (1981) for extended relevant derivations.

6.2.2 Experimental survey design: The *D*-criterion

The main goal of experimental survey design is to select a network geometry or data subset that would minimize the computational and/or acquisition costs while optimizing the benefit of an inversion problem (*Maurer et al.*, 2010). This benefit or "goodness" can best be described in terms of the potential information content that can be obtained from a dataset, namely the eigenvalue content ($\lambda_i : i = 1, ..., N$) of matrix $\mathbf{G}^T\mathbf{G}$ (*Curtis*, 2004).

One important property of eigenvalue content is its relationship to error propagation. Errors in the data space propagate into the solution $\mathbf{m}^{est}$ with an amplification of $1/\lambda_i$, parallel to their corresponding eigenvector. This means that for small eigenvalues the propagation error can be quite large if not making the solution unstable altogether (ill-conditioned problem). As a matter of fact, the covariance matrix of the solution to Eq. 6.2 is given by (*Menke*, 2012):

$$cov(\mathbf{m}) = \sigma^2(\mathbf{G}^T\mathbf{G})^{-1} \tag{6.3}$$

where σ^2 corresponds to the variance of onset-time determination. Assuming a constant σ^2, the shape of the precision ellipsoid is given by eigenvectors and eigenvalues of $1/(\mathbf{G}^T\mathbf{G})$ and its volume is proportional to $1/\det(\mathbf{G}^T\mathbf{G})$ (*Buland*, 1976; *Flinn*, 1965).

Several design quality measures based on matrix $\mathbf{G}^T\mathbf{G}$ have been proposed, compared, and analyzed in previous experimental design works (e.g. *Curtis*, 1999b, 2004; *Maurer et al.*, 2010). However one popular measure in earthquake location problems is given by the determinant of $\mathbf{G}^T\mathbf{G}$, also known as the *D-criterion* due to its sensibility to the entire eigenvalue spectrum (*Hardt and Scherbaum*, 1994; *Kijko*, 1977; *Rabinowitz and Steinberg*, 1990). After testing different quality measures based on the *D-criterion*, we chose to work with a modified version of the multi-source function defined by *Rabinowitz and Steinberg* (1990) for best results. We thus define our quality measure Θ as:

$$\Theta = \sum_{i=1}^{N} \gamma_i \log \left(\frac{1}{\det(G_i^T G_i) + \delta} \right) \tag{6.4}$$

where N stands for the total number of earthquakes, and γ_i corresponds to a weighting factor assigned to each event i ($\gamma_i = 1$ for all events studied in this work). In a Bayesian framework, weights γ_i could be regarded as prior probabilities for the hypocenters (*Chaloner and Verdinelli*, 1995). In this study however, the weights reflect a combination of a prior probability and an event importance (*Steinberg and Rabinowitz*, 2003). We introduce a small value δ in Eq. 6.4 to stabilize the optimization procedure for cases where the determinant would be zero (under-determined case). With this objective function we would in some sense minimize for the confidence ellipsoid volume of all events.

Sensitivities in $\mathbf{G}$ are solely related to the survey design. Hence the "goodness" of matrix $\mathbf{G}^T\mathbf{G}$ can be maximized by selecting the source-receiver configuration that would result in the highest eigenvalue content (minimizing quality measure Θ). In a destructive sequential design framework, $\mathbf{G}$ is first comprised of all possible sensitivity entries, namely all detecting station positions. Later, Θ values are calculated after removing each recording sensor. These values are then compared and the position associated to the minimum Θ value (possibly redundant information) is removed. This process is carried out in a step-wise fashion depleting the *potential deploying area.*

6.2.3 Event detectability

To address the design problem of defining this *potential deploying area* we examine the event detectability in space (e.g. *Coles and Curtis*, 2011a; *Hardt and Scherbaum*, 1994; *Kraft et al.*, 2013). The original amplitude of a seismic phase is influenced mainly by the following factors: magnitude, wave propagation effects (namely geometrical spreading and attenuation), and source processes. The first two factors are addressed in this work only in an approximate manner. Then, events are detected at a point only when their recorded amplitudes are greater than the noise levels at that recording point.

We use the empirical local magnitude-attenuation relation used by the national seismic network in Iceland (South Iceland Lowland or SIL system) to compute recorded amplitudes (*Jakobsdóttir*, 2008):

$$M_L = \log_{10} A + 2.1 * \log_{10} \Delta - 4.8 \tag{6.5}$$

Eq. 6.5 is based on the maximum peak-to-peak amplitude in a 10 seconds interval around the S-wave at all stations, where Δ represents the earthquake-station distance in km, and A is the maximum velocity amplitude of high-pass filtered waveforms with cutoff frequency at 2Hz and a scaled response of a Lennartz 1Hz sensor and a Nanometrics RD3 digitizer.

To construct a detection radius, A is chosen to match a minimum amplitude above an expected noise level. In this work we assume rms noise amplitudes of around 42 nm/s throughout the available space. This rms ground velocity amplitude (v_{rms}) was obtained using the following relation (*Bormann*, 1998):

$$v_{rms} \approx \sqrt{2 \cdot \langle P_a/\omega^2 \rangle \cdot (f_2 - f_1)} \tag{6.6}$$

where P_a corresponds to the most probable noise level at a given frequency interval obtained from the probabilistic power spectral density (PPSD) for ground acceleration (*McNamara and Buland*, 2004) at a given station. Then $\langle P_a/\omega^2 \rangle$ corresponds to the mean converted ground velocity function over a frequency range between f_1 and f_2. Finally, ω stands for the angular frequency. In this work we chose a seismic station located north to the Krafla region in Iceland (*Lees*, 2004), computed its corresponding PPSD using ObsPy (*Beyreuther et al.*, 2010), and calculated the v_{rms} associated to frequencies above 2 Hz.

Then we selected a large signal to noise ratio (SNR $\approx$ 15) for detection threshold construction. Authors like *Hardt and Scherbaum* (1994) point out that a SNR of 3 should be enough to detect a seismic phase onset. However given that only the maximum amplitude in a time window is taken into consideration for the detection, as well as the uncertainties of lateral noise amplitude variations, we chose a much more conservative SNR value to construct the detection thresholds. The *potential deploying area* would then correspond to the region within this detection radius.

Detectability is not the main focus of this work and is therefore roughly addressed. Amplitudes, noise, and magnitude values used are regarded as estimates only, and are merely utilized to define a region to include stations for both the test cases and Case study I, which corresponds to a region neighboring Krafla. It is advisable, where there would be available preliminary seismic data, to compute laterally-variant noise estimates as done by *Kraft et al.* (2013), as well as refining variable values of SNR. Hence, we recommend to update detection models and repeat optimizations once more information on the target sites becomes available. We have also not accounted for different radiation patterns given the typically unknown source parameters in unexplored areas. We encourage to explore this variable when more information is available.

6.2.4 Test Case A: survey design for a single source

To demonstrate the use of the destruction sequential survey design algorithm (DSSD), Fig. 6.1 shows the construction of a 5 (Fig. 6.1a) and a 115 (Fig. 6.1b) station network for locating a single event of M_L 0.8 and 3 km depth in a homogeneous media of constant P-wave velocity (V_p) of 4 km/s. The possible station locations consist of the nodes of a triangular grid with mean spacing of 3.5 km, obtained using the *Persson and Strang* (2004) open-source mesh generator. The triangular mesh was chosen in accordance with the work of *Kraft et al.* (2013).

First, we construct the *potential deploying area* (region within dashed red lines in Fig. 6.1a and Fig. 6.1b) for the given event and the sensitivity matrix **G** for the total number of recording sensors (115 for this case). Next, we remove one station and calculate the quality value Θ for the remaining 114 station network. We put this station back into the network, remove another station, and calculate Θ again. This process is carried out for all recording stations to obtain a list of 115 Θ values. Then we permanently remove the point with lowest associated Θ, and assign to it the last placement number position (115 in this case). In

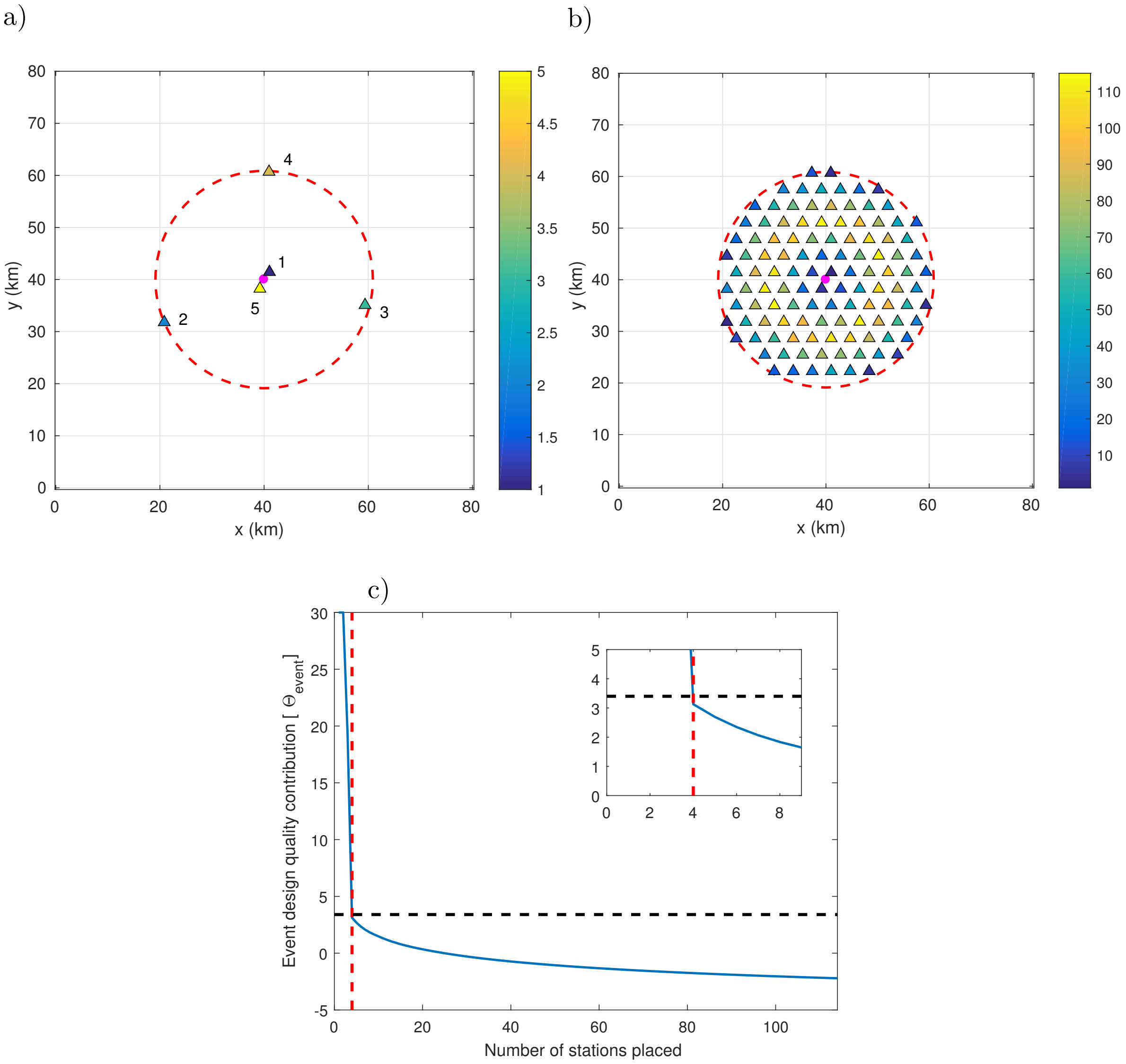

Figure 6.1: Test case A. Survey design example for an event at 3 km depth with M_L 0.8. a) 5 stations setup. b) 115 stations setup. The colorbar expresses the order of placed stations. c) Design quality or "goodness" of the survey setup for each number of placed stations. The dashed red line represents station point 4, and the horizontal dashed black line the limit of $\Theta = 3.4$.

other words we search for the station whose removal would worsen the network quality the least, and would therefore be the last one we would need to place for optimally constraining the hypocenter. Next, we repeat this procedure with the remaining 114 stations to look for the second to last placement number position. This process is repeated until the total 115 available receivers are removed (triangles in Fig. 6.1b) and the full placement order sequence is created (colorbar in Fig. 6.1a and Fig. 6.1b). Notice how when displaying the first 4 seismic stations of the placement sequence (Fig. 6.1a), the distribution has a quadripartite geometry in accordance with results of *Rabinowitz and Steinberg* (1990) and *Hardt and Scherbaum* (1994), with the closest point to the epicenter as the very first station position. When further adding a fifth sensor, notice how this receiver is placed again at a position close to the epicenter. Given the proximity of this location to Station #1, this position can be regarded as redundant information. In the framework of *D*-optimality this clustering or redundance can be interpreted as a high regional importance (*Kraft et al.*, 2013). In this particular case, the double positioning is the result of no station candidate located right above the earthquake epicenter. It is for this reason that the resulting station position sequence must be carefully assessed before ultimately defining a network. Later, after displaying the entire sequence (Fig. 6.1b) we clearly see that the first deployed stations (in darker blue) correspond to those close to the source and to those bordering the detection radius limit.

Fig. 6.1c shows the variation of the design quality value Θ after using -n station positions. Low Θ values indicate good array quality. This curve is a good representation of the benefit/cost relations of the survey design problem. The cost is interpreted as the number of placed stations and the benefit is defined by the value of Θ itself, proportional to the logarithm of the resulting confidence ellipsoid volume. Notice how this value decreases rapidly with the first 4 stations, after which this decrease does not vary significantly. This means it takes only a few optimally positioned stations to reach good network quality. We define a benefit threshold of $\Theta = 3.4$ for this case (dashed blue line) to select a minimum number of stations (4). Using additional receivers will further decrease the confidence ellipsoid volume and it would then be up to the user to decide the number of needed stations to meet the objectives of an experiment, however some attention must be given to potential station clustering. Notice also after placing enough stations, this decrease is not significant, hence the benefit/cost curve tends to flatten with large number of stations.

Though the proposed algorithm can potentially use both P-wave (Vp) and S-wave (Vs) velocities for building the sensitivity matrix, we chose to work only with Vp. Errors in Vs can considerably influence towards constructing a suboptimal station network. On one hand Vs is typically lower than Vp, hence providing higher sensitivities to t_S measurements. At the same time, S-wave picks are often hard to acquire, especially in the presence of noisy data. *Gomberg et al.* (1990) point out that although S-wave data can significantly improve the accuracy of hypocenter location and reduce the trade-off between origin time and source depth, incorrect estimates can also significantly degrade it. In this work we therefore consider S-wave travel-time measurements merely as added values improving the location accuracies at a later stage however not in the design experiment.

6.2.5 Test Case B: small multi-event survey design

In this example we will build a seismic network dedicated to constrain 3 known event targets at a depth of 3 km with varying local magnitudes (M_L 0.8, 0.6, and 0.5). As an initial step, and similar to the previous example, we construct the *potential deploying areas* for all three events. On a second step, the multi-event quality measure Θ is computed after removing each recording station in the system, while carefully accounting for their contribution only to the events that are detected by them. Values are then compared and the station that effectively minimizes Θ is removed. As in the previous exercise, this procedure is repeated until all 231 stations are removed.

Fig. 6.2a and Fig. 6.2b show the resulting 12 and 231 station networks, respectively. Similar to Test Case A, the first stations of the placement order sequence are those close to the event epicenters and those close to the detection boundaries (dark blue triangles). However, no perfect quadripartite geometry is provided for all the events (Fig. 6.2a). This failure to arrive to a perfect 4 station geometry occurs when *potential deploying areas* overlap (as is the

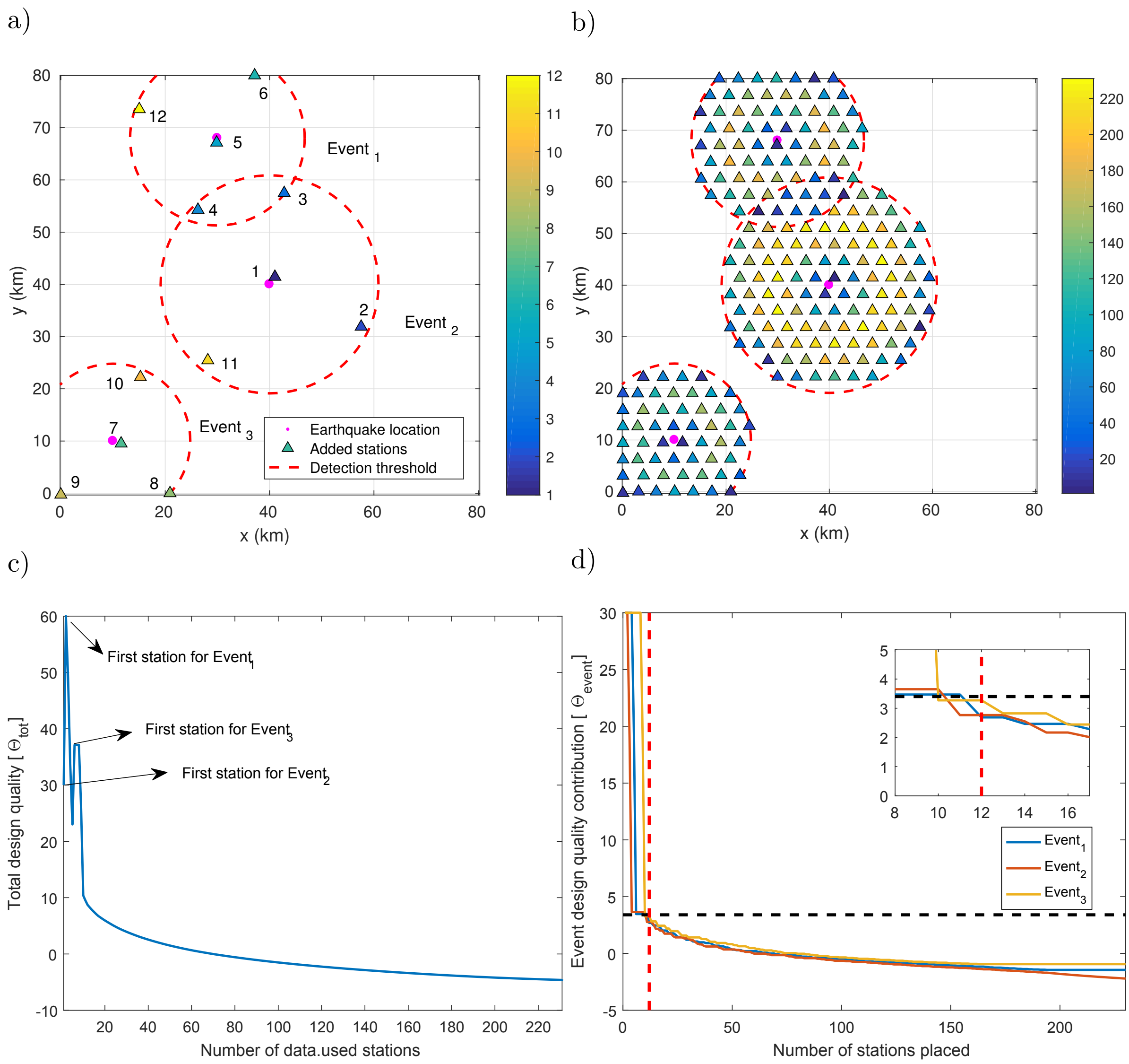

Figure 6.2: Test case B. Survey design example for three events 3 km deep. Events have M_L 0.8 (center), 0.6 (top), and 0.5 (bottom left). a) 12 stations setup. b) 231 stations setup. The colorbar expresses the order of placed stations. c) Total design quality or "goodness" of the survey setup after progressively placing stations. d) Design quality contribution per event for the whole experiment. The dashed red line represents station point 12, and the horizontal dashed black line the limit of $\Theta_{event} = 3.4$.

case of Event$_1$ and Event$_2$). The multi-source objective function will naturally favor these areas given that their contribution to more than one event will reduce Θ most (hence the deep blue triangles all through this region in Fig. 6.2b). Overlapping areas will be even more favored when these regions are considerably large. In these cases, stations would be very hardly placed outside of them, yet it will keep the pattern of putting stations close and far from the epicenters within them. The algorithm could then potentially return a poorer convergence to a perfect quadripartite geometry. To obtain better geometries for particular events, one can assign them higher weighting values γ_i (Eq. 6.4).

The benefit/cost curves, namely the total design quality values Θ_{tot} and the individual event contributions Θ_{event}, are shown in Fig. 6.2c and Fig. 6.2d respectively. Design quality curve Θ_{tot} reveals two marked peaks which correspond to the points where the routine has placed the first station at an event deploying area (e.g. station # 7 would be the first sensor placed for Event$_3$). The contribution of a single sensor at a deploying space yields $\Theta_{event} = 30$, which is result of the sole influence of δ in an under-determined case (Eq. 6.4). An increase of 30 in Θ_{tot} is also visible at these points, hence the peaks in the curve. Naturally, before this first station is introduced no contribution to Θ_{tot} or Θ_{event} is made for this event. Placing a second station would barely reduce this value of 30, for which Θ_{tot} and Θ_{event} hardly decrease (still under-determined case). It is only after introducing the third and fourth stations at a deploying space (reaching an even-determined case) that Θ_{event} is reduced to a value between 3 and 4 (Fig. 6.2d). If we now define a benefit limit per curve of $\Theta_{event} = 3.4$ (dashed blue line), we would then require the 12 stations shown in Fig. 6.2a.

6.2.6 Test Case C: large multi-event survey design

So far, we have addressed the network design for locating a single or very few known events, in practice however, microseismicity studies for geothermal monitoring typically present hundreds if not thousands of events. The next question is how to construct a seismic network for optimizing a large number of earthquakes. Like the previous two cases we assume a constant Vp of 4 km/s throughout the domain, but this time we introduce 1089 events of M$_L$ 0.5 and depth of 3 km placed in a grid-like manner every 2.5 km in x and y directions.

Similar to the previous exercises we use the DSSD algorithm to construct the station placement sequence and their associated quality curves. Fig 6.3a and Fig. 6.3b show the resulting 100 and a 598 station networks, respectively, and Fig. 6.3c and Fig. 6.3d depict the experiment design qualities Θ_{tot} and Θ_{event}. Notice the overall decreasing trend of Θ_{tot} after first reaching a maximum at $\approx$ 26 stations. This is the point where most events have at least one seismic station in their *deploying area* ($\approx$60% of stations).

Once more, from the cost curve (Figure 6.3d) we may observe and select a number of stations that would best constrain most of the 1089 events. It is important to note that constraining all events will be very expensive and at times not realistic. More often than not, we should be ready to sacrifice the benefit or location accuracies of some events for cost reasons. In this case, we select 100 stations (Fig. 6.3a), given that most event cost curves reach a benefit $\Theta_{event} \leq 3.4$ (horizontal black dashed line in Fig. 6.3d). In the resulting network, receivers are scattered in a quasi-regular way throughout the domain with few stations placed at the boundaries. The overall station sequence presents a very similar quasi-regular behavior in Fig. 6.3b.

6.3 Case study I: Theistareykir geothermal field

Theistareykir is a high temperature geothermal field located in NE Iceland that extends from the Öxarfjördur Bay to the center of the country and is associated to the Baejarfjall volcano (Fig. 6.4). It is characterized by a set of large normal faults that strike N22°E with maximum offset of around 200-300 meters, and various rift fissures (*Sveinbjornsdottir et al.*, 2013). This geothermal field has undergone intermittent exploration (1972-1974 and 1981-1984) and monitoring (1991-2000) to assess its capabilities for drilling and production (*Ármannsson*, 2008), and is currently under the administration of Landsvirkjun, the national power company of Iceland. Between 2002 to 2008 seven deep wells were drilled with depths of 1723 m to 2799

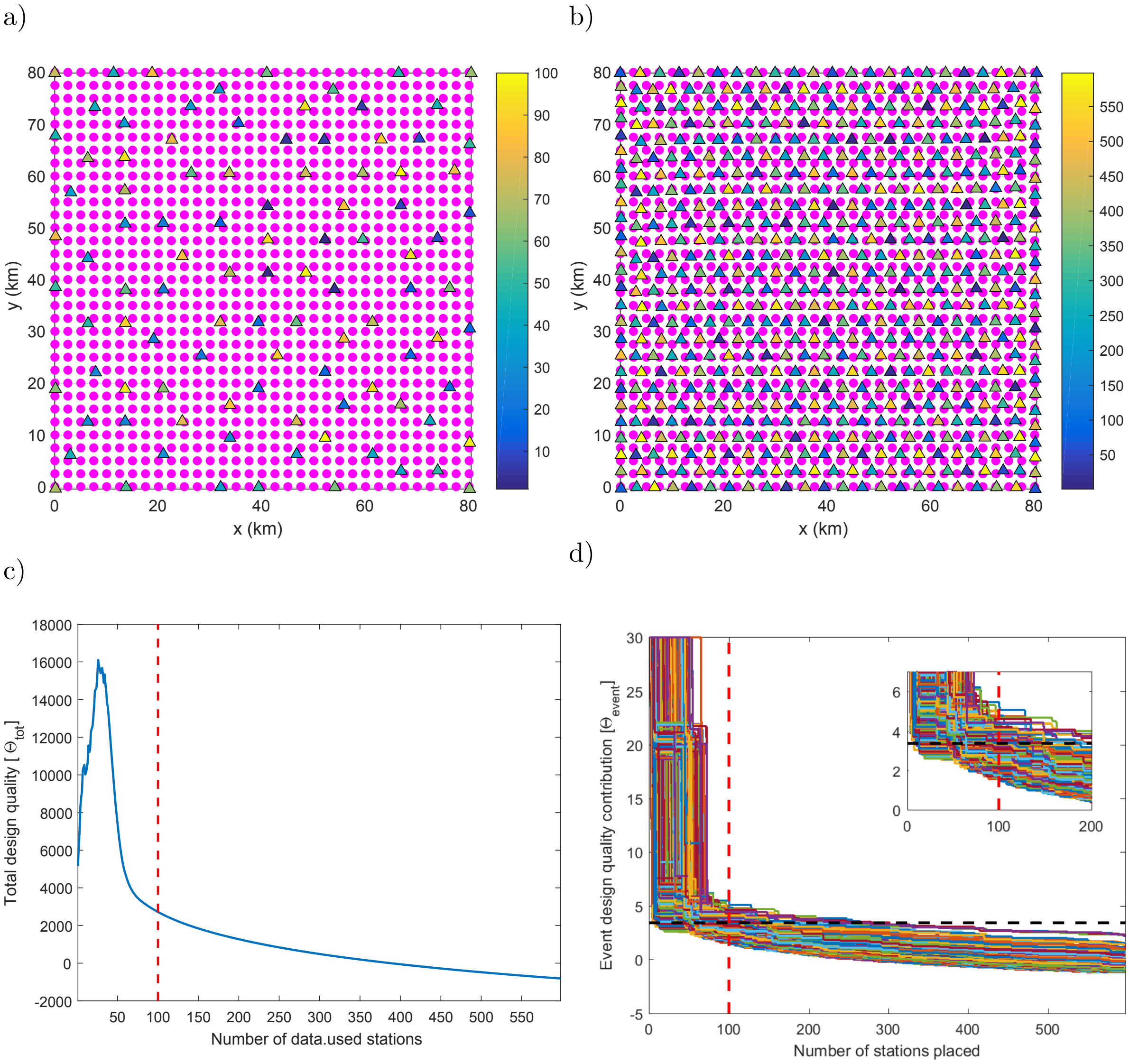

Figure 6.3: Test case C. Survey design example for multiple events of M_L 0.5 located at 3 km depth. Pink points indicate epicenter locations and triangles stand for station locations. The colorbar expresses the order of placed stations. a) 100 stations setup. b) 598 stations setup. c) Total design quality or "goodness" of the survey setup after progressively placing stations. d) Design quality contribution per event for the whole experiment. The dashed red line represents station point 100, and the horizontal dashed black line the limit of $\Theta_{event} = 3.4$.

m, and up to 8 additional wells were included by the end of 2017 (*Landsvirkjun*, 2016). Many of these wells were drilled almost horizontally and the power plant is producing at a capacity of 90 MW since spring 2018.

According to a Landsvirkjun report on seismic data recorded between November 1st 2016 and March 31st 2017 (*Blanck et al.*, 2017a), most of the activity is clustered in the form of vertical chimneys close to the production zone. The report shows a total of 140 earthquakes located mainly at depths between 2 and 5 km with an array consisting of mainly 4 seismic stations in the close vicinity: 1 from the national seismic array (SIL system) and 3 operated by Iceland Geosurvey (ISOR) for Landsvirkjun. These events have mostly local magnitudes of 0.5 and higher, exhibiting a Gutenberg-Richter b-value relation of 2.16. *Blanck et al.* (2017a) interpreted that the large amount of higher magnitude events could be the result of either a strong crust at the site, or the side-effects of a small seismic network.

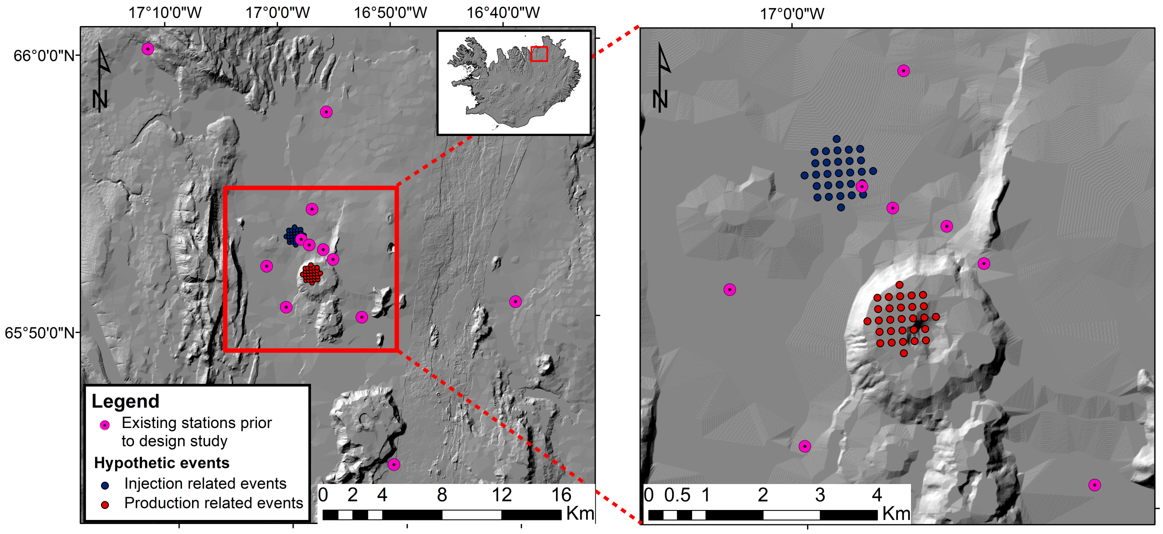

Figure 6.4: Initial receiver positions and synthetic epicenters defined prior to the design study.

6.3.1 Experimental design setup, results and discussion

To better understand the structures and behavior of the reservoir, a seismic network consisting of 12 broadband stations will be augmented to monitor the Theistareykir geothermal field (Fig. 6.4). This network is part of a larger deployment effort to monitor the exploitation activity with an array of multi-parameter stations including gravimeters, GNSS receivers, and seismic sensors (*Jousset et al.*, 2018, EGU abstract). From the seismic stations depicted in Fig. 6.4, seven are permanent stations belonging to the Icelandic Meteorological Office (IMO) and Iceland Geosurvey (ISOR), and five stations belonging to the German Research Center for Geosciences (GFZ) will be fixed at the gravimeter station positions. In this exercise an additional 11 seismic station positions has been defined for a total of 23 receivers across the geothermal field.

Following the proposed sequential survey design recipe, we first specify the target areas where we may expect future microseismic events. These regions correspond to the production and injection zones depicted by the red and blue cluster of points, respectively (Fig. 6.4). As a next step we generate a synthetic earthquake catalog (196 events) using these points as epicenters, and the depth and magnitude distributions of the catalog studied by *Blanck et al.* (2017a) (Fig. 6.5). We chose to focus on local magnitudes between 0.5 and 0.8. Fig. 6.5a depicts the 1D P- and S-wave velocity profiles typically used by the IMO for earthquake locations, though for the design experiment we shall once more only use the 1D P-wave velocity profile.

As in the first test cases the domain is discretized to a 2D triangular grid with node distances of roughly 3.5 km. After defining *deploying areas* for each event, we perform the DSSD algorithm two times: the first time using only the 12 deployed stations as "potential location points", and the second one right after, to account for the remaining positions in the full *deploying space*. Results of the first survey design experiment provide an order of importance of the fixed stations positions and determine which are the critical ones among them. The second exercise is performed to augment the array.

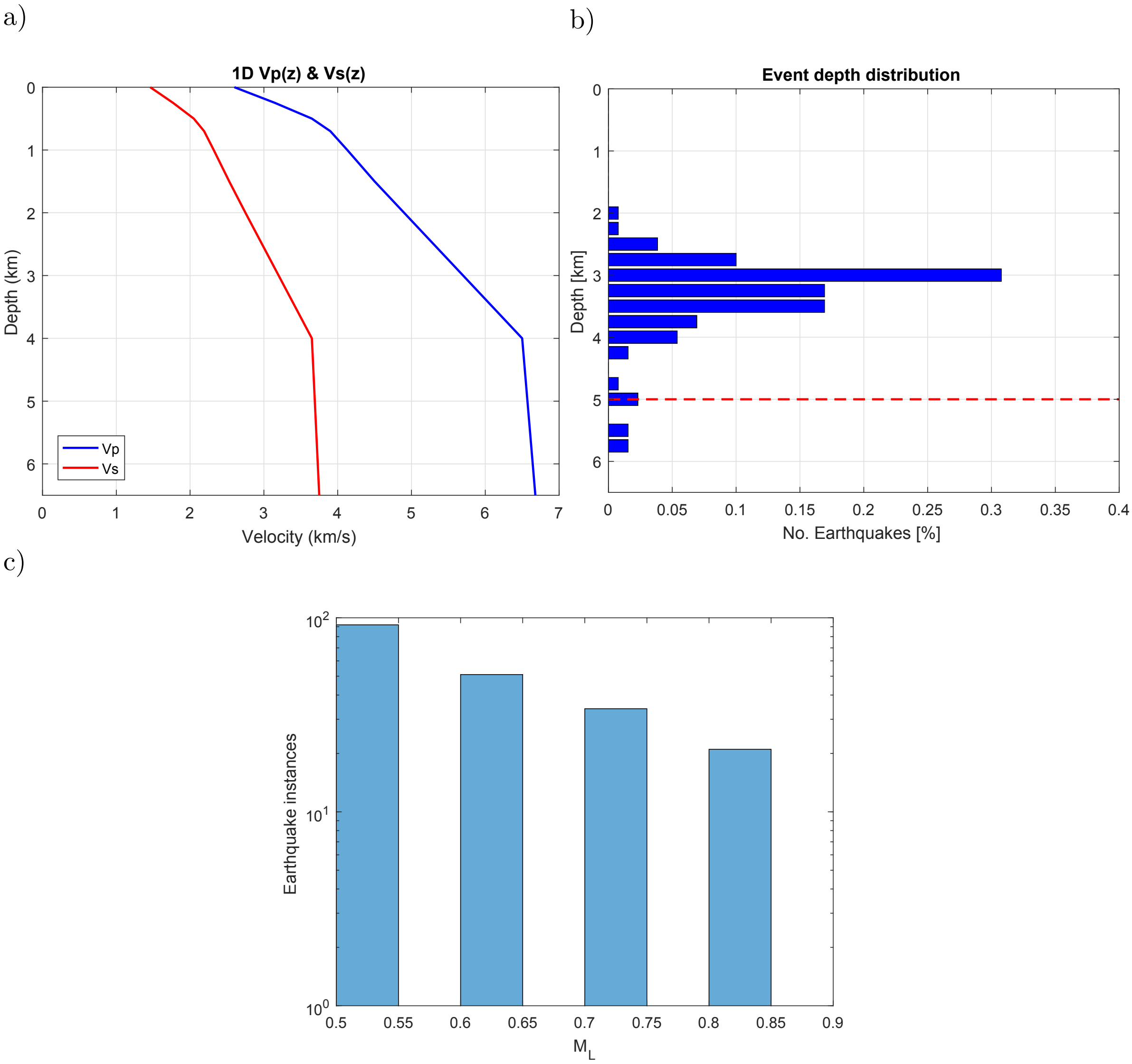

Figure 6.5: Synthetic earthquake catalog specifications. a) 1D P- and S-wave velocity profiles from the SIL system (*Bjarnason et al.*, 1993). c) Event depth distribution. The red line indicate the depth above which 95 % of events are located. This limit is also known as the brittle-ductile boundary. d) Magnitude distribution of the synthetic earthquake catalog. b value = 2.16

6.3.2 Theistareykir experimental survey design

Fig. 6.6a and Fig. 6.6b show the resulting 23 and 135 (complete) station networks. Notice how on the first network the selected stations are located at the outer limits of *deploying areas* with smaller detection radii. However, few stations are anyways placed at the northwest of the epicenters. According to *Steinberg and Rabinowitz* (2003), for velocities varying with depth, receivers recording both direct and refracted waves are necessary for optimal location results. It is also noticeable for the entire sequence of 135 stations (Fig. 6.6b) how, unlike the test cases, the inner stations are selected first and the outermost positions last (corresponding to larger event magnitudes). However within the innermost region, the behavior is similar to that of the test cases, and stations are first located both close and further away from the epicenters. This behavior is the result of having clustered events, with large or entirely overlapping *deploying areas*. A possible solution to better consider the optimization of larger events is to assign them a higher weighting value γ_i (Eq. 6.4). However, given the network objectives to potentially

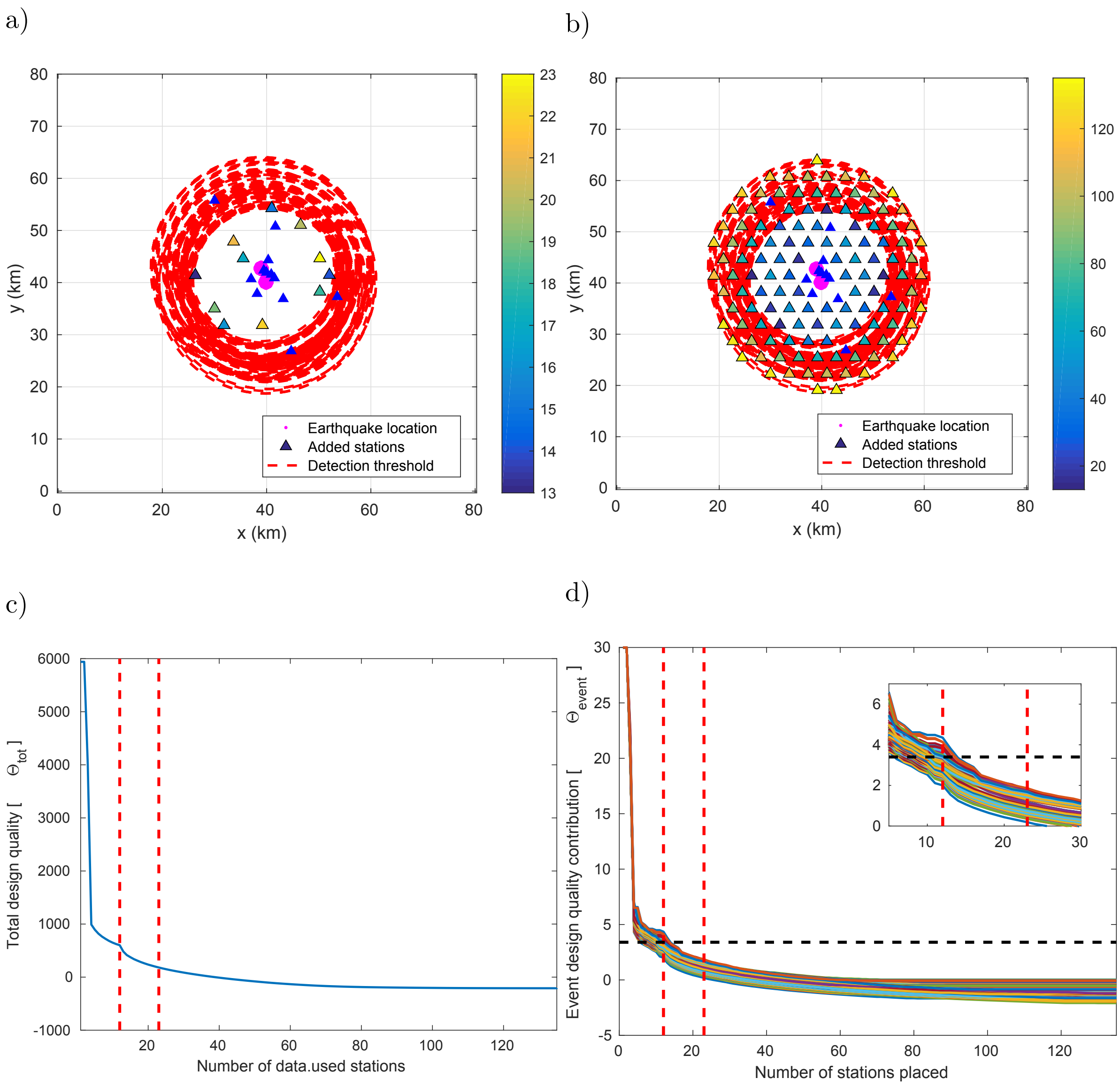

Figure 6.6: a) 23 stations network. b) 135 stations network. The colorbar expresses the order of the added stations. c) Total design quality of the survey setup after progressively adding stations. d) Design quality contribution per event for the whole experiment. The dashed red line on the left indicates the limit for the initial 12 stations, and the red line on the right the limit for a 23 stations network. The horizontal dashed black line indicates the limit of $\Theta_{event} = 3.4$.

detect and locate much smaller earthquakes as well as the easier access to this much reduced area, we have decided to keep $\gamma_i = 1$ for the earthquakes studied.

Similar to Test Case A, Fig. 6.6a presents few areas with some clustered stations (e.g. the westernmost and the northern regions). Although one could argue that some of the additional stations may represent redundant information, we have decided to keep them. In this exercise we have assumed homogenous noise amplitudes and SNR, which might not be the case in reality. Therefore, by keeping the additional stations we are in some sense attempting to ensure traveltime recordings in these regions. We thus recommend to carry out a noise analysis once more seismic data becomes available and assess if and which station positions can be removed, and alternatively be placed elsewhere.

Fig. 6.6c and Fig. 6.6d depict the total Θ_{tot} and individual Θ_{event} design quality or cost curves. Notice the marked decrease in both Θ_{event} and Θ_{tot} curves after introducing only one additional sensor (station # 13). When analyzing the curves for Θ_{event}, we observe how after introducing the initial 12 stations, most curves lie below a value of 3.4. The placement of additional 11 stations results in $\Theta_{event} \leq 2$ for almost all curves. Adding many more stations would enhance the benefit much less significantly as the curves tend to flatten towards the end. As a matter of fact, Θ_{tot} stops decreasing significantly after ≈ 35 stations.

6.3.3 Spatial quality measure distribution

If we now take the opposite problem where the station positions are fixed and a series of hypocenters are located every 2.5 km in the x and y directions, and every 0.5 km in the z direction in a rectangular grid-like manner, we can estimate the "goodness" of the network for constraining each of these additional points by computing their corresponding quality measure Θ_{event}. Therefore this exercise consists on the observation of the network benefit for earthquakes in the region different from those in the catalog used in the design phase. Fig. 6.7 shows these design quality or "goodness" maps for events of magnitudes: M_L 0.5 (left column) and M_L 0.8 (right column). Uncolored areas lie outside detectable bounds and are thus not considered for the goodness calculation. Areas marking higher values of Θ_{event} (colored in yellow) correspond to points with few readings. Conversely, low values of Θ_{event} indicate best quality and hence lower error propagation in the inversion results (Eq. 6.2). Notice how for both cases (3 km depth slice), the regions with low values Θ_{event} lie within the array, and is best where the network is denser especially right below the station positions in the center (Fig. 6.7c and Fig. 6.7d). This is to be expected given that these regions correspond to some of the target event locations used for the network design. The extents of the high quality area (dark blue) reach a radius of $\sim$20 km from the epicenters shown in Fig. 6.4.

In a similar way, we can observe how for a E-W profile (located at approximately the domain center, y = 37.5 km) the area with best design quality has a rough semi-circular shape and is best under the denser network region, with low values (best quality) roughly reaching 10 km below the surface for both cases (Fig. 6.7e and Fig. 6.7f). For both cases, the potentially best invertible hypocenter locations match the injection and production areas, hence reaching our goal for the Theistareykir survey design with a $\Theta_{event} \approx 2$. Overall, goodness maps prove good quick tools for providing a qualitative character of the inversion errors for points across an area.

6.3.4 Earthquake location accuracies

As a final step, we analyze the effects of seismic array configuration on hypocenter location accuracies. For this purpose, we follow a Monte Carlo approach proposed by *Billings et al.* (1994) and calculate the standard deviation of resulting hypocentral parameters after the least-squares inversion procedure of several perturbed P- and S- wave datasets. We define these standard deviations as earthquake location accuracies. In this exercise, synthetic P- (t_P) and S-(t_S) wave arrival times were contaminated with normally distributed errors with means at 0.2 s and 0.4 s, respectively. Considered sources correspond to the same grid points of the design quality map exercise, at a depth of 3 km. The velocity model used is shown in Fig. 6.5a. We subsequently invert for each dataset using a damping factor of 0.1. Initial values x_0 and y_0 were taken as the true values with normally distributed errors of 2 km, and z_0 was set

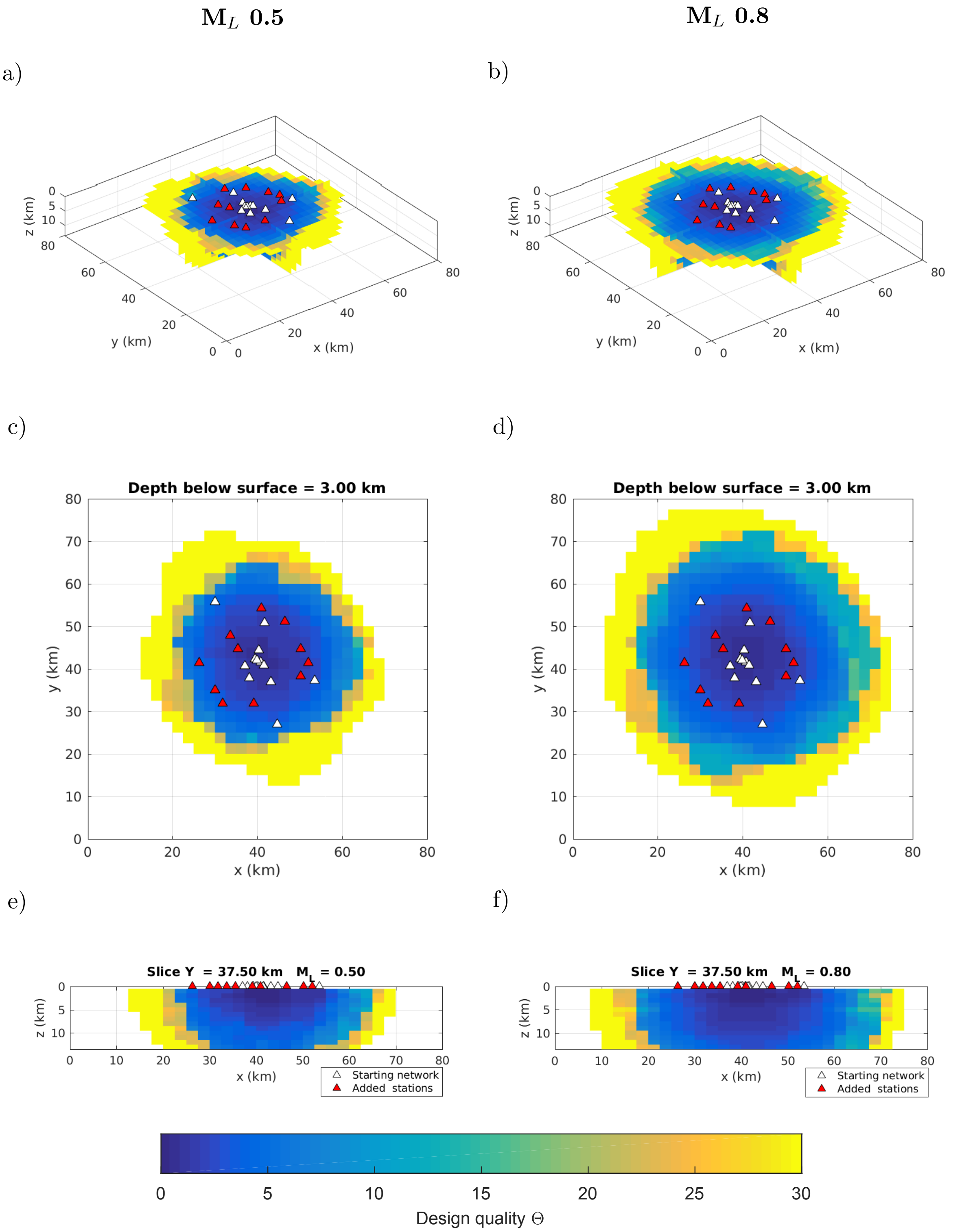

Figure 6.7: Measures of design quality or network goodness according to event position and magnitude. The first column indicates values associated to events of M_L 0.5, the second to M_L 0.8. White triangles mark the starting station positions. The red triangles stand for the added stations after the design experiment. a) and b) show a 3D view, c) and d) depict a depth slice at 3 km, and e) and f) an YZ profile cutting at y = 37.5 km.

to 1.5 km. These values are used assuming that a previous automatic detection scheme has been used and the inversions are merely a refinement step. This is usually the procedure in microseismic problems.

Fig. 6.8 depicts the resulting accuracy or standard deviation maps after performing the inversions. Notice how accuracies in x and y are slightly lower than accuracies in z. This is to be expected as we have a 2D receiver configuration for a 3D problem. Events located inside the array present resulting accuracies of around 0.3 km, 0.3 km, and 0.6 km for the x, y, and z components respectively in both magnitude cases. The position errors in the inner regions (difference between true and mean inverted values in Fig. 6.9a and Fig. 6.9b) are of around half a kilometer. The areas external to the seismic network present higher accuracy values and location errors, due to the fewer travel time readings and the limited azimuthal coverage. The uncolored areas in Fig. 6.8 and Fig. 6.9 do not entirely match those provided by Fig. 6.7 given that only points with at least 6 data entries were inverted to avoid non-converging results.

To further study the uncertainty improvements after introducing the new stations we repeated the previous exercise, this time for the synthetic earthquake catalog used in the design phase (Fig. 6.5). Hence, several synthetic travel time datasets were inverted for the original 12 and final 23 station networks. Their resulting accuracy and error differences are depicted in Fig. 6.10. Notice how the accuracies have improved around 0.2 km for all hypocentral components and location errors. The network symmetry around the epicenters contribute to better epicentral estimates, whereas positions on top and far from them contribute to better depth estimates (*Steinberg and Rabinowitz*, 2003).

Overall, inversion results are subject to changes depending on the initial values and travel time (picking) errors. In this study we have overestimated these values, so better results should be expected with lower picking errors. Errors in the velocity model were also not accounted for in this analysis. All things considered, the resulting accuracies and errors are acceptable for the seismic network purposes, therefore validating this final 23 station array as adequate.

6.4 Case study II: Reykjanes seismic data and network performance

The Reykjanes peninsula is a region located in SW Iceland (Fig. 6.11a) characterized by high volcanic and seismic activity resulting in a large number of high temperature geothermal areas (*Blanck et al.*, 2018b, this issue). A total of 6 fields are currently being exploited in this region and are associated to four NE-SW oriented fissure swarms connected to 4 different volcanic systems (*Harðardottir et al.*, 2009). Particularly the Reykjanes field located at the tip of the peninsula has a capacity of 100 MWe (*Friðleifsson et al.*, 2018, this issue).

Within the framework of the IMAGE project (Integrated Methods for Advanced Geothermal Exploration) a passive seismic array consisting of 86 on-land sensors and OBS distributed on and around the peninsula was used to monitor the seismicity, and enhance and develop existing and new passive seismic techniques for imaging geothermal fields (Fig. 6.11a). The array consisted of 30 temporary on-land seismometers distributed in a concentric fashion around the Reykjanes peninsula, 26 OBS surrounding the peninsula, 8 seismic stations handled by ISOR for the permanent monitoring of the Reykjanes geothermal field, 15 stations of the Czech Academy of Science (CAS) used for monitoring the Krýsuvík geothermal system, and 7 permanent stations handled by the IMO as part of the national seismic network (*Blanck et al.*, 2018b, this issue). The array recorded from march 2014 to august 2015, and the resulting dataset

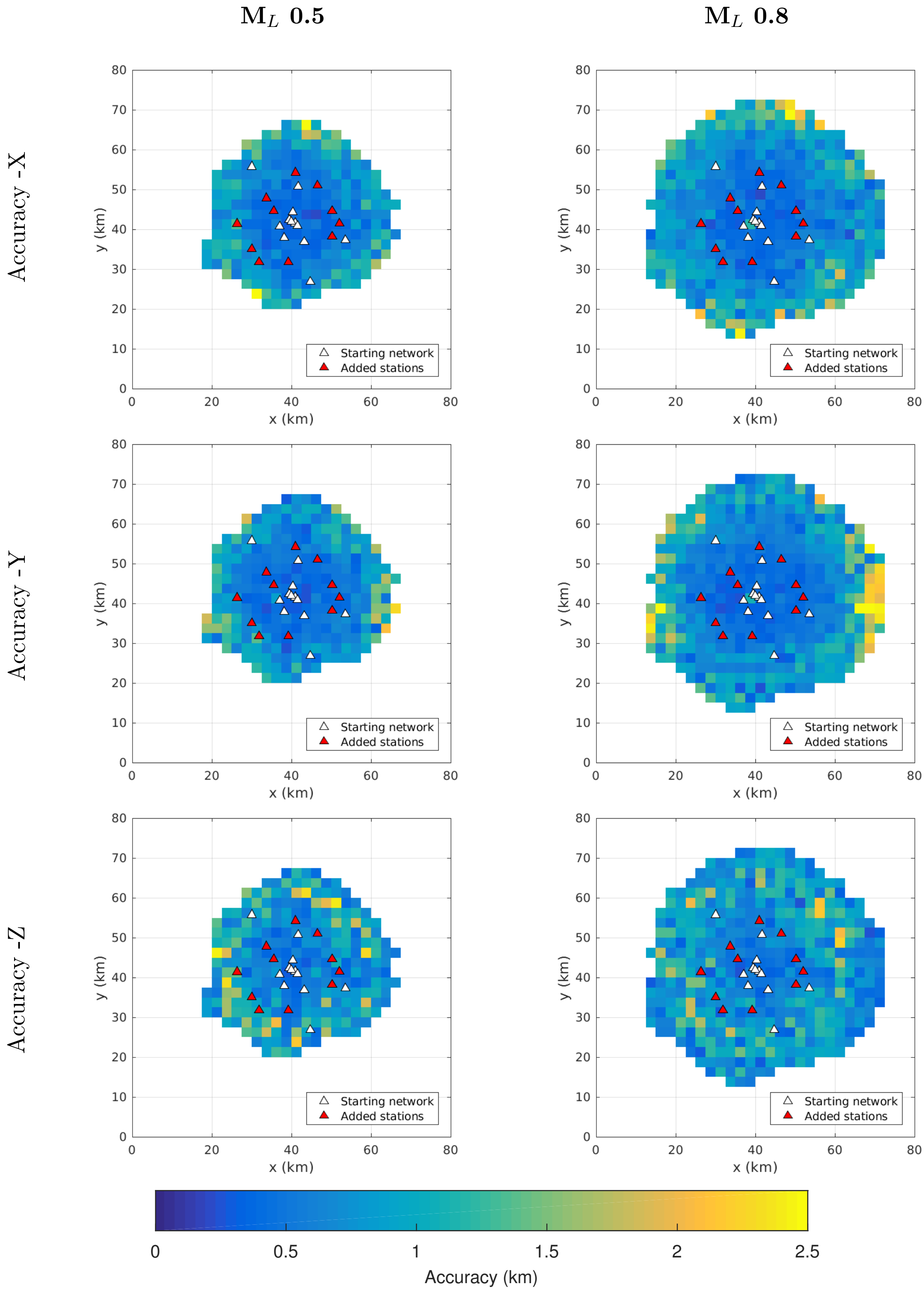

Figure 6.8: Accuracies of hypocentral coordinates for events at 3 km depth. The first column indicates events of M$_L$ 0.5 and the second of M$_L$ 0.8. Red triangles mark station positions.

was used to study the regional seismicity and structures by means of re-localization and focal mechanism analysis (*Blanck et al.*, 2018b, this issue), travel time tomography (*Jousset et al.*, 2016), ambient noise analysis (*Weemstra et al.*, 2016), and seismic interferometry (*Martins et al.*, 2020b; *Verdel et al.*, 2016, this issue). *Einarsson et al.* (2018, this issue) additionally analyzed the natural and exploitation related stress field changes of the region.

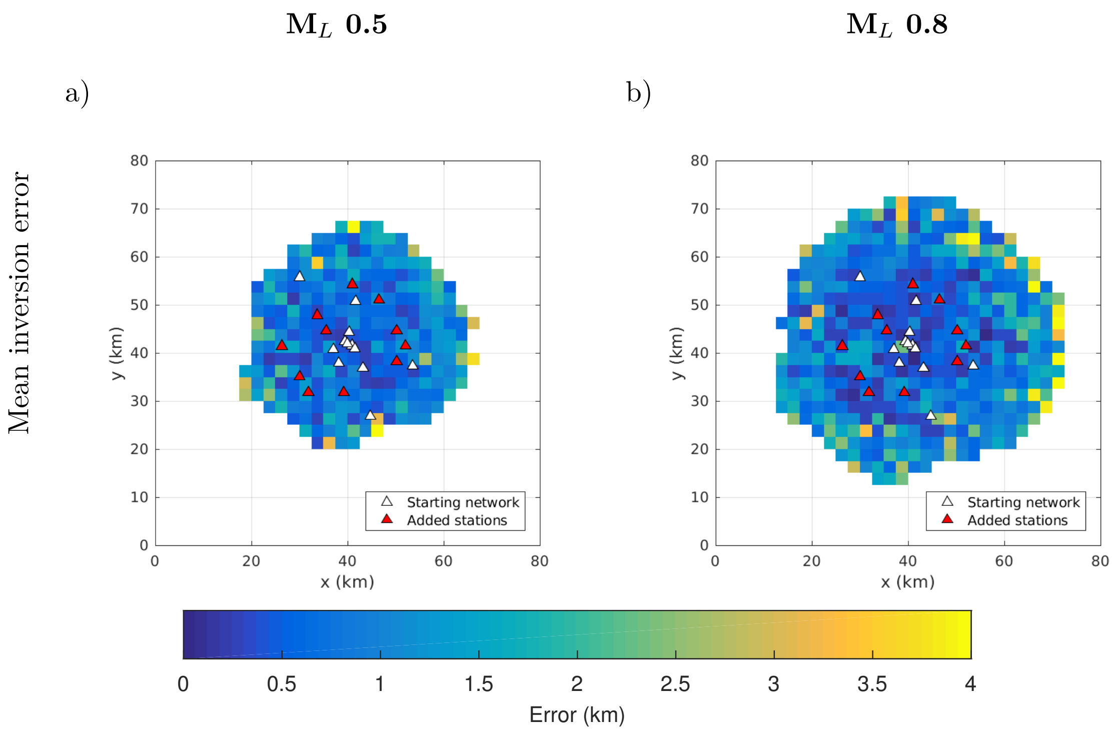

Figure 6.9: Mean inversion errors for events at 3 km depth and magnitudes a) M$_L$ 0.5 and b) M$_L$ 0.8.

6.4.1 Seismic network quality

A total of 2066 earthquakes were automatically detected with an STA/LTA approach after which P- and S- wave arrivals were picked manually. An initial earthquake location was carried out by *Blanck et al.* (2018b, this issue) using the 1D SIL velocity model (*Bjarnason et al.*, 1993), and later relocated the hypocenters using the model derived by *Jousset et al.* (2016) shown in Fig. 6.12a. For the exercise of qualifying the network design we reduce the seismic catalog to account only for events placed within the network and located with at least 3 P- and 3 S- wave picks. The remaining 1981 seismic events are displayed as blue points in Fig. 6.11a and Fig. 6.11b. Seismic events are mostly distributed along the mid-ocean ridge, with the majority located close to the Reykjanes peninsula tip (third cluster on the right). These earthquakes reach a maximum depth of around 6km, marking the brittle-ductile boundary of that region in accordance to a previous study by *Kristjánsdóttir* (2013). Fig. 6.12b depicts the maximum station-event distance relationship per earthquake needed to construct theoretical *deploying areas*. Notice how a significant number of events reach a maximum distance of around 10 km corresponding, in a large degree, to events located under the Reykjanes peninsula.

To assess the quality of the Reykjanes seismic array with respect to the located earthquakes we ran the DSSD algorithm using the 86 station positions as hypothetic "location points". Fig. 6.13a illustrates the resulting order of importance of the receiver positions. As in previous design exercises the routine has primarily selected stations located above most seismic events (close to the Reykjanes peninsula tip), followed by some outer stations. Fig. 6.13b and Fig. 6.13c depict design qualities Θ_{tot} and Θ_{event}, respectively. Like before, cost curves decrease progressively and become almost flat with the total number of stations. The quality Θ_{event} limit for the total 86 sensors range from -1.83 to 8.4, corresponding to an average per event

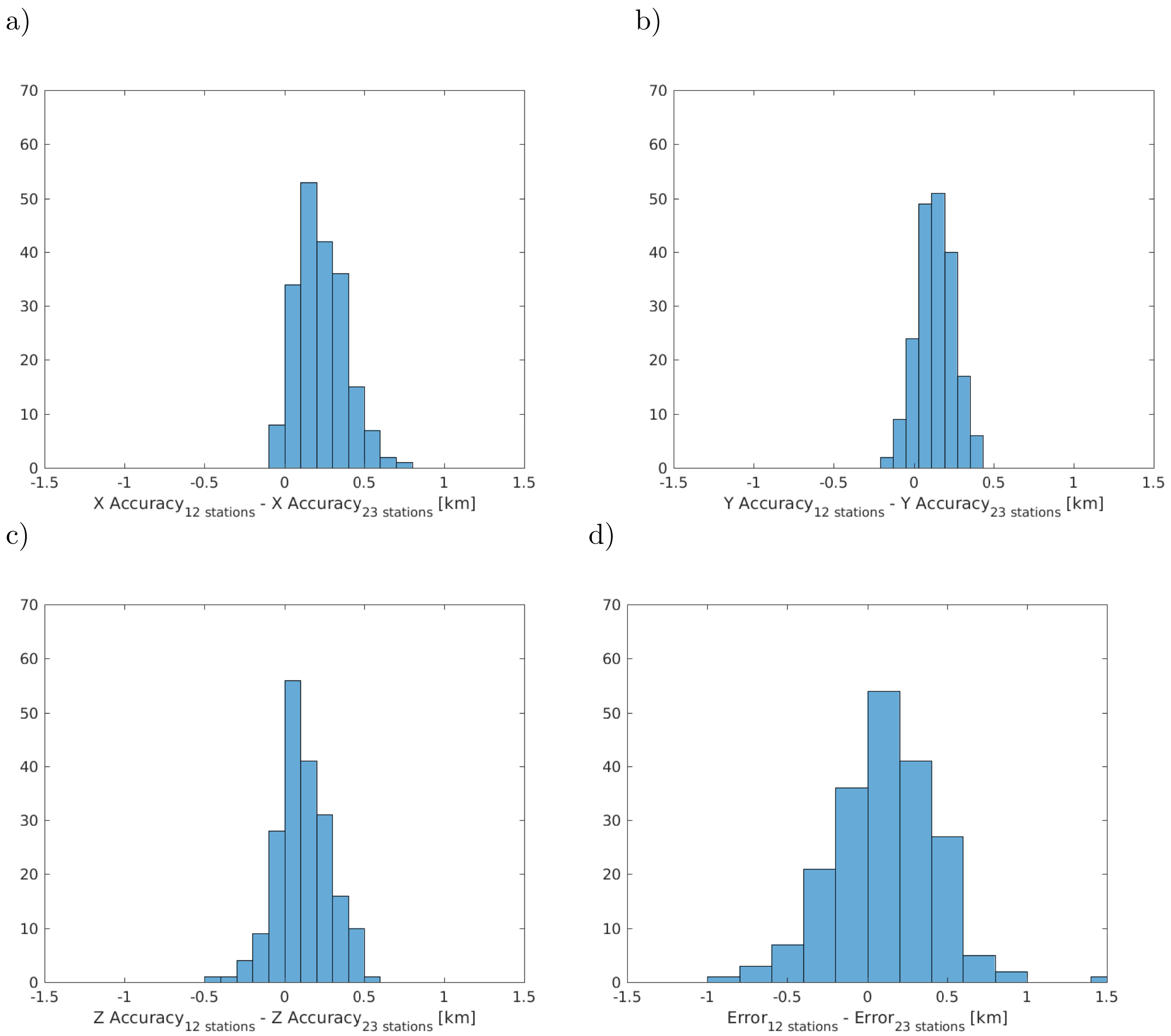

Figure 6.10: Location accuracy and error differences between the original (12) and final (23) station networks for events in the synthetic earthquake catalog of Fig. 6.5

of 2.35 obtained from Θ_{tot}. If we move to 80% of the seismic stations (71 sensors) the range of Θ_{event} is of -1.60 to 8.4 and a mean 2.41 per event from Θ_{tot}. This means that some ~18 stations could be spared to provide similar confidence ellipsoid volumes, therefore hinting the importance of a preliminary survey design experiment to optimize costs. In a similar sense, these theoretical results highlight the importance of some of the OBS deployed (in dark blue). OBS deployment was originally not contemplated in the project but by this study, their eventual placement is justified.

Fig. 6.14 shows the resulting accuracies and expected errors of inverted datasets associated to smaller arrays. The Vp/Vs ratio was taken at 1.78 (*Blanck et al.*, 2018b, this issue). P- and S- wave synthetic datasets were contaminated with normal distributed errors with means at 0.15 s and 0.30 s, respectively, and later inverted to obtain hypocentral parameter accuracies and errors. It is clear once more how accuracies seem to remain stable from 80% stations on. The 86 station network was nevertheless chosen to account for alternative seismic techniques such as ambient noise tomography (*Martins et al.*, 2020b, this issue). For this analysis we have once more ignored effects of different source mechanisms, heterogeneous noise distribution, a)

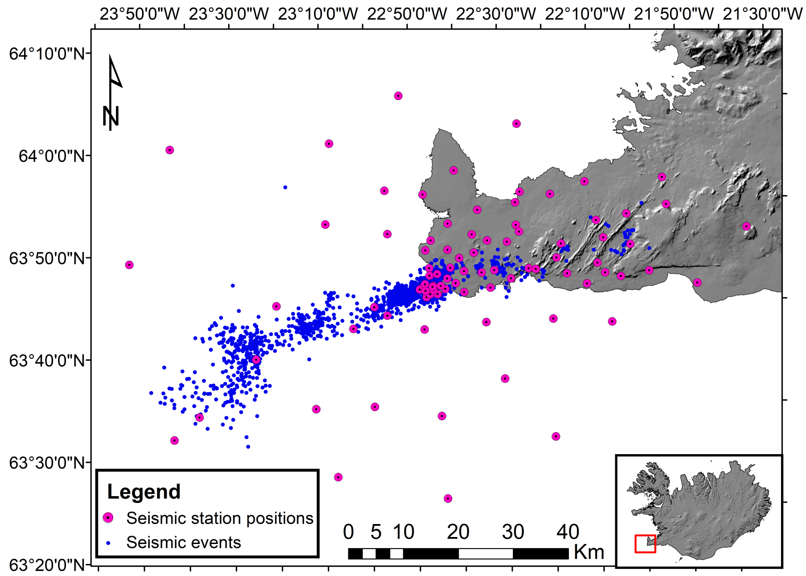

b)

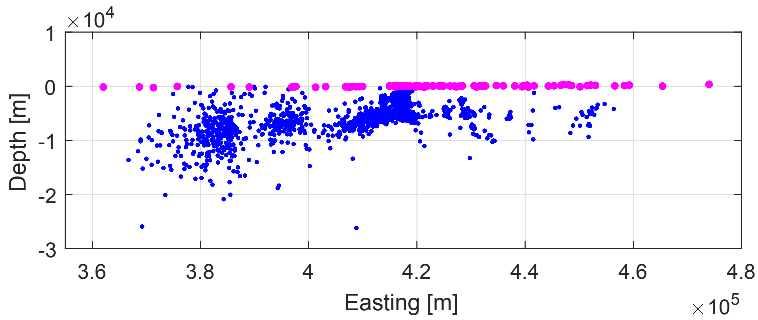

Figure 6.11: a) Seismic events, seismometers, and OBS positions. b) EW profile. Topography is ignored for its rather small variation.

a)

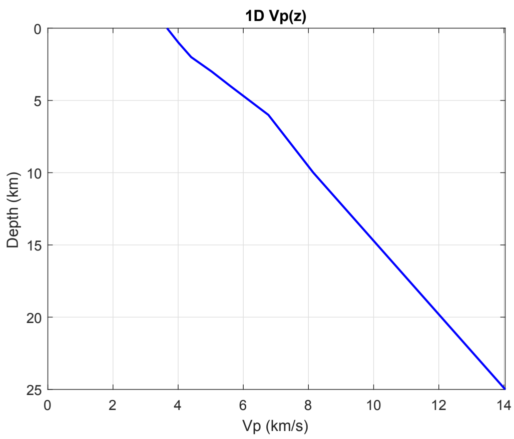

b)

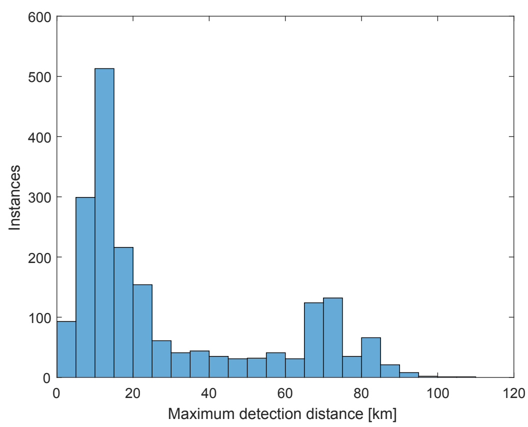

Figure 6.12: a) 1D Vp velocity model (*Jousset et al.*, 2016). b) Maximum detection distances.

and sensor installation quality, though we encourage further studies accounting this additional information.

a)

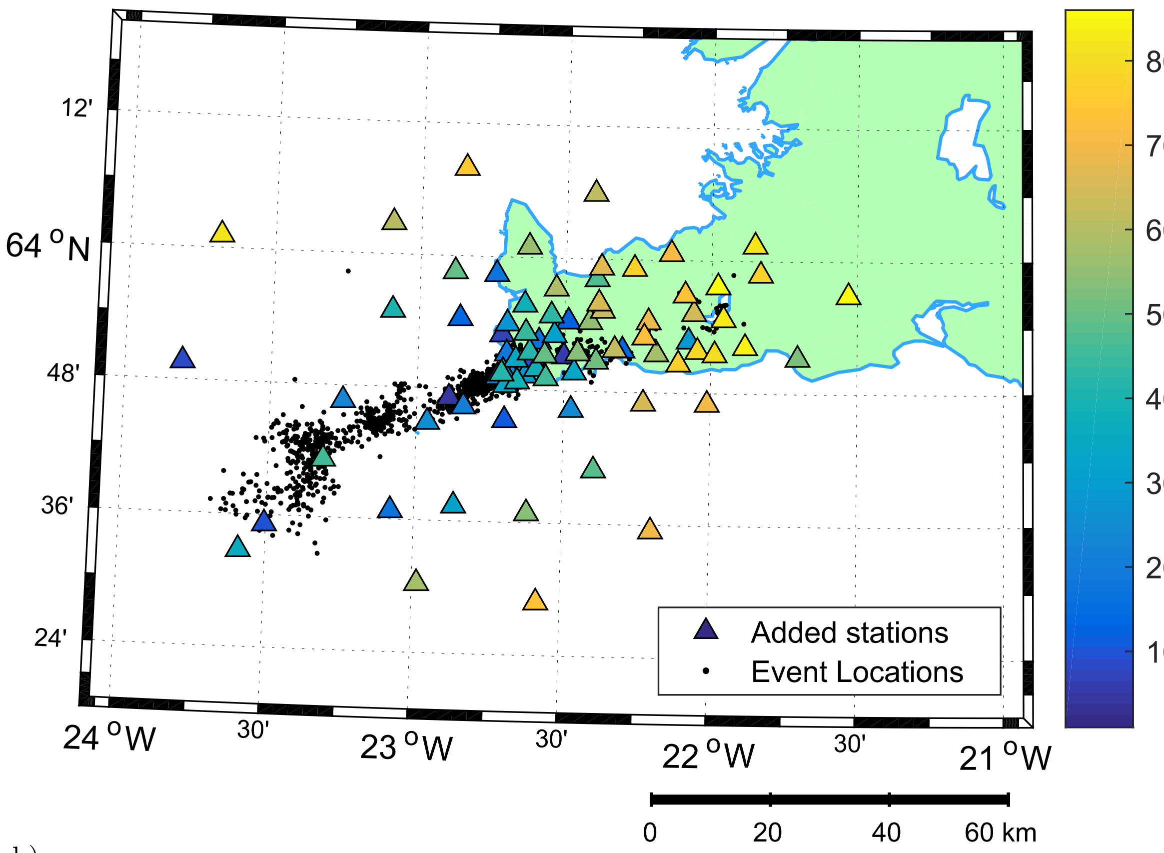

b)

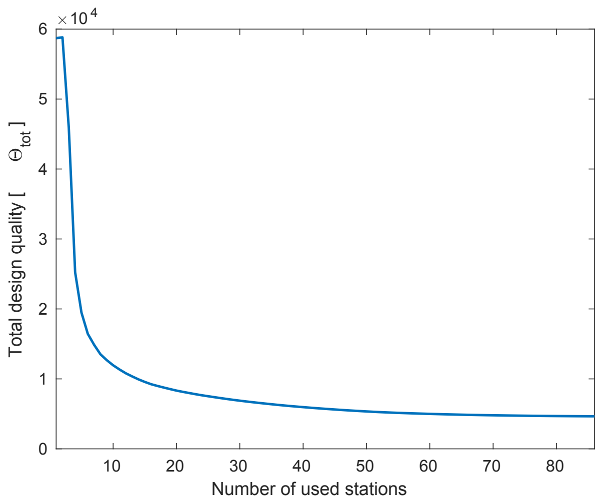

c)

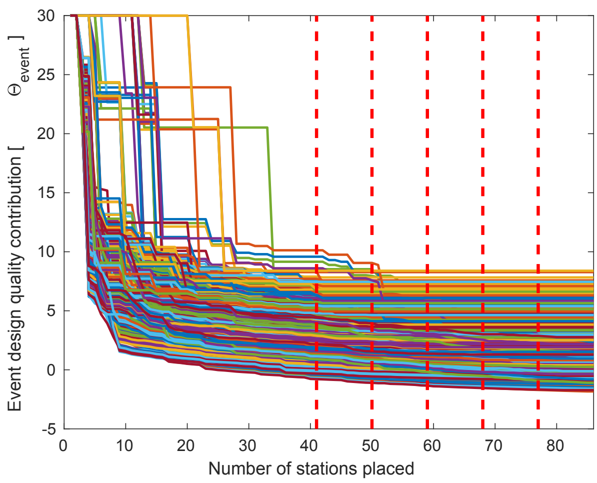

Figure 6.13: Reykjanes network quality. a) Order of importance of the Reykjanes seismic stations. b) Total design quality of the survey setup after progressively adding stations. c) Design quality contribution per event for the whole experiment. The dashed red lines indicate the limits of 50%, 60%, 70%, 80%, and 90% stations.

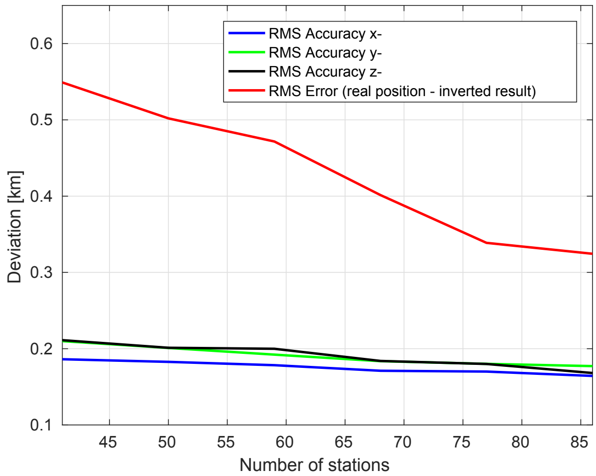

Figure 6.14: Location accuracies given by a station number reduction

6.5 Discussion

The linearized sequential survey design hereby explored is a rather simple method for building and qualifying seismic networks; however, it presents some drawbacks that must be addressed to obtain optimal designs.

6.5.1 *D-optimality*

Results using the chosen objective function Θ are very influenced by overlapping deploying areas, favoring them when these are very large. While this behavior could favor locating receivers that record as many possible events, it could also compromise the optimization of single events. It is therefore of importance to first identify main target earthquakes to allocate them high weighting factors γ_i (Eq. 6.4) prior to design. When no *a priori* accurate locations are known, an experiment similar to the one shown in Fig. 6.3 can be used.

Another issue that must be considered when using the *D-criterion* is station clustering. This phenomena is particularly likely in problems involving large number of stations to be placed in reduced *deploying areas* (e.g. Case I), or when failing to place stations right above a studied epicenter (e.g. Test Case A). Station clustering is the consequence of Θ ignoring model error correlations. One way to account for this correlation is by introducing an inter-station distance weight as performed by *Hardt and Scherbaum* (1994). In this work we decided to overlook this correction, and interpret the clustering as regions of importance instead (e.g. *Kraft et al.*, 2013).

6.5.2 Linearized destruction sequential survey design

In this work, we have explored a linearized destruction sequential survey design algorithm for its robustness, simplicity, and its ability to obtain optimal network configurations. A big advantage of sequential routines is their ability to quickly take into account changes of station positions (had they not been placed exactly at theoretical locations) and recompute design experiments for new geometries. Additionally, sequential survey design allows for an intuitive analysis of benefit/cost relations.

However, one disadvantage of destruction schemes comes with the computational expense when dealing with large number of earthquakes and candidate station positions. With destruction techniques one has to build the entire sequence/order of stations to obtain the position of even a few of them. Construction algorithms on the other hand provide much faster and cheaper results however possibly compromising global optimality. Given that at each iteration a new station is placed, these algorithms require only as many iterations as stations needed. This technique could then provide a framework for potential design-during-deployment. However, one main drawback of construction design is its need for good initialization (setting the first station position) which can seriously influence design optimality. Another sequential design option with better global optimality is exchange design (*Coles and Curtis*, 2011b). These algorithms scan through all observation points and replace station positions that extremize the objective function. Although quite robust in achieving global optimality, this routine requires twice as much computation than the previous two, given that each iteration needs two steps: construction and deletion.

Overall, although global optimality cannot be guaranteed with linearized sequential design approaches, these techniques provide fast optimal designs nonetheless. The simplicity of these routines is particularly useful in cases that require quick designs like post-earthquake aftershock studies, or simply building quick temporal networks. All the same, for cases requiring permanent stations or extended monitoring we recommend alternative design approaches such as global search algorithms like simulated annealing, and/or non-linear experimental design. Although some of these schemes may represent higher computational demands, they do ensure global optimality.

6.5.3 Detectability

Another key aspect to address in survey design is detectability. Detectability is very roughly considered in this work, however it is critical for defining candidate points for deployment. In our experiments we have considered homogeneous noise levels and SNR. In reality, these values are laterally variant and are very much site-specific. Authors like *Kraft et al.* (2013) for example calculated a first order ambient noise model to observe the lateral noise variations in Switzerland. Then, they compared these values with phase amplitudes modeled using Brune's source model (*Brune*, 1970, 1971) to determine the detecting stations. This procedure was possible given the availability of prior seismic data for this region. In practice, detailed knowledge of lateral velocity variations, anisotropy, attenuation, site-specific noise, SNR levels, etc. is largely unknown in unstudied areas. Hence the need of a seismic array in the first place. Inevitably, we would in many cases rely on oversimplified models and assumptions that could potentially lead to suboptimal designs. For this reason we recommend repeating optimization experiments once more information on the target site becomes available, especially in cases requiring permanent or extended monitoring. Survey design could in these cases be regarded as an iterative procedure that improves with our knowledge of the target area.

6.5.4 Design and qualification of seismic arrays

Case study I offers a real case for constructing a small microseismic array in Theistareykir geothermal field. This case however considers very clustered events as location targets which directly affects station placement due to large deploying areas overlap. Nonetheless we have judged that the region considered is appropriate for fieldwork conditions and therefore decided not to assign higher γ_i values for larger events. With the introduced routine we have constructed a 23 station network. The network performance was later tested by carrying out several Monte Carlo experiments to calculate standard deviations of the inversion results with theoretical noisy data. Monte Carlo experiments however can be very computationally expensive. For this reason we discussed the use of "goodness maps" which are simply the spatial distribution of quality measure Θ. These maps are much faster to compute and can qualitatively reveal the extents of areas where events would be better constrained by the network.

Case study II uses the same design scheme to qualify an existing seismic array at the Reykjanes peninsula. The algorithm is applied in the same fashion as in Case I, however with the deployed stations as potential placement points. This approach results in the construction of a station order of importance. We later tested the effects of removing least important stations in the resulting location uncertainties. It was noticeable for the Reykjanes network, that we would arrive to similar location uncertainties with only 71 stations out of 86. These findings are of critical importance especially with constrained project budgets, hinting the value of experimental survey design prior to deployment. On a similar tone, many seismic experiments require moving stations to different positions at some point in time. Therefore similar analysis can help identify which stations are crucial to the experiment and which can be moved without affecting location uncertainties significantly.

6.6 Conclusions

We have successfully constructed and applied a DSSD algorithm for designing new optimized seismic networks, and qualifying existing ones for geothermal studies in the framework of sequential survey design based on the *D-criterion*. The DSSD scheme hereby explored uses a 1D velocity model for sensitivity computations, and was first tested with simple test-cases where concepts like benefit and cost were introduced. The routine was then applied to two case studies, one for designing (Theistareykir) and a second one for qualifying (Reykjanes) an existing seismic array.

After constructing a synthetic earthquake catalog in accordance with previously observed seismic data, the Theistareykir network was augmented with the DSSD algorithm, from 12 to 23 sensors, reaching hypocentral accuracies of around $\sim$0.5 km for normally distributed picking errors of mean 0.2 s (for t_P) and 0.4 s (for t_S).

Finally the Reykjanes network was tested with the same algorithm to observe whether its design was adequate for the recovered earthquake catalog. From the design quality values it became apparent that up to $\sim$18 stations could be spared for the survey, or conversely relocated for better results. It is therefore of importance to conduct a survey design experiment prior to deployment to obtain best possible location results. In this study we have not considered the effects of variable seismic noise, for which a better detectability study could be carried out in the future to refine results. Another interesting topic for future research is the building of a multi-purpose network design for both velocity model and seismic event locations, and the use of alternative non-linear quality metrics.

Acknowledgements

We gratefully acknowledge the help of M. Weber for the fruitful discussions and comments on this paper. We are equally very grateful for the comments of two anonymous reviewers, whose remarks vastly helped improving this manuscript.

This work received funding from the European Union's Horizon 2020 research and innovation program under grant agreement No. 727550 (GEMex project).

7

Local earthquake tomography of a geothermal field

This chapter focuses on the calculation and interpretation of a local earthquake tomography at the producing Los Humeros geothermal field in Mexico. In addition to the traditional inversion method described in Chapter 4, resolution enhancement is explored in this publication by inverting and averaging the inversion results of several initial parametrizations.

Local earthquake tomography at Los Humeros geothermal field (Mexico)

Tania Toledo, Emmanuel Gaucher, Philippe Jousset, Anna Jentsch, Christian Haberland, Hansruedi Maurer, Charlotte Krawczyk, Marco Calò, Ángel Figueroa

Accepted for publication in *Journal of Geophysical Research: Solid Earth.*

`https://doi.org/10.1029/2020JB020390`

A passive seismic experiment using 25 broad-band and 20 short-period stations was conducted between September 2017 and September 2018 at Los Humeros geothermal field, an important natural laboratory for superhot geothermal systems in Mexico. From the recorded local seismicity, we derive a minimum 1D velocity model and obtain 3D Vp and Vp/Vs structures of Los Humeros. We improved the classical local earthquake tomography by using a post-processing statistical approach. Several inversions were computed and averaged to reduce artifacts introduced by the model parametrization and to increase the resolution of the investigated region. Finally, the resulting Vp and Vp/Vs structures and associated seismicity were integrated with newly acquired geophysical and petrophysical data for comprehensive interpretation. The recorded seismicity is mainly grouped in three clusters, two of which seem directly related to exploitation activities. By combining new laboratory measurements and existing well data with our Vp model we estimate possible geological unit boundaries. One large intrusion-like body in the Vp model, together with neighboring high Vp/Vs anomalies hint at a region of active resurgence or uplift due to the intrusion of new magma at the northern portion of the geothermal field. We interpret high Vp/Vs features as fluid bearing regions potentially favorable for further geothermal exploitation. Deep reaching permeable faults cutting the reservoir unit could explain fluid flow from a deeper local heat source in the area.

Introduction

Los Humeros Volcanic Complex (LHVC) is a superhot geothermal system located at the eastern edge of the Trans-Mexican Volcanic Belt (TMVB), a volcanically active region favorable for geothermal energy exploitation. It is one of the oldest producing fields in the region, with more than 60 wells drilled up to ∼3 km deep since the early 80s (*Arellano et al.*, 2003; *Cedillo-Rodríguez*, 1999; *Gutierrez-Negrin and Izquierdo-Montalvo*, 2010; *Rocha-López et al.*, 2010). Currently, it has an installed capacity of ∼95 MW electric power and is administered by the Comisión Federal de Electricidad (C.F.E.) (*Romo-Jones et al.*, 2018). Temperatures as high as 400°C have been measured in several producing wells at ∼2.5 km depth. However geothermal fluids at these temperatures are presently not being exploited. Despite the large number of studies on the geochemical (e.g. *Martinez and Alibert*, 1994), geological (e.g. *Carrasco-Núñez et al.*, 2017a,b), structural (e.g. *Norini et al.*, 2015), and geothermal (e.g. *Gutierrez-Negrin and Izquierdo-Montalvo*, 2010) properties of the reservoir, a solid understanding of the conditions and underground structures at depth is still rather sparse. Only a few deep probing geophysical studies (resistivity 2D profiles and seismic surveys) in recent years have provided notions of the local stress field and structures of the geothermal field (*Arzate et al.*, 2018; *Gutierrez-Negrin and Quijano-Leon*, 2004; *Lermo et al.*, 2001, 2008, 2016; *Norini et al.*, 2019; *Urban and Lermo*, 2013).

One objective of this study is to investigate the deeper structures of the geothermal system, to locate and better understand the deep super-hot fluids for their exploitation. Passive seismic methods are to this purpose widely exploited in geothermal prospecting (e.g. *Calò and Dorbath*, 2013; *Jousset et al.*, 2011; *Muksin et al.*, 2013). Seismic properties such as the compressional P- (Vp) and shear S- (Vs) wave velocities, and the Vp/Vs ratio structures have proven reliable tools to describe lithologies and possible variations due to changes in fluid composition, rock porosity, and temperature (e.g. *Gritto and Jarpe*, 2014; *Husen et al.*, 2004; *Ito et al.*, 1979; *Mavko and Mukerji*, 1995). These are key features in geothermal exploration and monitoring.

One conventional approach to obtain the seismic properties of a target area is the 3D tomographic inversion of P- and S- wave arrival times from local earthquakes, as observed in records of seismometers deployed in the area of interest. The 3D velocity structure is typically obtained through a joint inversion of hypocenter locations and velocity structures using an *a priori* parameterized 3D grid model of the subsurface. Classical tomographic results are strongly influenced by the inversion grid or node spacing choice, and hence its adequate selection is fundamental to retrieve the main features of the subsurface for reliable interpretation. A too fine model could, for example, lead to poor resolution values and/or artifacts such as grid oscillations, whereas a too coarse model (especially a coarse fixed grid) could overlook smaller underground features. In addition, significant smearing can be introduced when the chosen grid does not follow the orientation of the main anomalies. In this work, we extend the conventional tomographic method of a single fixed model grid by using a post-processing statistical approach. We compute and average several inversions using different model parametrizations to achieve higher spatial accuracy, reduce the effects of poor parametrization selection, and overall increase model resolution.

In this study, we image the 3D Vp and Vp/Vs structures, along with the seismicity distribution at Los Humeros geothermal field. In the first part of this study, we compile information on the geological and structural setting of Los Humeros area. Later, we describe the passive seismic experiment and the data processing workflow followed to detect and locate the local seismic events. We use the retrieved earthquake catalog to derive a new so-called minimum 1D velocity model in part 3. In part 4, we compute and average the 3D tomography of several parametrized models using the minimum 1D velocity model as initial input. Finally, part 5 proposes a first interpretation of the obtained results in relation to existing geological information and newly acquired petrophysical, geochemical, and geophysical data (*Bär and Weydt*, 2019; *Benediktsdóttir et al.*, 2019; *Jentsch et al.*, 2020; *Lucci et al.*, 2020; *Urbani et al.*, 2020).

7.1 Geologic and tectonic setting

LHVC is a Quaternary geological complex constituted by two nested calderas: the older (ca 460 ky) outer 18-20 km wide Los Humeros caldera, and the younger (70 ky) subordinate 5-8 km wide Los Potreros caldera (*Calcagno et al.*, 2018; *Carrasco-Núñez et al.*, 2017a,b, 2018), where most of the injection and geothermal production activities take place (Figure 7.1). An extensive fault network crosses the main production zone of the geothermal field and is responsible for secondary permeability in the reservoir. Several faults (e.g. Los Humeros fault and the Loma Blanca fault) favor fluid flow and present strong hydrothermal alteration at the surface (*Norini et al.*, 2015, 2019). The main fault system runs around 8 km in a NNW-SSE direction, and includes the Maztaloya fault and Los Humeros fault. A second set of faults parting from the main system runs N-S, NE-SW, and E-W. Both sets disappear at the surface when approaching Los Potreros caldera rim (Figure 7.1).

From a geological perspective, Los Humeros geothermal field can be divided into four distinct groups: (1) regional meta-sedimentary basement, (2) pre-caldera, (3) caldera, and (4) post-caldera volcanic phases, which can be subdivided into nine local lithostratigraphic units (*Calcagno et al.*, 2018; *Carrasco-Núñez et al.*, 2017b). Here, we briefly describe the lithologies found in the four major groups. The lower portion of the basement, also called the Teziultlán Massif, is mainly composed of old instrusive igneous and metamorphic rocks (Paleozoic granites, greenschists, and granodiorites) (*Quezadas-Flores*, 1961; *Viniegra*, 1965; *Yáñez and García*, 1982). These rocks are covered by an up to 3 km-thick Mesozoic sedimentary basement mostly constituted of limestones, with some silts and shales. The basement is overlain

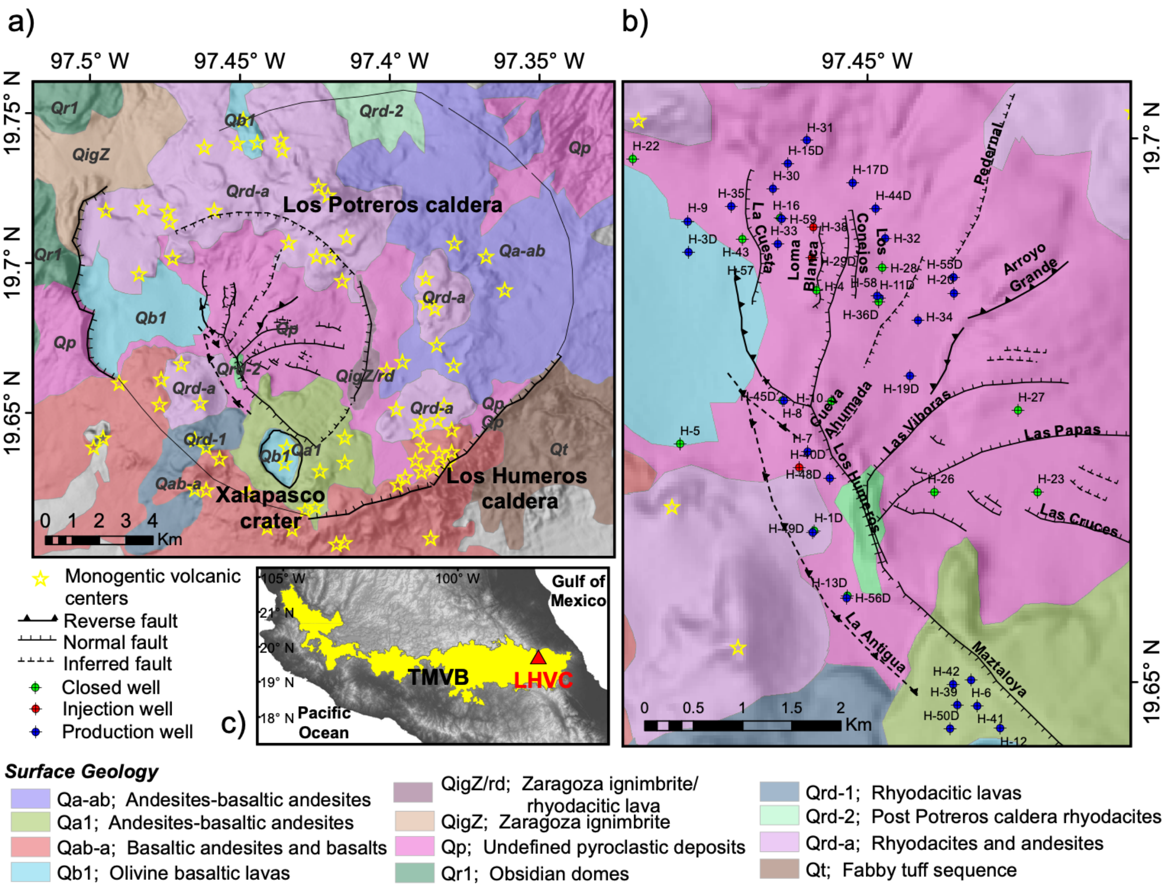

Figure 7.1: a) Surface geology, b) main structures and well locations at LHVC (modified from *Carrasco-Núñez et al.*, 2017a; *Norini et al.*, 2015). c) Locations of the Trans-Mexican Volcanic Belt (TMVB) and LHVC (red triangle).

by the pre-caldera group (10.5 – 0.155 Ma) mainly composed of andesitic, dacitic, and to a minor extent, basaltic lavas also known as Teziutlán andesites. The Teziutlán volcanic unit hosts the active geothermal reservoir and has a thickness larger than 1500 m in some of the geothermal wells within LHVC (*Arellano et al.*, 2003; *Carrasco-Núñez et al.*, 2017a,b; *Cedillo-Rodríguez*, 1997, 1999; *Ferriz and Mahood*, 2009; *Gutierrez-Negrin and Izquierdo-Montalvo*, 2010; *Lorenzo-Pulido*, 2008; *Norini et al.*, 2019; *Yáñez and García*, 1982). The basalts and andesites are sealed above by low-permeability Quaternary ignimbrites of variable thickness belonging to the caldera stage (*Arellano et al.*, 2003; *Cedillo-Rodríguez*, 1997, 1999; *Gutierrez-Negrin and Izquierdo-Montalvo*, 2010; *Lorenzo-Pulido*, 2008; *Norini et al.*, 2019). This unit is characterized primarily by eruptive events which resulted in the formation of Los Humeros and Los Potreros calderas (*Carrasco-Núñez and Branney*, 2005; *Carrasco-Núñez et al.*, 2012; *Ferriz and Mahood*, 2009; *Norini et al.*, 2019). The post-caldera stage (0.05 – <0.003 Ma) was influenced by different intra-caldera eruptive phases (effusive and explosive). Rhyodacitic, andesitic, and basaltic lavas as well as pyroclastic material (*Carrasco-Núñez et al.*, 2018) were produced by various monogenetic volcanic centers which are scattered between Los Potreros and Los Humeros caldera rims (*Norini et al.*, 2015, 2019). During that time, another significant eruption took place which resulted in the 1.7 km oval shaped Xalapazco crater in the south of the complex (*Carrasco-Núñez et al.*, 2018).

7.2 Seismic monitoring and data processing

7.2.1 Seismic network

From September 2017 to September 2018, we deployed and maintained a temporary seismic network comprising 25 three-component broadband (Trillium Compact 120s) and 20 three-component short-period (Mark L-4C-3D) sensors recording continuous seismic data at sampling rates of 200 Hz and 100 Hz, respectively (*Toledo et al.*, 2019). The array consisted of two complementary sub-networks each configured to characterize shallow and deeper structures using different seismic processing techniques (Figure 7.2). A denser (∼1.6-2 km inter-station distance) pseudo-rhomboidal array was located mainly in the inner Los Potreros caldera where previous studies have identified the occurrence of local seismicity (*Gutierrez-Negrin and Quijano-Leon*, 2004; *Lermo et al.*, 2001, 2008, 2016; *Urban and Lermo*, 2013), and where most of the producing and injecting wells are located. This sub-network was primarily designed for local microseismicity retrieval (*Gaucher et al.*, 2019), local earthquake tomography, beamforming of ambient noise (*Löer et al.*, 2020), time-reverse imaging (*Werner and Saenger*, 2018), and autocorrelation techniques (*Verdel et al.*, 2019). The second much sparser network (∼5-10 km inter-station distance) was placed around the outer Los Humeros caldera and was mainly intended for imaging deeper large-scale structures with techniques such as ambient noise tomography (*Granados et al.*, 2020; *Martins et al.*, 2020a), among others.

7.2.2 Local earthquake detection

We focused the event detection mainly on Los Potreros caldera (*Gaucher et al.*, 2019) using Python tools based on the ObsPy library (*Beyreuther et al.*, 2010). We calibrated a recursive STA/LTA detection algorithm (*Trnkoczy*, 2012; *Withers et al.*, 1998) on several days of the recently acquired seismic dataset (2017-2018) and on a set of local seismic events recorded between 2005 and 2006 by the permanent network operated by the C.F.E. (*Lermo et al.*, 2008). We exhaustively tested the detection performance through several days of the recent seismic database using a wide range of parameter combinations. The optimum parameters selected were a combination of bandpass filter between 10-30 Hz, STA and LTA windows of 0.2 s and 2 s, respectively, and on and off trigger thresholds of the computed STA/LTA function at 3.5 and 1.0, respectively. To account for the P- and S-wave arrivals, the STA/LTA function was computed from a single amplitude trace determined by the square root of the sum of the 3 single component squared traces for each station. Finally, a detection was declared as such when the triggering window of at least 5 stations from the dense sub-network coincided in time (*Trnkoczy*, 2012; *Withers et al.*, 1998). We reviewed each triggered detection and manually picked P- and S-wave arrivals of local events and their associated empirical uncertainty range using the Python Obspyck tool (*Megies*, 2016).

From a total of 1586 detections, 488 were identified as local events. After picking P- and S- phases, these earthquakes were located using an oct-tree search (*Lomax et al.*, 2000, 2009) in a homogeneous 3D volume with a P-wave velocity of 3.5 km/s and a Vp/Vs ratio of 1.73 (Figure 7.3). Later, we re-selected the seismic events with a greatest angle without observation (GAP) of less than 180°, and at least 3 P- and 3 S- wave arrivals (333 events in total) for the calculation of a minimum 1D velocity model and their relocation. The recorded seismicity is

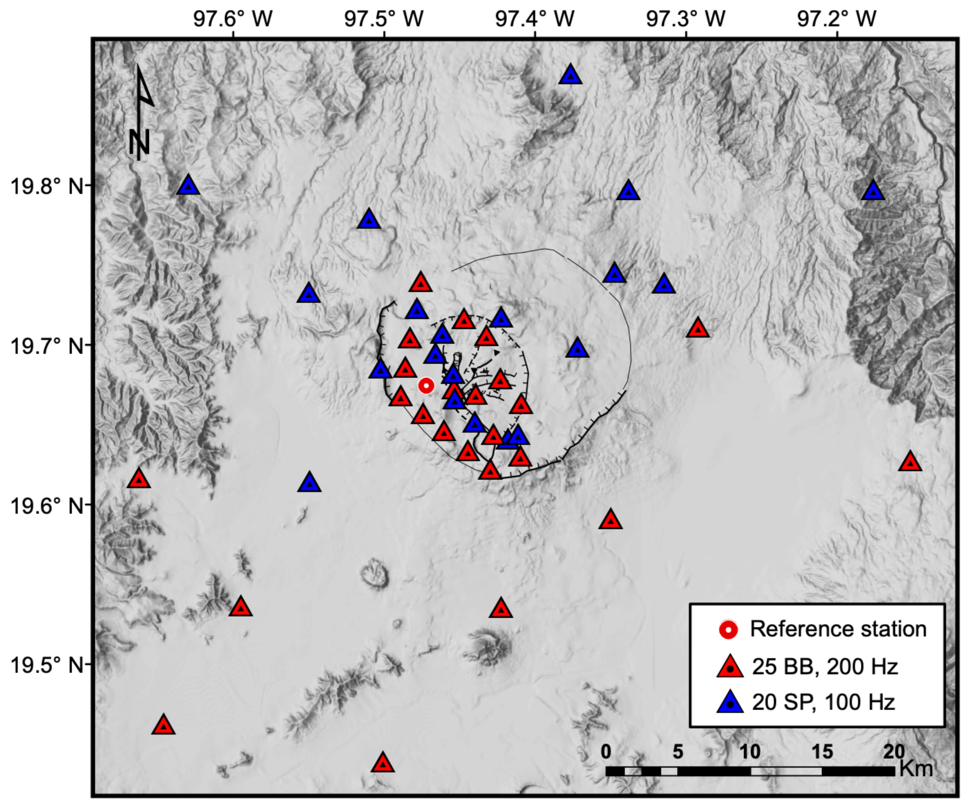

Figure 7.2: Topographic map and temporary seismic network at Los Humeros geothermal field. Blue and red triangles mark the positions of three component short-period (Mark L-4C-3D) and three-component broadband (Trillium Compact 120s) sensors, respectively. The reference station for the 1D inversions (also a three-component broadband Trillium Compact 120s sensor) is marked as a red circle. Several indentified and inferred structures are delineated in black (modified from *Carrasco-Núñez et al.*, 2017a; *Norini et al.*, 2015).

mostly located below the dense array within Los Potreros caldera, and mainly grouped into three distinctive clusters, marked as C1, C2, and C3 in Figure 7.3.

7.3 1D velocity model

We use the retrieved travel time data from the filtered catalog (333 events with 2146 P-wave and 2146 S-wave picks) as input for a joint inversion to determine the so-called minimum 1D Vp and Vs models, and the hypocenter relocations using the code Velest (*Kissling et al.*, 1994). The code Velest iteratively computes forward modeled data (predicted travel times), using a ray tracer in an initial model (1D velocity model, hypocenter locations, and station corrections), compares the synthetic data to the observed dataset and updates the model such that the RMS (root-mean-squared) misfit between the two is minimized (*Tarantola*, 2005). This procedure uses regularization parameters (damping factors) to tackle instabilities due to data uncertainties (*Levenberg*, 1944; *Marquardt*, 1963) and continues until a maximum number of iterations is reached.

The estimation of a minimum 1D model consists of a trial and error process in which typically a broad range of plausible initial models is tested to ensure covering as many potential

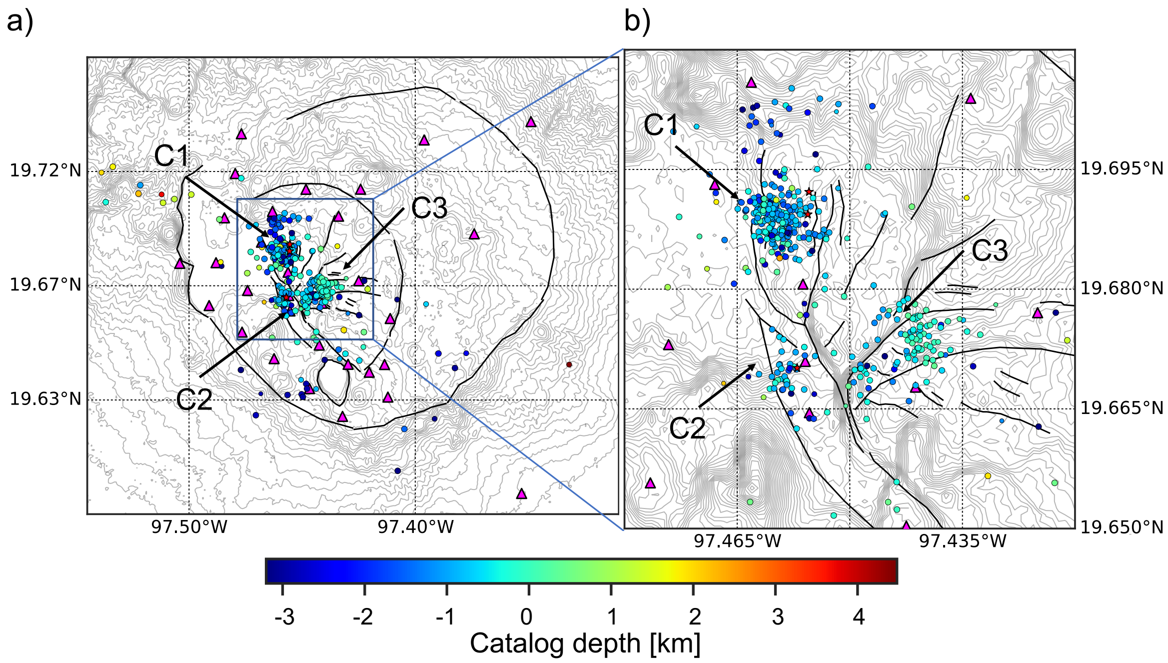

Figure 7.3: Distribution of the detected local earthquakes after a nonlinear localization in a homogeneous 3D volume with a P-wave velocity of 3.5 km/s and a Vp/Vs ratio of 1.73. Triangles mark the station positions and dark solid lines indicate structures inferred at the surface. Red stars mark the positions of three injection wells. C1, C2, and C3 indicate the positions of three main seismic clusters. Depths are defined relative to sea level.

solutions as possible and select the best fitting model. This procedure is necessary because the inversions are based on linearization and thus strongly depend on the initial model. In this work, we performed the inversion of 10648 initial models with varying P-wave velocities at the surface, vertical velocity gradients, and Vp/Vs ratios (thus also varying Vs models) over 5 iterations. The software Velest allows tracing rays to the true station elevations. However this option poses the limitation of locating all stations within the first layer. With this in mind, we set the uppermost layer thickness to more than 1 km, which corresponds to the approximate elevation difference between the highest and lowest recording stations. The following layers are then defined roughly every 0.5 km at shallow depths, and progressively increase to 1 and 2 km for deeper levels. The depth intervals were chosen taking into account well data interpretation (*Norini et al.*, 2015, 2019) and exhaustive testing. We define depths relative to sea level throughout this manuscript. The uncertainty of P- and S-arrivals were defined by the weighting factors 0, 1, 2, and 3 corresponding to the estimated picking uncertainties of up to 0.03 s, 0.08 s, 0.12 s, and higher, respectively. Finally, we selected station DB13 as the reference station given its location at approximately the center of the dense array and geothermal field, and its high number of recorded P- and S- arrivals (red circle in Figure 7.2).

Figure 7.4a and Figure 7.4b depict all the initial (yellow lines) and the 35 resulting velocity models with lowest associated RMS misfit values (gray lines) for Vp and Vs, respectively. The misfit values for this set of best models range from 95.0 ms to 96.1 ms. Note the good agreement for several layers of the resulting velocity models, particularly between -1.0 and 1.5 km depth where most of the seismicity is located. This coherence becomes less obvious at shallower and greater depths, where only a few hypocenters are located. Few models show values with large deviations from the more obvious trend. We create a heat map with this set of final models in Figure 7.4c and Figure 7.4d to better reveal the most frequent velocity values in each layer. Finally we manually select the model with the lowest misfit value (black lines in Figure 7.4a and Figure 7.4b) that best coincides with the main trend of most frequent velocity values (red lines in Figure 7.4c and Figure 7.4d) as the minimum 1D velocity model.

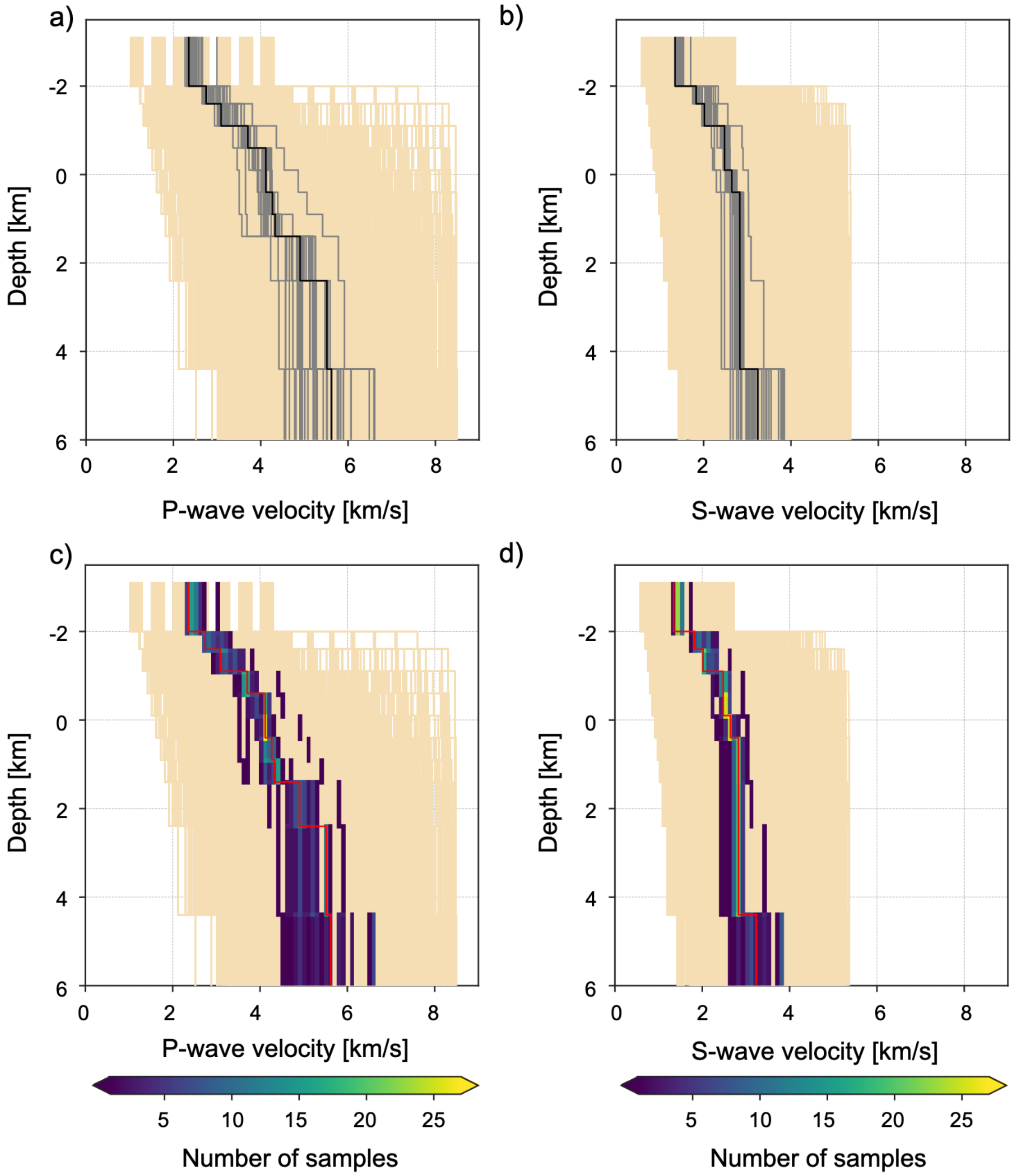

Figure 7.4: Results of the 1D inversions using Velest. The 35 best a) P-wave and b) S-wave final velocity models (gray lines). Heat maps for the same c) P-wave and d) S-wave set of final models. The yellow lines indicate all initial velocity models used. The selected minimum 1D models are indicated in black lines in panels a) and b), and in red lines in panels c) and d).

Figure 7.5 depicts the resulting P- and S-wave velocity models, the associated Vp/Vs ratio and the final event distribution for the selected minimum 1D velocity model. The model is best resolved between -2 to 2 km depth approximately, which is consistent with the hypocenter distribution shown in Figure 7.5c. The seismic events are restricted up to approximately 4 km depth from the surface, with a maximum number of events between -0.5 and 0.2 km depth. The seismicity presents a systematic shift towards ∼0.5-0.8 km greater depths and some improvements in clustering after the 1D inversion. Two velocity models proposed by *Lermo et al.* (2008) (P-wave) and *Löer et al.* (2020) (S-wave) are marked in green and magenta, respectively, in Figure 7.5a. The Vp model proposed by *Lermo et al.* (2008) was derived using a seismic reflection profile and reaches an approximate depth of -0.5 km, below which a default value of 5.18 km/s is assigned. The Vs model derived by *Löer et al.* (2020) was obtained using three-component ambient noise beamforming and is most sensitive in the interval between -0.5 and 10 km depth. Notice the good correlation between the derived minimum 1D Vp model and the model obtained by *Lermo et al.* (2008), especially between -2.0 and -0.5 km. Similarly, there is a good agreement between the derived minimum 1D Vs model and the model obtained by *Löer et al.* (2020) between -1.0 and 2.2 km depth.

The station delays associated with the selected minimum 1D velocity model are also consistent with the local geology and are further described in Appendix 7.A.

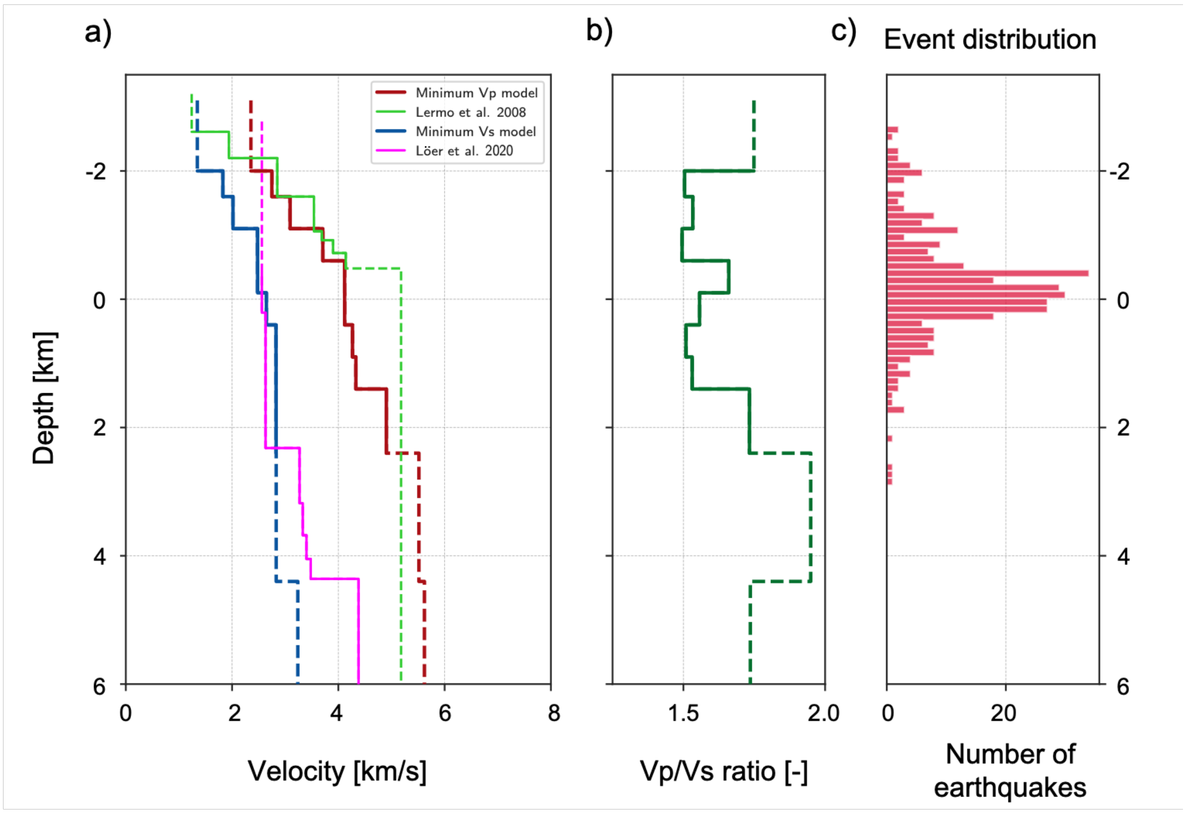

Figure 7.5: Minimum 1D model showing: a) the selected Vp and Vs models along with 2 available models (*Lermo et al.*, 2008; *Löer et al.*, 2020), b) the resulting Vp/Vs ratio, and c) the earthquake distribution over depth after the 1D inversion. Solid lines indicate the depth intervals with best sensitivity for each model.

7.4 3D seismic tomography

After selecting the reference 1D velocity model and hypocenter locations, we used the 3D travel time inversion code SIMUL2000 (*Eberhart-Phillips*, 1990; *Eberhart-Phillips and Michael*, 1998; *Evans et al.*, 1994; *Thurber*, 1983) to estimate the 3D velocity structure of the geothermal field. Forward calculations are computed using a pseudo bending method (*Um and Thurber*, 1987) and inversions are performed using an iterative damped least-squares scheme. The software SIMUL2000 allows for the simultaneous inversion of Vp and Vp/Vs ratio instead of Vs to account for the generally lower resolution of Vs models due to larger uncertainties of S-wave arrival determination, most of them being hampered by the coda of the P-wave (*Thurber*, 1993; *Thurber and Eberhart-Phillips*, 1999). Inversions in this section are computed using the minimum 1D Vp model and a homogeneous Vp/Vs of 1.71 obtained from a Wadati diagram analysis of the stacked events.

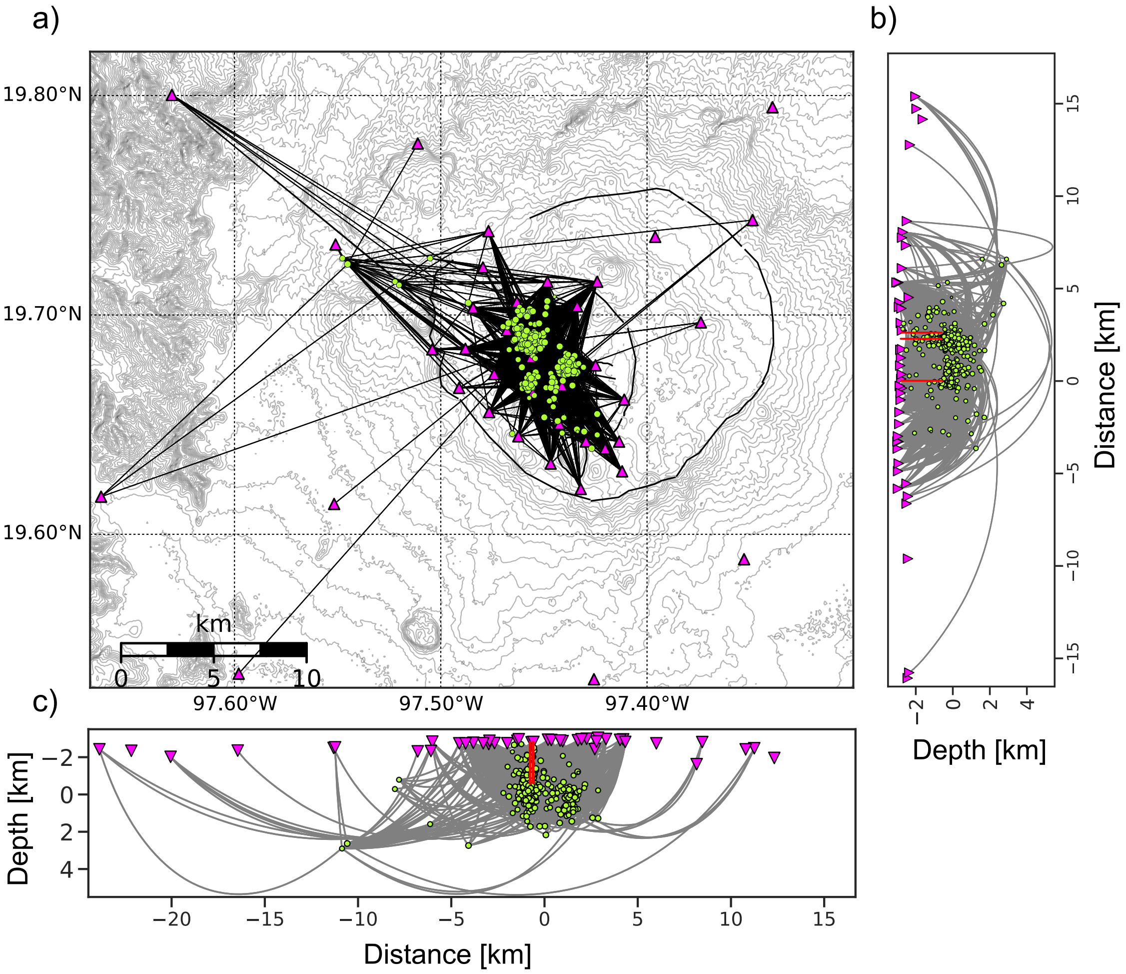

Figure 7.6: Ray path distribution after the 1D inversion: a) map view, b) N-S, and c) E-W projections. Seismic stations are represented as purple triangles, local events as green circles. The projections of three injection wells are marked as red lines in the cross sections. Dark solid lines in the map view indicate structures inferred at the surface, and the gray lines correspond to topographic contours.

7.4.1 Model parametrization

An appropriate model parametrization is suggested by *Evans et al.* (1994) and *Husen et al.* (2000, 2003) as that with the finest possible node spacing, which allows inversions without strong derivative weighted sum (DWS) heterogeneities. The DWS is a measure for ray density which takes into account the number of crossing rays, ray-node separation and raypath length in the vicinity of each node (*Evans et al.*, 1994; *Husen et al.*, 2000). *Kissling et al.* (2001) advise taking into account both *a priori* information about the underground structure and resolution capabilities of a dataset when selecting appropriate model parametrization. Accounting for known subsurface features could lead to a too fine model node spacing which in turn could result in lower resolution values and sparse imaging. On the other hand, a coarse model parametrization, although yielding higher resolution values due to increased ray density, could potentially overlook smaller features in the subsurface. To avoid this effect, some authors (e.g. *Abers and Roecker*, 1991; *Bijwaard et al.*, 1998) use uneven node spacing in their inversions. This technique could, however, complicate interpretations given some velocity changes may be inadvertedly interpreted as underground features. One methodology often used is a graded inversion approach (*Evans et al.*, 1994; *Husen et al.*, 2003). Iterations are performed through finer grids using a coarse model output as input for a new inversion with a finer grid.

Some novel post-processing techniques include the averaging and weighted averaging of several inversion results using different initial model parametrizations (e.g. *Calò et al.*, 2013; *Haberland et al.*, 2009). This technique helps enhancing velocity anomalies, reduces possible smearing effects and model noise due to the parametrization choice, overcomes the fixed coarse parametrization limitation of the inversion code, and improves the model resolution. In this study, similar to *Calò and Dorbath* (2013), we compute several inversions using different model parametrizations which we later average on a finer grid.

Figure 7.6 shows the event to station raypath configuration in the initial minimum 1D velocity model. Raypaths are unevenly distributed and mostly located within Los Potreros caldera, reaching ~1.5 km depth for the most part. Taking into account the raypath configuration, we chose an initial lateral parametrization of 1 x 1 km^2 (Figure 7.7) and 0.5 km inter-node spacing with depth within Los Humeros caldera region (Figure 7.8). We then progressively increased the node spacing in regions outside Los Humeros caldera and below the seismicity. Figure 7.7 and Figure 7.8 show the DWS distribution after a 3D inversion using the chosen grid. DWS values are, as expected, larger within the regions above the seismic clusters (higher ray density), and extend to 0 to -1 km depth. After the inversion, the seismicity presents a systematic shift towards ~0.5-0.8 km shallower depths which could be attributed to initially setting the station delays of the minimum 1D model to zero. To avoid decreases in retrieved velocity amplitudes, we fixed the hypocenter locations during the first iteration and updated the new relocations after each velocity inversion (*Husen et al.*, 2003).

We constructed several inversion grids starting off with the previous grid, and then rotated it in 15° steps. A similar procedure was carried out after displacing the inversion grid center 0.2 and 0.5 km towards the north, south, east, west, northwest, northeast, southeast, and southwest. Figure 7.9 depicts the nodes of the 228 inversion grids used. Although *Calò* (2009) proposes the use of fewer models to reach a decent benefit of the post-processing technique, we opted for a larger number of inversions to yield a more statistically stable final model.

Note that both Los Potreros and Los Humeros calderas are densely covered by nodes. To construct a new averaging grid, we interpolated all outputs post inversion onto a regular finer grid with 0.1 km spacing using the same interpolation scheme as applied in SIMUL2000 (*Thurber*, 1983). Then we averaged each point of the new grid. Figure 7.10 shows several depth slices for the average DWS using the new grid. The covered gray areas (regions with any ray density) become larger than when using a single initial inversion grid, which could be attributed to both the averaging of DWS values, but also to taking into account model parametrizations that favor different ray orientations.

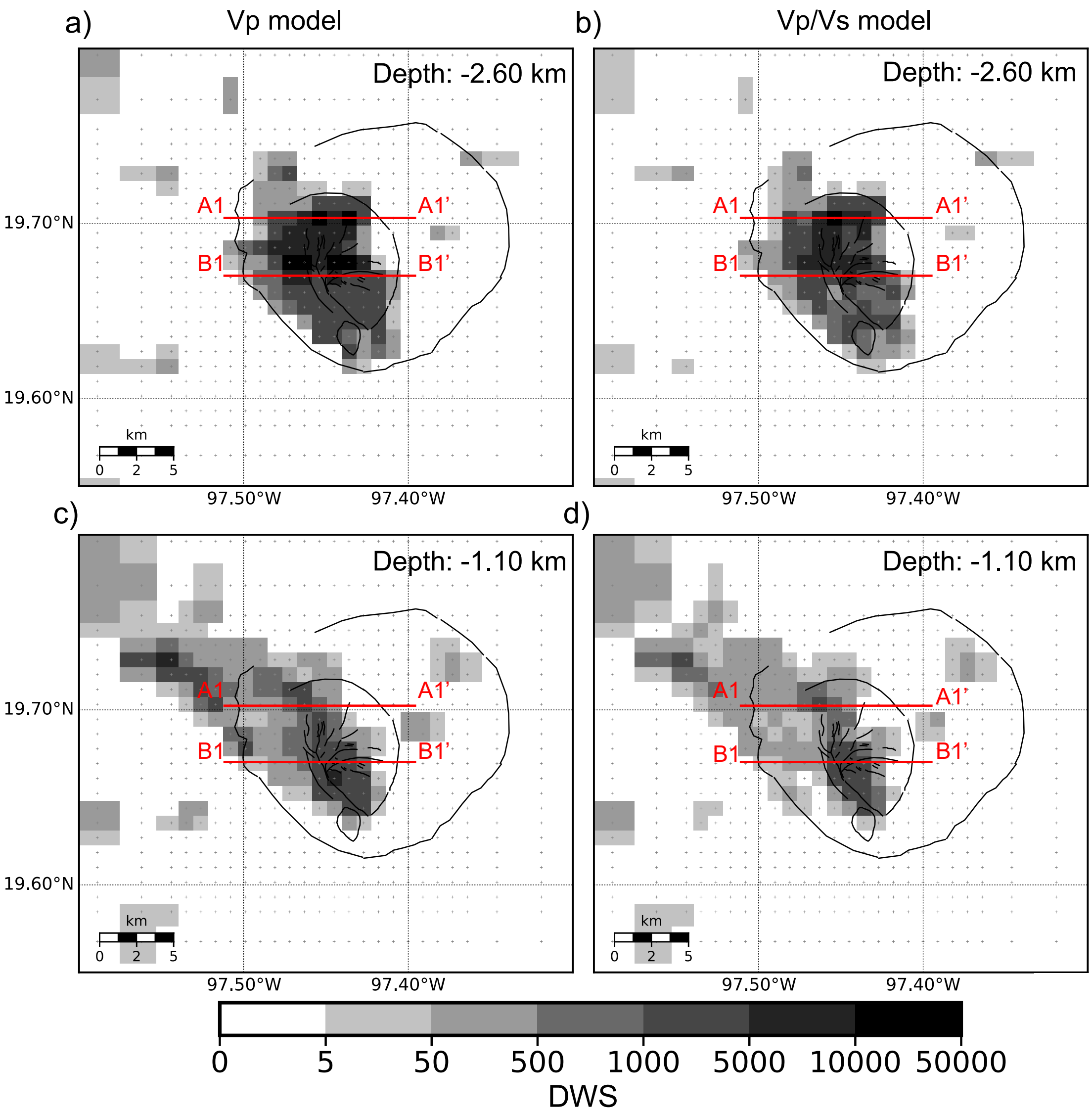

Figure 7.7: Model parametrization and DWS distribution at different depth levels for an initial (unrotated) inversion grid. Panels a) and c) show two depth slices for the Vp model DWS distribution at -2.6 km and -1.10 km depth. Panels b) and d) show the depth slices for the Vp/Vs model DWS distribution at -2.6 km and -1.10 km depth. Darker shading indicates regions of higher ray density. Gray crosses indicate node positions.

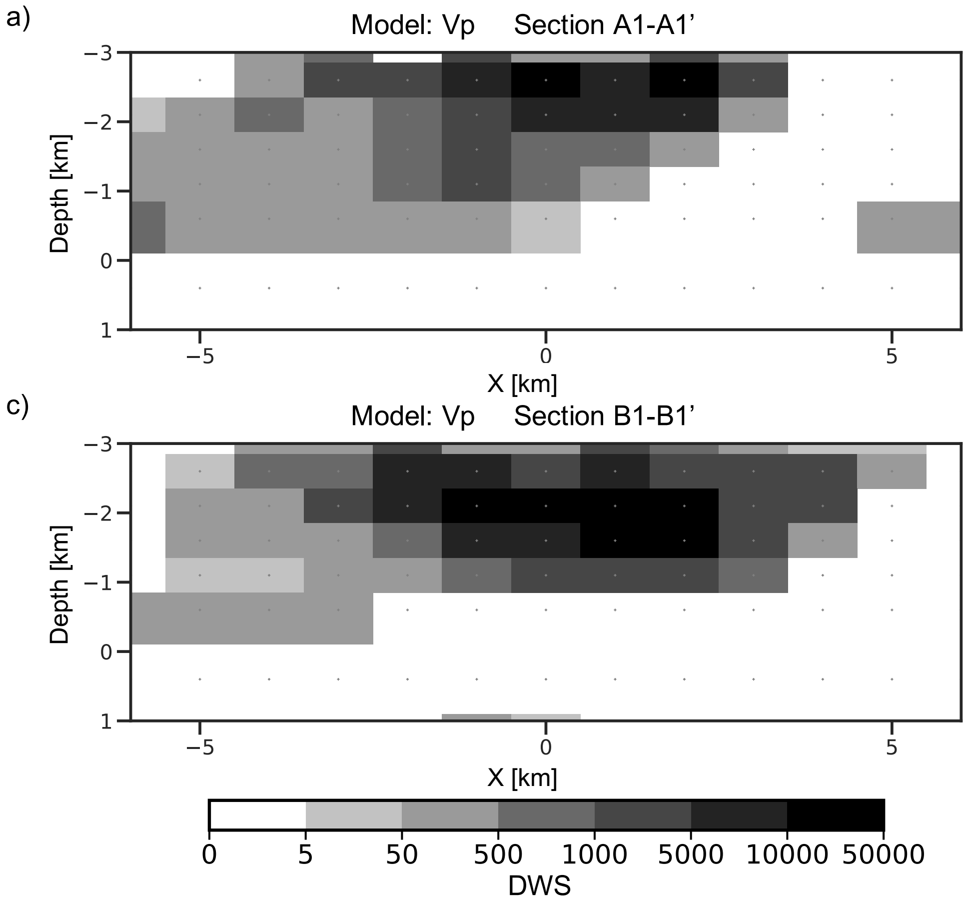

Figure 7.8: Cross sections A1-A1' and B1-B1' for the Vp model DWS distribution (Figure 7.7). Darker shading indicates regions of higher ray density. Black crosses indicate the node positions.

7.4.2 Regularization

We performed a tradeoff test (Appendix 7.B) to select adequate damping values for a single inversion grid (*Eberhart-Phillips*, 1990). Given the node spacing remained the same for all 228 inversion grids, we kept these damping factors fixed. Figure 7.11 shows the misfit value changes with each progressive iteration for the 228 inversions. The misfits start at 0.2 s for all models and progressively reduce to a mean value of ∼0.102 s, which falls within the range of the picking uncertainties, thus confirming the successful inversion of the models used with the chosen regularization parameters.

7.4.3 Model quality and uncertainty

An adequate quality assessment of the solution is typically carried out to validate inversion performance. The main objective is the identification of poorly resolved areas and unrealistic model perturbations or artifacts that may have been introduced and affect interpretation. Several parameters and procedures that analyze ray distribution and density include the evaluation of the hit count, the diagonal element of the model resolution matrix (MRM), the spread function (*Michelini and McEvilly*, 1991; *Toomey and Foulger*, 1989), the smearing information of each node provided by the MRM, tests with synthetic data such as checkerboard (*Zelt*, 1998) and recovery tests. In this study we calculate and display the results of a

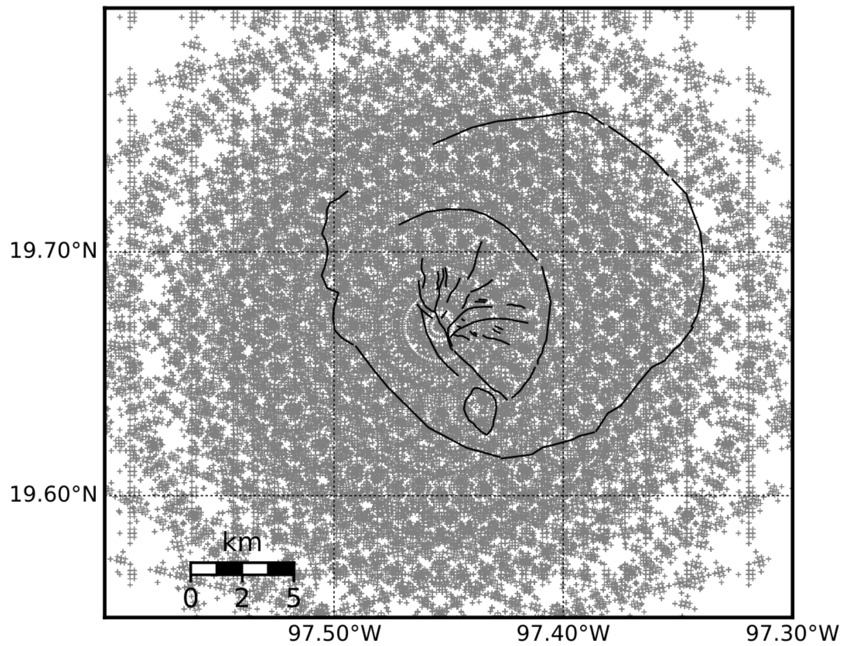

Figure 7.9: Nodes of the 228 inversion grids used to estimate the average velocities.

checkerboard test. Averaged spread values and diagonal elements of the MRM (RDE) are shown in Appendix 7.C and 7.D, respectively.

We carried out a checkerboard test to determine what kind of anomalies can be retrieved with the seismic network and catalog used. We perturbed the minimum 1D Vp model with alternating ±12% anomalies and the starting Vp/Vs model (constant value of 1.71) with ±10% perturbations. These anomalies are in agreement with the range of velocities obtained after the 3D inversion. Positive and negative anomalies are indicated in blue and red colors, respectively (Figure 7.12 and Figure 7.13). They are comprise 4 nodes of the single grid (Figure 7.7) in the horizontal directions (∼ 1.5 km x 1.5 km) and 2 nodes in the vertical direction (∼0.7-1 km). These perturbations have the approximate size of some of the main anomalies obtained in the real data inversion. We computed synthetic traveltimes using the retrieved seismic catalog and added Gaussian noise with ±0.065 s standard deviation, which corresponds to the standard deviation of the uncertainty distribution of the manual picks. Similar to the real data inversion, we determined the damping parameters by performing a tradeoff test. Then, we carried out inversions for the 228 grids of Figure 7.9 and averaged the results.

Figure 7.12 shows the recovered velocity anomalies for Vp and Vp/Vs across several depth slices. Regions with higher ray density, particularly those closer to the identified seismic clusters, appear to be best recovered. These areas coincide with those of lower spread and high RDE values in Figure 7.21 and Figure 7.20, respectively. Depths between ∼-2.10 km to -1.6 km seem best resolved (Figure 7.12a, b, c, d), with errors of approximately ±2-3 % in the best cases for both Vp and Vp/Vs. At shallower and deeper levels (Figure 7.12e, f) the polarity of the anomalies are recovered only towards the center and smeared towards the edges

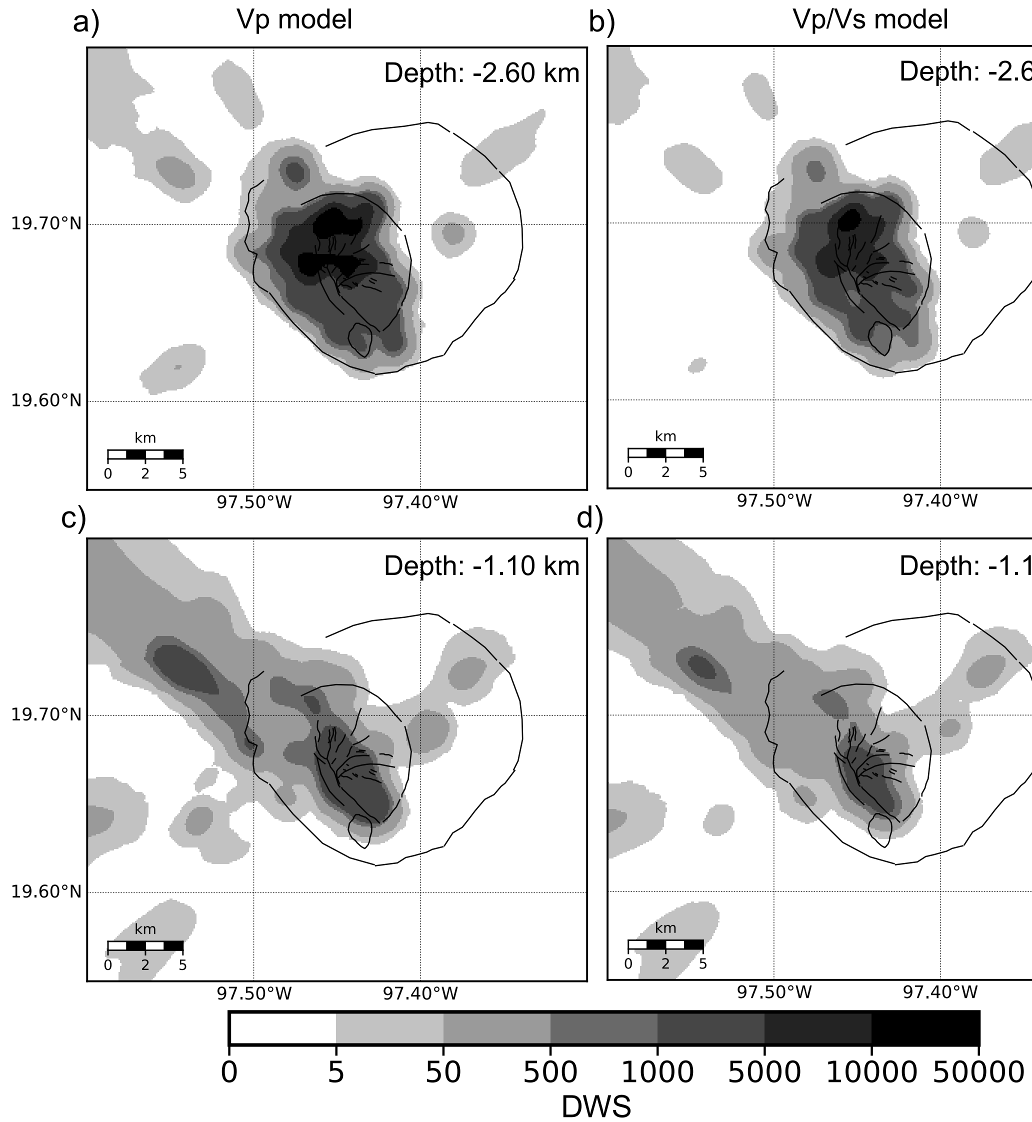

Figure 7.10: Averaged DWS distribution at different depth levels. Panels a) and c) show two depth slices for the Vp model DWS distribution at -2.6 km and -1.10 km depth. Panels b) and d) show the depth slices for the Vp/Vs model DWS distribution at -2.6 km and -1.10 km depth. Darker shading indicates regions of higher ray density.

of Los Potreros caldera. Velocity uncertainties in these regions vary around ±5-8 %. The checkerboard is also well reproduced in some regions of the vertical sections (Figure 7.13). The recovery looks best at the center of the cross sections A2-A2', B2-B2', and C2-C2' to a depth of -1 km, after which anomalies become smeared once more. The polarities of some velocity anomalies, however, are reproduced to 0 to -0.2 km depth towards the center of section B2-B2'. Overall, the uneven seismicity distribution (raypath configuration) marks a very limited area (shallow north-central portion of Los Potreros caldera) of good recovery. This region coincides with the area where spread values fall below a value of 1.5.

It is worth noting that a single inversion using the same grid configuration as the one used to produce the synthetic model perturbations is able to retrieve these anomalies accurately. However, when the parametrization is considerably different (e.g. a shifted or rotated grid), the recontruction is worsened and significant smearing is introduced, distorting the anomalies.

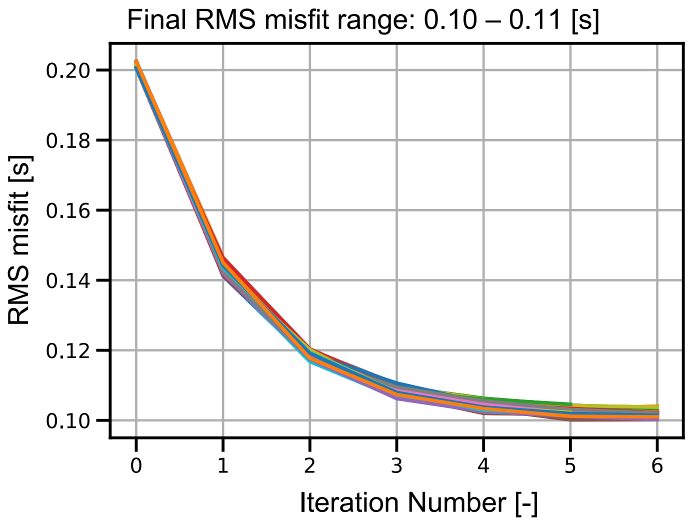

Figure 7.11: RMS misfit variation for the 228 inverted models.

In reality it is complicated to know beforehand the location and direction of the perturbations. By averaging several inversions using different model configurations, the dependence of the results on a single model parametrization is reduced, therefore significantly enhancing the accuracy of the final model.

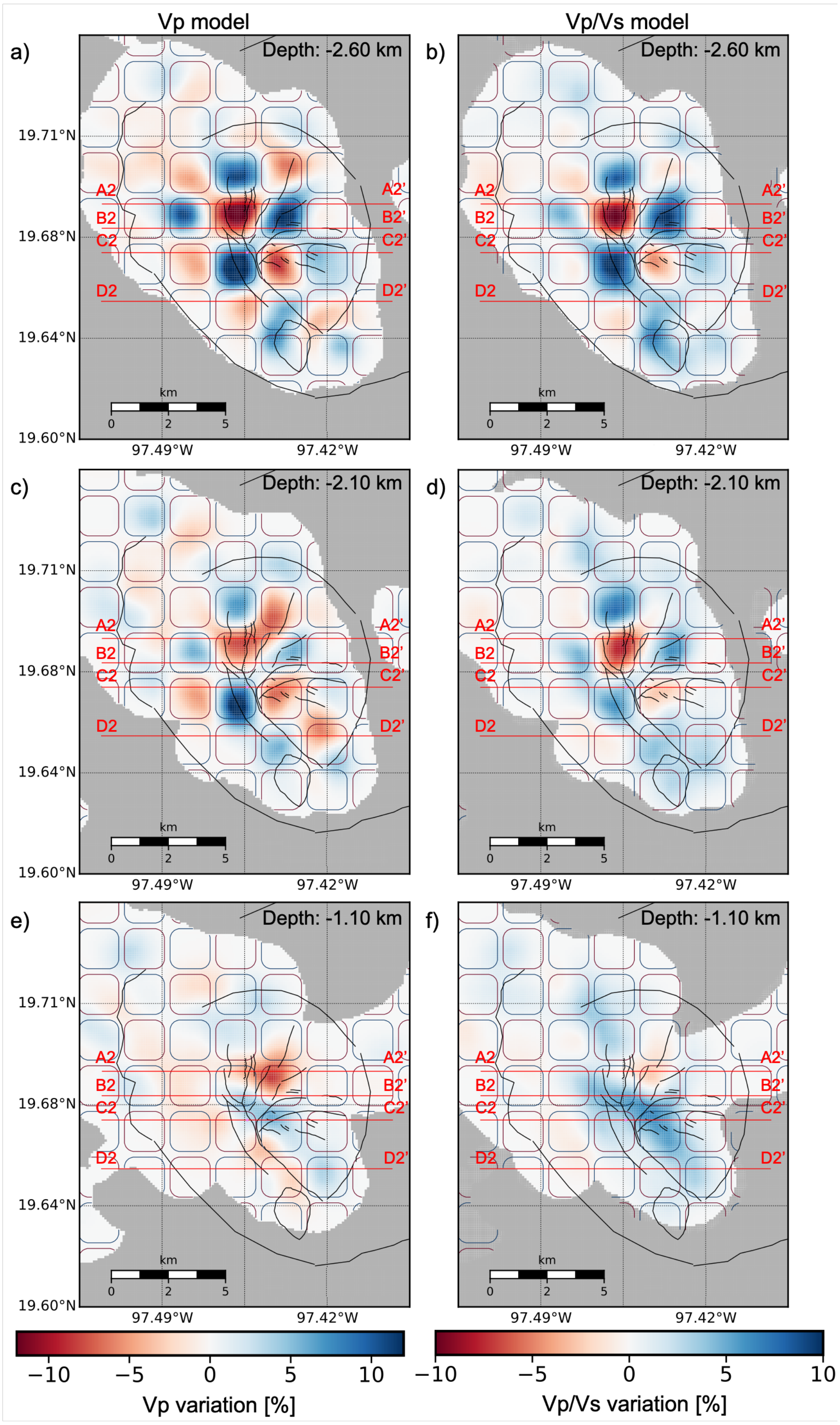

Figure 7.12: Checkerboard recovery. Panels a), c), and e) show three depth slices for the recovered Vp anomalies at -2.6 km, -2.10 km, and -1.10 km depth. Panels b), d), and f) show the recovered Vp/Vs anomalies at -2.6 km, -2.10 km, and -1.10 km depth. The red and blue squares mark the positions of the synthetic high and low velocity anomalies. Gray areas mark the regions where the DWS is less than or equal to 5.

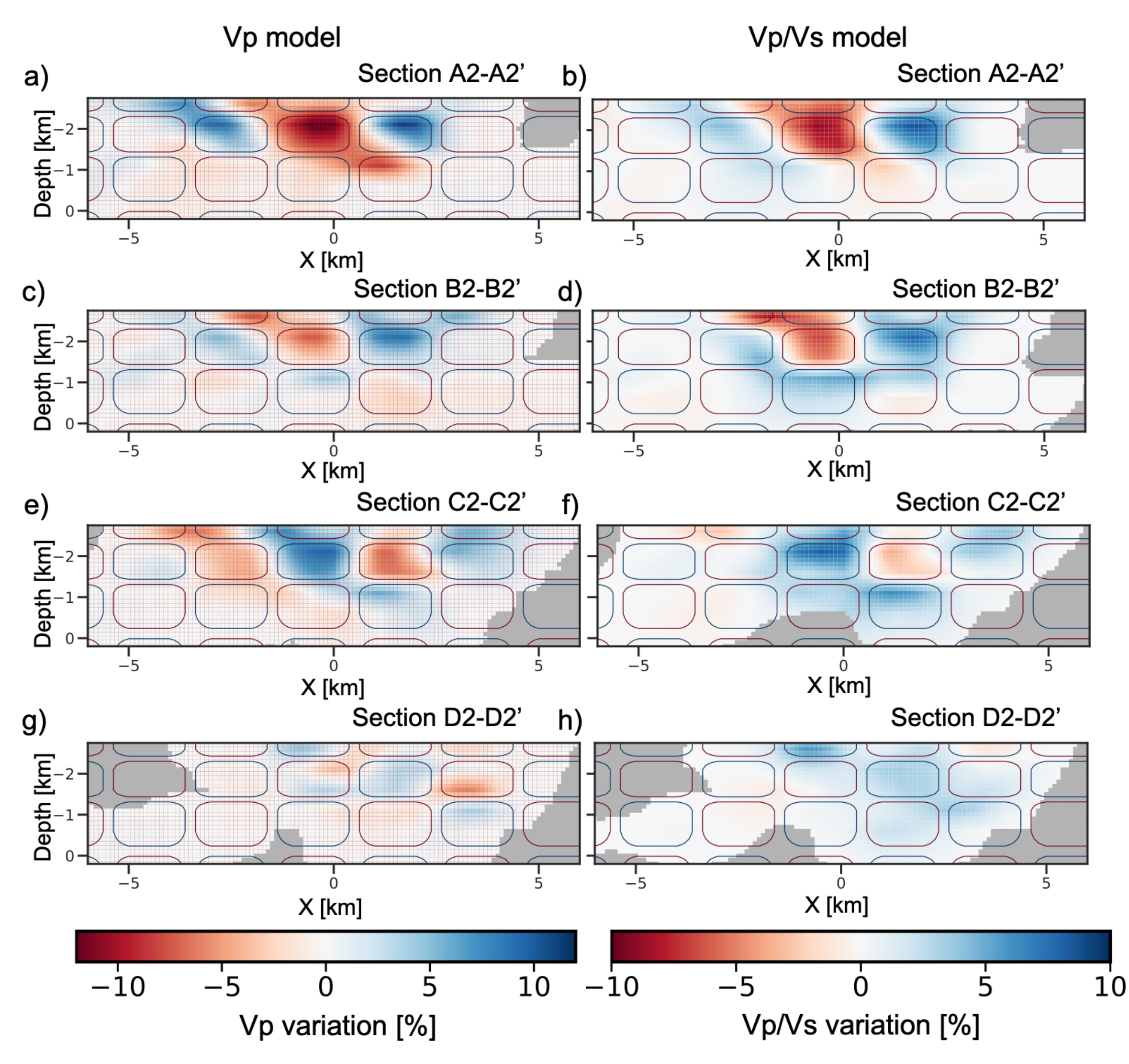

Figure 7.13: Cross sections A2-A2', B2-B2', C2-C2', and D2-D2' (Figure 7.12) for the retrieved Vp and Vp/Vs model variations. Panels a), c), e), and g) show the recovered Vp anomalies, and panels b), d), f), and h) show the recovered Vp/Vs anomalies of the checkerboard test. Gray areas mark the regions where the DWS is less than or equal to 5.

7.5 Results and discussion

The retrieved Vp (Figure 7.14 and Fine 7.15) and Vp/Vs (Figure 7.16 and Fine 7.17) models together with the seismicity distribution provide new insights on the geometry of the different geological units of LHVC, and the relation between some of the main structures and the geothermal system. In this section, we describe and discuss the results of the 1D and 3D velocity inversions in relation to existing geological and newly acquired petrophysical, geochemical, and geophysical data at Los Humeros geothermal field.

7.5.1 1D velocity model

The selected minimum 1D velocity model (Figure 7.5) not only shows a good agreement with alternative studies on the region (*Lermo et al.*, 2008; *Löer et al.*, 2020), it also shows one possible geological boundary observed in retrieved well data (*Norini et al.*, 2019). A prominent discontinuity is seen at $\sim$ -1.2 km depth in Figure 7.5 for both Vp and Vs models. This discontinuity could potentially mark an average transition between the pre-caldera group and the sedimentary basement, as it is also seen in well data at $\sim$ -1.5 to -0.2 km depth (*Norini et al.*, 2019). Vp/Vs ratio values are fairly constant but rather low at different depth levels, with the exception between -0.5 and 0 km depth, where most of the seismicity is concentrated (hence the larger average value of 1.71). These unusually low values could be the consequence of lateral averaging and the irregular distribution of sources and receivers. For this reason, we consider that the minimum 1D velocity model should not be overinterpreted.

7.5.2 Seismicity distribution

Main results

The final earthquake catalog was obtained by averaging the coordinates and origin times of the output catalogs of each inversion. The standard deviation of each component was used to quantify the location uncertainties which were on average 131 m, 127 m, 214 m, and 0.027 s for x, y, z, and origin time, respectively. These values represent in some way the intrinsic tradeoff between the errors of the model and hypocenter estimations.

Discussion

Similar to the catalog obtained after the initial relocation, the seismicity is grouped in three clusters (Figure 7.3). The northernmost cluster (C1 in Figure 7.3) has already been evidenced in *Lermo et al.* (2008) and is situated close to the main production area, where two out of three neighboring injection wells are located (red stars in Figure 7.3). The southwestern cluster (C2 in Figure 7.3) is located to the west of Los Humeros fault, close to a third injection well. Finally, a deeper cluster (C3 in Figure 7.3) is located towards the east, between Las Papas and Las Viboras faults. The remaining events are scattered within the geothermal field, with some following major structures such as the Maztaloya fault.

Cluster C1 (Figure 7.15a and Figure 7.17a) has a narrow sub-vertical distribution relating to Los Humeros Fault Zone at the surface. We define Los Humeros Fault Zone as the combination of very closely spaced ($\sim$100-250 m) N-S fault strands (Loma Blanca fault, Los Humeros fault, and Los Conejos fault). In a similar manner, cluster C2 (Figure 7.15c and Figure 7.17c) reflects the position of Los Humeros fault further south. Given their vicinity to injection wells (see green vertical lines in Figure 7.15 and Figure 7.17), most of them could probably be induced/triggered events. The third cluster (C3) is located at a deeper level towards the east (Figure 7.15b, c and Figure 7.17b, c). At the surface, this region coincides with the area between the E-W trending Las Papas and Las Viboras faults, but does not seem directly associated with any geothermal wells. However, the proximity of this cluster to C2 could potentially indicate a deeper fluid pathway towards the east. These two faults show no hydrothermal alteration along their strike at the surface (*Norini et al.*, 2019). However, the presence of this cluster could hint to an increase of permeability of these faults at greater depths.

7.5.3 Vp structure

Main results

Our results provide new detailed insights into the 3D P-velocity structure of Los Humeros geothermal field. We present our results in a series of horizontal depth slices (Figure 7.14) followed by E-W vertical sections (Figure 7.15) across Los Potreros caldera. Average P-wave velocities range from $\sim$ 2-4.1 km/s, with standard deviations in the order of $\pm$0.06 km/s (Figure 7.22 in Appendix 7.E). We show velocity perturbations relative to the minimum 1D Vp model, as it is easier to observe the physical properties of rocks (e.g. presence of fluids and temperature) in this form. Nevertheless, we show absolute velocity values with contour lines in the cross sections to ease interpretation.

Close to the surface (Figure 7.14a), a large low velocity anomaly ($\sim$ -8 to -12%) marked as *a* (Figure 7.14a) is located at a highly faulted region towards the center of Los Potreros caldera. This anomaly is surrounded by high velocity anomalies ($\sim$ +6 to +10%) to the northeast, south, and west (marked as *b*). Further in depth (Figure 7.14b), a clear division between high ($\sim$ +10%) and low ($\sim$ -5%) velocity anomalies (*c* and *d*) is separated by the main Los Humeros fault. This velocity contrast remains at depth, although the low velocity anomaly to the east appears attenuated ($\sim$ -3%) at deeper levels. One large high ($\sim$ +10 to +13%) velocity anomaly (*h*) appears at -1.60 km depth (Figure 7.14c) almost following Los Humeros and Maztaloya faults, which extends in a much narrower corridor at -1.10 km depth (*j* in Figure 7.14d).

If we observe the Vp variations in cross sections (Figure 7.15a, b, and c), the high velocity anomaly is located mostly towards the east of Los Humeros normal fault. At larger depths, a second minor high ($\sim$ +3%) velocity anomaly (mainly visible in sections B-B' and C-C') appears further to the east where cluster C3 is located. This feature barely reaches the limits of the imaging capabilities of our dataset, and must therefore be interpreted with caution.

A smaller low ($\sim$ -5 to -3%) velocity anomaly appears west of the northern portion of Los Humeros Fault and is traceable at depth (*f*, *g*, and *i* in Figure 7.14). This anomaly is also seen in the cross sections (Figure 7.15a, b, and c), mostly west of the buried La Antigua fault. The low velocity region visible to the east in cross sections B-B' and C-C' is associated to *d* in Figure 7.14b.

Discussion

Some of the velocity anomalies at -2.6 km depth (Figure 7.14a) accurately follow the surface geology (See Figure 7.1). The low velocity anomaly marked as *a* is located where undefined pyroclastics belonging to the post-caldera stage are deposited (Figure 7.1). In a similar manner, the high velocity anomalies marked as *b*, are related to regions with rhyodacitic, andesitic, and basaltic volcanic rocks.

The high velocity anomalies observed at depth correspond to intrusive-like bodies in the absolute velocity contour lines. Similar structures have been indicated by the combined interpretation of structural field analysis, and analog modelling at Los Potreros caldera and interpreted by *Norini et al.* (2019) and *Urbani et al.* (2020) as discontinuous resurgence associated with the intrusion of multiple magma bodies rather than a single magma chamber.

The shallow low velocity anomalies in cross sections B-B' and C-C' indicate the increased thickness of the post-caldera unit in these areas and reveal the variable deposition of volcanic materials during the complex volcanic history of the caldera.

To determine possible unit boundaries, we marked the positions of several neighboring interpreted wells (*Carrasco-Núñez et al.*, 2017b) in the cross sections shown in Figure 7.15. We compared the depth ranges of the units seen in the interpreted wells with ultrasonic pulse velocity measurements of collected core and outcrop rock samples (Table 7.1) and our retrieved velocities. Then, we marked approximate unit boundaries with solid gray lines in Figure 7.15. We deduced the post-caldera stage (pyroclastics) with Vp around $\sim$ 2.2-2.4 km/s at shallow depths. This velocity range is well within the range of laboratory measurements of collected rock samples (2.0-3.7 km/s). The caldera stage (mainly ignimbrites) lower boundary was interpreted at around -2.0 km depth with average Vp of 2.8 km/s. Laboratory measurements range between $\sim$ 1.8-3.5 km/s for rocks found in this unit. Below, we interpreted the pre-caldera unit (andesites) with Vp up to $\sim$3.8-3.9 km/s. After that the marbles and limestones belonging to the basement start in our sections with Vp $\geq$ 3.9 km/s. The basement boundary is shallower close to Los Humeros fault zone.

7.5.4 Vp/Vs structure

Main results

Average Vp/Vs values varied between 1.50 and 1.77 throughout the studied region (Figure 7.16 and Figure 7.17), with standard deviations in the order of $\pm$0.02 (Figure 7.22 in Appendix 7.E).

At shallow depth (Figure 7.16a), a prominent low Vp/Vs anomaly ($\leq$ 1.60) is located at the northern portion of Los Humeros fault system with the lowest values concentated between Los Humeros, La Cuesta, and Cueva Ahumada faults (*k*). This anomaly extends at depth towards the southeast (*l* and *n* in Figure 7.16). This behavior is also seen in the cross sections of Figure 7.17, where in many cases the anomaly extends at depth mostly towards the east of Los Humeros fault.

On the other hand, two higher Vp/Vs anomalies ($\geq$ 1.71) are observed at the northern portion of Los Potreros caldera (*o* in Figure 7.16) at -1.10 km depth. These anomalies are

Table 7.1: Approximate mean P- velocities obtained from laboratory measurements of different core and outcrop rock samples. Modified from *Bär and Weydt* (2019)

.

Stage	Lithology	P-wave velocity (km/s)	Stage	Lithology	P-wave velocity (km/s)	Stage	Lithology	P-wave velocity (km/s)	Stage	Lithology	P-wave velocity (km/s)
Basement	Limestone J	4.5	**Pre-caldera unit**	Andesite (core) dry/ saturated	4.1	**Caldera unit**	Xaltipan Ignimbrite (outcrop) altered	3.0	**Post-caldera unit**	Ash fall (outcrop)	2.0
	Limestone K	4.7		Teziutlan Andesite (outcrop) porous	3.0		Xaltipan Ignimbrite (outcrop)	1.8		Basalt (core)	2.5
	Skarn (outcrop)	4.3		Teziutlan Andesite (outcrop)	4.8		Ignimbrite (core)	3.5		Basalt (outcrop)	3.7
	Marble (core) dry	3.0		Alseca andesite	2.8		Ignimbrite (outcrop) dry	2.3		Inner caldera ignimbrite (outcrop)	2.2
	Marble (core)	4.1		Cuyoaco andesite	3.0						

particularly evident in Figure 7.17a and Figure 7.17b. In Figure 7.17a the high Vp/Vs anomalies are divided by the Los Humeros fault and the anomaly towards the east is higher.

Discussion

Although Vp/Vs values appear low in Los Humeros (minimum ∼1.5), they are not uncommon in volcanic and geothermal regions (e.g. *Husen et al.* (2004) (minimum ∼1.57), *Muksin et al.* (2013) (minimum ∼1.47)). The shallow low Vp/Vs anomaly coincides in shape and position with a conductive body (≤10 Ω m) imaged by a new MT survey at Los Humeros geothermal field (*Benediktsdóttir et al.*, 2019), hinting at the location of the cap rock composed of ignimbrites. If we consider porous media (and low Vp), this region of low Vp/Vs values can be inferred as a gas bearing chamber (*Gassmann*, 1951). Such interpretation is supported by the modelling of low Vp and low Vp/Vs anomalies in porous volcanic rocks in *Husen et al.* (2004). This hypothesis is confirmed by a new survey of CO_2 emissions at the surface (*Jentsch et al.*, 2020), where higher flux regions coincide with k in Figure 7.16a.

Further in depth, the high Vp/Vs anomalies could hint at regions with increased liquid content (*Gassmann*, 1951). The anomaly to the east of Los Humeros fault zone (Figure 7.17a) coincides with a region close to the bottom of a neighboring injection well. West of Los Humeros fault zone, the second high Vp/Vs anomaly coincides with generally lower Vp values (3.2-3.4 km/s), which could be an indication of rocks, namely the andesites, influenced by the presence of liquid. These areas could potentially be considered for further exploration and exploitation of the geothermal field.

A local heat source could be assumed as located at greater depths transporting heat along permeable faults especially in the region close to Los Humeros Fault zone. Such a hypothesis would be in correlation with the analog and structural work by *Urbani et al.* (2020) that suggests recent shallow magma emplacement in the region close to the Loma Blanca fault. Given the limited imaging capabilities of the dataset used, this hypothesis would need to be confirmed with other geophysical and seismic imaging techniques such as ambient noise tomography.

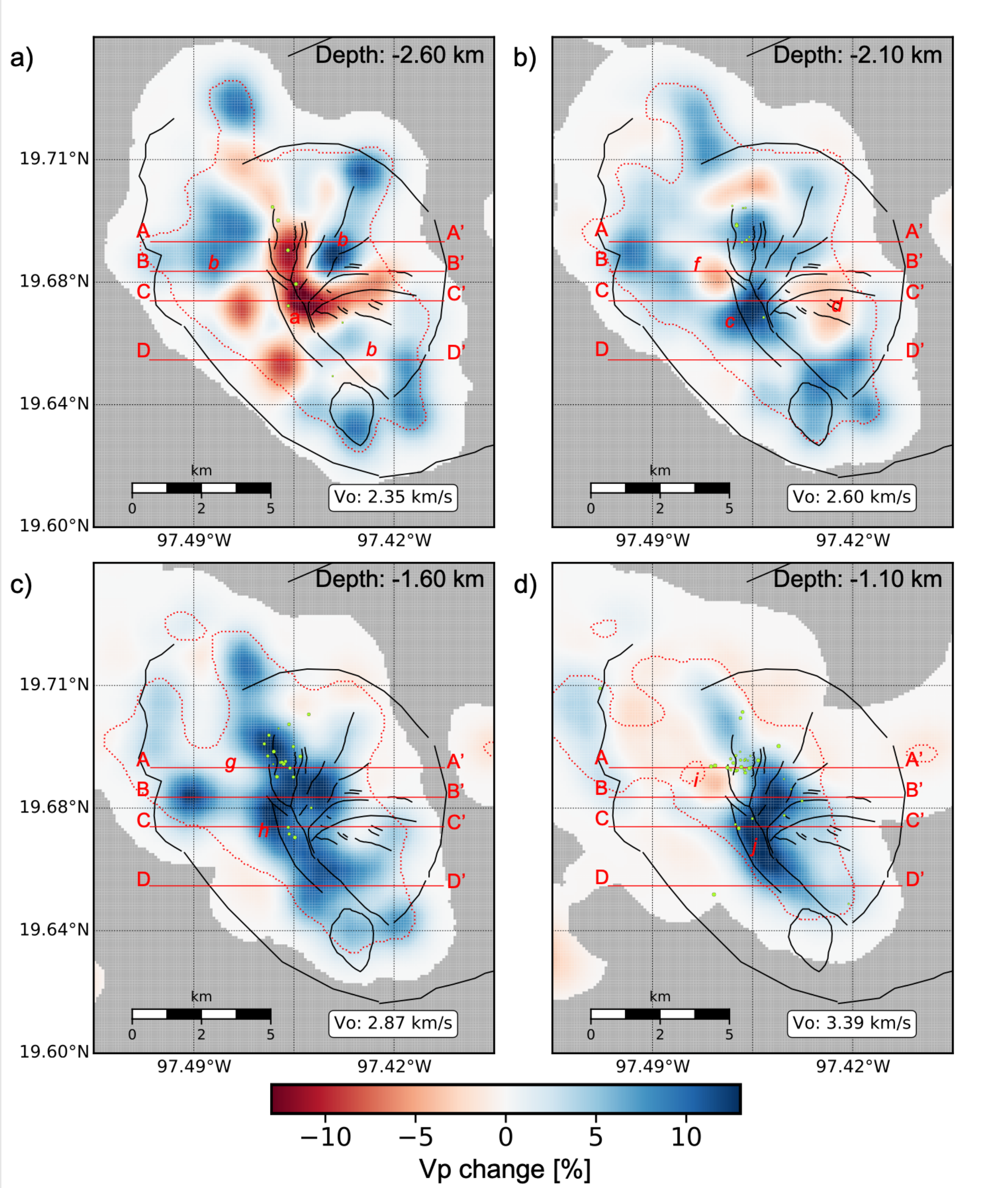

Figure 7.14: Vp model variations with respect to the minimum 1D velocity model at different depth levels. Panels a), b), c), and d) show depth slices for the resulting Vp model variations at -2.60 km, -2.10 km, -1.60 km, and -1.10 km depth, respectively. Green circles mark the location of earthquakes +/- 150 m away from slice. Dashed red lines indicate the boundary at which spread values are less than or equal to 1.5. Gray areas mark the regions where the DWS is less than or equal to 5.

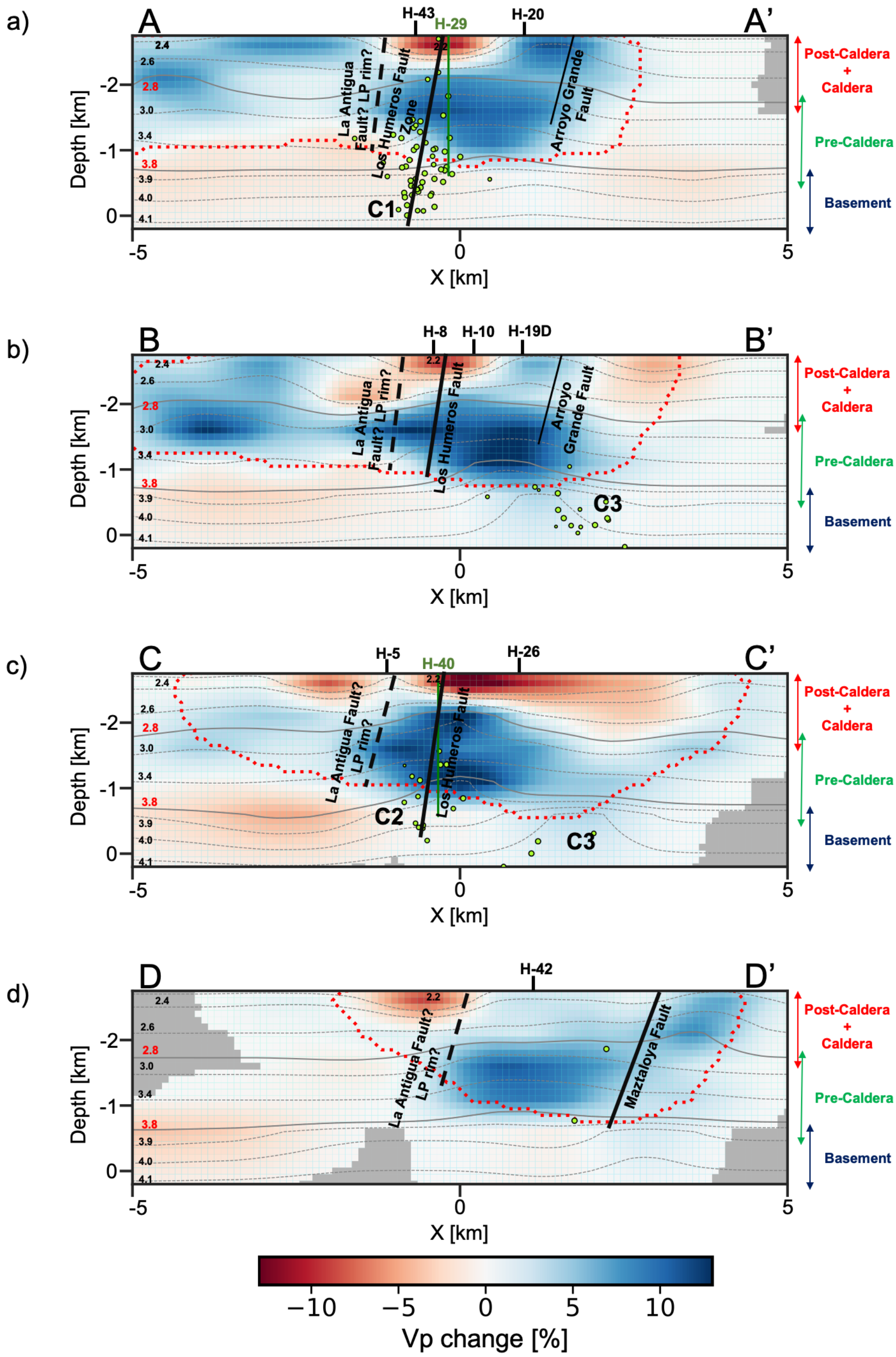

Figure 7.15: Cross sections for the Vp model variations (Figure 7.14). Green circles mark the locations of earthquakes +/- 200 m away from the slice. Dashed red lines indicate the boundary at which spread values are less than or equal to 1.5. Gray areas mark the regions where the DWS is less than or equal to 5. Dashed gray lines indicate different absolute velocity levels, and solid gray lines mark approximate unit boundaries. Approximate locations of main structures are indicated in black. Vertical green lines indicate the positions of neighboring injection wells.

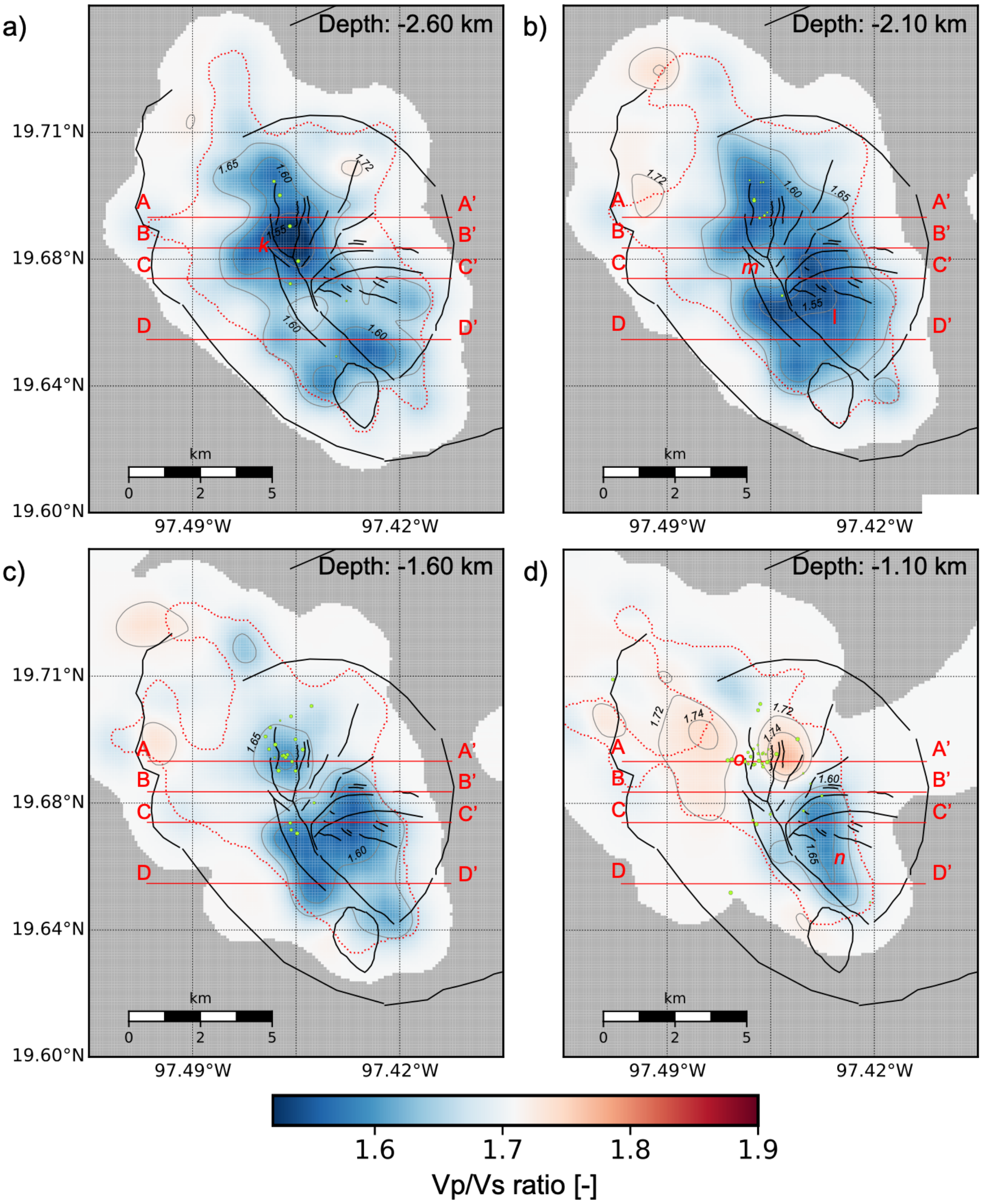

Figure 7.16: Vp/Vs structure at different depth levels. Panels a), b), c), and d) show depth slices for the resulting Vp/Vs model at -2.60 km, -2.10 km, -1.60 km, and -1.10 km depth, respectively. Green circles mark the locations of earthquakes +/- 150 m away from the slice. Dashed red lines indicate the boundary at which spread values are less than or equal to 1.5. Gray areas mark the regions where the DWS is less than or equal to 5.

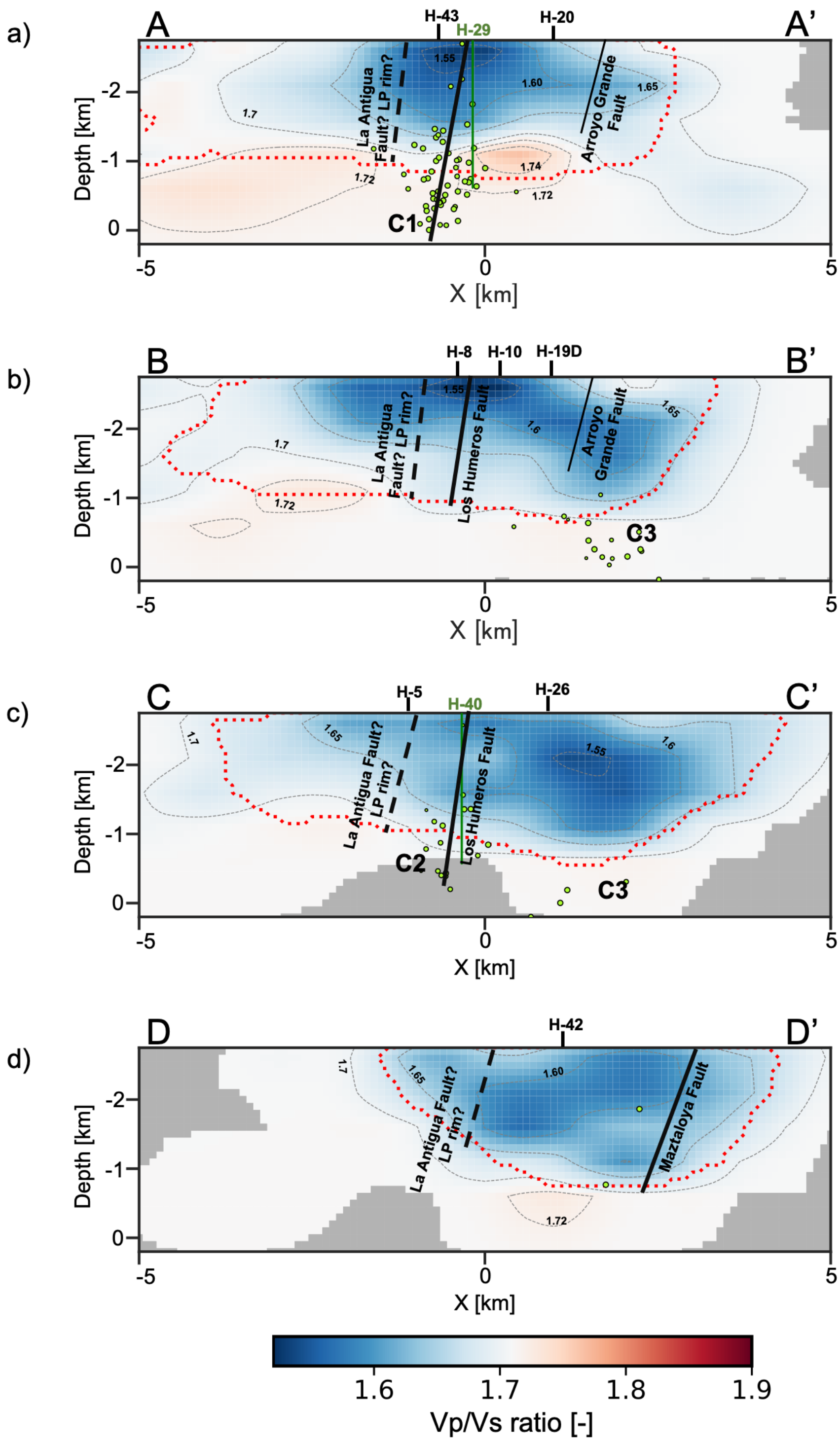

Figure 7.17: Cross sections for the Vp/Vs model (Figure 7.16). Green circles mark the locations of earthquakes +/- 200 m away from the slice. Dashed red lines indicate the boundary at which spread values are less than or equal to 1.5. Gray areas mark the regions where the DWS is less than or equal to 5. Approximate locations of main structures are indicated in black. Vertical green lines indicate the positions of neighboring injection wells.

7.6 Conclusions

A new seismological analysis using a dense temporary seismic network was undertaken at Los Humeros geothermal field. We collected high quality earthquake data to image the Vp and Vp/Vs models for the first time in this region. These models were obtained by extending the classical local earthquake tomography using a post-processing statistical approach. Several models were inverted and averaged to reduce the potential bias introduced by the choice of model parametrization and enhance the final spatial resolution. The results were then carefully integrated with new geophysical, geological, and petrophysical data for interpretation.

The statistical approach reduces the potential smearing resulting from selecting model parametrizations that do not align with anomaly location and orientations, which are in many cases unknown prior to computing a tomography. The consideration of different initial grids allows for a much finer solution and helps overcome the code restriction of using a fixed coarse grid. It also allows assesing and reducing the error bars of the final solution.

From this analysis, we identified three seismogenic areas within Los Potreros caldera, one of which does not appear in direct relation to any geothermal wells. A deep earthquake cluster was located between Las Papas and Las Viboras faults. Although these faults show no hydrothermal alteration at the surface (*Norini et al.*, 2019), the presence of this seismic cluster suggests that these faults may increase permeability at depth. The vicinity of this new cluster to another one close to an injection well could potentially highlight a deeper fluid pathway towards the east.

The main geological boundaries found from well and new petrophysical data were also found in our Vp model. The presence of two instrusive bodies supports the idea of resurgence at Los Potreros caldera (*Norini et al.*, 2019; *Urbani et al.*, 2020). *Urbani et al.* (2020) suggest that intrusions in the region are the result of the inflation of the magma chamber at depth, and may represent locations of local heat source(s).

The Vp/Vs model also supports the resurgence or uplift due to the intrusion of new magma at Los Potreros caldera. High Vp/Vs ratio anomalies are located to each side of Los Humeros Fault zone, where the hypocenters in between have a sub-vertical configuration. This could hint at a deeper heat source transporting hot fluids upwards along permeable faults. A new petrological study (*Lucci et al.*, 2020) also suggests such a system, with several (ephemeral) magma pockets in the crust being fed by multiple magma transport and storage layers. The high Vp/Vs values in this region could potentially indicate higher fluid content. Therefore, this area could be further studied.

Above this anomaly, a low Vp/Vs region coincides with the conductive clay cap seen in a new MT study (*Benediktsdóttir et al.*, 2019). The low Vp/Vs in combination with low Vp values could indicate gas bearing regions (*Gassmann*, 1951; *Husen et al.*, 2004). This hypothesis is also supported by a new CO_2 emissions survey at the surface (*Jentsch et al.*, 2020). The shallower portions with the lowest Vp/Vs value coincide with regions of higher CO_2 fluxes.

Further steps to be considered for better understanding of the geothermal system include an attenuation tomography and the imaging of deeper structures with techniques such as ambient noise tomography. In addition, a more quantitative approach such as a cluster analysis of different physical properties will be performed to improve the accuracy of the interpretation and to build a conceptual model.

Appendix 7.A Station corrections associated with the 1D velocity model

Station corrections are defined as scalar terms accounting for near-surface velocity variations below each seismic station. In other words, they are potential indicators of surface geology and/or site conditions. Figure 7.18 shows the a) P-wave and b) S-wave station corrections associated with the minimum 1D velocity model. There are slightly higher P- delays at stations located towards the southeast of Los Potreros caldera. This is a region characterized by several fault outcrops and undefined pyroclastic deposits. The delays decrease towards the north-western edge of Los Humeros caldera. This area is characterized by basalts and andesites at the surface (Figure 7.1). Station delays for stations further away from Los Humeros caldera show higher values than those within the dense array, which could be associated with larger picking uncertainties. S-delays (Figure 7.18b) are also relatively balanced within Los Potreros caldera.

Table 7.2 shows the retrieved station correction values. Locations, elevations, and sensor types are available as the seismic network associated metadata in *Toledo et al.* (2019).

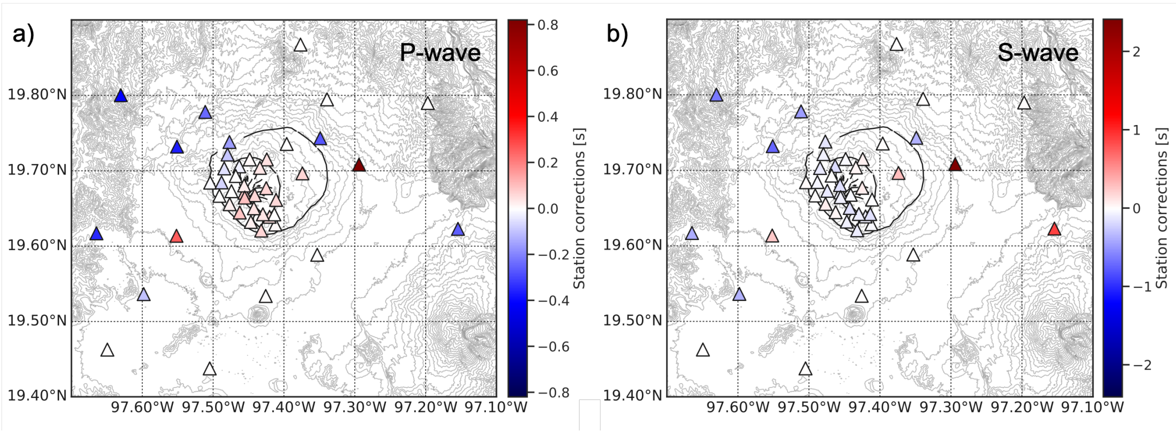

Figure 7.18: a) P-wave and b) S-wave station corrections associated with the 1D velocity models. Topographic lines are indicated in gray and main structures are shown in black.

Table 7.2: Station corrections associated to the minimum 1D velocity model

Station network	Station code	P-delay [s]	S-delay [s]
6G	DB01	0.01	-0.02
6G	DB02	0.08	-0.06
6G	DS03	0.03	-0.15
6G	DS04	-0.01	0.03
6G	DB05	0.01	-0.02
6G	DS06	0.05	-0.06
6G	DB07	0.02	-0.06
6G	DS08	0.0	-0.14
6G	DS09	-0.02	-0.16
6G	DS10	0.05	0.06
6G	DB11	-0.16	-0.12
6G	DB12	0.0	0.01
6G	DB13	-	-0.11
6G	DB14	0.04	-0.09
6G	DB15	0.06	-0.02
6G	DB16	0.06	-0.01
6G	SS17	0.07	0.32
6G	SS18	-0.27	-0.36
6G	SB19	0.82	2.41
6G	DS20	0.04	-0.15
6G	SB21	-	-
6G	SB22	-	-
6G	SS23	0.26	0.26
6G	SB24	-0.34	-0.39
6G	DB25	0.04	0.04
6G	SB26	-	-
6G	DB27	0.09	0.04
6G	DB28	0.02	0.09
6G	DB29	0.07	-0.08
6G	SB30	-0.26	0.9
6G	DB31	-0.05	-0.11
6G	SS32	-0.36	-0.73
6G	DS33	-0.09	-0.07
6G	DS34	0.1	-0.06
6G	SS35	-0.41	-0.64
6G	SS36	-0.24	-0.46
6G	SS37	-	-
6G	SS38	-	-
6G	SS39	-	-
6G	SB40	-0.1	-0.37
6G	SS41	-	-
6G	DB42	-0.07	-0.05
6G	DB43	0.07	0.08
6G	SB44	-	-
6G	DS45	-	-

Appendix 7.B Tradeoff test sample for a single model parametrization

Damping parameters for an inversion using a single model parametrization are chosen such that the data variance is minimized at a moderate model variance. We first determine the damping factor for Vp by testing several values while fixing the damping factor for Vp/Vs. In a similar manner we select a damping factor for Vp/Vs by testing a range of values in combination with the selected Vp damping factor. Through this approach, the damping parameters chosen for this experiment were 7 and 10 for Vp and Vp/Vs models, respectively (Figure 7.19). Given the node spacing did not vary when inverting for the different inversion grids, damping factors remained the same throughout all inversions perfomed.

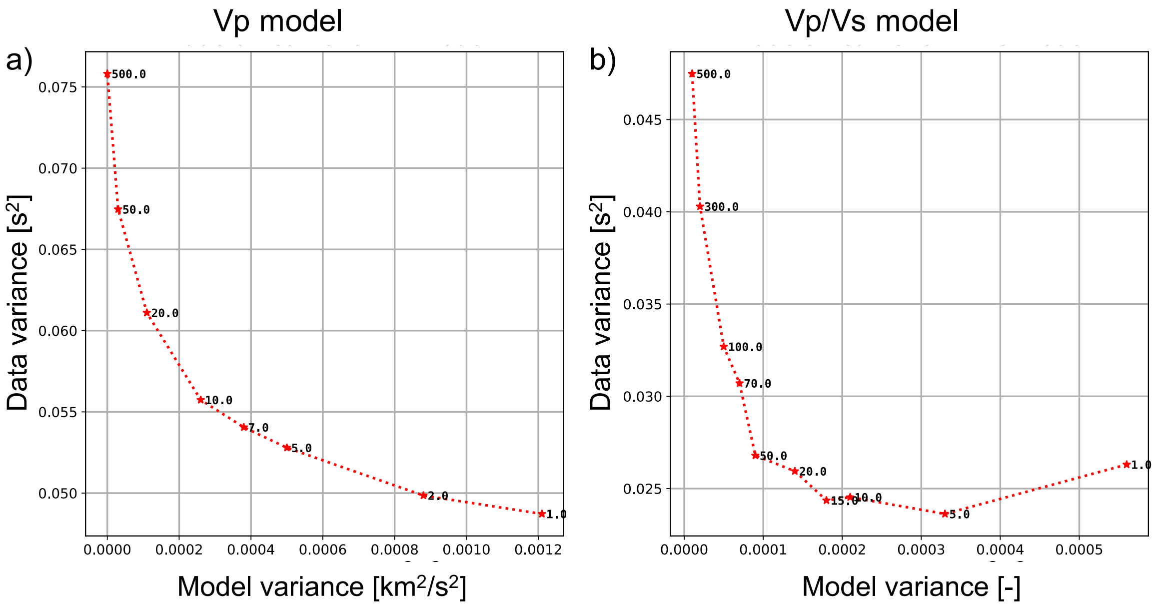

Figure 7.19: Tradeoff curves for a) Vp and b) Vp/Vs to select the optimal damping values. The parameters selected were 7 and 10 for Vp and Vp/Vs models, respectively.

Appendix 7.C Diagonal elements of the MRM (RDE)

Diagonal elements are representative of the inversion resolution, with values closer to 1 indicating better resolved areas. Figure 7.20 depicts the averaged RDE distribution for Vp and Vp/Vs at different depth levels. Higher RDE values (>0.3) are found in the topmost layers, especially in the region neighboring the northermost seismic cluster (C1 in Figure 7.3) for both Vp and Vp/Vs models. Surrounding this area, RDE values then decrease to 0.1-0.3 for both models, and are reduced at deeper levels due to decreased ray coverage. Overall good resolution is restricted to Los Potreros caldera, and is best towards the north.

Appendix 7.D Spread values

Off diagonal elements of the MRM contain information on the dependency of the solution of each node with respect to neighboring nodes. Smaller values indicate that the solution for a particular node is more independent, hence less smearing is associated with it. Figure 7.21 shows the averaged spread distribution for the Vp and Vp/Vs models for different depth slices. Smaller spread values (<1-2) coincide roughly with regions of RDE of 0.1-0.9 (7.C). As in the case of higher DWS values, the areas of lower spread values are for the most part concentrated within Los Potreros caldera.

Spread and RDE values are closely related to model parametrization and regularization. Therefore in a strict mathematical sense, these parameters may not be directly interpolated and averaged. We opted to recover this information for a rough estimate of resolvable areas. However, these final values should be treated with caution.

Appendix 7.E Model statistics

We computed and displayed the associated standard deviation of the final models in Figure 7.22. Variations of the standard deviation for the Vp model have a fairly homogeneous distribution across the areas of greater sensitivity (regions within dashed red lines in Figure 7.22), with some locations reaching a maximum value of around ± 0.10 km/s. Standard deviation values are lower and more evenly distributed at -2.10 km depth, which coincides with the depth slice with the highest ray density. Similarly, maximum variations for the obtained Vp/Vs model are in the order of ± 0.026. As in the case of the Vp model, variations appear more homogeneous at -2.10 km depth.

Acknowledgements

The GEMex project is supported by the European Union's Horizon 2020 programme for Research and Innovation under grant agreement No 727550 and the Mexican Energy Sustainability Fund CONACYT-SENER, project 2015-04-68074. The authors thank the Geophysical Instrument Pool Potsdam (GIPP) for facilitating the seismic equipment used in this project (GIPP-Grant number GIPP201719), and the Comisión Federal de Electricidad (CFE) of Mexico for granting access to the geothermal concession area.

Waveform data and associated metadata are archived at the GEOFON seismological archive, FDSN code 6G (2017-2018) (*Toledo et al.*, 2019), and are embargoed until January 2023.

The authors thank Dr. James Mechie, the editor, and two anonymous reviewers for their comments and observations which vastly improved this manuscript.

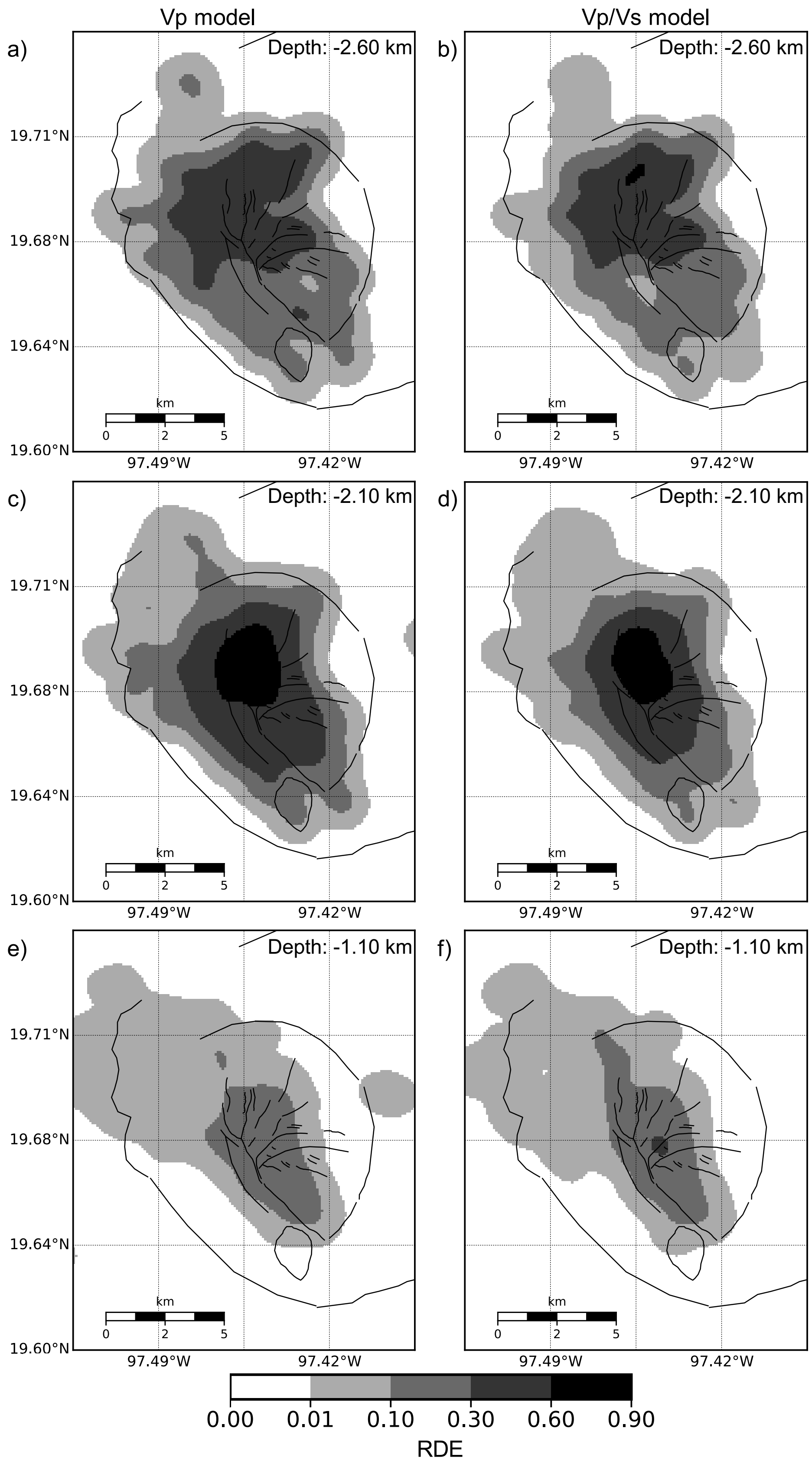

Figure 7.20: Average RDE distribution at different depth levels. Panels a), c), and e) show three depth slices for the Vp model RDE distribution at -2.6 km, -2.10 km, and -1.10 km depth. Panels b), d), and f) show the depth slices for the Vp/Vs model RDE distribution at -2.6 km, -2.10 km, and -1.10 km depth. Darker shading indicates higher resolution values.

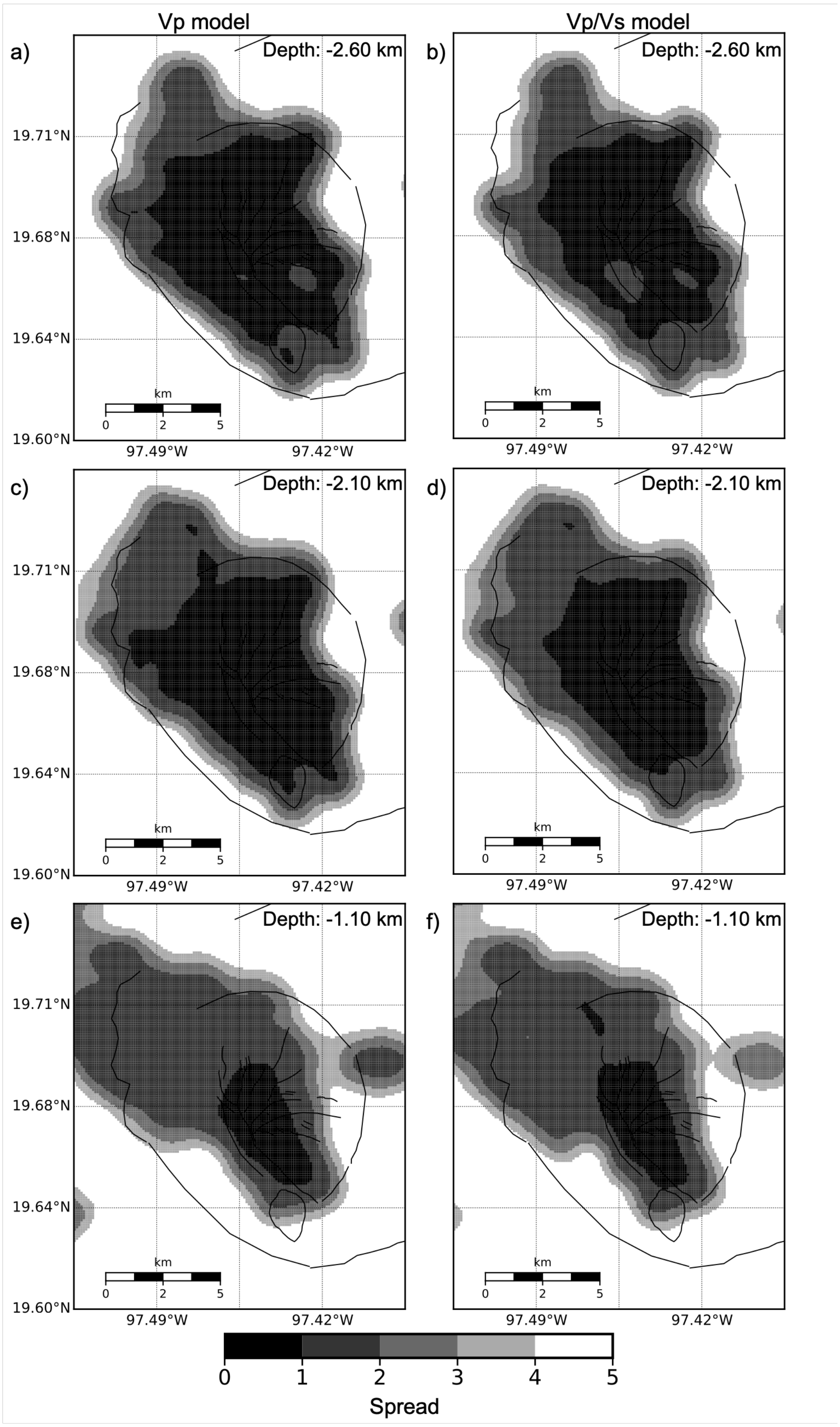

Figure 7.21: Averaged spread distribution at different depth levels. Panels a), c), and e) show three depth slices for the Vp model spread distribution at -2.6 km, -2.10 km, and -1.10 km depth. Panels b), d), and f) show the depth slices for the Vp/Vs model spread distribution at -2.6 km, -2.10 km, and -1.10 km depth. Darker shading indicates regions with less smearing.

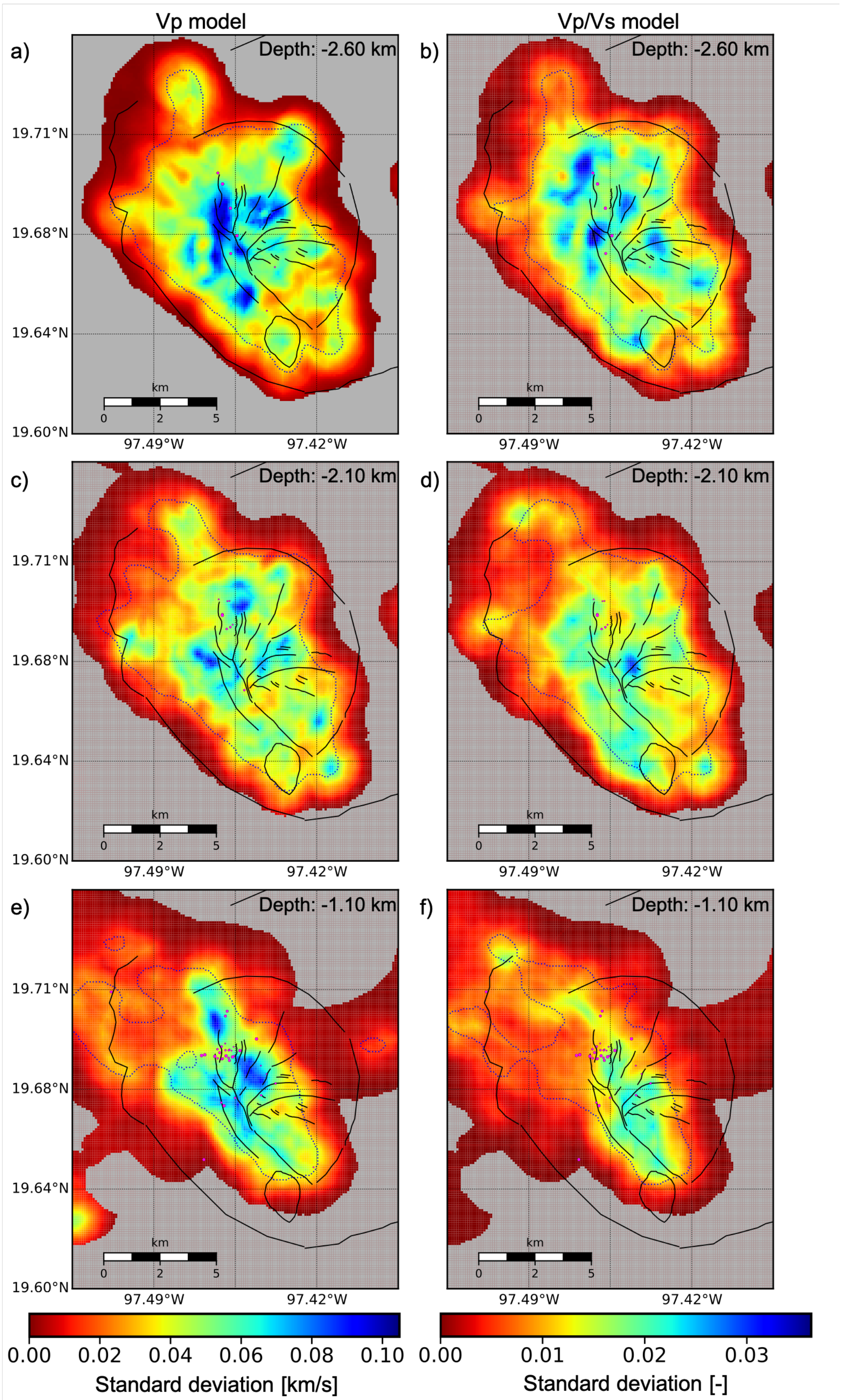

Figure 7.22: Standard deviation distribution at different depth levels associated with the averaged models. Panels a), c), and e) show three depth slices for the Vp model standard deviation distribution at -2.60 km, -2.10 km, and -1.10 km depth. Panels b), d), and f) show the depth slices for the Vp/Vs model standard deviation distribution at -2.60 km, -2.10 km, and -1.10 km depth. Pink circles mark the locations of earthquakes +/- 150 m away from the slice. Dashed blue lines indicate the boundary at which spread values are less than or equal to 1.5. Gray areas mark the regions where the DWS is less than or equal to 5.

8

Seismic interferometry for imaging and monitoring a geothermal field

This chapter consists in the application of seismic interferometry techniques to image and monitor a producing geothermal in NE Iceland.

Ambient seismic noise monitoring and imaging at the Theistareykir geothermal field (Iceland)

Tania Toledo, Anne Obermann, Philippe Jousset, Arie Verdel, Joana Martins, Kemal Erbas, Anette Mortensen, Charlotte Krawczyk

Article in *preparation* 2021.

From autumn 2017 to the present date, a network of 14 broadband seismic stations was deployed to improve the monitoring (previously with 7 short period sensors) of the high temperature Theistareykir geothermal field (NE Iceland). This experiment is conducted as part of the current efforts to characterize the main structures, and short and long term variations in the geothermal field due to the ongoing operations which started in autumn 2017/spring 2018. In this work, we use two years seismic records to compute the ambient noise tomography and to detect possible stress changes related to the injection and production activities. Cross correlations and auto correlations were computed from the vertical component of continuous noise records using a phase cross correlation approach. We measure the Rayleigh wave group velocity dispersion curves from the cross correlation functions to obtain 2D group velocity maps between 1 and 5 s. Subsequently, we use a neighborhood algorithm to retrieve the 3D shear wave velocity model of Theistareykir. Mainly, two sets of high and low elongated velocity anomalies are oriented in a NW/WNW direction, parallel to the lineaments of the active Tjörnes fracture zone. The velocity reductions west of Ketilfjall and at Baerjafjall could indicate the location of a magmatic reservoir or hydrothermal system. This hypothesis is supported by existing and newly acquired geological and geophysical data. We compute the temporal velocity changes of autocorrelations using coda wave interferometry and observe their behavior in relation to the geothermal field operations. We detect two possible velocity changes associated to drops in the injection rates. Additionally, we notice a small seismic velocity decrease of 0.05%/year in the reservoir compared to the outer regions (0.04%/year).

8.1 Introduction

Theistareykir is a high temperature geothermal field located in NE Iceland (Figure 8.1a). It is situated atop the Mid-Atlantic Ridge, at the divergent boundary between the North American and the Eurasian plates, a region rich in recent volcanism, seismicity, and geothermal activity. Presently, 17 deep wells (up to $\sim$ 2 km depth) have been drilled in the region with the hottest well registering temperatures exceeding 300°C at 1.1 km depth (*Khodayar et al.*, 2018). Since spring 2018, the geothermal power plant at Theistareykir generates 90 MW electric power and is administered by the national power company of Iceland (Landsvirkjun) (*Landsvirkjun*, 2016).

Several exploration and monitoring studies have been conducted since the late 70s to assess the geothermal field's energy production capabilities (*Ármannsson*, 2014; *Gautason et al.*, 2000). First gravity and aeromagnetic maps were reported by *Gíslason et al.* (1984). *Karlsdóttir et al.* (2012) performed a 3D inversion of MT and TEM data to obtain the field's resistivity structure and better locate the heat source. *Khodayar and Björnsson* (2013) used aerial photos to identify main fracture patterns. *Khodayar et al.* (2015, 2018) combined these results with geological mapping, surface alteration, gas geochemistry, and water geochemistry in a multidisciplinary analysis that defined the basis for the choice of drilling targets at Theistareykir (*Kristinsson et al.*, 2013a,b; *Óskarsson*, 2011; *Saemundsson*, 2007). Finally, *Blanck et al.* (2017a,b, 2018a) recorded and analyzed the local seismicity at Theistareykir using a seismic network of four stations.

The start of electric production at Theistareykir triggered new studies to improve its characterization and monitoring prior and during production. In the framework of the Microgravimotis project, a multiparameter network was installed to monitor the geothermal field starting in autumn 2017. A set of 27 time-lapse micro-gravity stations were measured at different time periods in 2017, 2018, and 2019 to analyze the field's mass distribution changes (*Portier et al.*, 2020). This data was complemented with 4 permanent superconducting gravity meter stations deployed at the injection and production areas (*Erbas et al.*, 2020). The permanent stations are equipped with GPS receivers, tiltmeters, and meteorological stations. Vertical displacements were obtained through an INSAR analysis by *Drouin* (2020). Finally, a set of 14 seismic broadband stations was deployed to support the permanent monitoring and to provide detailed insights on the seismicity, underground structure, and stress and deformation changes of the geothermal field. The present study expands on the seismicity study of *Naranjo* (2020) and *Ágústsson et al.* (2020) to investigate the seismic structure and temporal velocity changes at Theistareykir.

Local earthquake tomography (LET) is a technique commonly used to investigate deep structures in seismically active geothermal settings (e.g. *Calò and Dorbath*, 2013; *De Matteis et al.*, 2008; *Jousset et al.*, 2011; *Karastathis et al.*, 2011; *Muksin et al.*, 2013; *Toledo et al.*, 2020a). 3D compressional P- (Vp) and shear S- (Vs) wave velocity models are obtained using P- and S-wave arrival times from local earthquakes (*Kissling*, 1988; *Thurber*, 1983). Although LET provides reliable information of the subsurface, high resolution is limited to regions characterized by high seismicity rates and adequate ray coverage (homogeneous distribution of local earthquakes and seismic stations). This is a major limitation at Theistareykir, where the seismicity is mostly clustered at the producing geothermal field (*Blanck et al.*, 2018a; *Naranjo*, 2020).

Ambient noise tomography (ANT) is an alternative method that has rapidly gained popularity in geothermal exploration due to its increased resolution achieved by turning receivers into (virtual) sources (e.g. *Granados et al.*, 2020; *Lehujeur et al.*, 2017; *Martins et al.*, 2020a,b; *Planès et al.*, 2020). ANT is based on the reconstruction of Green's functions between different receiver pairs retrieved from the cross correlation of long duration ambient noise records (*Campillo and Paul*, 2003; *Wapenaar*, 2004; *Wapenaar and Fokkema*, 2006).

Noise-based methods have also been applied for monitoring geothermal systems. Small elastic and structural changes in the medium are detected by measuring the distortions of so called "coda" waves (*Sens-Schönfelder and Wegler*, 2006; *Snieder*, 2002). This technique is commonly known as coda wave interferometry (CWI). *Obermann et al.* (2015) used CWI to detect a likely gas infiltration in the St. Gallen geothermal site (Switzerland). Similarly, *Hillers et al.* (2015) detected structural changes due to a reservoir stimulation in Basel (Switzerland). *Taira et al.* (2018) measured the response of the Salton Sea geothermal field (California) to earthquakes and fluid extraction. Finally, *Sánchez-Pastor et al.* (2019) reported on short and long-term variations of the Reykjanes geothermal field (Iceland), due to injection and production activities.

In this study, we image the 3D Vs structure and assess the temporal velocity variations at the Theistareykir geothermal field using seismic interferometry. First, we report on the geological setting and the seismic network deployed at Theistareykir. We describe the data processing steps to retrieve the surface Rayleigh waves in part 2. Part 3 addresses the 3D ambient seismic noise Rayleigh wave tomography. We assess the time-lapse changes in velocity using CWI in part 4. Finally, part 5 discusses the obtained results in relation to existing and newly acquired geophysical and geological data.

8.2 Geologic setting and seismic network

8.2.1 Geologic and tectonic setting

The Mid-Atlantic Ridge (MAR) spreads at an average rate of 2 cm/year (*Einarsson*, 2008). In Iceland, the MAR consists of a series of active rift and transform segments that bring forth numerous high temperature areas with the potential for geothermal energy exploitation. Theistareykir is located at the intersection between the active Northern Rift Zone (NRZ) and the active Tjörnes Fracture Zone (TFZ) (Figure 8.1a).

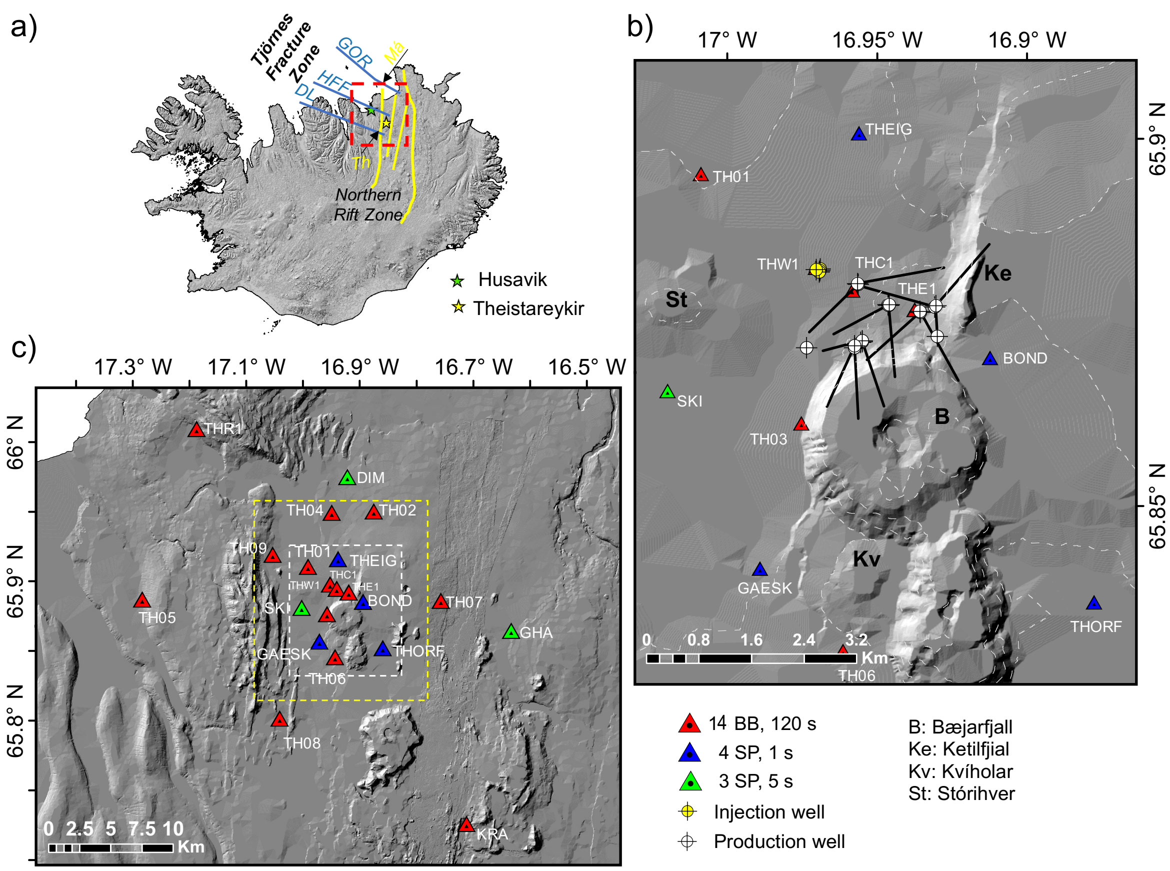

Figure 8.1: a) Map of Iceland and location of the Theistareykir geothermal field. The rift fissure swarms GOR (Grímsey Oblique-Rift), HFF (Húsavík-Flatey Fault), and DL (Dalvík Lineament) of the TFZ (Tjörnes Fracture Zone) are shown with blue lines. The fissure swarm Th (Theistareykir)/Má (Mánáreyjar) of the NRZ (Northern Rift Zone) is shown with a yellow line. b) Main exploitation area. The location of injection and production wells are marked with yellow and white circles, respectively. Approximate well deviations are shown as black lines. c) Temporary (red triangles) and permanent (blue and green triangles) seismic networks at the Theistareykir geothermal field. The location of panel b) is shown with white dashed lines. The yellow dashed lines indicate the region shown in Figure 8.7.

The NRZ comprises five N-S fissure swarms. Theistareykir/Mánáreyjar is the westernmost of them, with a roughly 9 km wide area and N-S extensional fractures that extend towards the sea (*Khodayar et al.*, 2018; *Saemundsson et al.*, 2012; *Thoroddsen*, 1983). The TFZ consists of three main WNW lineaments: the Grímsey Oblique Rift (GOR), the Húsavík-Flatey Fault (HFF), and the Dalvík Lineament (DL). It is characterized by dextral and dip slip-motions, and high seismicity rates (*Stefánsson et al.*, 2008). More specifically, our study area lies between the Theistareykir/Mánáreyjar Fissure Swarm, and the HFF and DL lineaments.

At the surface, Theistareykir is mostly covered by lava flows originated in the last stages of the Ice Age (*Saemundsson*, 2007). The bedrock is composed by hyaloclastites produced by sub-glacial eruptions, and basaltic interglacial and recent lava flows (younger than 10,000 years) (*Ármannsson et al.*, 1986). Neighboring the geothermal field, Ketilfjall is the oldest hyaloclastite formation (Figure 8.1b) and was formed during the eruption of a 4 km long fissure below the Quaternary ice-sheet. Further south, two younger table mountains (Baejarfjall and Kvíhólafjöll in Figure 8.1b) were formed by either eruptions on short fissures or single volcanic events. The surface geothermal activity is most intense to the north and northwestern slopes of Baejarfjall and from there northwards to the western part of Ketilfjall (*Ármannsson et al.*, 2000). A resistivity survey (*Karlsdóttir et al.*, 2012) suggests that the heat source and upflow zones of geothermal fluids are located below Ketilfjall, Bæjarfjall and north of Stórihver.

8.2.2 Seismic network

From September 2017 to the present date, a temporary seismic network comprising 14 three-component broadband (Trillium Compact 120s) sensors records continuous seismic data at a sampling rate of 200 Hz (red triangles in Figure 8.1b and Figure 8.1c). This network was primarily designed to monitor the local microseismicity associated with the exploitation of the geothermal field (*Toledo et al.*, 2020b). Two permanent seismic networks within the region bring an additional 4 three-component short period 3DLite MkII (1s) sensors (blue triangles in Figure 8.1b and Figure 8.1c) and 3 three component short period LE-3D 5s sensors (green triangles in Figure 8.1b and Figure 8.1c). These networks are operated by the Icelandic Geosurvey (ISOR) and Landsvirkjun, and the Icelandic Meteorological Office (IMO), respectively.

8.3 Data processing

In this study we analyze the continuous seismic records between September 2017 and October 2019 of the stations belonging to the temporary network (120s sensors) and to the ISOR/IMO permanent network (5s sensors). We cut the seismic traces of the vertical components into 2 hour long segments. Then, we downsample the traces to 5 Hz, apply a band-pass filter between 0.1-2.0 Hz, and remove the instrumental response using the MSNoise Python package (*Lecocq et al.*, 2014).

We compute the cross correlations and auto correlations using a phase cross correlation approach (PCC; *Schimmel*, 1999). The PCC functional is based on the coherence of instantaneous phases of analytical traces. Its main advantage over the classical cross-correlation scheme (*Bensen et al.*, 2007) is that it is amplitude unbiased and therefore does not require any preprocessing that could inflict waveform distortion (*Schimmel et al.*, 2011, 2018). This technique has successfully been used in other noise-based studies for imaging and monitoring (e.g. *D'Hour et al.*, 2015; *Sánchez-Pastor et al.*, 2018, 2019).

Finally, we stack the correlations linearly over a 2, 5, and 10 day sliding data window for monitoring structural changes in the media, and over their full recording period to compute the ambient noise tomography. In the latter case, we additionally average positive and negative lag-times to enhance the symmetric part of the signal and to increase the signal-to-noise ratio (SNR) (e.g. *Obermann et al.*, 2016).

8.4 Ambient noise tomography

8.4.1 Group velocity dispersion analysis

We perform a Frequency Time Analysis (FTAN, *Levshin et al.*, 1989) to extract the group velocity dispersion curves from the retrieved cross-correlation functions (CCFs). Then, we manually revise and pick the fundamental mode of the dispersion curves with inter-station distances larger than 1.5 wavelengths and SNR $\geq$ 10 (e.g. *Mordret et al.*, 2015; *Obermann et al.*, 2016; *Planès et al.*, 2020). Figure 8.2a shows the complete set of extracted group velocity dispersion curves. Notice the increment in group velocities with increasing periods for most dispersion curves. Based on the number of measurements per period (Figure 8.2b), we restrict our analysis to the range between 1 and 5 s.

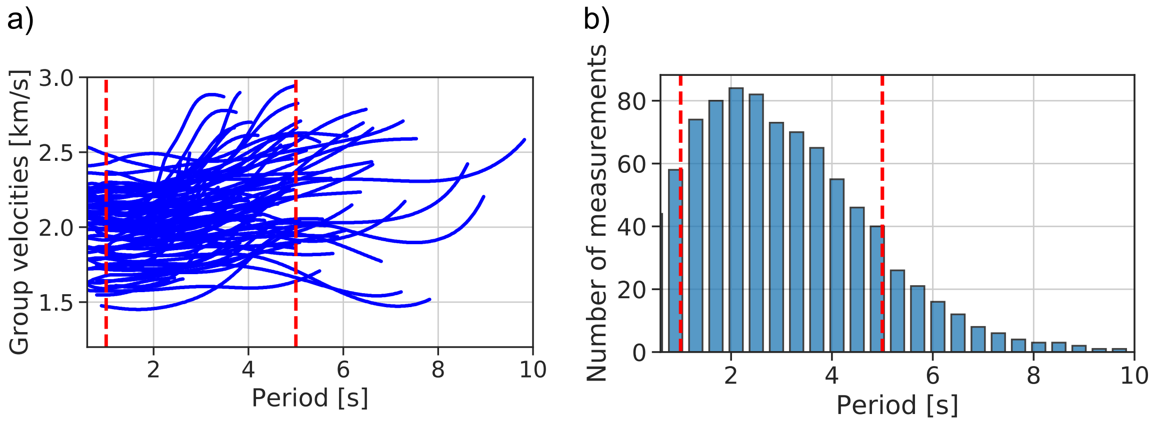

Figure 8.2: a) Full set of picked Rayleigh wave dispersion curves. b) Number of measurements per period. The vertical red lines indicate the limits of the measurements used in this study.

To assess the dataset distribution we display the raypath maps at two different periods (Figure 8.3a and Figure 8.3b). Note the increase in velocities with increasing period, especially to the west and to the south east of the geothermal field. We then discretize the study area into cells of $\sim$ 3.5 x 3.5 km. This value was chosen after exhaustive testing taking into account the raypath distribution and the resulting spatial resolution. Figure 8.3b and Figure 8.3d shows the ray path density (number of rays per cell) associated with the chosen grid discretization for 2 and 5 s. Notice the inhomogeneous ray density distribution for both periods due to the irregular seismic network configuration, originally deployed for recovering local seismicity. A higher ray density is observed towards the center of the geothermal field, where a higher number of closely spaced stations are located.

8.4.2 2D group velocity tomography

We perform 40 tomographic inversions for periods between 1 and 5 s (with 0.1 s step) following the methodology proposed by *Barmin et al.* (2001) and *Mordret et al.* (2013). The inversions are based on ray theory coupled with a damping constraint and a Gaussian-shaped lateral smoothing term. Group times for each period are calculated by integrating the group slowness along each ray path. We ignore the effects of the topography, assuming they are negligible on the retrieved traveltimes (e.g. *Mordret et al.*, 2015). A first inversion is computed for each period using the mean group velocity as the initial model. The aim is to reject measurements with time residuals larger than 0.01 standard deviations. The remaining travel times are then used in a second inversion using the obtained velocities of the previous step as the initial model. These results correspond to the final group velocities for each period.

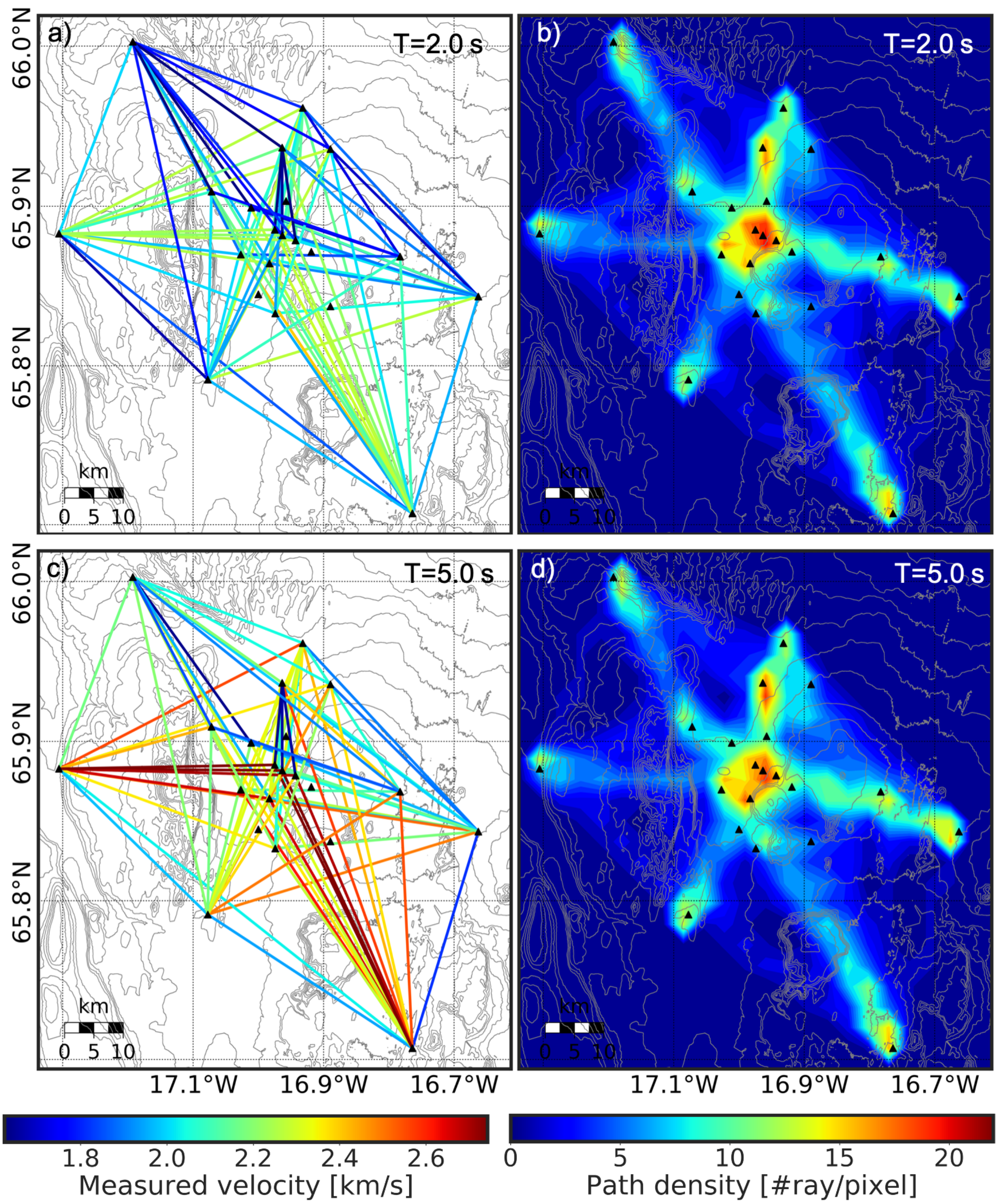

Figure 8.3: Raypath (a, c) and ray density (b, d) maps for periods of 2 and 5 s. Raypaths in a) and c) are colored with their associated measured group velocity. The chosen cell size is $\sim$ 3.5 x 3.5 km. Black triangles indicate the seismic stations positions and the gray lines correspond to topographic contours.

Figure 8.4a-d illustrate the obtained group velocities at periods of 2, 3, 4, and 5 s, respectively. Following the inversions, the variance is reduced $\sim$80 % for all periods. The group velocities increase with greater periods and range between 1.62 and 2.74 km/s. Two large elongated velocity anomalies stretch with a NW-SE direction. The high velocity anomaly is located to the west and to the southeast, and is discontinuous below the Baejarfjall table mountain. North to this anomaly, a low velocity anomaly crosses the Ketilfjal formation.

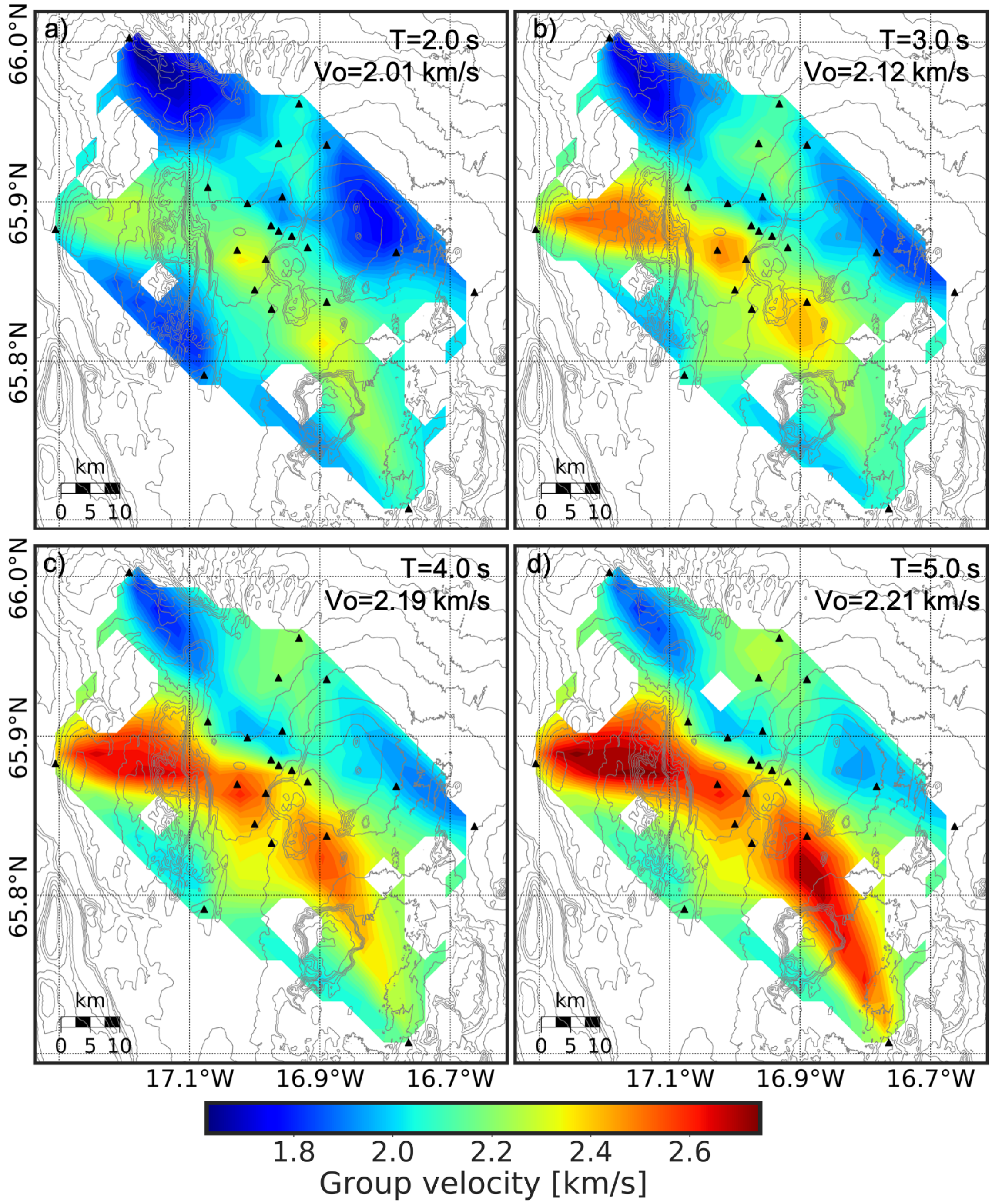

Figure 8.4: Rayleigh wave group velocity maps at a) 2, b) 3, c) 4, and d) 5 s. Initial velocities used in each inversion are shown in the upper right corner. Black triangles indicate the seismic stations positions and the gray lines correspond to topographic contours.

8.4.3 Model quality

To identify the location of poorly resolved areas we analyze the inversions associated model resolution matrices (MRM). The diagonal elements of the MRM provide an estimate of the inversion resolution. Off-diagonal elements contain information on the dependency of the solution of each cell with respect to neighboring cells.

As in *Mordret et al.* (2015), we define the spatial resolution as the equivalent diameter of a fitted ellipse to the contour level at 40 % of each row of the MRM. The minimal resolution value is estimated as twice the distance between two cells, in this case $\sim$ 7 km. Then the resolution shift is defined as the distance between the center of each ellipse and the target cell coordinate. The latter is an indicator of smearing. Figure 8.5a and Figure 8.5c show the calculated spatial resolution at 1.0 s and 5.0 s, respectively. The values range between 7 and $\geq$ 13 km, and is lower towards the main exploitation area, where the seismic array is denser. Similarly, Figure 8.5b and Figure 8.5d show the resolution shift for 1 and 5 s, respectively. Shift values are, once more, lower towards the center of the geothermal field. We display the contour level at 80 % (red lines in Figure 8.5a-d) for three rows of the MRM to observe the direction of the smearing associated to three cells (red crosses in Figure 8.5a-d). Seemingly, the contours at the center indicate a more focused solution, whereas the contours to the west indicate strong EW smearing product of a single ray direction (Figure 8.3a and Figure 8.3c). For the interpretation, we thus restrict our analysis to the center of the geothermal field.

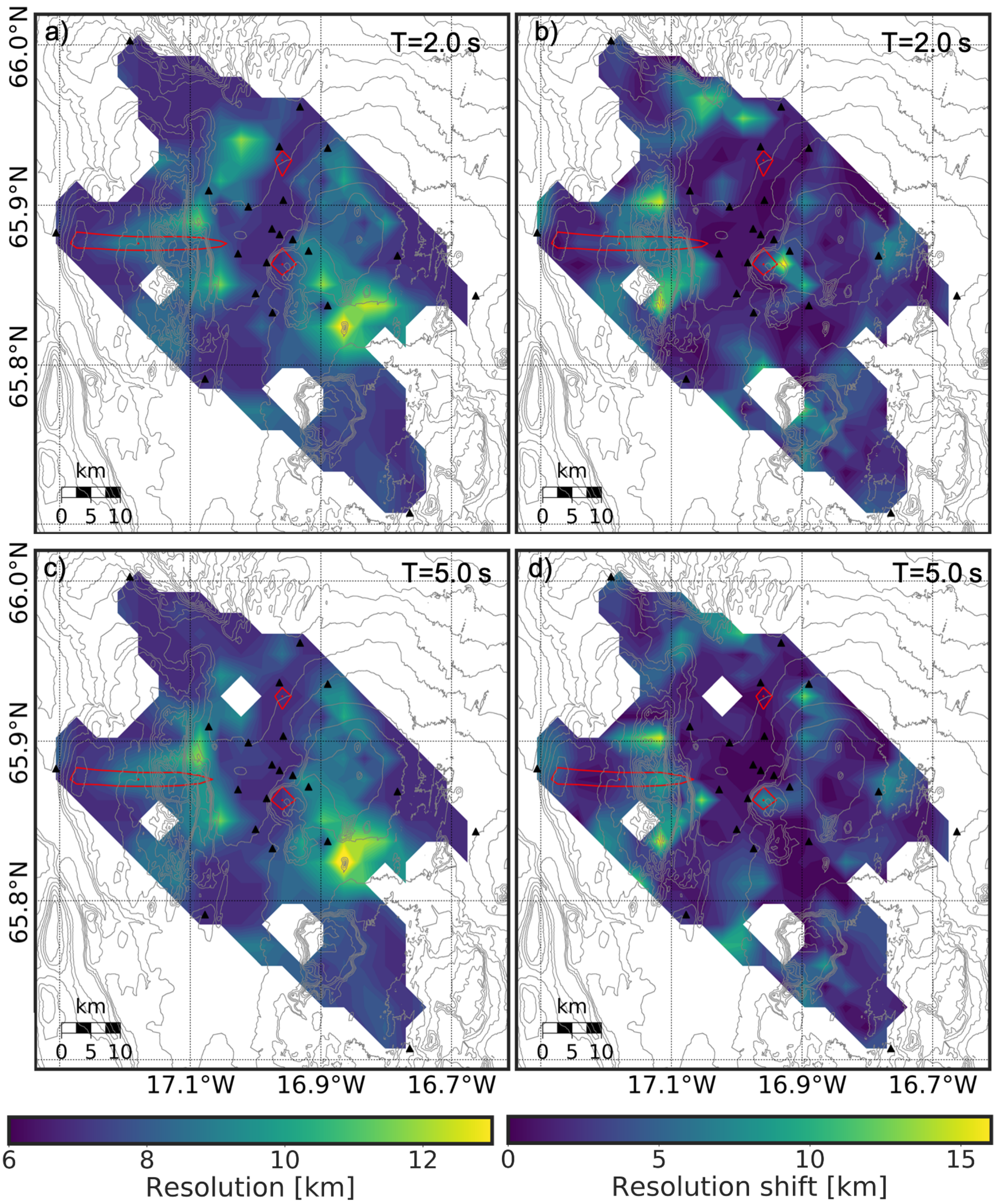

Figure 8.5: Spatial resolution (a, c) and resolution shift (b, d) at 2 and 5 s. The red lines indicate the 80 % contour levels of the MRM associated to three cells points (red crosses). Black triangles indicate the seismic stations positions and the gray lines correspond to topographic contours.

8.4.4 Retrieval of 3-D Vs model

We perform a second series of inversions to associate the 2D Rayleigh group velocity results to a precise depth. First, we construct local group velocity dispersion curves at all cell points by combining the tomographic inversions at different periods. Each of these dispersion curves are then inverted to obtain single 1D local layered velocity models which are later assembled into the final 3D S-wave velocity (Vs) model.

The 1D velocity profiles are obtained following a Monte Carlo inversion approach called the Neighborhood Algorithm (NA, *Sambridge*, 1999). For each cell, we first generate a large set (N_{ini}) of random continuous Vs functions that are later discretized into layered models of constant thicknesses and velocities. We define these functions as power law velocity profiles overlaid by three splines to reduce the number of inverting parameters (otherwise $2n_l$, where n_l is the number of layers) (*Mordret et al.*, 2014, 2015). The associated dispersion curves are then calculated using the Computer Programs in Seismology package (*Herrmann*, 2013). We evaluate the misfit between these synthetic models and the data dispersion curves. Later, we select the N_b best fitting models and randomly resample N_r new models in their neighborhood. This procedure is carried for N_{iter} iterations or until the misfit is reduced at a given threshold. In this work, we select $N_{ini} = 1000$, $\mathrm{N}_b = 750$, $N_r = 2$, and $N_{iter} = 20$, giving a total of 31,000 probed models. Figure 8.6a and Figure 8.6b display an example of the synthetic dispersion curves and the associated 1D Vs models, respectively, for the 1D inversion of a single grid point. The lines in these figures are colored according to the logarithm of their misfit. Figure 8.6c shows the recovered 1D Vs models for all the locations in the 2D plane. Up to ~ 2 km depth, the models show a good agreement with the 1D Vs model used in Iceland for earthquake locations (South Iceland Lowland -SIL- model, *Stefánsson et al.*, 1993).

In Figure 8.7a-f we present several depth slices of the retrieved 3D Vs model for the central part of the geothermal field (best resolution). Similar to the 2D group velocity maps, two main trends of anomalies are oriented in NW-SE direction. Two high velocity anomalies ($\sim$ +10 %) are located to the west and to the south of the Baejarfjall mountain, and become weaker at shallow and deeper levels ($\sim$ +6 %). An elongated low velocity anomaly is located to the northeast of Baejarfjall, and is slightly discontinuous at the Ketilfjal formation. The low velocity anomaly to the west of Ketilfjal becomes stronger with depth ($\sim$ -9 % at ≥ 2 km b.s.l.). North to this anomaly, another high velocity anomaly with smaller amplitude ($\sim$ +4 %) is visible mostly at shallow levels (≤ 2 km b.s.l.).

8.5 Determination of time-lapse changes

Seismic monitoring using CWI has been successfully implemented in various applications using techniques like the moving-window cross-spectra analysis (MWCS, *Ratdomopurbo and Poupinet*, 1995), the observation of waveform similarity evolution (*D'Hour et al.*, 2015), and the stretching technique (*Lobkis and Weaver*, 2003; *Sens-Schönfelder and Wegler*, 2006). A thorough comparison between the MWCS and the stretching method was performed by *Hadziioannou et al.* (2009) showing more stable results for the latter. In this work, we compute and analyze the velocity variations using the stretching technique on the auto correlations (AC)

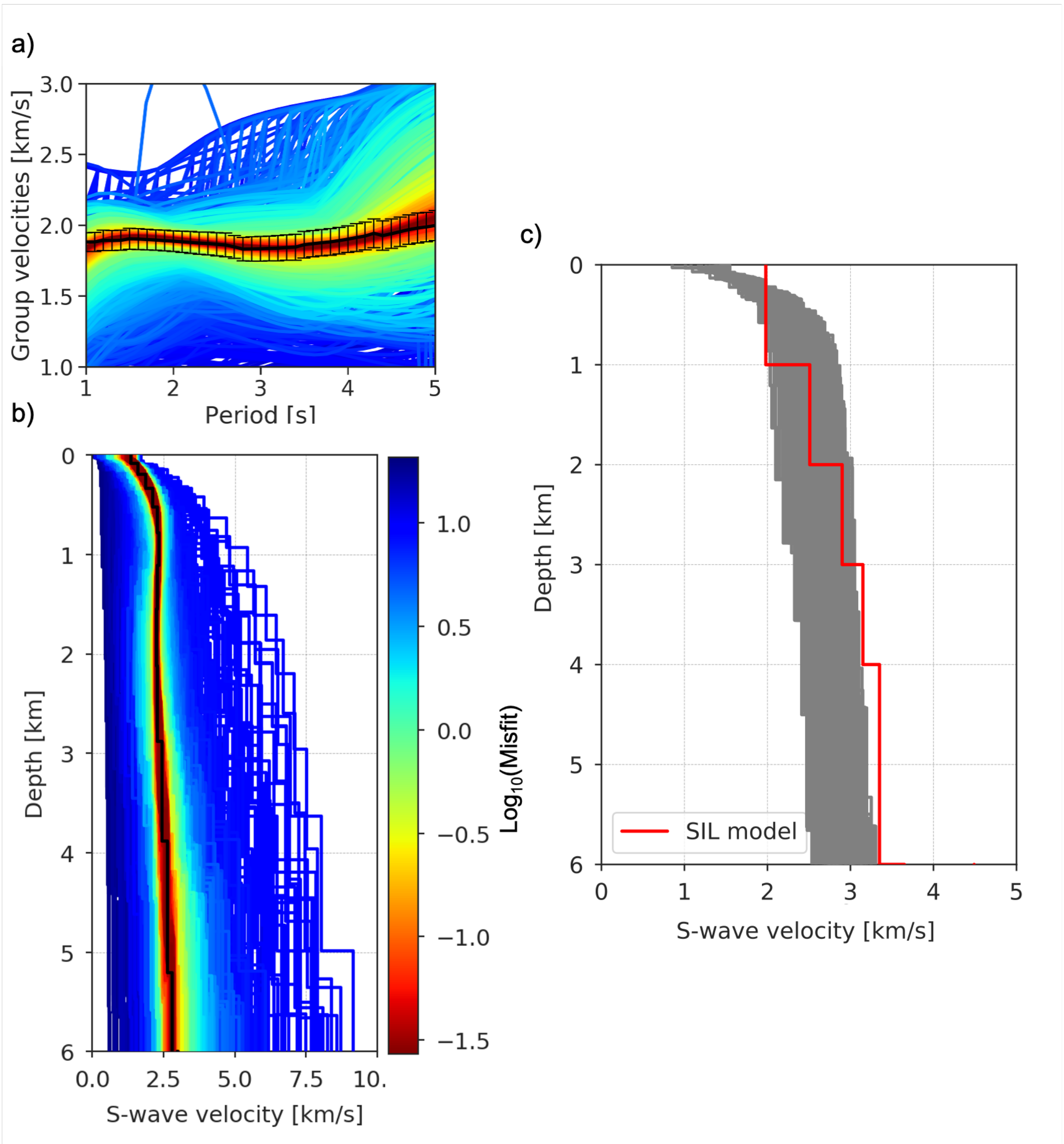

Figure 8.6: a) Example of synthetic local dispersion curves and b) their associated 1D Vs models. The local (data) dispersion curve is represented as a thick black line. Lines are colored according to their corresponding misfit. c) Best fitting 1D Vs profiles for each grid cell (gray lines). The 1D model that is routinely used for earthquake locations in Iceland (SIL model, *Stefánsson et al.*, 1993) is shown with a red line.

for a period of 2 years (October 2017 - October 2019). ACs are known to be more sensitive to local changes and to probe larger depths (*D'Hour et al.*, 2015; *Sánchez-Pastor et al.*, 2018).

8.5.1 Waveform stretching

To quantify the temporal evolution of seismic velocities, we analyze the waveform changes of "current" CCFs (φ^{curr}) with respect to a reference CCF (φ^{ref}). We define the φ^{ref} as the stacked daily CCFs over the entire recording period, and φ^{curr} as the daily stacked CCFs over a 2, 5, and 10 day sliding window. Each φ^{curr} is then stretched or compressed in time

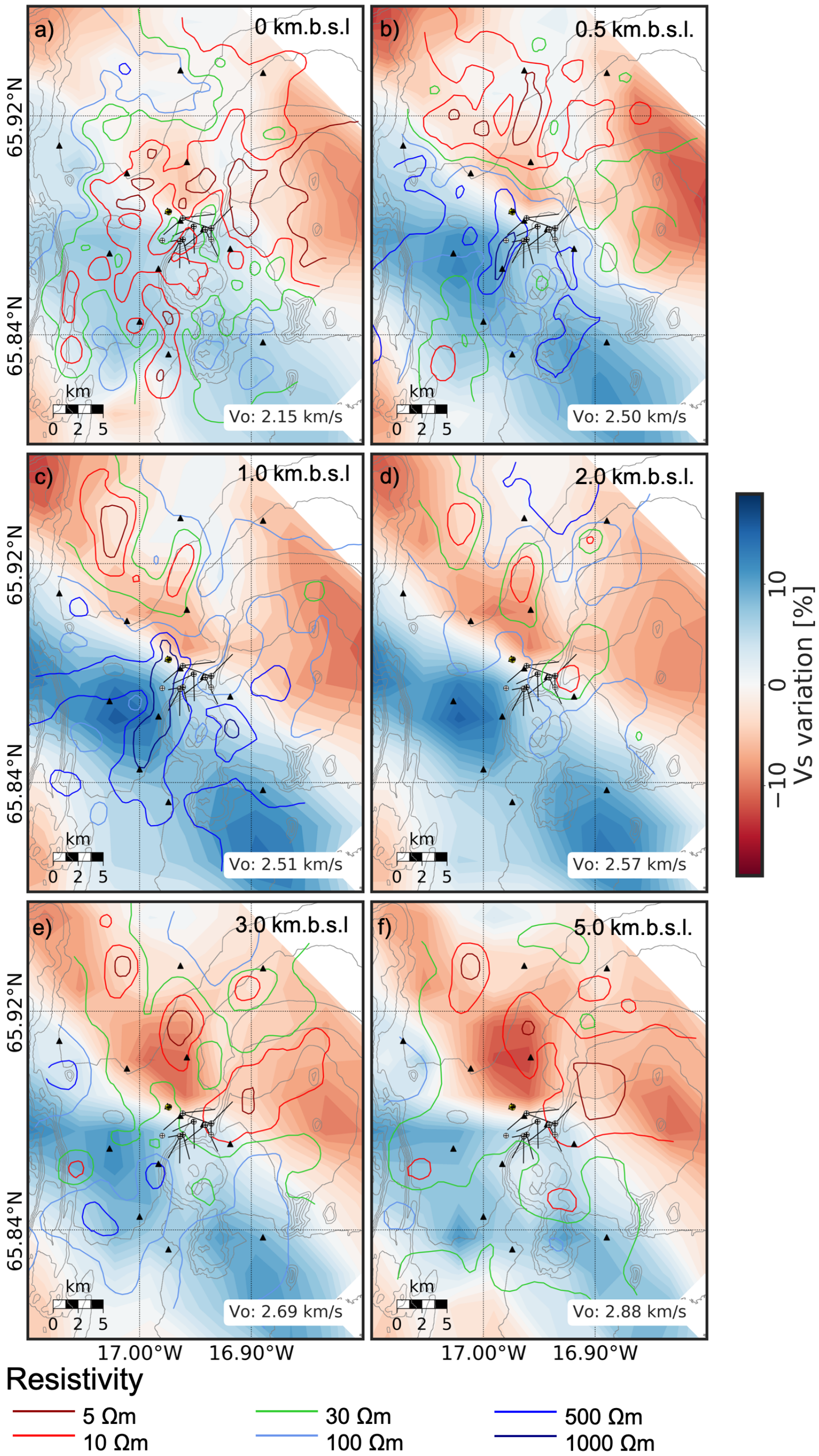

Figure 8.7: Vs depth slices. Resistivity contour lines are taken from *Karlsdóttir et al.* (2012). Black triangles indicate the seismic stations positions and the gray lines correspond to topographic contours. White circles represent the location of injection and production wells, and the approximate well deviations are shown with black lines. The location of these maps are shown with yellow dashed lines in Figure 8.1c.

by a factor $t(1+\epsilon)$ and compared to φ^{ref}. The stretching factor ϵ by which the correlation coefficient (CC) between φ^{ref} and φ^{curr} is maximized corresponds to the apparent velocity change ($\epsilon^{app} = -\frac{\Delta v}{v}$) (*Nakata et al.*, 2019; *Sens-Schönfelder and Wegler*, 2006).

Figure 8.8 displays the velocity variations computed on two ACs between 1 and 21 s lag time. The ACs are associated to a station close (SKI) and a station further away (TH05) from the injection/production site. Except for a few points, most CCs are $\sim$0.9, and the peak-to-peak velocity variations are $\sim$0.3 %. The most prominent feature in both cases is a sinusoid with period of $\sim$365 days, maxima in January 2018 and January 2019, and minima in August 2018 and August 2019. Additionally, similar short-term fluctuations at various lag times are visible in both curves which could be associated to a range of factors like weather and seismicity. Although both curves have similar shapes, the velocity changes for SKI-SKI has occasionally lower values than TH05-TH05.

We group the stretching results from ACs of stations inside (blue lines in Figure 8.9a-c) and outside (orange lines in Figure 8.9a-c) the region within Figure 8.1b to evaluate whether local changes exist due to the exploitation activities. We single out the results of the station closest to the injection site with red lines. Notice how the results are very stable for all ACs. Both the sinusoidal behavior and several short term fluctuations are similar in the three curves. However, it is evident that $\frac{\Delta v}{v}$ of locations within the exploitation area are, in many instances, lower than for those outside it. In fact, when fitting the average velocity changes of both groups to a linear function, we observe larger decreases in velocity for the curve associated to the producing geothermal field (Figure 8.9d).

We highlight three local perturbations (labeled as I, II, and III in Figure 8.9) accompanying two prominent changes in injection/production rates and one change in local seismicity rate (Figure 8.9e). Region I and III show a window where the injection was abruptly shut down for a few days. In III, the velocity variation curves show larger differences in amplitudes between the stations inside and outside the exploitation zone (mostly in Figure 8.9c). Region II indicates a time window leading to an increase of recorded seismicity below Baejarfjall (see change of slope of the pink line in Figure 8.9d).

In Figure 8.10, we remove the sinusoidal trend of the average velocity variations of the two station groups and compare their spectrograms. To remove the sinusoid feature, we first fit one of curves to a sine function *f(t)* of the form:

$$f(t) = A * \sin(\omega * t + \phi) + c \tag{8.1}$$

where A, ω, ϕ, and c correspond to the amplitude, angular frequency, phase, and offset, respectively. In this case we assume $\omega = 2 * \pi / T$, where the period (T) is 365 days. The corrected curves then correspond to difference between the original and the fitted *f(t)*.

Although the corrected curves (Figure 8.10b and Figure 8.10d) exhibit similar waveforms, their spectra (Figure 8.10a and Figure 8.10c) reveal several differences. In many instances, the spectrogram associated to the production site presents slightly higher amplitudes than the one associated to distant stations. Region III, for example, shows somewhat higher amplitudes for frequencies $\geq 10^{-1}$ days^{-1} for the curve neighboring the exploitation zone.

[1]

[1]Production rates are not complete and I am waiting for this data

8.6 Interpretation and discussion

8.6.1 Ambient noise tomography

The ambient noise tomography in Section 8.4 (Figure 8.7) shows a clear separation between high (N and NE) and low (S and SW) velocity anomalies trending with a NW/WNW orientation. This direction is almost parallel to the HFF lineament (Figure 8.1a), and follows the location of a series of fractures (narrow weak zones) with WNW and NW dextral oblique-slip mapped at the surface (*Khodayar et al.*, 2018). The boundary of the velocity anomaly separation is located a few kilometers to the north of the Baejarfjall mountain, where the injection and several production wells are located. This pattern is consistent at all depth levels, and matches the direction of several MT resistivity anomalies (colored line contours in Figure 8.7, taken from *Karlsdóttir et al.* (2012)) .

The low velocity anomalies (∼-7 %) to the N and NE coincide with the location of various low resistive bodies *Karlsdóttir et al.* (2012). One major low velocity anomaly to the north of Baejarfjall and west of Ketilfjall becomes stronger (∼-10 %) starting from ∼2 km b.s.l. (Figure 8.7d-f). Studies have shown that rocks saturated with hydrothermal fluids have typically lower shear wave velocities than those same unaltered rocks (*De Matteis et al.*, 2008; *Vanorio et al.*, 2005). In a lithologically homogenous subsurface, the decrease of Vs in this region could point to the location of either magmatic material or an upflow zone. Such a hypothesis is consistent with the MT survey, which highlights the heat source(s) beneath Ketilfjall, Bæjarfjall, and north of Stórihver below a shallow cap rock composed of zeolite/ smectite alterations (*Karlsdóttir et al.*, 2012). This region the north of Baejarfjall and west of Ketilfjall is also known to experience high decreases in microgravity variations (*Portier et al.*, 2020) and negative vertical displacements (*Drouin*, 2020) with time. In addition, surface geothermal manifestations (*Kristinsson et al.*, 2015) and emanating gases (*Gíslason et al.*, 1984) have been reported mostly at the northern and northwestern flank of Bæjarfjall.

The high velocity anomalies (∼+10 %) to the west and south/southwest of Bæjarfjall coincide with medium to high resistivity bodies (≥ 100 Ωm) at depths between 0.5-3 km b.s.l. Between these two anomalies, a lower high velocity anomaly (∼+5 %) sits below Bæjarfjall, which reduces its amplitude mostly at depths ≥3 km b.s.l. (∼+1 %). This reduction could, once more, hint to the presence of hot fluids at Bæjarfjall. Another weaker high velocity anomaly is located further to the north following, once more, some resistive bodies.

8.6.2 Time-lapse changes

To analyze possible structural changes we monitor the differences between the ACs at different times with respect to a reference. In a geothermal context, some of these velocity variations have been successfully linked to the operation activities (*Obermann et al.*, 2015; *Sánchez-Pastor et al.*, 2019). Figure 8.9a-c shows the velocity variations associated to the ACs of all stations computed with the stretching technique. The results are colored according to their distance with respect to the injection and production wells (red and blue lines for stations close to the geothermal field, and orange lines for distant stations). Several short term fluctuations are consistent among all the curves, however, most of them are difficult to directly associate to natural or man-made processes.

We distinguish two regions (I and III) where there is an abrupt change of injection volume in Figure 8.9a-c. Region I shows a large $\frac{\Delta v}{v}$ fluctuation for both station groups which coincides with a significant injection drop and rise. The curves in region III not only show changes in $\frac{\Delta v}{v}$, they reveal some clear differences between the two station groups. We average the velocity changes of both station groups, remove their sinusoid trend, and display their spectrogram in Figure 8.10. Higher amplitudes at frequencies $\geq 10^{-1}$ days $^{-1}$ are visible for the curve associated to the operations site. This confirms the likelihood of this fluctuation to be associated to the field's operations. For the remaining time period, the injection and production changes are too low for their effect to be seen in the $\frac{\Delta v}{v}$ short term fluctuations.

A third region (marked as II), is a special case where we observe distinct velocity variations (drop then rise) prior to the increase of local seismicity. During this period, the injection rates were doubled for the first time, leading to the increase of induced seismicity (abrupt change in the earthquake frequency slope in Figure 8.9d) to the northwest of Baejarfjall (*Naranjo*, 2020). Such short precursor behavior is observed in similar studies (*Obermann et al.*, 2013, 2015).

Long term noise studies typically exhibit seasonal variations (e.g. *Sánchez-Pastor et al.*, 2019; *Sens-Schönfelder and Wegler*, 2006) which are evident in the distortion of the ballistic waves (e.g. *Hadziioannou et al.*, 2011). These variations are mostly the consequence of changes in the oceans noise sources at different seasons (*Stutzmann et al.*, 2009). In this study, the seasonal variation appears as a sinusoidal trend which is evident for the $\frac{\Delta v}{v}$ curves of all station positions (Figure 8.9a-c). We average the velocity variation curves for the two station groups and compute their linear regression to distinguish the difference between their long term variations (Figure 8.9d). There is a slow velocity decrease for both station groups. However this reduction is stronger for the production area (0.05%/year vs 0.04%/year). Such a local decrease in velocities is consistent with the negative microgravity variations reported in the production zone (*Portier et al.*, 2020). Additionally, (*Drouin*, 2020) reports a subsidence in this region of $\sim$ 7 mm/year since the start of the operations in 2017.

8.7 Conclusions

Upon the deployment of a temporary seismic network at the Theistareykir geothermal field, we collected and analyze the ambient noise records for the period of 2 years. We compute a 3D ambient noise Rayleigh wave tomography and compare the results with available geophysical, geochemical, and geological data. We could identify velocity anomalies oriented in a NW/WNW direction almost following the orientation of the HFF lineament. This observation is consistent with the direction of reported resistivity anomalies at Theistareykir (*Karlsdóttir et al.*, 2012).

A clear division between high and low velocity anomalies follows the location of weak active fractures with dextral oblique-slip (*Khodayar et al.*, 2018). We observe a velocity reduction in two anomalies: one to the west of Ketilfjall (depths $\geq$ 2 km b.s.l.) and one at Baejarfjall (depths $\geq$ 3 km b.s.l.). We interpret these regions as locations of possible magmatic or hydrothermal bodies. Such hypothesis is consistent with geophysical and geochemical data (*Gíslason et al.*, 1984; *Karlsdóttir et al.*, 2012; *Kristinsson et al.*, 2015). In addition, the low velocity anomaly to the west of Ketilfjall roughly coincides with the region of high decreases in residual micro-gravity variations (*Portier et al.*, 2020) and negative vertical displacement (*Drouin*, 2020).

We compute the temporal velocity changes for the 2 year period using CWI and compare the results associated to the stations close and far from the geothermal field. Several short term fluctuations are inconsistent with the injection and production variations, and could be associated with several other medium instabilities. Alternatively, various injection and production changes may be too low for their effect to be seen in the $\frac{\Delta v}{v}$ short term fluctuations. Furthermore, we report on a slow velocity decrease (0.05%) within the geothermal system, possibly associated to a deficit of water in this region.

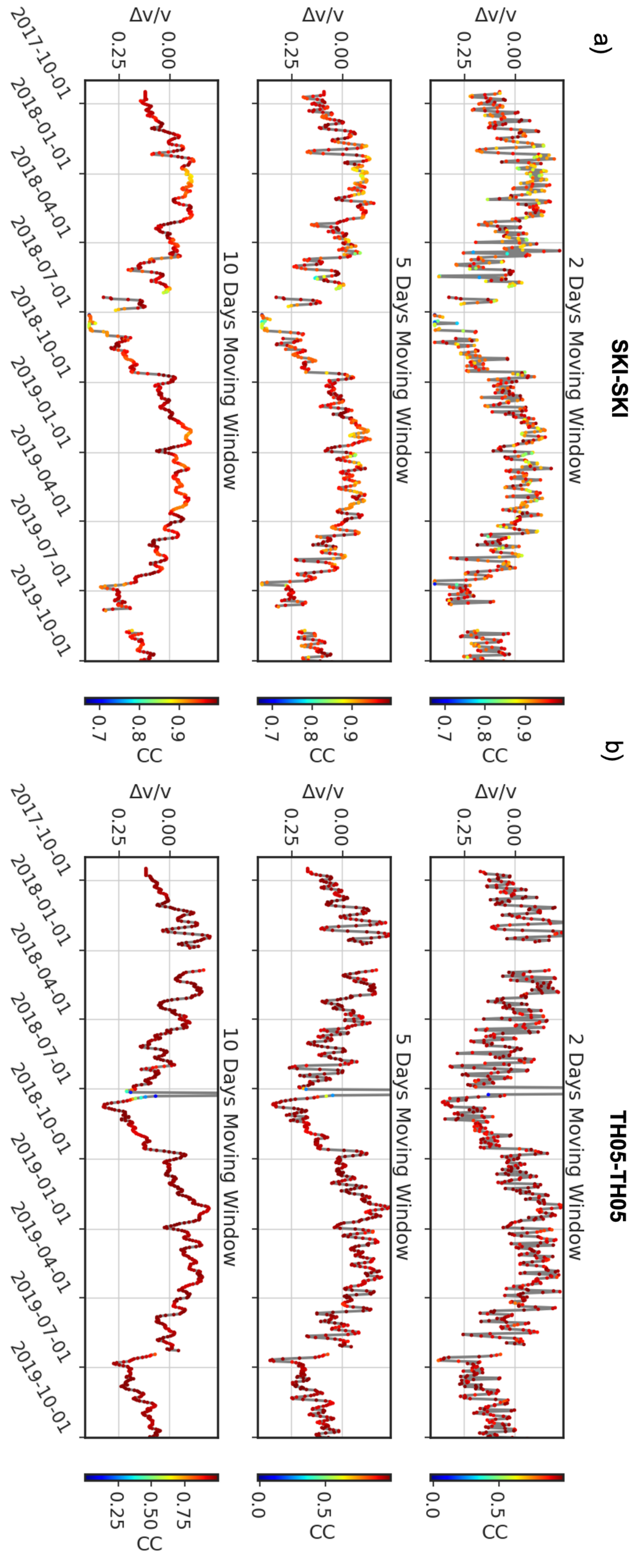

Figure 8.8: Velocity changes computed with the stretching technique for the ACs of stations a) SKI and b) TH05. The color scale represents the associated CC. Results for 2, 5, and 10 day stacks are shown in the upper, middle, and lower panels, respectively.

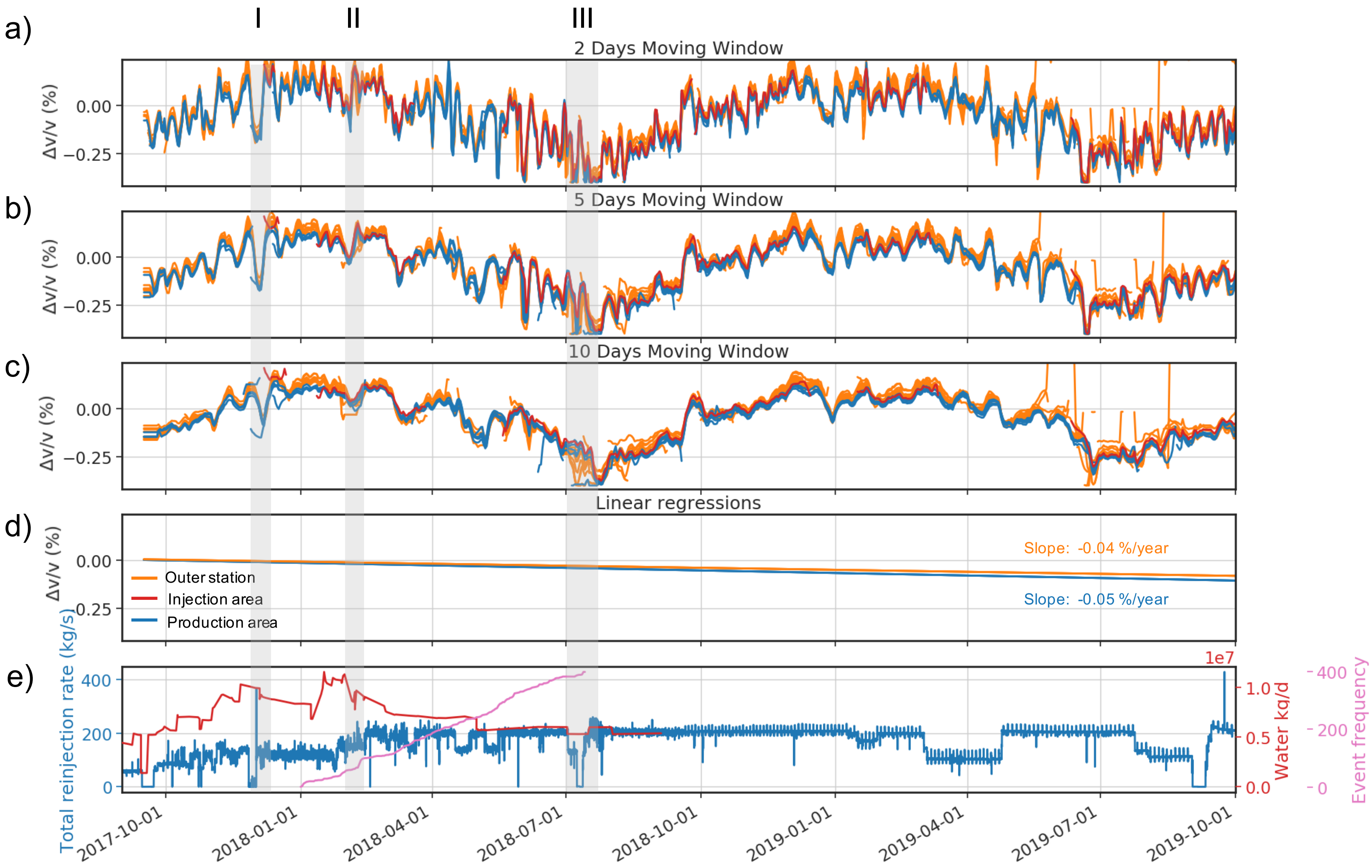

Figure 8.9: Velocity changes computed for all available ACs. Results for a) 2, b) 5, and c) 10 day stacks times. Line colors represent three station groups: station neighboring the injection site (red), stations close to the production sites (blue, located within 8.1c), stations far from the exploitation zone (orange). We discarded $\frac{\Delta v}{v}$ values with CC ≤ 0.35. d) Linear regressions of the velocity variation averages for stations inside and outside the exploitation area. e) Total production (red) and injection (blue) rates at the geothermal field, and local seismicity rates (pink) from the 1 January 2018 to 15 July 2018 (taken from *Naranjo* (2020)). The gray boxes highlight the fluctuations I, II, and III. See main text for more details.

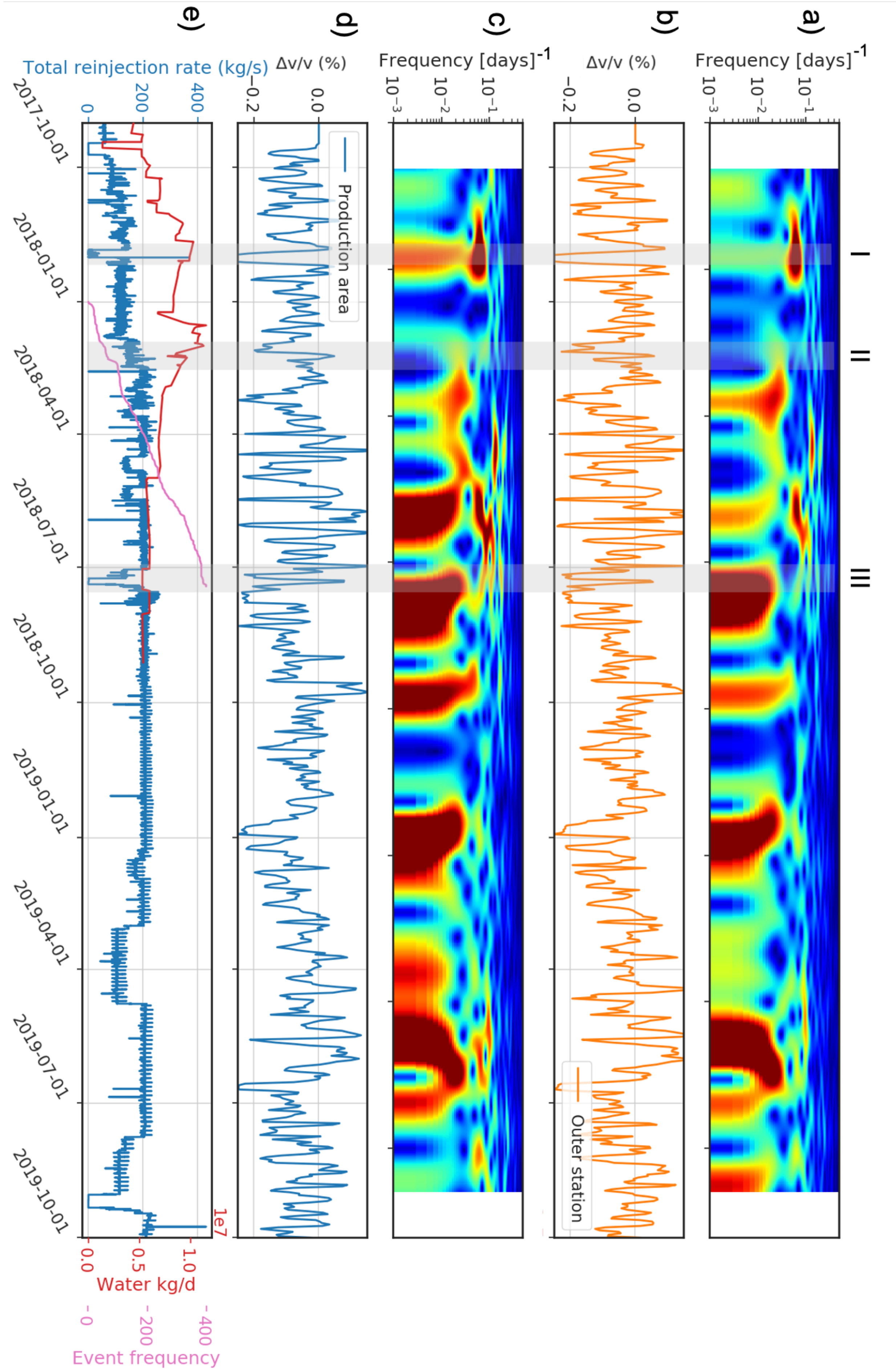

Figure 8.10: (a, c) Spectrograms and (b, d) velocity variation averages (2-day stack window) for stations inside and outside the exploitation area (within 8.1c). The sinusoidal trend has been removed for both curves. e) Total production (red) and injection (blue) rates at the geothermal field, and local seismicity rates (pink) from 1 January 2018 to 15 July 2018 (taken from *Naranjo* (2020)). The gray boxes highlight the fluctuations I, II, and III. See main text for more details.

Part III

Discussions and Conclusions

9

Discussions of results

This thesis evaluates, extends, and applies survey design theory for microseismic monitoring, passive seismic imaging, and coda wave interferometry for the exploration and monitoring of three geothermal fields: Los Humeros (Mexico), Theistareykir (Iceland), and Reykjanes (Iceland). Although specific to these fields, the results are discussed in this chapter in consideration to future geothermal studies. Furthermore, a comprehensive analysis of the advantages and disadvantages of the methods is presented, as well as a comparison with other similar studies.

9.1 Optimized experimental network design for microseismicity location and monitoring

The exploitation of geothermal resources often results in stress changes that give way to induced/triggered seismicity (*Evans et al.*, 2012). When the magnitudes are large enough, this seismicity can pose risks for the continuation of the exploitation activities (e.g. Basel, Switzerland; St. Gallen, Switzerland; Pohang, South Korea in *Deichmann and Giardini*, 2009; *Diehl et al.*, 2017; *Grigoli et al.*, 2018, respectively), hence the need for permanent seismic monitoring.

High quality microseismic event retrieval and locations can be achieved with optimal seismic network geometries. In some cases, these geometries are fixed depending on the seismic tool choice. More often, however, the design follows a heuristic strategy with few azimuthal and/or distance guidelines (e.g. azimuthal GAP $\leq 180°$ and average inter-station distances in the order of expected hypocentral depths). The first approach is limited by field and/or instrumentation restrictions. The second strategy can lead to difficulties in evaluating prior error estimates and risks missing necessary data to resolve a target parameter. Although one could argue the use of a large number of sensors, in practice, geothermal experiments are highly constrained by budget.

In Chapter 6 (*Toledo et al.*, 2020b) a destructive sequential survey design (DSSD) algorithm (with quality measure based on the *D-criterion*) was developed for constructing new optimized networks and for qualifying existing ones. The studied scheme was based on well-established survey design concepts, that although have been applied for a broad range of applications (e.g. *Coles and Curtis*, 2011a; *Kraft et al.*, 2013; *Maurer and Boerner*, 1998; *Nuber et al.*, 2017), they had yet to be applied in a geothermal exploration context. The selected algorithm was simple and fast to compute and was successfully used to extend (Theistareykir) and to qualify (Reykjanes) two seismic networks.

9.1.1 Survey design experiments at Reykjanes and Theistareykir (Iceland)

After defining candidate station locations and building a synthetic earthquake catalog that takes into account the region's seismic history, the Theistareykir network was augmented from 12 to 23 sensors. We estimated that for earthquakes located within the network and with mean picking errors of t_p =0.2 s and t_s =0.4 s, there was an improvement of $\sim$ 0.2 km for all estimated hypocentral components using the augmented array. The picking errors were overestimated in the computations, therefore, better results should be expected in practice.

The algorithm was later applied to the deployed Reykjanes network, this time using the existing station positions as candidate station locations. Doing so, we obtained an order of station importance. By analyzing both the station order and the resulting benefit/cost curve, we observed that, although the placement of OBS stations around the Reykjanes peninsula was necessary for the experiment, approximately 18 stations could be spared and still obtain earthquake location estimates with comparable errors. Such observations are essential for project budget management hinting the importance of survey design experiments prior to deployment. In addition, these experiments can be used to identify stations that could be removed or relocated if necessary during a project.

9.1.2 General considerations for survey design experiments

Several considerations are necessary prior to a survey design experiment. These include the selection of a quality measure and an optimization scheme. The selected choices are discussed in the following sections, where their advantages and disadvantages are addressed. In addition, the aspect of detectability is discussed to improve the definition of candidate station positions. Finally, a few outlooks for future studies are outlined.

9.1.2.1 Quality measure choice

In the previous case studies we used a quality measure (Θ) based on the *D-criterion*. One main advantage of the selected measure (Eq. 3.5) is its sensitivity to the entire eingenvalue spectrum of matrix $\mathbf{G}^T\mathbf{G}$. In addition by minimizing function Θ, one would in some sense also minimize the confidence volumes of all the studies seismic events. Another advantage is its weighting factor term. This term can be modified to favor more interesting event targets at a geothermal field (e.g. events close to injection and production wells).

One main drawback of the selected quality metric is station clustering. This effect is the result of Θ ignoring model error correlations. In our work we interpreted station clustering as regions of higher importance, however, this clustering can be alleviated by introducing an interstation weight (*Hardt and Scherbaum*, 1994).

Eq. 3.5 is a linearized quality metric. Another approach for a more robust assessment is the application of fully nonlinearized quality measures such as the one used in *Guest and Curtis* (2009). However, the latter would be more costly to compute.

9.1.2.2 Optimization choice

One main advantage of sequential optimizations is the analysis of benefit/cost curves, which is important for geothermal exploration planning. In addition, these schemes are flexible and relatively fast to compute. They can be quickly modified to take into account possible changes of station positions due to field constraints.

A major disadvantage of sequential optimizations is it does not guarantee global optimality. However, they do provide good solutions to design temporal networks. A better approach is the use of global search algorithms and/or non-linear experimental design. Although, they require higher computational costs, they are strongly recommended especially for permanent networks.

9.1.2.3 Detectability

An important aspect to be considered prior to a survey design experiment is the analysis of the varying noise conditions throughout a target field (SNR studies). Such exercise allows a better constraint on the candidate station location areas, and avoids placing stations in noisy sites (where the target microseismic signals are masked in the background noise).

We considered the noise levels to be homogeneous throughout the analyzed geothermal fields. A better approach, however, is proposed by *Kraft et al.* (2013) where they estimated noise levels by correlating them with land use to expand the permanent seismic network in Switzerland.

9.1.2.4 Outlooks

The applications for survey design techniques are multifold. A possible new exercise is the extension of the algorithm to build networks dedicated for local earthquake tomographies (assuming there is an adequate earthquake distribution at a region), or better yet for an ambient noise tomography (where the seismicity distribution is not necessary). These exercises will depend, however, on the research objectives of the network.

9.2 Passive seismic imaging for the exploration of geothermal fields

A vital aspect for geothermal exploration is seismic imaging. This can be achieved, among others, by means of a local earthquake tomography (LET) or an ambient noise tomography (ANT). These are the techniques applied at Los Humeros geothermal field in Mexico (Chapter 7) and at Theistareykir in Iceland (Chapter 8), respectively.

9.2.1 Local earthquake tomography at Los Humeros geothermal field

A passive seismic network comprising 45 stations was deployed and maintained at Los Humeros for the period of one year (*Toledo et al.*, 2019). We collected high quality earthquake data (488 events) to compute the 3D Vp and Vp/Vs models (333 events) for the first time at this field (*Toledo et al.*, 2020a).

Aside from the classical earthquake tomography approach (Chapter 4), we applied a post-processing scheme where 228 models were inverted and averaged to enhance the spatial resolution of the final models. This approach has the advantage of obtaining a much finer final resolution, thus overcoming the limits of a coarse grid used by the SIMUL2000 code. In addition, the post-processing approach reduces the potential smearing that can be introduced by model parametrization choices that favor preferential velocity anomaly and/or ray directions (*Calò*, 2009). A similar post-processing approach in a geothermal context was performed at Soultz-sous-Fôrets in France (*Calò and Dorbath*, 2013), where instead of a simple averaging they computed a weighted average of several models with respect to the ray density values (DWS).

The quality of the 3D final models was assessed by analyzing the model resolution matrix (diagonal elements and spread function) and by computing a checkerboard test (Section 7.4.3). Nodes with high diagonal elements and low spread values are considered to be well resolved (Section 2.4.3). With this information and the computed synthetic tests we defined as well resolved the region within the inner Los Potreros Caldera and up to $\sim$ 2.5 km depth for Vp and up to $\sim$ 2.0 km depth for Vp/Vs. Tomography quality assessments are important to define regions where meaningful interpretations can be obtained.

9.2.2 Joint interpretation at Los Humeros geothermal field

Seismicity distribution

Retrieved seismic events are excellent tools to potentially delineate structures, reservoir boundaries, and preferential fluid pathways (e.g. *Muksin et al.*, 2013; *Philips et al.*, 2002).

From the recorded seismicity at Los Humeros we identified three seismogenic areas, two of which are possibly associated to the exploitation activities. A third deeper cluster was located between Las Papas and Las Viboras faults. These faults showed no hydrothermal alterations at the surface (*Norini et al.*, 2019), however, the presence of the seismicity could indicate a permeability enhancement at deeper levels in this region. Such observations are important for future drilling and development of a geothermal field.

Vp model

We combined the retrieved Vp model with well log interpretations (*Norini et al.*, 2019) and new petrophysical data (ultrasonic pulse measurements of collected rock samples in *Bär and Weydt*, 2019) to estimate possible geological unit boundaries. This exercise is important for defining the geometry of, for example, the reservoir unit which is necessary for the future development of a geothermal field.

Vp/Vs model

We used our Vp/Vs model in combination with a newly acquired resistivity model (*Benediktsdóttir et al.*, 2019) to identify the location and geometry of the conductive clay cap above the reservoir (Vp/Vs $\leq$ 1.65 and resistivities $\leq$ 10 Ωm). In addition, we interpreted the areas with lowest Vp/Vs values (Vp/Vs $\leq$ 1.55 and Vp reduction) as gas bearing regions. This interpretation was supported by the high CO_2 emissions at the surface in these areas (*Jentsch et al.*, 2020).

Finally we interpreted the zones with high Vp/Vs values ($\geq$ 1.71), Vp reduction, and resistivities between $\sim$ 10-60 Ωm as possible fluid bearing zones. These areas can potentially be considered for further exploration and exploitation of the geothermal field.

General remarks on Los Humeros geothermal field

We could identify an important intrusion in the Vp model located at the main production site. We combined this intrusion, the neighboring subvertically aligned earthquakes, and the high Vp/Vs anomalies (higher fluid content) on both sides of the seismicity to interpret hot fluids being transported upwards along deep reaching permeable faults. Such behavior is called resurgence, and consists of shallow magma emplacements (several local heat source(s)) from a deeper magma chamber. Such hypothesis is consistent with new analog, structural, and petrological studies in the area (*Lucci et al.*, 2020; *Norini et al.*, 2019; *Urbani et al.*, 2020).

9.2.3 Ambient noise tomography at the Theistareykir geothermal field

In seismically quiet areas or in regions with uneven ray path distributions (from the earthquake-station geometries), a LET may not be feasible to retrieve the seismic structure of a geothermal field. In these cases, the use of ambient noise techniques are powerful to image the subsurface. In Chapter 8, we successfully computed the 3D ambient noise Rayleigh wave tomography of Theistareykir following the methodology described in Part I (Section 5.3.2).

The quality of the retrieved velocity maps was assessed by analyzing their associated model resolution matrices. We defined the spatial resolution as the equivalent diameter of a fitted ellipse to the 40 % contour level of each row in the matrix, and the resolution shift as the distance between the center of this ellipse with its associated cell coordinate (to indicate smearing). We defined as well resolved the region at the center of the geothermal field, where the seismic array is denser (resolution 7-9 km).

Resolution values are directly related to the network geometry (inter-station rays) and can be improved by adding more sensors to the field. However, it is advisable to perform synthetic or survey design experiments beforehand to estimate optimal locations for improving the tomography.

9.2.4 Joint interpretation at the Theistareykir geothermal field

From the derived 3D Vs model we observed a division between high and low velocity anomalies following the orientation of the HFF lineament (belonging to the Tjörnes Fracture Zone). This geometry was consistent with the direction of the region's resistivity anomalies as shown in

Karlsdóttir et al. (2012) and with a series of fractures (WNW and NW dextral oblique-slip) mapped at the surface in *Khodayar et al.* (2018).

Slight Vs reductions were visible in two anomalies starting at $\sim$ 2 km b.s.l. and $\sim$ 3 km b.s.l.: one west of Ketilfjall and the other below Baejarfjall, respectively, indicating the location of rocks possibly saturated with fluids. In a lithologically homogeneous subsurface, these regions could correspond to locations of magmatic and/or hydrothermal bodies. Such interpretation is consistent with resistivity and geochemical data of the region (*Gíslason et al.*, 1984; *Karlsdóttir et al.*, 2012; *Kristinsson et al.*, 2015).

In addition, the locations of these velocity anomalies coincide with the main production area and with regions of higher decreases in micro-gravity variations (*Portier et al.*, 2020) and negative vertical displacement (*Drouin*, 2020). The latter properties could imply a depletion in these zones.

9.2.5 Advantages and disadvantages of the methods

LET and ANT are powerful tools for geothermal exploration. Both methods provide the seismic structure and, to some extent, information of additional rock properties such as fluid content.

One advantage of LET is the additional structural information derived from the seismicity distribution. Furthermore, the study of the focal mechanisms can help understand the stress field of a geothermal reservoir, which is important for drilling, resource assessment, and resource management. Another follow-up study of LET is the computation of an attenuation tomography. Seismic attenuation is more sensitive to rock properties such as pore, crack, fracture, and fluid content than solely the Vp and Vp/Vs structures. Therefore, its computation is highly recommended in geothermal contexts.

One main advantage of ANT over LET is the increased extensions of the obtained models, which can be managed to a certain extent with the network geometry. In addition, ANT is independent of the earthquake distribution of a target zone and does not require the extended recording periods needed for LET. Given that these two techniques work at different frequency ranges, their recovered information is highly complementary. Therefore, whenever possible, it is strongly recommended the computation and analysis of both.

One interesting ongoing field of research is the computation of body wave tomographies using the ambient noise field retrieved from very dense seismic arrays. This technique does not require extended recording periods and have not yet been tested in a geothermal context.

9.2.6 Multi-parameter interpretations

We performed a joint interpretation at both Los Humeros and Theistareykir geothermal fields by combining their seismic parameters with additional geophysical, geological, and geochemical data. We observed that such approach avoids ambiguities, provides robust interpretations regarding the structure and dynamics of a geothermal field, and helps building their conceptual models.

A more quantitative approach, however, is the cluster analysis of the different physical parameters. A pattern recognition technique was, for example, employed by *Muksin et al.* (2013) to quantitatively delineate fluid and gas bearing regions from the computed Vp and

Vp/Vs models at the Tarutung geothermal area (Indonesia). Similarly, a k-means cluster analysis technique was applied to three geophysical parameters (resistivity, Vp, and density) at the geothermally active Solfatara-Pisciarelli area of the Campi Flegrei caldera (Italy) to identify differences in local rock rheologies and locate the brittle-to-ductile transition (*Di Giuseppe et al.*, 2018).

9.3 Coda wave interferometry for monitoring geothermal fields

9.3.1 The Theistareykir case study

Changes in the coda waves (obtained from the auto- or cross-correlations of ambient noise records) are the result of structural changes in the medium. We computed the temporal velocity changes with the stretching technique (CWI) using two years ambient noise records at Theistareykir (Chapter 8). We compared the obtained $\Delta v/v$ with injection and production rates to evaluate the effects of the exploitation activities on the geothermal reservoir.

Although we could identify slight variations in the short term $\Delta v/v$ fluctuations after two injection cuts, typically the injection/production variations were too small for their effect to be seen in the $\Delta v/v$ curves. We could, however, observe a slightly higher long term velocity decrease within the production area (-0.05 %/year), as opposed to the surrounding regions (-0.04 %/year). This observation was consistent with decreases in micro-gravity variations (*Portier et al.*, 2020) and negative vertical displacement (*Drouin*, 2020) reported at the production zone and could therefore indicate a slow mass depletion in this area (subsidence).

Overall, the small effects of the exploitation activities in the medium changes could favor an open system behavior. Fluids may migrate from and out the system without over or under pressuring it significantly (large $\Delta v/v$ changes) at the present injection and production rates. This information is important for safe long-term continuation of operations at a geothermal field.

9.3.2 Importance of coda wave interferometry for monitoring geothermal operations

From the Theistareykir case study we observed no significant velocity changes due to variations in injection and production rates. Other geothermal studies, however, had different experiences. *Obermann et al.* (2015), for example, reported significant losses in the waveform coherence of coda waves obtained in St. Gallen (Switzerland) 4 days prior to a gas kick which also resulted in large earthquake (M_L 3.5). Another CWI study at Reykjanes (*Sánchez-Pastor et al.*, 2019) showed prominent medium changes due to sharp variations of water injection volume and energy production. With their observations they could estimate a production rate threshold above which the elastic properties of the medium change significantly.

Overall, monitoring the changes of coda waves can be useful for observing aseismic processes prior to potentially large triggered/induced seismic events and would be complementary to microseismic monitoring. In addition, this technique helps to better understand the reservoir dynamics and mitigate the associated risks of geothermal operations.

10

Conclusions

From the gained experience, this chapter gathers a set of conclusions and recommendations for the exploration and monitoring of future geothermal targets.

First, the application of survey design algorithms are useful for designing, extending, and qualifying seismic arrays. Heuristic approaches (e.g. designs with few azimuthal and/or distance guidelines) can become costly to a seismic experiment while resulting in no meaningful reduction of hypocentral errors. Using survey design techniques like the one we apply in this work (destructive sequential suvery design with quality measure based on the *D-criterion*) can ultimately help optimize the expenses (number of seismic stations) dedicated for a geothermal project and obtain comparable results (location errors of target events) at the same time.

Two powerful techniques for characterizing geothermal reservoirs are local earthquake tomography and ambient noise tomography. The first technique relies on high seismicity rates and a good earthquake/station distribution, while the second depends only on a good and sufficiently dense station distribution.

While seismicity locations help identify structures and permeability enhancements of faults, Vp models in combination with well and petrophysical data can indicate geologic unit boundaries. Using a Vp/Vs model together with resistivity and geochemical data, for instance, can enable the geometry identification of conductive clay caps (low Vp/Vs and low resistivity). Changes of Vp/Vs (or Vs) can potentially hint to variations in the fluid content of rocks to detect fluid-rich areas (Vp reduction, high Vp/Vs, and intermediate resistivity; or Vs reduction and intermediate resistivity) and gas filled regions (very low Vp/Vs and high surface CO_2 concentrations). Ultimately, joint interpretations will help avoid ambiguities and to better understand the structures and behavior of a geothermal system. This approach is, therefore, highly recommended for future exploration studies.

Changes in the coda waves are the result of structural changes in a medium. Velocity decreases in combination with decreases in micro-gravity variations and negative vertical displacements will help point at regions of subsidence due to slow mass depletion (from the extracted water). Short-term velocity changes due to variations in injection and production rates are useful for the safe exploitation of a geothermal field. Although not yet a standard practice, it is strongly advisable to continuously monitor the changes in the coda waves along with the seismicity monitoring. This practice allows for the observation and control of aseismic processes prior to stress drops that could result in large earthquake generation and helps to understand better the reservoir dynamics.

References

Abers, G. A., and S. W. Roecker (1991), Deep structure of an arc-continent collision: earthquake relocation and inversion for upper mantle P and S wave velocities beneath Papua New Guinea, *Journal of Geophysical Research: Solid Earth*, *96*, 6379–6401.

Ágústsson, K., H. Blanck, A. K. Mortensen, and A. Guðmundsson (2020), The Seismic Network of Landsvirkjun/Iceland GeoSurvey in Krafla, NE-Iceland, and Some Results, *Proceedings World Geothermal Congress, paper 13059.*

Aki, K. (1957), Space and time spectra of stationary stochastic waves, with special reference to microtremors, *Bulletin of the Earthquake Research Institute*, *24*, 415–457.

Aki, K., and P. Richards (1980), Quantitative seismology: Theory and methods, *WH Freeman & Co.*

Anthony, R. E., R. C. Aster, D. Wiens, A. Nyblade, S. Anandakrishnan, A. Huerta, J. P. Winberry, T. Wilson, and C. Rowe (2014), The seismic noise environment of Antarctica, *Seismological Research Letters*, *86*(1), 89–100.

Ardhuin, F., L. Gualtieri, , and E. Stutzmann (2015), How ocean waves rock the Earth: two mechanisms explain seismic noise with periods 3 to 300 s, *Geophysical Research Letters*, *42*, 764–772.

Arellano, V. M., A. Garcia, R. Barragan, A. Izquierdo, G.and Aragon, and D. Nieva (2003), An updated conceptual model of the Los Humeros geothermal reservoir (Mexico), *Journal of Volcanology and Geothermal Research*, *124*, 67–88.

Ármannsson, H. (2008), The Theistareykir geothermal system, northeast Iceland. Case History, *Presented at Short Course III on exploration for Geothermal Resources.*

Ármannsson, H. (2014), The Theistareykir geothermal system, northeast Iceland. Case History, *Presented at Short Course IX on exploration for Geothermal Resources.*

Ármannsson, H., G. Gíslason, and H. Torfason (1986), Surface exploration of the Theistareykir high-temperature geothermal area, with special reference to the application of geochemical methods, *Applied Geochemistry*, *1*, 47–64.

Ármannsson, H., H. Kristmannsdóttir, H. Torfason, and M. Ólafsson (2000), Natural changes in unexploited high-temperature geothermal areas in Iceland., *Proceedings World Geothermal Congress 2000, Kyushu, Tohoku, 28 May-10 June*, pp. 521–526.

Arzate, J., F. Corbo, G. Carrasco-Núñez, J. Hernández, and V. Yutsis (2018), The Los Humeros (Mexico) geothermal field model deduced from new geophysical and geological data., *Geothermics*, *71*, 200–211.

Baig, A. M., M. Campillo, and F. Brenguier (2009), Denoising seismic noise cross correlations, *Journal of Geophysical Research: Solid Earth*, *114*, doi:10.1029/2008JB006085.

Bär, K., and L. Weydt (2019), Comprehensive report on the rock and fluid samples and their physical properties in the Acoculco and Los Humeros regions, *Deliverable 6.1 of GEMex project.*

Barmin, M., M. Ritzwoller, and A. Levshin (2001), A fast and reliable method for surface wave tomography, *Pure and Applied Geophysics*, *158*, 1351–1375, doi:10.1007/PL00001225.

Benediktsdóttir, A., G. P. Hersir, A. M. Vilhjálmsson, A. Manzella, A. Santillano, and S. Held (2019), Report on resistivity modelling and comparison with other SHGS, *Deliverable 5.2 of GEMex Project.*

Bensen, G. D., M. H. Ritzwoller, M. P. Barmin, A. L. Levshin, F. Lin, M. P. Moschetti, N. M. Shapiro, and Y. Yang (2007), Processing seismic ambient noise data to obtain reliable broad-band surface wave dispersion measurements, *Geophysical Journal International*, *169*(3), 1239–1260, doi:10.1111/j.1365-246X.2007.03374.x.

Bensen, G. D., M. H. Ritzwoller, and N. M. Shapiro (2008), Broadband ambient noise surface wave tomography across the United States, *Journal of Geophysical Research: Solid Earth*, *113*, B05,306, doi: 10.1029/2007JB005248.

Beyreuther, M., R. Barsch, L. Krischer, T. Megies, Y. Behr, and J. Wassermann (2010), ObsPy: A Python Toolbox for Seismology, *SRL*, *81*(3), 530–533.

Bijwaard, H., W. Spakman, and R. E. Engdahl (1998), Closing the gap between regional and global traveltime tomography, *Journal of Geophysical Research: Solid Earth*, *103*, 30 055–30 078.

Billings, S., M. Sambridge, and B. Kennett (1994), Errors in hypocenter location: picking, model, and magnitude dependence, *Bulletin of the Seismological Society of America*, *84*(6), 1978–1990.

Bjarnason, I. T., W. Menke, O. G. Flóvenz, and D. Caress (1993), Tomographic image of the Mid-Atlantic Plate Boundary in southwestern Iceland, *Journal of Geophysical Research: Solid Earth*, *98*, 6607–6622.

Blanck, H., K. Ágústsson, and K. Gunnarsson (2017a), Seismic monitoring in Theistareykir, Krafla and Námafjall: November 2016 to March 2017, *Landsvirkjun Report*, *LV-2017-046.*

Blanck, H., K. Ágústsson, and K. Gunnarsson (2017b), Seismic monitoring in Krafla and Námafjall, and Theistareykir: April to August 2017, *Landsvirkjun Report*, *LV-2017-086.*

Blanck, H., K. Ágústsson, and K. Gunnarsson (2018a), Seismic monitoring in Krafla and Námafjall, and Theistareykir: November 2017 to November 2018, *Landsvirkjun Report*, *LV-2018-103.*

Blanck, H., P. Jousset, G. P. Hersir, K. Ágústsson, and O. G. Flóvenz (2018b), Analysis of seismological data on Reykjanes Peninsula, SW-Iceland, *Journal of Volcanology and Geothermal Research.*

Bommer, J. J., S. Oates, J. M. Cepeda, C. Lindholm, J. Bird, R. Torres, G. Marroquín, and J. Rivas (2006), Control of hazard due to seismicity induced by a hot fractured rock geothermal project, *Engineering Geology*, *83*(4), 287–306, doi:10.1016/j.enggeo.2005.11.002.

Bormann, P. (1998), Conversion and comparability of data presentations on seismic background noise, *Journal of Seismology*, *2*, 37–45.

Bormann, P., B. Engdahl, and R. Kind (2012), Seismic Wave Propagation and Earth models, in *New Manual of Seismological Observatory Practice 2 (NMSOP-2), Potsdam: Deutsches GeoForschungsZentrum GFZ*, pp. 1–105, doi:10.2312/GFZ.NMSOP-2_ch2.

Boué, P., P. Roux, M. Campillo, and X. Briand (2014), Phase velocity tomography of surface waves using ambient noise cross correlation and array processing, *Journal of Geophysical Research: Solid Earth*, *119*, 519–529.

Bourouis, S., and P. Bernard (2007), Evidence for coupled seismic and aseismic fault slip during water injection in the geothermal site of Soultz (France), and implications for seismogenic transients, *Geophysical Journal International*, *169*, 723–732.

Brenguier, F., M. Campillo, C. Hadziioannou, N. M. Shapiro, R. M. Nadeau, and E. Larose (2008a), Postseismic relaxation along the San Andreas fault at Parkfield from continuous seismological observations, *Science*, *321*(5895), 1478–1481, doi:10.1126/science.1160943.

Brenguier, F., N. M. Shapiro, M. Campillo, V. Ferrazzini, Z. Duputel, O. Coutant, and A. Nercessian (2008b), Towards forecasting volcanic eruptions using seismic noise, *Nature Geoscience*, *1*(2), 126–130, doi:10.1038/ngeo104.

Bromirski, P., and P. Gerstopft (2009), Dominant source regions of the Earth's "hum" are coastal, *Geophysical Research Letters*, *36*(13).

Brune, J. B. (1970), Tectonic stress and spectra of seismic shear waves from earthquakes, *Journal of Geophysical Research*, *75*(26), 4997–5009.

Brune, J. B. (1971), Correction to "Tectonic stress and spectra of seismic shear waves from earthquakes", *Journal of Geophysical Research*, *75*(20), 5002.

Buland, R. (1976), The mechanics of locating earthquakes, *Bulletin of the Seismological Society of America*, *66*(1), 173–187.

Calcagno, P., G. Evanno, E. Trumpy, L. Gutiérrez-Negrín, J. Macías, G. Carrasco-Núñez, and D. Liotta (2018), Preliminary 3-D geological models of Los Humeros and Acoculco geothermal fields (Mexico) – H2020 GEMex Project, *Advances in Geosciences*, *45*, 321–333.

Calò, M. (2009), Tomography of subduction zones using regional earthquakes: methodological developments and application to the Ionian slab., *Geophysics [physics.geo-ph]. Université de Strasbourg.*

Calò, M., and C. Dorbath (2013), Different behaviours of the seismic velocity field at Soultz-sous-Forêts revealed by 4D seismic tomography: case study of GPK3 and GPK2 injection tests, *Geophysical Journal International*, *194*(2), 1119–1137, doi:10.1093/gji/ggt153.

Calò, M., L. Parisi, and D. Luzio (2013), Lithospheric P- and S-wave velocity models of the Sicilian area using WAM tomography: Procedure and assessments, *Geophysical Journal International*, *195*, 625–649, doi:10.1093/gji/ggt252.

Campillo, M., and A. Paul (2003), Long-range correlations in the diffuse seismic coda, *Science*, *299*(5606), 547–549.

Campillo, M., H. Sato, N. M. Shapiro, and R. D. van der Hilst (2011), New developments on imaging and monitoring with seismic noise, *Comptes Rendus Géoscience, Elsevier Masson*, *343*(8-9), 487–495.

Carrasco-Núñez, G., and M. J. Branney (2005), Progressive assembly of a massive layer of ignimbrite with normal-to-reverse compositional zoning: the Zaragoza ignimbrite of central Mexico, *Bulletin of Volcanology*, *68*, 3–20.

Carrasco-Núñez, G., M. McCurry, M. Branney, M. Norry, and C. Willcox (2012), Complex magma mixing, mingling, and withdrawal associated with an intraplinian ignimbrite eruption at a large silicic caldera volcano: Los Humeros of central Mexico, *Geological Society of America Bulletin*, *124*, 1793–1809.

Carrasco-Núñez, G., J. Hernández, L. De León, P. Dávila, G. Norini, J. P. Bernal, B. Jicha, M. Navarro, and P. López (2017a), Geologic Map of Los Humeros volcanic complex and geothermal field, eastern Trans-Mexican Volcanic Belt, *Terra digitalis*, *1*, 1–11.

Carrasco-Núñez, G., M. López-Martínez, J. Hernández, and V. Vargas (2017b), Subsurface stratigraphy and its correlation with the surficial geology at Los Humeros geothermal field, eastern Trans-Mexican Volcanic Belt, *Geothermics*, *67*, 1–17.

Carrasco-Núñez, G., J. P. Bernal, P. Dávila, B. Jicha, G. Giordano, and J. Hernández (2018), Reappraisal of Los Humeros volcanic complex by new U/Th zircon and 40Ar/39Ar dating: Implications for greater geothermal potential, *Geochemistry, Geophysics, Geosystems*, *19*, 132–149.

Cedillo-Rodríguez, F. (1997), Geología del subsuelo del campo geotérmico de Los Humeros, Pue., *Internal Report HU/RE/03/97. Comisión Federal de Electricidad, Gerencia de Proyectos Geotermoeléctricos, Residencia Los Humeros, Puebla*, p. 30.

Cedillo-Rodríguez, F. (1999), Modelo hidrogeológico de los yacimientos geotérmicos de Los Humeros, Puebla, México, *Geotermia Revista Mexicana de Geoenergía*, *15*, 159–170.

Cesca, S., and F. Grigoli (2015), Full waveform seismological advances for microseismic monitoring, *Advances in Geophysics*, *56*.

Chaloner, K., and I. Verdinelli (1995), Bayesian experimental design: A review, *Statistical Science*, *10*(3), 273–304.

Claerbout, J. F. (1968), Synthesis of a layered medium from its acoustic transmission response, *Geophysics*, *33*(2), 264–269.

Coles, D., and A. Curtis (2011a), Efficient nonlinear Bayesian survey design using D_N optimization, *Geophysics*, *76*(2), Q1–Q8.

Coles, D., and A. Curtis (2011b), A free lunch in linearized experimental design?, *Computers and Geosciences*.

Cuenot, N., C. Dorbath, and L. Dorbath (2008), Analysis of the microseismicity induced by fluid injections at the EGS Site of Soultz-sous-Forêts (Alsace, France): Implications for the characterization of the geothermal reservoir properties, *Pure and Applied Geophysics*, *165*, 797–828.

Cupillard, P., L. Stehly, and B. Romanowicz (2011), The one-bit noise correlation: a theory based on the concepts of coherent and incoherent noise, *Geophysical Journal International*, *184*, 1397–1414.

Curtis, A. (1999a), Optimal design of focused experiments and surveys, *Geophysics Journal International*, *139*(1), 205–2015.

Curtis, A. (1999b), Optimal experiment design: Cross-borehole tomographic examples, *Geophysics Journal International*, *136*, 637–650.

Curtis, A. (2004), Theory of model-based geophysical survey and experimental design. part a—linear problems, *The Leading Edge*, *23*, 997–1004.

Curtis, A., and D. Halliday (2010), Directional balancing for seismic and general wavefield interferometry, *Geophysics*, *75*, doi:10.1190/1.3298736.

Curtis, A., A. Michelini, D. Leslie, and A. Lomax (2004), A deterministic algorithm for experimental design applied to tomographic and microseismic monitoring surveys, *Geophysical Journal International*, *157*, 595–606.

De Matteis, R., T. Vanorio, A. Zollo, S. Ciuffi, A. Fiordelisi, and E. Spinelli (2008), Three-dimensional tomography and rock properties of the Larderello-Travale geothermal area, Italy, *Physics of the Earth and Planetary Interiors*, *168*(1), 37–48.

Deichmann, N., and D. Giardini (2009), Earthquakes Induced by the Stimulation of an Enhanced Geothermal System below Basel (Switzerland), *Seismological Research Letters*, *80*(5), 784–798, doi:10.1785/gssrl.80.5.784.

Derode, A., E. Larose, M. Campillo, and M. Fink (2003a), How to estimate the Green's function of a heterogeneous medium between two passive sensors? Application to acoustic waves, *Applied Physics Letters*, *83*, 3054.

Derode, A., E. Larose, M. Tanter, J. de Rosny, A. Tourin, M. Campillo, and M. Fink (2003b), Recovering the Green's function from field-field correlations in an open scattering medium (L), *The Journal of the Acoustical Society of America*, *113*, 2973.

D'Hour, V., M. Schimmel, A. F. Do Nascimento, J. M. Ferreira, and H. C. Lima Neto (2015), Detection of subtle hydromechanical medium changes caused by a small-magnitude earthquake swarm in NE Brazil, *Pure and Applied Geophysics*, *173*(4), 1097–1113, doi:https://doi.org/10.1007/s00024-015-1156-0.

Di Giuseppe, M., A. Troiano, D. Patella, M. Piochi, and S. Carlino (2018), A geophysical k-means cluster analysis of the Solfatara-Pisciarelli volcano-geothermal system, Campi Flegrei (Naples, Italy), *Journal of Applied Geophysics*, *156*, 44–54, doi:10.1016/j.jappgeo.2017.06.001.

Díaz, J. (2016), On the origin of the signals observed across the seismic spectrum, *Earth Science Reviews*, *161*, 224–232.

Diehl, T., T. Kraft, E. Kissling, and S. Wiemer (2017), The induced earthquake sequence related to the St. Gallen deep geothermal project (Switzerland): Fault reactivation and fluid interactions imaged by microseismicity, *Journal of Geophysical Research: Solid Earth*, *122*(9), 7272–7290, doi:10.1002/2017JB014473.

Drouin, V. (2020), InSAR Monitoring of Krafla, Bjarnarflag and Þeistareykir Geothermal Areas, *Landsvirkjun Report*, *LV-2020-038*.

Dyer, B. C., U. Schanz, and T. Spillman (2008), Microseismic imaging of a geothermal reservoir stimulation, *The Leading Edge*, *27*(7).

Ebeling, C., and S. Stein (2011), Seismological identification and characterization of a large hurricane, *Bulletin of the seismological society of America*, *101*(1), 399–403.

Eberhart-Phillips, D. (1990), Three-dimensional P and S velocity structure in the Coalinga region, California, *Journal of Geophysical Research*, *95*(B10), 15,343–15,363.

Eberhart-Phillips, D. (1993), Local earthquake tomography: earthquake source regions, *Seismic Tomography: Theory and Practice*, p. 613–643.

Eberhart-Phillips, D., and A. Michael (1998), Seismotectonics of the Loma Prieta, California, region determined from three-dimensional Vp, Vp/Vs, and seismicity, *Journal of Geophysical Research*, *103*(B9), 21,099–21,120.

Einarsson, P. (2008), Plate boundaries, rifts and transforms in iceland, *Jökull*, *58*, 35–58.

Einarsson et al. (2018), title pending, *Journal of Volcano and Geothermal Research*.

Ellsworth, W. L. (1977), Three dimensional velocity structure of the crust and mantle beneath the island of Hawaii, *PhD Dissertation. MIT, Cambridge U.S.A*, p. 327.

Erbas, K., et al. (2020), Continuous Microgravity Monitoring in a Volcanic Geothermal Field: Integrated Observational Approach in Þeistareykir, NE Iceland, *Proceedings World Geothermal Congress 2020*.

Evans, J., D. Eberhart-Phillips, and C. Thurber (1994), User's Manual for Simulps12 for Imaging Vp and Vp/Vs: a derivative of the "Thurber" tomographic inversion Simul3 for local earthquakes and explosions, *Open File Rep. No. 94-431, U.S. Geological Survey, Washington, D.C.*

Evans, K. F., A. Zappone, T. Kraft, N. Deichmann, and F. Moia (2012), A survey of the induced seismic responses to fluid injection in geothermal and CO_2 reservoirs in Europe, *Geothermics*, *41*, 30–54, doi: 10.1016/j.geothermics.2011.08.002.

Ferriz, H., and G. A. Mahood (2009), Eruption rates and compositional trends at Los Humeros Volcanic Center, Puebla, Mexico, *Journal of Geophysical Research*, *89*(B10), 171–209.

Flinn, E. A. (1965), Confidence region and error determinations for seismic event location, *Reviews of Geophysics*, *3*(1), 157–185.

Foulger, G., R. Long, and P. Einarsson (1983), Implosive earthquakes at the active plate boundaries in Iceland, *Nature*, *337*, 640–642.

Friðleifsson et al. (2018), title pending, *Journal of Volcanology and Geothermal Research*.

Garnier, J., and G. Papanicolaou (2009), Passive sensor imaging using cross correlations of noisy signals in a scattering medium, *SIAM Journal on Imaging Sciences*, *2*(2), 396–437.

Gassmann, F. (1951), Über die Elastizität poröser Medien, *Vierteljahrschrift der Naturforschenden Gesellschaft in Zürich*, *96*, 1–23.

Gaucher, E., T. Toledo, M. Metz, A. G. Figueroa-Soto, and M. Calò (2019), One year of passive seismic monitoring of the Los Humeros (Mexico) geothermal field, *European Geothermal Congress 2019. Den Haag, The Netherlands.*

Gautason, B., H. Ármannsson, K. Árnason, K. Saemundsson, O. G. Flóvenz, and S. Thórhallsson (2000), Thoughts on the next steps in the exploration of the Theistareykir geothermal area (in Icelandic), *Orkustofnun BG-HÁ-KÁ-KS-ÓGF-STh-2000/04*.

Geiger, L. (1912), Probability method for the determination of earthquake epicenters from the arrival time only, *Bulletin of St. Louis University*, *8*, 60–71.

Gilbert, P. (1972), Iterative methods for the three-dimensional reconstruction of an object from projections, *Journal of Theoretical Biology*, *36*(1), 105–117.

Gíslason, G., G. Johnsen, H. Ármannsson, H. Torfason, and K. Árnason (1984), Theistareykir. Surface exploration of the high-temperature geothermal area (in Icelandic), *Orkustofnun, report OS-84089/JHD-16*.

Glenn, W. E., and S. H. Ward (1976), Statistical evaluation of electrical sounding methods, part 1: Experimental design, *Geophysics*, *41*, 1207–1221.

Gomberg, J. S., K. M. Shedlock, and S. W. Roecker (1990), The effect of s-wave arrival times on the accuracy of hypocenter estimation, *Bull Seism. Soc. Am.*, *80*(6), 1605–1628.

Gordon, R., R. Bender, and G. T. Herman (1970), Algebraic reconstruction techniques (ART) for three-dimensional electron microscopy and X-ray photography, *Journal of theoretical Biology*, *29*(3), 471–481.

Granados, I., M. Calò, A. Figueroa, and P. Jousset (2020), 3D Anisotropic velocity model of the Los Humeros geothermal field, Mexico, using seismic ambient noise tomography, *EGU General Assembly 2020, Vienna, Austria*, doi:10.5194/egusphere-egu2020-12544.

Grigoli, F., et al. (2018), The November 2017 Mw 5.5 Pohang earthquake: A possible case of induced seismicity in South Korea, *Science*, *360*(6392), doi:10.1126/science.aat2010.

Gritto, R., and S. Jarpe (2014), Temporal variations of Vp/Vs-ratio at The Geysers geothermal field, USA, *Geothermics*, *52*, 112–119.

Grob, M., A. Maggi, and E. Stutzmann (2011), Observations of the seasonality of the Antarctic microseismic signal, and its association to sea ice variability, *Geophysical Research Letters*, *38*(11).

Groos, J. C., S. Bussat, and J. R. R. Ritter (2012), Performance of different processing schemes in seismic noise cross-correlations, *Geophysics Journal International*, *188*, 498–512.

Guest, T., and A. Curtis (2009), Iteratively constructive sequential design of experiments and surveys with nonlinear parameter-data relationships, *Journal of Geophysical Research*, *114*.

Gutemberg, B. (1936), On microseisms, *Bulletin of the Seismological Society of America*, *26*(2), 111–117.

Gutierrez-Negrin, L. C. A., and G. Izquierdo-Montalvo (2010), Review and Update of the Main Features of the Los Humeros Geothermal Field, Mexico, in *Proceedings World Geothermal Congress 2010 Bali, Indonesia, 25–29 April 2010*, pp. 1–7.

Gutierrez-Negrin, L. C. A., and J. L. Quijano-Leon (2004), Analysis of seismicity in the Los Humeros, Mexico, geothermal field, *Geothermal Resources Council Annual Meeting; Geothermal energy: the reliable renewable; Indian Wells, Calif.*, *28*, 467–472.

Haberland, C., A. Rietbrock, D. Lange, K. Bataille, , and T. Dahm (2009), Structure of the seismogenic zone of thesouthcentral Chilean margin revealed by local earthquake traveltime tomography, *Journal of Geophysical Research*, *114*, B01,317, doi:10.1029/2008JB005802.

Hadziioannou, C., E. Larose, O. Coutant, P. Roux, and M. Campillo (2009), Stability of monitoring weak changes in multiply scattering media with ambient noise correlation: Laboratory experiments, *The Journal of the Acoustical Society of America*, *125*(6), 3688–3695, doi:10.1121/1.3125345.

Hadziioannou, C., E. Larose, A. Baig, P. Roux, and M. Campillo (2011), Improving temporal resolution in ambient noise monitoring of seismic wave speed, *Journal of Geophysical Research*, *116*, B07,304, doi: 10.1029/2011JB008200.

Hamza, V. M., R. R. Cardoso, and C. F. Ponte Neto (2008), Spherical Harmonic Analysis of Earth's Conductive Heat Flow, *International Journal of Earth Sciences*, *97*(2), 205–226.

Hanasoge, S. M., and M. Branicki (2013), Interpreting cross-correlations of one-bit filtered noise, *Geophysics Journal International*, *195*, 1811–1830.

Hardt, M., and F. Scherbaum (1994), The design of optimum networks for aftershock recordings, *Geophysics Journal International*, *6*.

Häring, P. C., U. Schanz, F. Ladner, and B. C. Dyer (2008), Characterisation of the Basel 1 enhanced geothermal system, *Geothermics*, *37*(5), 469–495.

Harðardottir, V., K. L. Brown, T. Friðriksson, J. W. Hedenquist, M. D. Hannington, and S. Thórhalsson (2009), Metals in deep liquid of the Reykjanes geothermal system, southwest Iceland: implications for the composition of seafloor black smoker fluids, *Geology*, *37*, 1103–1106.

Herrmann, R. B. (2013), Computer programs in seismology: An evolving tool for instruction and research, *Seismological Research Letters*, *84*, 1081–1088, doi:10.1785/0220110096.

Hillers, G., M. Campillo, and K. Ma (2014), Seismic velocity variations at TCDP are controlled by MJO driven precipitation pattern and high fluid discharge properties, *Earth Planetary Science Letters*, *391*, doi:10.1016/j.epsl.2014.01.040.

Hillers, G., S. Husen, A. Obermann, T. Planès, E. Larose, and M. Campillo (2015), Noise-based monitoring and imaging of aseismic transient deformation induced by the 2006 Basel reservoir stimulation, *Geophysics*, *80*(4), KS51–KS68.

Hirschberg, S., S. Wiemer, and P. Burgherr (Eds.) (2015), *Energy from the Earth. Deep Geothermal as a Resource for the Future?*, vdf Hochschulverlag AG an der ETH Zürich, doi:10.3218/3655-8.

Huenges, E., and P. Ledru (Eds.) (2010), *Geothermal Energy Systems. Exploration, Development, and Utilization*, Wiley, 2010, doi:10.1002/9783527630479.

Husen, S., E. Kissling, and E. R. Flueh (2000), Local earthquake tomography of shallow subduction in north Chile: a combined onshore and offshore study, *Journal of Geophysical Research*, *105*(28), 183–198.

Husen, S., R. Quintero, E. Kissling, and B. Hacker (2003), Subduction-zone structure and magmatic processes beneath Costa Rica constrained by local earthquake tomography and petrological modelling, *Geophysical Journal International*, *155*, 11–32.

Husen, S., R. B. Smith, and G. P. White (2004), Evidence for gas and magmatic sources beneath the Yellowstone volcanic field from seismic tomographic imaging, *Journal of Volcanology and Geothermal Research*, *131*, 397–410.

International Energy Agency (2011), *Technology Roadmap: Geothermal Heat and Power*, 52 pp pp.

IPCC (2013), *Climate Change 2013: The Physical Science Basis. Contribution of Working Group I to the Fifth Assessment Report of the Intergovernmental Panel on Climate Change*, 1535 pp pp., Cambridge University Press.

IPCC (2014), *Climate Change 2014: Synthesis Report. Contribution of Working Groups I, II and III to the Fifth Assessment Report of the Intergovernmental Panel on Climate Change*, 151 pp pp.

Ito, H., J. DeVilbiss, and A. Nur (1979), Compressional and shear waves in saturated rock during water-steam transition, *Journal of Geophysical Research*, *84*, 4731–4735.

Jakobsdóttir, S. S. (2008), Seismicity in Iceland: 1994-2007, *Jökull*, *58*.

Jentsch, A., E. Jolie, D. G. Jones, H. Taylor-Curran, L. Peiffer, M. Zimmer, and B. Lister (2020), Magmatic volatiles to assess permeable volcano-tectonic structures in the Los Humeros geothermal field, Mexico, *Journal of Volcanology and Geothermal Research*, *394*, doi:10.1016/j.jvolgeores.2020.106820.

Jones, A. G., and J. H. Foster (1986), An objective real-time data-adaptive technique for efficient model resolution improvement in magnetotelluric studies, *Geophysics*, *51*, 90–97.

Jousset, P., C. Haberland, K. Bauer, and K. Arnasson (2011), Hengill geothermal volcanic complex (Iceland) characterized by integrated geophysical observations, *Geothermics*, *40*(1), 1–24, doi:10.1016/j.geothermics.2010.12.008.

Jousset, P., et al. (2016), Seismic Tomography in Reykjanes, SW Iceland, *In European Geothermal Congress*.

Jousset et al. (2018), Title pending, *EGU conference*.

Julian, B. R., and D. Gubbins (1977), Three-dimensional seismic ray tracing, *Journal of Geophysics*, *43*, 95–113.

Kao, H., and S. J. Shan (2007), Rapid identification of earthquake rupture plane using source-scanning algorithm, *Geophysical Journal International*, *168*, 1011–1020.

Karastathis, V., J. Papoulia, B. D. Fiore, J. Makris, A. Tsambas, A. Stampolidis, and G. Papadopoulos (2011), Deep structure investigations of the geothermal field of the North European Gulf, Greece, using 3-D local earthquake tomography and Curie point depth analysis, *Journal of Volcanology and Geothermal Research*, *206*(3), 106–120.

Karlsdóttir, R., A. M. Vilhjálmsson, K. Árnason, and A. T. Beyene (2012), Theistareykir Geothermal Area, Northern Iceland: 3D inversion of MT and TEM data, *Report ÍSOR-2012/046*, pp. 1–173.

Khodayar, M., and S. Björnsson (2013), Preliminary fracture analysis of Theistareykir geothermal field and surroundings, Northern Rift Zone and Tjörnes Fracture Zone, *Landsvirkjun Report*, *LV-2013-116*.

Khodayar, M., S. Björnsson, R. Karlsdóttir, K. Ágústsson, and M. Ólafsson (2015), Tectonic control of alteration, gases, resistivity, magnetics and gravity in Theistareykir area. Implications for Northern Rift Zone and Tjörnes Fracture Zone, *Landsvirkjun Report*, *LV-2015-039*.

Khodayar, M., S. Björnsson, S. G. Kristinsson, R. Karlsdóttir, M. Ólafsson, and S. Víkingsson (2018), Tectonic control of the Theistareykir geothermal field by rift and transform zones in north Iceland: a multidisciplinary approach, *Open Journal of Geology*, *8*, 543–584.

Kijko, A. (1977), An algorithm for the optimum distribution of a regional seismic network-I, *Pure and applied geophysics*, *115*, 999–1009.

Kirkpatrick, S., C. Gelatt, and M. Vecchi (1983), Optimization by simulated annealing, *Science*, *220*, 671–680.

Kissling, E. (1988), Geotomography with local earthquake data, *Reviews of Geophysics*, *26*, 659– 698.

Kissling, E., W. L. Ellsworth, D. Eberhard-Phillips, and U. Kradolfer (1994), Initial reference models in local earthquake tomography, *Journal of Geophysical Research: Solid Earth*, *99*, 19,635–19,646.

Kissling, E., S. Husen, and F. Haslinger (2001), Model parameterization in seismic tomography: a choice of consequences for the solution quality, *Physics of the Earth and Planetary Interiors*, *123*, 89–101.

Kraft, T., A. Mignan, and D. Giardini (2013), Optimization of a large-scale microseismic monitoring in northern Switzerland, *Geophysical Journal International*, *195*, 474–490.

Kristinsson, S. G., T. Friðriksson, M. Ólafsson, S. H. Gunnarsdóttir, and S. Níelsson (2013a), Háhitasvæðin á Þeistareykjum, í Kröflu og Námafjalli. Vöktun á yfirborðsvirkni og grunnvatni., *Iceland GeoSurvey, ISOR-2013/037, LV-2013-091*.

Kristinsson, S. G., F. Óskarsson, M. Ólafsson, A. A. Óladóttir, H. Tryggvason, H., and T. Friðriksson (2013b), Háhitasæðin í Námafjalli, Kröflu og á Þeistareykjum. Vöktun á yfirborðsvirkni og grunnvatni árið 2013, *Iceland GeoSurvey, ISOR-2013/060, LV-2013-132*.

Kristinsson, S. G., F. Óskarsson, A. A. Óladóttir, and M. Ólafsson (2015), The High Temperature Geothermal Areas at Þeistareykir, Krafla and Námafjall. Monitoring of Surface Geothermal Activity and Groundwater in the Year 2015, *Iceland GeoSurvey, Report ÍSOR-2015/059, LV-2015-125*.

Kristjánsdóttir, S. (2013), Microseismicity in Krýsuvík Geothermal Field. SW Iceland, from May to October 2009, *Master thesis*.

Landès, M., F. Hubans, N. M. Shapiro, A. Paul, and M. Campillo (2010), Origin of deep ocean microseisms by using teleseismic body waves, *Journal of Geophysical Research: Solid Earth*, *115*(B5), B05,302.

Landsvirkjun (2016), Geothermal power station at Theistareykir: Energy utilisation in Northeast Iceland, *Landsvirkjun 2016 newsletter*.

Larose, E., A. Derode, M. Campillo, and M. Fink (2004), Imaging from one-bit correlations of wideband diffuse wave fields, *Journal of Applied Physics*, *95*, 8393–8399.

Lecocq, T., C. Caudron, and F. Brenguier (2014), MSNoise, a Python Package for Monitoring Seismic Velocity Changes Using Ambient Seismic Noise, *Seismological Research Letters*, *85*, 715–726.

Lee, W. H. K., and S. W. Stewart (1981), Principles and applications of microearthquake networks, *Office of earthquake studies. U.S.G.S. Academic Press*.

Lees, J. (2004), Seismic imaging of fractures at Krafla, Iceland, *International Federation of Digital Seismograph Networks. Other/Seismic Network. 10.7914/SN/XY_2004*.

Lehujeur, M., J. Vergne, A. Maggi, and J. Schmittbuhl (2017), Ambient noise tomography with non-uniform noise sources and low aperture networks: case study of deep geothermal reservoirs in northern Alsace, France, *Geophysical Journal International*, *208*(1), 193–210.

Lermo, J., J. Soto, and A. Flores y Hurtado (2001), Estudio de la sismicidad del campo geotérmico de Los Humeros, Puebla, *Fase III, Informe Técnico Final, Instituto de Ingeniería, UNAM, elaborado para la CFE-Gerencia de proyectos Geotermoeléctricos, DEX-HU-00/2001, proyecto 0563, Internal Report*.

Lermo, J., Y. Antayhua, L. Quintanar, and C. Lorenzo (2008), Estudio sismológico del campo geotérmico de Los Humeros, Puebla, México. Parte I: Sismicidad, mecanismos de fuente y distribución de esfuerzos, *Geotermia, Revista Mexicana de Geoenergía*, *21*(1), 25–41.

Lermo, J., C. Lorenzo, Y. Antayhua, E. Ramos, and N. Jiménez (2016), Sísmica pasiva en el campo geotérmico de Los Humeros, Puebla-México y su relación con los pozos inyectores, *XVIII Congreso Peruano de Geología*, pp. 1–5.

Levenberg, K. (1944), A method for the solution of certain non-linear problems in least squares, *Q. Appl. Math*, *2*, 164–168.

Levshin, A., T. Yanocskaya, A. Lander, B. Bukchin, M. Barmin, L. Ratnikova, and E. Its (1989), Seismic surface waves in a laterally inhomogeneous earth, *Springer-Verlag*.

Lobkis, O., and R. Weaver (2003), Coda-wave interferometry in finite solids: Recovery of P-to-S conversion rates in an elastodynamic billiard, *Physical Review Letters*, *90*, 254,302, doi:10.1103/PhysRevLett.90.254302.

Löer, K., T. Toledo, G. Norini, X. Zhang, A. Curtis, and E. H. Saenger (2020), Imaging the deep structures of the Los Humeros geothermal field, Mexico, using three-component ambient noise beamforming, *Seismological Research Letters*, *91*(6), 3269–3277, doi:10.1785/0220200022.

Lomax, A. (2005), A reanalysis of the hypocentral location and related observations for the great 1906 California Earthquake, *Bulletin of the Seismological Society of America*, *95*, 861–877.

Lomax, A., J. Virieux, P. Volant, and C. Thierry-Berge (2000), Probabilistic earthquake location in 3D and layered models, in *Advances in seismic event location. Modern Approaches in Geophysics*, vol. 18, edited by Thurber, C. H. and Rabinowitz, N., p. 101–134.

Lomax, A., A. Michelini, and A. Curtis (2009), Earthquake Location, Direct, Global-Search Methods, in *Encyclopedia of Complexity and System Science, Part 5*, edited by Meyers, R. A., Springer, New York, pp. 2449–2473, doi:10.1007/978-0-387-30440-3.

Lorenzo-Pulido, C. D. (2008), Borehole geophysics and geology of well H-43, Los Humeros geothermal field, Puebla, México, *Geothermal Training Programme Report. 9. Orkustofnun, Grensásvegur, Reykjavik, Iceland*, *9*(23), 387–426.

Lucci, F., G. Carrasco-Núñez, F. Rossetti, T. Theye, J. C. White, S. Urbani, H. Azizi, Y. Asahara, and G. Giordano (2020), Anatomy of the magmatic plumbing system of Los Humeros Caldera (Mexico): implications for geothermal systems, *Solid Earth*, *11*, 125–159.

Majer, E. L., R. Baria, M. Stark, S. Oates, J. Bommer, B. Smith, and H. Asanuma (2007), Induced seismicity associated with enhanced geothermal systems, *Geothermics*, *36*, 185–222.

Marquardt, D. W. (1963), An algorithm for least-squares estimation of nonlinear parameters, *J. Soc. Ind. Appl. Math.*, *11*, 431–441.

Martinez, S., and C. Alibert (1994), Características geoquímicas de las rocas volcánicas del sistema geotérmico Los Humeros, Puebla y su relación con la mineralogía de alteración., *Geofísica Internacional*, *33*(4), 585–605.

Martins, J. E., A. Obermann, A. Verdel, , and P. Jousset (2020a), 3D-S wave velocity model of the Los Humeros geothermal field, Mexico, by ambient-noise tomography, *Abstract from EGU General Assembly 2020, Vienna, Austria*, doi:10.5194/egusphere-egu2020-21956.

Martins, J. E., C. Weemstra, E. Ruigrok, A. Verdel, P. Jousset, and G. P. Hersir (2020b), 3D S-wave velocity imaging of Reykjanes Peninsula high-enthalpy geothermal fields with ambient-noise tomography, *Journal of Volcanology and Geothermal Research*, *391*, 106,685, doi:10.1016/j.jvolgeores.2019.106685.

Maurer, H. (1993), Seismotectonics and upper crustal structure in the western swiss alps, *PhD Dissertation. ETH Zurich.*

Maurer, H., and D. E. Boerner (1998), Optimized and robust experimental design: a non-linear application to EM sounding, *Geophysics Journal International*, *132*, 458–468.

Maurer, H., A. Curtis, and D. Boerner (2010), Recent advances in optimized geophysical survey design, *Geophysics*, *75*(5).

Mavko, G., and T. Mukerji (1995), Seismic pore space compressibility and Gassman's relation, *Geophysics*, *60*, 1743–1749.

Maxwell, T. (2009), Microseismic location uncertainty, *CSEG Recorder*, *34*(4), 41–46.

McMechan, G. A. (1982), Determination of source parameters by wavefield extrapolation, *Geophysical Journal of the Royal Astronomical Society*, *71*, 613–628.

McNamara, D. E., and R. P. Buland (2004), Ambient noise levels in the continental united states, *Bulletin of the Seismological Society of America*, *94*(4), 1517–1527.

Megies, T. (2016), Obspyck 0.4.1., in *https://github.com/megies/obspyck/wiki.*

Menke, W. (2012), Geophysical data analysis: discrete inverse theory, *Elsevier/Academic Press.*

Michelini, A. (1995), An adaptative-grid formalism for traveltime tomography, *Geophysics Journal International*, *121*, 489–510.

Michelini, A., and T. McEvilly (1991), Seismological studies at Parkfield. I. Simultaneous inversion for velocity structure and hypocenters using cubic B-splines parameterization, *Bulletin of the Seismological Society of America*, *81*, 524–552.

Mitchell, T. J. (1974), An algorithm for construction of "D-optimal" experimental design., *Technometrics*, *16*, 201–210.

Mordret, A., M. Landès, N. M. Shapiro, S. Singh, P. Roux, and O. Barkved (2013), Near-surface study at the Valhall oil field from ambient noise surface wave tomography, *Geophysical Journal International*, *193*(3), 1627–1643.

Mordret, A., M. Landès, N. M. Shapiro, S. Singh, and P. Roux (2014), Ambient noise surface wave tomography to determine the shallow shear velocity structure at Valhall: depth inversion with a Neighbourhood Algorithm, *Geophysical Journal International*, *198*(3), 1514–1525, doi:10.1093/gji/ggu217.

Mordret, A., D. Rivet, M. Landès, and N. M. Shapiro (2015), Three-dimensional shear velocity anisotropic model of Piton de la Fournaise Volcano (La Réunion Island) from ambient seismic noise, *Journal of Geophysical Research: Solid Earth*, *120*, 406– 427, doi:10.1002/2014JB011654.

Mordret, A., T. D. Mikesell, C. Harig, B. P. Lipovsky, and G. A. Prieto (2016), Monitoring southwest Greenland's ice sheet melt with ambient seismic noise, *Science Advances*, *2*(5), e1501,538–e1501,538, doi: 10.1126/sciadv.1501538.

Mosegaard, K., and M. Sambridge (2002), Monte Carlo analysis of inverse problems, *Inverse Problems*, *18*, R29–R54.

Moser, T. J. (1989), Efficient seismic ray tracing using graph theory, *Society of Exploration Geophysics. 1990 Meeting., Expanded Abstracts*, p. 1106–1108.

Moser, T. J. (1991), Shortest path calculation of seismic rays, *Geophysics*, *56*, 59–67.

Muksin, U., K. Bauer, and C. Haberland (2013), Seismic Vp and Vp/Vs structure of the geothermal area around Tarutung (North Sumatra, Indonesia) derived from local earthquake tomography, *Journal of Volcanology and Geothermal Research*, *260*, 27–42, doi:10.1016/j.jvolgeores.2013.04.012.

Nakata, N., J. P. Chang, J. F. Lawrence, and P. Boué (2015), Body wave extraction and tomography at Long Beach, California, with ambient-noise interferometry, *Journal of Geophysical Research: Solid Earth*, *120*, 1159–1173, doi:10.1002/2015JB011870.

Nakata, N., L. Gualtieri, and A. Fichtner (Eds.) (2019), *Seismic Ambient Noise*, Cambridge University Press, doi:10.1017/9781108264808.

Naranjo, D. (2020), Seismological characterization of the Theistareykir geothermal field (Iceland), *Master Thesis. IDEA League-ETH Zurich.*

Norini, G., G. Groppelli, R. Sulpizio, C.-N. nez, P. G., Dávila-Harris, C. Pellicioli, F. Zucca, and R. De Franco (2015), Structural analysis and thermal remote sensing of the Los Humeros Volcanic Complex: Implications for volcano structure and geothermal exploration, *Journal of Volcanology and Geothermal Research*, *301*, 221–237, doi:10.1016/j.jvolgeores.2015.05.014.

Norini, G., et al. (2019), The structural architecture of the Los Humeros volcanic complex and geothermal field, *Journal of Volcanology and Geothermal Research*, *381*, 312 – 329, doi:10.1016/j.jvolgeores.2019.06.010.

Nuber, A., E. Manukyan, and H. Maurer (2017), Optimising measurement geometry for seismic near-surface full waveform inversion, *Geophysical Journal International*, *accepted manuscript*.

Obermann, A. (2014), Etude des proprietés elastiques de la croûte: analyse numerique et applications au bruit de fond sismique, *Sciences de la Terre. Université de Grenoble*.

Obermann, A., T. Planès, E. Larose, and M. Campillo (2013), Imaging preeruptive and coeruptive structural and mechanical changes of a volcano with ambient seismic noise, *Journal of Geophysical Research: Solid Earth*, *118*(12), 6285–6294, doi:10.1002/2013JB010399.

Obermann, A., T. Kraft, E. Larose, and S. Wiemer (2015), Potential of ambient seismic noise techniques to monitor the St. Gallen geothermal site (Switzerland), *Journal of Geophysical Research: Solid Earth*, *120*(6), 4301–4316, doi:10.1002/2014JB011817.

Obermann, A., M. Lupi, A. Modret, S. S. Jakobsdóttir, and S. A. Miller (2016), 3D-ambient noise Rayleigh wave tomography of Snæfellsjökull volcano, Iceland, *Journal of Volcanology and Geothermal Research*, *317*, 42–52.

Óskarsson, F. (2011), Háhitaholur á Þeistareykjum. efnasamsetning vökva og gufu, *Iceland GeoSurvey, report, ISOR-2011/068*.

O'Neel, S., H. P. Marshall, D. E. McNamara, , and W. T. Pfeffer (2007), Seismic detection and analysis of icequakes at Columbia Glacier, Alaska, *Journal of Geophysical Research: Earth Surface*, *112*(F3).

Pavlis, G. L. (1986), Appraising earthquake hypocenter location errors: a complete, practical approach for single-event locations, *Bulletin of the Seismological Society of America*, *76*, 1699–1717.

Persson, P.-O., and G. Strang (2004), A simple mesh generator in MATLAB, *SIAM Journal on Applied Mathematics*, *46*(2), 329–345.

Philips, W. S., J. T. Rutledge, and L. House (2002), Induced micro-earthquake patterns in hydrocarbon and geothermal reservoirs: six case studies, *Pure and Applied Geophysics*, *159*, 345–369.

Planès, T., and E. Larose (2013), A review of ultrasonic Coda Wave Interferometry in concrete, *Cement and Concrete Research*, *53*, 248 – 255.

Planès, T., A. Obermann, V. Antunes, and M. Lupi (2020), Ambient-noise tomography of the Greater Geneva Basin in a geothermal exploration context, *Geophysical Journal International*, *220*, 370–383, doi:10.1093/gji/ggz457.

Podvin, P., and I. Lecomte (1991), Finite difference computations of travel-times in very contrasted velocity models: a massive parallel approach and its associated tools, *Geophysical Journal International*, *105*, 271–284.

Portier, N., et al. (2020), 2017-2019 hybrid micro-gravity monitoring of the Theistareykir geothermal field (North Iceland), *EGW 2020*.

Poupinet, G., W. Ellsworth, and J. Frechet (1984), Monitoring velocity variations in the crust using earthquake doublets: An application to the Calaveras Fault, California, *Journal of Geophysical Research: Solid Earth*, *89*(4), 5719–5731, doi:10.1029/JB089iB07p05719.

Quezadas-Flores, A. (1961), Las rocas del basamento de la cuenca Tampico-Mizantla: México, D.F., *Boletín de la Asociación Mexicana de Geólogos Petroleros*, *13*, 289=305.

Rabinowitz, N., and D. Steinberg (1990), Optimal configuration of a seismographic network: a statistical approach, *Bulletin of the Seismological Society of America*, *80*, 187–196.

Ratdomopurbo, A., and G. Poupinet (1995), Monitoring a temporal change of seismic velocity in a volcano: Application to the 1992eruption of Mt. Merapi (Indonesia), *Geophysical Research Letters*, *22*(7), 775–778.

Rawlinson, N., and M. Sambridge (2003), Seismic traveltime tomography of the crust and lithosphere, *Advances in Geophysics*, *46*, 81–199.

Rocha-López, S., G. Ramírez-Silva, E. Jiménez-Salgado, and C. Lorenzo-Pulido (2010), Results of geological–geophysics drilling of the well H–43 the geothermal field in Humeros, Pue. Mexico., in *Proceedings World Geothermal Congress 2010, Bali, Indonesia.*

Roecker, S. W. (1981), Seismicity and tectonics of the Pamir-Hindu Kush region of central Asia, *PhD Dissertation. MIT, Cambridge, U.S.A.*, p. 140.

Romo-Jones, J., L. Gutiérrez-Negrín, C. Sánchez-Cornejo, G.-A. N., and A. García-Gutiérrez (2018), 2017 Mexico country report, *In: IEA Geothermal*, p. 1–7.

Sabra, K. G., P. Gerstoft, P. Roux, W. A. Kuperman, and M. C. Fehler (2005a), Extracting timedomain Green's function estimates from ambient seismic noise, *Geophysical Research Letters*, *32*(3), L03,310.

Sabra, K. G., P. Gerstoft, P. Roux, W. A. Kuperman, and M. C. Fehler (2005b), Surface wave tomography from microseisms in Southern California, *Geophysical Research Letters*, *32*(14), L14,311.

Saemundsson, K. (2007), The geology of Theistareykir (in Icelandic), *Iceland GeoSurvey, report ÍSOR-07270.*

Saemundsson, K., A. Hjartarson, I. Kaldal, Sigurgeirsson, S. G. M.Á., Kristinsson, and S. Víkingsson (2012), Geological Map of Northern Volcanic Zone, Iceland. Northern Part. 1:100.000. Reykjavík, Iceland, *Iceland GeoSurvey and Landsvirkjun.*

Sambridge, M. (1999), Geophysical inversion with a neighborhood algorithm. I. Searching a parameter space., *Geophysical Journal International*, *138*(2), 479–494.

Sambridge, M., and K. Mosegaard (2002), Monte Carlo methods in geophysical inverse problems, *Reviews of Geophysics*, *40*(3), 1009, doi:10.1029/2000RG000089.

Sambridge, M. S., and B. L. N. Kennett (1986), A novel method of hypocenter location, *Geophysical Journal International*, *87*(2), 679–697, doi:10.1111/j.1365-246X.1986.tb06644.x.

Sambridge, M. S., and B. L. N. Kennett (1990), Boundary value ray tracing in a heterogeneous medium: A simple and versatile algorithm, *Geophysical Journal International*, *101*, 157–168.

Sambridge, M. S., and B. L. N. Kennett (2001), Seismic event location: nonlinear inversion using a neighbourhood algorithm, *Pure applied Geophysics*, *158*, 241–257.

Sánchez-Pastor, P., A. Obermann, and M. Schimmel (2018), Detecting and locating precursory signals during the 2011 El Hierro, Canary Islands, *Geophysical Research Letters*, *45*(19), 10,288–10,297, doi:10.1029/2018GL079550.

Sánchez-Pastor, P., A. Obermann, M. Schimmel, C. Weemstra, A. Verdel, and P. Jousset (2019), Short- and long-term variations in the Reykjanes geothermal reservoir from seismic noise interferometry, *Geophysical Research Letters*, *46*(11), 5788–5798, doi:10.1029/2019GL082352.

Schimmel, M. (1999), Phase cross-correlations: Design, comparisons, and applications, *Bulletin of the Seismological Society of America*, *89*.

Schimmel, M., and H. Paulssen (1997), Noise reduction and detection of weak, coherent signals through phase-weighted stacks, *Geophysical Journal International*, *130*, 497–505.

Schimmel, M., E. Stutzmann, and J. Gallart (2011), Using instantaneous phase coherence for signal extraction from ambient noise data at a local to a global scale, *Geophysical Journal International*, *184*(1), 494–506, doi:10.1111/j.1365-246X.2010.04861.x.

Schimmel, M., E. Stutzmann, and S. Ventosa (2018), Low-frequency ambient noise autocorrelations: Waveforms and normal modes, *Geophysical Journal International*, *89*(4), 1488–1496, doi:10.1785/0220180027.

Seats, K. J., J. F. Lawrence, and G. A. Prieto (2012), Improved ambient noise correlation functions using Welch's method, *Geophysical Journal International*, *188*, 513–523.

Sens-Schönfelder, C., and U. Wegler (2006), Passive image interferometry and seasonal variations of seismic velocities at Merapi Volcano, Indonesia, *Geophysical Research Letters*, *33*(21), doi:10.1029/2006GL027797.

Shapiro, N. M., and M. Campillo (2004), Emergence of broadband Rayleigh waves from correlations of the ambient seismic noise, *Geophysical Research Letters*, *31*, doi:10.1029/2004GL019491.

Shapiro, N. M., M. Campillo, L. Stehly, and M. H. Ritzwoller (2005), High resolution surface-wave tomography from ambient seismic noise, *Science*, *307*(5715), 1615–1618.

Shearer, P. (Ed.) (2009), *Introduction to Seismology*, Cambridge: Cambridge University Press.

Shimsoni, Y., E. Mizrachi, D. M. Steinberg, and N. Rabinowitz (1992), OPTINET: A computer program for designing the optimal configuration of a seismographic network, *Inst. Petroleum Res. and Geophys.*, *Report No 321/47/91(4)*.

Snieder, R. (2002), Coda wave interferometry and the equilibrium of energy in elastic media, *Physical review E: Statistical, Nonlinear and Soft Matter Physics*, *66*, 046,615.

Snieder, R., A. Grêt, H. Douma, and J. Scales (2002), Coda wave interferometry for estimating nonlinear behavior in seismic velocity, *Science*, *295*(5563), 2253–2255.

Stefánsson, R., G. B. Guðmundsson, and P. Halldórsson (2008), Tjörnes Fracture Zone. New and Old Seismic Evidences for the Link between the North Iceland Rift Zone and the Mid-Atlantic Ridge, *Tectonophysics*, *447*, 117–126, doi:10.1016/j.tecto.2006.09.019.

Stefánsson, R., et al. (1993), Earthquake prediction research in the South Iceland seismic zone and the SIL project , *Bulletin of the Seismological Society of America*, *83*(3), 696–716.

Stehly, L., M. Campillo, and N. M. Shapiro (2006), A study of the seismic noise from its long-range correlation properties, *Journal of Geophysical Research: Solid Earth*, *111*, B10,306, doi:10.1029/2005JB004237.

Stehly, L., P. Cupillard, and B. Romanowicz (2011), Towards improving ambient noise tomography using simultaneously curvelet denoising filters and SEM simulations of seismic ambient noise, *Comptes Rendus Geoscience*, *343*, 591–599, doi:10.1016/j.crte.2011.03.005.

Steinberg, D. M., and N. Rabinowitz (2003), Optimal seismic monitoring for event location with application to on site inspection of the comprehensive nuclear test ban treaty, *Metrika*, *58*(1), 31–57.

Steinberg, D. M., N. Rabinowitz, Y. Shimshoni, and D. Mizrachi (1995), Configuring a seismographic network for optimal monitoring of fault lines and multiple sources, *Bulletin of the Seismological Society of America*, *85*(6), 1847–1857.

Stutzmann, E., M. Schimmel, G. Patau, and A. Maggi (2009), Global climate imprint on seismic noise, *Geochemistry, Geophysics, Geosystems*, *10*, Q11,004, doi:10.1029/2009GC002619.

Sufri, O., K. D. Koper, R. Burlacu, and B. de Foy (2014), Microseisms from superstorm sandy, *Earth and Planetary Science Letters*, *402*, 324–336.

Surono, M., et al. (2012), The 2010 explosive eruption of Java's Merapi volcano - a '100-year' event, *Journal of Volcanology and Geothermal Research, Elsevier*, *241-242*, 121–135.

Sveinbjornsdottir, A. E., H. Ármannsson, M. Ólafsson, F. Óskarsson, S. Markússon, and S. Magnusdóttir (2013), The Theistareykir geothermal field, NE Iceland. isotopic characteristics and origin of circulating fluids, *Procedia Earth and Planetary Science*, *7*, 822–825.

Taira, T., A. Nayak, F. Brenguier, and M. Manga (2018), Monitoring reservoir response to earthquakes and fluid extraction, Salton Sea geothermal field, California, *Science Advances*, *4*(1), doi:10.1126/sciadv.1701536.

Tarantola, A. (2005), Inverse problem theory and methods for model parameter estimation, *Society for Industrial and Applied Mathematics, Philadelphia.*

Tester, J. W., et al. (2006), The future of geothermal energy – impact of enhanced geothermal systems (EGS) on the United States in the 21st century, *MIT - Massachusetts Institute of Technology, Cambridge, MA.*

Thoroddsen, T. (1983), Die Geschichte der Isländischen Vulkane, *Det Kongelige Danske Vidernskabernes Selskab, Höst og Sön, Copenhagen.*

Thurber, C. (1993), Local earthquake tomography: velocities and Vp/Vs – theory, in *Seismic Tomography: Theory and Practice*, edited by H. Iyer and K. Hirahara, p. 563–583, Chapman and Hall.

Thurber, C. H. (1983), Earthquake locations and three-dimensional crustal structure in the Coyote Lake area, central California, *Journal of Geophysical Research: Solid Earth*, *88*, 8226–8236.

Thurber, C. H. (1992), Hypocenter-velocity structure coupling in local earthquake tomography, *Physics of the Earth and Planetary Interiors*, *75*(1), 55–62.

Thurber, C. H., and D. Eberhart-Phillips (1999), Local earthquake tomography with flexible gridding, *Computers & Geosciences*, *25*, 809–818.

Toledo, T., E. Gaucher, M. Metz, M. Calò, A. Figueroa, J. Angulo, P. Jousset, K. Kieling, and E. Saenger (2019), Dataset of the 6G seismic network at Los Humeros, 2017-2018., *GFZ Data Services. Other/Seismic Network*, doi:10.14470/1T7562235078.

Toledo, T., E. Gaucher, P. Jousset, A. Jentsch, C. Haberland, H. Maurer, C. Krawczyk, M. Calò, and A. Figueroa (2020a), Local earthquake tomography at Los Humeros geothermal field (Mexico), *Journal of Geophysical Research: Solid Earth*, *125*, doi:10.1029/2020JB020390.

Toledo, T., P. Jousset, H. Maurer, and C. Krawczyk (2020b), Optimized experimental network design for earthquake location problems: applications to geothermal and volcanic field seismic networks., *Journal of Volcanology and Geothermal Research*, pp. 0377–0273, doi:10.1016/j.jvolgeores.2018.08.011.

Toledo, T., A. Obermann, P. Jousset, A. Verdel, J. Martins, K. Erbas, A. Mortensen, and C. Krawczyk (2021), Ambient seismic noise monitoring and imaging at the Theistareykir geothermal field (Iceland), *In preparation.*

Toomey, D., and G. Foulger (1989), Tomographic inversion of local earthquake data from the Hengill–Grensdalur Central Volcano Complex, Iceland. , *Journal of Geophysical Research*, *94*(B12), 17,497–17,510.

Trnkoczy, A. (2012), Understanding and parameter setting of STA/LTA trigger algorithm, in *New Manual of Seismological Observatory Practice 2 (NMSOP-2), IS 8.1*, p. 20, doi:0.2312/GFZ.NMSOP-2_IS_8.1.

Uhrhammer, R. (1980), Analysis of small seismographic station networks, *Bulletin of the Seismological Society of America*, *70*, 1369–1379.

Um, J., and C. Thurber (1987), A fast algorithm for two-point seismic ray tracing, *Bulletin of the Seismological Society of America*, *77*, 972–986.

Urban, E., and J. Lermo (2013), Local seismicity in the exploitation of Los Humeros geothermal field, Mexico, in *38th Workshop on Geothermal Reservoir Engineering, Stanford, CA, USA, SGP-TR-198.*

Urbani, S., G. Giordano, F. Lucci, F. Rossetti, V. Acocella, and G. Carrasco-Núñez (2020), Estimating the depth and evolution of intrusions at resurgent calderas: Los Humeros (Mexico), *Solid Earth*, *11*, 527–545.

Valtonen, O., M. Uski, A. Korja, T. Tiira, and J. Kortström (2013), Optimal configuration of a micro-earthquake network, *Advances in Geosciences*, *33*, 33–36.

Vanorio, T., J. Virieux, P. Capuano, , and G. Russo (2005), Three-dimensional seismic tomography from P wave and S wave microearthquake travel times and rock physics characterization of the Campi Flegrei Caldera, *Journal of Geophysical Research: Solid Earth*, *110*, B03,201, doi:10.1029/2004JB003102.

Červený, V. (1987), Ray tracing algorithms in three-dimensional laterally varying layered structures, in *Seismic tomography: With applications in global seismology and exploration geophysics*, edited by G. Nolet, pp. 99–133, D. Reidel, Dordrecht.

Červený, V. (2001), *Seismic Ray Theory*, 99-133 pp., Cambridge University Press, Cambridge.

Verdel, A., B. Boullenger, J. Martins, A. Obermann, T. Toledo, and P. Jousset (2019), Ambient noise seismic reflection interferometry at the Los Humeros geothermal field, Mexico, *Proceedings of the European Geothermal Congress 2019, Den Haag, The Netherlands.*

Verdel, A., et al. (2016), Reykjanes ambient noise reflection interferometry., *Proceedings of the European Geothermal Congress 2016, Strasbourg, France.*

Vidale, J. (1988), An overview of full-waveform inversion in exploration geophysics, *Bulletin of the Seismological Society of America*, *78*(6), 2062–2076.

Vidale, J. (1990), Finite-difference calculations of traveltimes in three dimensions, *Geophysics*, *55*, 521–526.

Viniegra, F. (1965), Geología del macizo de Teziutlán y la Cuenca Cenozoica de Veracruz., *Asociación Mexicana de Geólogos petroleros*, *17*, 101–163.

Wapenaar, K. (2004), Retrieving the elastodynamic Green's function of an arbitrary inhomogeneous medium by cross correlation, *Physical Review Letters*, *93*(25), 254,301.

Wapenaar, K., and J. Fokkema (2006), Green's function representations for seismic interferometry, *Geophysics*, *71*(4), SI33–SI46.

Webb, S. C. (2007), The Earth's 'hum' is driven by ocean waves over the continental shelves, *Nature*, *445*, 754–756.

Weemstra, C., A. Obermann, A. Verdel, B. Paab, H. Blanck, E. A. Gudnason, G. P. Hersir, P. Jousset, and O. Sigurdsson (2016), Time-lapse seismic imaging of the Reykjanes geothermal reservoir, *Proceedings of the European Geothermal Congress 2016, Strasbourg, France.*

Wegler, U., and C. Sens-Schönfelder (2007), Fault zone monitoring with passive image interferometry, *Geophysical Journal International*, *168*(3), 1029–1033, doi:10.1111/j.1365-246X.2006.03284.x.

Welch, P. D. (1967), The use of fast Fourier transform for the estimation of power spectra: A method based on time-averaging over short, modified periodograms, *IEEE Transactions on Audio and Electroacoustics*, *15*, 70–73.

Werner, C., and E. H. Saenger (2018), Obtaining reliable source locations with time reverse imaging: limits to array design, velocity models and signal-to-noise ratios, *Solid Earth*, *9*(6), 1487–1505.

White, D. J. (1989), Two-dimensional seismic refraction tomography, *Geophysical Journal International*, *97*(2), 223–245.

Wilkinson, P., P. Meldrum, J. Chambers, O. Kuras, and R. Ogilvy (2006), Improved strategies for the automatic selection of optimized sets of electrical resistivity tomography measurement configurations, *Geophysical Journal International*, *167*, 1119–1126.

Wilkinson, P. B., P. I. Meldrum, J. E. Chambers, O. Kuras, and R. D. Ogilvy (2004), Improved strategies for the automatic selection of optimized sets of electrical resistivity tomography measurement and configurations, *Geophysical Journal International*, *167*, 1119–1126.

Withers, M., R. Aster, C. Young, J. Beiriger, M. Harris, S. Moore, and J. Trujillo (1998), A comparison of select trigger algorithms for automated global seismic phase and event detection, *Bulletin of the Seismological Society of America*, *88*(1), 95–106.

Withers, M. M., R. C. Aster, C. J. Young, and E. P. Chael (1996), High-frequency analysis of seismic background noise as a function of wind speed and shallow depth, *Bulletin of the Seismological Society of America*, *86*(5), 1507–1515.

Witten, B., and B. Artman (2011), Signal-to-noise estimates of time reverse images, *Geophysics*, *76*(2), MA1–MA10.

Yáñez, C., and S. García (1982), Exploración de la región geotérmica Los Humeros-Las Derrumbadas, Estados de Puebla y Veracruz, *C.F.E. Internal report*, p. 96.

Zelt, C. (1998), Lateral velocity resolution from three-dimensional seismic refraction data, *Geophysical Journal International*, *135*, 1101–1112, doi:10.1046/j.1365-246X.1998.00695.x.

Zhan, Z., V. C. Tsai, and R. W. Clayton (2013), Spurious velocity changes caused by temporal variations in ambient noise frequency content, *Geophysical Journal International*, *194*(3), 1574–1581, doi:10.1093/gji/ggt170.

A

Contributions to the publications

This is a cumulative thesis based on articles that are published or in preparation status. It is submitted to the Faculty VI of the Technical University of Berlin and follows its guideline for cumulative dissertations. The results in Chapter 6 and Chapter 7 are published in Elsevier's *Journal of Volcanology and Geothermal Research* and AGU's *Journal of Geophysical Research: Solid Earth*, respectively. In addition, the data publication associated to Chapter 7 is available at the GFZ's GEOFON Data Center. Finally, the results of Chapter 8 correspond to a manuscript in preparation. In the following I outline the contribution of each author to each publication.

Chapter 6

Optimized experimental network design for earthquake location problems: Applications to geothermal and volcanic field seismic networks, *Journal of Volcanology and Geothermal Research*, 2020, (391) by Tania Toledo[1], Philippe Jousset[2], Hansruedi Maurer[3], Charlotte Krawczyk[4]

As a first author I programmed the sequential survey design algorithm described in the publication. I subsequently computed the test cases and applied the algorithm to the two case studies showcased therein. Then, I prepared the manuscript and figures, and discussed the final results. Authors 2 and 3 guided me through the principles and ideas behind survey design and vastly contributed in reshaping the methodology used. Finally, authors 2, 3, and 4 corrected and improved the submitted manuscript and greatly supported me with the received journal's revisions and modifications of the techniques used.

Chapter 7

Local Earthquake Tomography at Los Humeros Geothermal Field (Mexico), *Journal of Geophysical Research: Solid Earth*, 2020, 125, by Tania Toledo[1], Emmanuel

Gaucher[2], Philippe Jousset[3], Anna Jentsch[4], Christian Haberland[5], Hansruedi Maurer[6], Charlotte Krawczyk[7], Marco Calò[8], Ángel Figueroa[9]

Authors 1, 8, and 9 contributed with the seismic data acquisition. The set up and tunning of the earthquake detection algorithm was performed by authors 1 and 2, and the phase picking by authors 1, 2, and 3. The seismic processing (1D and 3D inversions) was computed by me with close guidance of authors 2, 3, 5, and 6. Authors 5 and 8 contributed with post-processing suggestions. Authors 2 and 4 assisted me with the integration of available geological and geophysical data collected at Los Humeros and with the results interpretation. I prepared the submitted manuscript, tables, and images therein. However, Figures 7.1, 7.15, and 7.17 and Table 7.1 were prepared in close collaboration with author 4. Then all co-authors critically revised and corrected the complete manuscript, contributed to the results discussion, and assisted me with the responses to the journal's revisions (especially authors 2, 5, and 7). My colleague James Mechie improved the writing as a native English speaker during the article resubmission.

Dataset of the 6G seismic network at Los Humeros, 2017-2018. *GFZ Data Services. Other/Seismic Network*, 2019, by Tania Toledo[1], Emmanuel Gaucher[2], Malte Metz[3], Marco Calò[4], Angel Figueroa[5], Joel Angulo[6], Philippe Jousset[7], Katrin Kieling[8], Erik Saenger[9]

Several tasks were required for the data acquisition, preparation, and quality control of the seismic database. The contributions to each of these tasks are listed as follows:

- **Network design**

  Authors 1, 2, 4, 5, 7, 9

- **Equipment preparation**

  Authors 1, 4, 5, 6, 7, 8, 9 in collaboration with Geophysical Instrument Pool Potsdam (GIPP), Universidad Nacional Autónoma de México (UNAM), and Universidad Michoacana de San Nicolás de Hidalgo (UMSNH) members.

- **Station position scouting and installation**

  Authors 1, 4, 5, 6 in collaboration with UNAM and UMSNH members.

- **Data collection**

  Authors 4, 5, 6 in collaboration with UNAM and UMSNH members.

- **Seismic database construction and QC**

  Authors 1, 2, 3

- **Metadata assembly**

  Authors 1, 2, 3

Chapter 8

Ambient seismic noise monitoring and imaging at the Theistareykir geothermal field (Iceland), *in preparation*, 2021, by Tania Toledo[1], Anne Obermann[2], Philippe Jousset[3], Arie Verdel[4], Joana Martins[5], Kemal Erbas[6], Anette Mortensen[7], Charlotte Krawczyk[8]

As a first author I carried out the seismic processing, wrote the manuscript, and prepared all the figures therein. Author 2 supported me with codes for obtaining the dispersion curves and for performing ANSWT workflow. Then authors 2, 3, 4, and 5 closely guided me through the theoretical principles of ANSWT and CWI, and vastly contributed in redirecting and reshaping the processing that I carried out. Authors 6 and 7 were responsible for the data collection and revision of the interpretation in relation to the available and new geophysical and geological data. Finally, all co-authors critically revised and corrected the complete manuscript which is currently in preparation.

B
Statutory declaration

I declare that I have authored this thesis independently, that I have not used any other than the declared sources, and that I have explicitly marked all the material which has been quoted either literally or by content from the used sources.

....
Date and signature